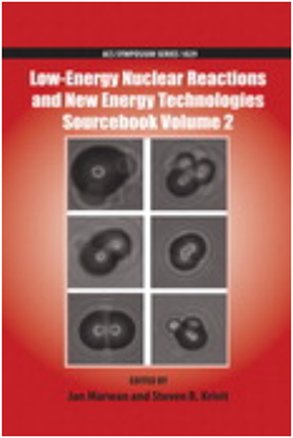

ACS SYMPOSIUM SERIES 1029

Low-Energy Nuclear Reactions and New Energy Technologies Sourcebook Volume 2

EDITED BY

Jan Marwan and Steven B. Krivit

Downloaded by 89.163.35.42 on June 28, 2012 | http://pubs.acs.org
Publication Date (Web): December 20, 2009 | doi: 10.1021/bk-2009-1029.fw001

Low-Energy Nuclear Reactions and New Energy Technologies Sourcebook Volume 2

Downloaded by 89.163.35.42 on June 28, 2012 | http://pubs.acs.org
Publication Date (Web): December 20, 2009 | doi: 10.1021/bk-2009-1029.fw001

Downloaded by 89.163.35.42 on June 28, 2012 | http://pubs.acs.org
Publication Date (Web): December 20, 2009 | doi: 10.1021/bk-2009-1029.fw001

ACS SYMPOSIUM SERIES **1029**

Low-Energy Nuclear Reactions and New Energy Technologies Sourcebook Volume 2

Jan Marwan, Editor
Dr. Marwan Chemie

Steven B. Krivit, Editor
New Energy Times

Sponsored by the
ACS Division of Environmental Chemistry

American Chemical Society, Washington DC

In Low-Energy Nuclear Reactions and New Energy Technologies Sourcebook Volume 2; Marwan, J., et al.;
ACS Symposium Series; American Chemical Society: Washington, DC, 2010.

Library of Congress Control Number: 2009280130

ISBN 978-0-8412-2454-4

The paper used in this publication meets the minimum requirements of American National Standard for Information Sciences—Permanence of Paper for Printed Library Materials, ANSI Z39.48−1984.

Copyright © 2009 American Chemical Society

Distributed by Oxford University Press

All Rights Reserved. Reprographic copying beyond that permitted by Sections 107 or 108 of the U.S. Copyright Act is allowed for internal use only, provided that a per-chapter fee of $40.25 plus $0.75 per page is paid to the Copyright Clearance Center, Inc., 222 Rosewood Drive, Danvers, MA 01923, USA. Republication or reproduction for sale of pages in this book is permitted only under license from ACS. Direct these and other permission requests to ACS Copyright Office, Publications Division, 1155 16th Street, N.W., Washington, DC 20036.

The citation of trade names and/or names of manufacturers in this publication is not to be construed as an endorsement or as approval by ACS of the commercial products or services referenced herein; nor should the mere reference herein to any drawing, specification, chemical process, or other data be regarded as a license or as a conveyance of any right or permission to the holder, reader, or any other person or corporation, to manufacture, reproduce, use, or sell any patented invention or copyrighted work that may in any way be related thereto. Registered names, trademarks, etc., used in this publication, even without specific indication thereof, are not to be considered unprotected by law.

PRINTED IN THE UNITED STATES OF AMERICA

About the Cover

The images on the front cover are of solid-state nuclear track detectors (SSNTDs) used in the SPAWAR LENR co-deposition experiments. Each image is a composite, an overlay of one image focused on the surface of the detector and another image focused on the bottom of the tracks. The SSNTD detectors used in the electrochemistry experiments provide evidence for the emission of both charged and neutral particles. Images taken by and used with permission of Pamela Mosier-Boss.

Downloaded by 89.163.35.42 on June 28, 2012 | http://pubs.acs.org
Publication Date (Web): December 20, 2009 | doi: 10.1021/bk-2009-1029.fw001

In Low-Energy Nuclear Reactions and New Energy Technologies Sourcebook Volume 2; Marwan, J., et al.;
ACS Symposium Series; American Chemical Society: Washington, DC, 2010.

Foreword

The ACS Symposium Series was first published in 1974 to provide a mechanism for publishing symposia quickly in book form. The purpose of the series is to publish timely, comprehensive books developed from the ACS sponsored symposia based on current scientific research. Occasionally, books are developed from symposia sponsored by other organizations when the topic is of keen interest to the chemistry audience.

Before agreeing to publish a book, the proposed table of contents is reviewed for appropriate and comprehensive coverage and for interest to the audience. Some papers may be excluded to better focus the book; others may be added to provide comprehensiveness. When appropriate, overview or introductory chapters are added. Drafts of chapters are peer-reviewed prior to final acceptance or rejection, and manuscripts are prepared in camera-ready format.

As a rule, only original research papers and original review papers are included in the volumes. Verbatim reproductions of previous published papers are not accepted.

ACS Books Department

Downloaded by 89.163.35.42 on June 28, 2012 | http://pubs.acs.org
Publication Date (Web): December 20, 2009 | doi: 10.1021/bk-2009-1029.fw001

Preface

Jan Marwan

Low-energy nuclear reaction research is unlike thermonuclear fusion research. Many publications report on various LENR methods by which nuclear reactions are produced and demonstrated at room temperature. The experimental methods to demonstrate these phenomena range from the use of gunpowder and laser techniques to the attempt to electrochemically induce nuclear fusion and fission and create significant excess heat within the palladium or nickel metal lattice exposed to a deuterium- or hydrogen-containing solution.

Palladium is well-known for its ability to absorb large quantities of hydrogen/deuterium into the bulk metal, where the nuclei, electrochemically inserted, occupy interstitial octahedral/tetrahedral sites dependent on the specific palladium–deuteride/hydride phase. Using this approach, Martin Fleischmann proposed the idea of electrochemically inserting deuterium into bulk palladium so that the probability for deuterium nuclei to react and collide efficiently might increase.

Based on this idea of generating nuclear fusion within the metal lattice in 1989, Fleischmann and his colleague Stanley Pons designed an experiment involving an electrochemical cell using a heavy-water solution with the corresponding electrolyte and a palladium cathode. The energetic output generated after many days of electrolysis was found to be many orders of magnitude higher than expected on the basis of any known chemical reaction, and from this Fleischmann and Pons concluded that a nuclear reaction involving deuterium nuclei inside the palladium metal had occurred.

This phenomenon, initially named “N-fusion” by Fleischmann and Pons and promoted by the University of Utah as an opportunity to solve the energy problems of the future, instantly attracted worldwide attention. As quickly as the fusion phenomenon became the most crucial and important science topic of the day, the interest declined because of the lack of reproducibility.

Research scientists from all over the world, after learning of the news announcement, attempted to replicate the experiment in their labs. Unfortunately, most of them lacked crucial information about the experiment. This, together with the well-known contradiction in physics that deuterons are very unlikely to collide efficiently at room temperature because of the enormous amount of energy required to overcome the Coulomb barrier, caused mainstream science to dismiss the entire subject as error.

Twenty years later, we can see that progress came slowly but steadily. The few scientists who maintained an open interest and continuing commitment to explore the unknown had to contend with the shame and disgrace of being associated with a field of science that had been labelled illegitimate.

Some of the LENR scientists have worked on replications of the original Fleischmann-Pons electrolysis experiment. Many others have explored new ground, performing experiments with deuterium gas and a variety of approaches.

Downloaded by 89.163.35.42 on June 28, 2012 | http://pubs.acs.org
Publication Date (Web): December 20, 2009 | doi: 10.1021/bk-2009-1029.pr001

Many of these approaches and effects go well beyond the initial Fleischmann-Pons electrolytic effect.

The researchers have set out to determine and evaluate the experimental parameters that may play a significant role in this process and to give plausible explanations to theoretical approaches. The work they have done is tremendous, and comparing the experimental results achieved, combined with the profound understanding of the LENR process they have acquired, suggests a promising research topic to discover and exploit perhaps the most auspicious alternative energy source.

With limited funding and maximum resistance from science orthodoxy, the LENR scientists succeeded, regardless of the small and at times non-existent research budgets available to them. Their efforts are characterised by hard work and intensive research performed in their mostly privately funded labs, in loneliness, without acknowledgment and recognition, separated and isolated from mainstream science. That was the past. The research has now achieved notable recognition as a new, legitimate field of science, and LENR is now poised to become a significant part of the future of science.

Although LENR may become an option to provide energy for private households, industry and the transportation sector, running the economy on the basis of an intensive use of a raw material as costly as palladium is impractical and, in the long term, perhaps impossible.

Therefore, it is useful to point out the LENR studies of the nickel-hydrogen system: raw materials that are far less expensive than palladium and heavy water and, hence, more likely to be considered as the materials on which to run a true hydrogen economy.

Considering the accelerating energy crisis, growing worldwide demands for increased energy, and geopolitical instabilities that are largely to do with energy resources, the possibilities suggested by LENR come at an ideal time. We are beginning to see this historic science development find inclusion as a research topic in university chemistry and physics settings worldwide. Although the promises of the field remain tentative, the interest in this exciting new field is nevertheless being received enthusiastically.

LENR does not appear to fit into current scientific understanding, and it raises uncomfortable questions about current and historical understandings of nuclear physics. The path forward will require new openness, receptivity and tolerance. It may require flexibility on the part of orthodox physicists to learn from LENR researchers. It may also require LENR researchers to learn from orthodox physics. Together, the disciplines of chemistry and physics are building and will continue to build the foundation of a new field of science.

LENR excess heat and transmutations may require science to throw away older conventions in order to make a new start based on a different fundamental perspective. On the other hand, perhaps a new perspective from conventional physics will arrive that will encompass the new knowledge of LENR without the abandonment of time-tested principles of science.

This book is a starting place that outlines fundamental aspects of a new science that may help us to provide solutions to make a more liveable world in the course of this century.

Downloaded by 89.163.35.42 on June 28, 2012 | http://pubs.acs.org
Publication Date (Web): December 20, 2009 | doi: 10.1021/bk-2009-1029.pr001

Acknowledgments

The editors thank the American Chemical Society Books Department and the ACS Division of Environmental Chemistry, Inc. for sponsoring this book. We also thank the authors who contributed chapters to this book and the volunteer reviewers who greatly improved the quality of this book. We would like to thank Cindy Goldstein for her help in the production of this book and express our appreciation to the sponsors of New Energy Institute for their support.

Jan Marwan

Dr. Marwan Chemie
Rudower Chaussee 29
12489 Berlin
Germany
info@marwan-chemie.fta-berlin.de
http://marwan-chemie.com/

Steven B. Krivit

Editor, *New Energy Times*
369–B Third Street
Suite 556
San Rafael, CA 94901
steven1@newenergytimes.com
http://newenergytimes.com/

Downloaded by 89.163.35.42 on June 28, 2012 | http://pubs.acs.org
Publication Date (Web): December 20, 2009 | doi: 10.1021/bk-2009-1029.pr001

Downloaded by 89.163.35.42 on June 28, 2012 | http://pubs.acs.org
Publication Date (Web): December 20, 2009 | doi: 10.1021/bk-2009-1029.ch001

Chapter 1

Introduction

Steven B. Krivit

This introduction presents views on the topics of low-energy nuclear reaction and bubble nuclear fusion research and provides an overview of the papers in this volume.

Low-Energy Nuclear Reactions and New Energy Technologies Sourcebook Volume 2 communicates recent exemplary work in low-energy nuclear reaction and new energy technology research.

This book is by no means a complete reference for the extensive work that has been performed in these fields. However, taken in the context of other volumes, it is a reliable resource and broad reference tool.

This sourcebook continues the presentation of some of the best experimental and theoretical research in the LENR field. As well, this volume includes another novel area of nuclear energy research, bubble nuclear fusion.

The evidence for a new class of inexpensive nuclear energy research topics is now unambiguous, though its road to recognition has been a bit slow, bumpy and, at times, treacherous for its intrepid explorers.

The roots of most of the work in this book began 20 years ago, triggered by the greatest science controversy in modern times: the cold fusion episode.

"Cold fusion" was the term used by the media 20 years ago to identify the discovery of Martin Fleischmann and Stanley Pons, at the University of Utah, of an unexplained source of heat resulting from an electrochemical cell using heavy water and palladium. The work of Fleischmann and Pons did not suddenly appear without context, despite appearances to the contrary. Fleischmann had been curious about the strange behavior of palladium and deuterium since his college days and his fascination with Nobel laureate Percy Bridgman's "cold nuclear explosions."

This volume contains two comprehensive reviews. The first, by Jean-Paul Biberian, reviews LENR research performed with deuterium gas. This review is particularly useful because potential LENR applications seem far more likely to use gas-based devices than the messy environment of electrochemistry.

The second review, by Mahadeva Srinivasan, provides an overview of perhaps the most significant government LENR research, that of the Bhabha Atomic Research Centre in India *(1)*. The researchers at BARC devised interesting experiments and produced results right away after hearing the news

In Low-Energy Nuclear Reactions and New Energy Technologies Sourcebook Volume 2; Marwan, J., et al.; ACS Symposium Series; American Chemical Society: Washington, DC, 2010.

of the Fleischmann-Pons discovery from the University of Utah. The directors at BARC demonstrated remarkable initiative and were able to marshal the resources of scientists in many fields and get them all to work together. Their work stopped in the early 1990s, not for lack of results but for lack of courage. A new administration took over in the early 1990s that was less-courageous in the face of the growing negative public opinion of the controversial research despite the positive results of its own researchers. Nevertheless, the BARC work shows what is possible when scientists and government leaders in a country are aggressive, open-minded and prepared.

Although the BARC work was performed two decades ago, its value has never been more appreciated because new insights into reproducible neutron signals *(2)* and neutron-based ideas, such as the work by Srivastava, Widom, and Larsen in this volume, have recently opened new vistas for the LENR field.

Four LENR experimental papers are presented in this volume. These papers represent but a fraction of the experimental knowledge that has been developed. Each author or group of authors naturally takes an approach with a certain hypothesis in mind. Some of the researchers explore the work from the aspect of a new form of room-temperature fusion or fission; others look at the work from the aspect of neutron-catalyzed reactions. The three approaches do not necessarily imply three distinct groups of phenomena; rather, they are more likely to be representative of each researcher's area of focus, perspective and expertise.

This book also contains a chapter on bubble nuclear fusion, a unique phenomenon that, through a multibubble sonoluminescence effect, produces a tabletop thermonuclear reaction. This work falls into the broader category of research called acoustic inertial confinement fusion. AICF has been studied for many years in single-bubble sonoluminescence research, but not until a group at Oak Ridge National Laboratory, led by nuclear engineer Rusi Taleyarkhan, applied its novel ideas to create multibubble sonoluminescence did the thermonuclear reactions take place.

The political backlash that occurred in 2007-09 against pioneer Taleyarkhan - largely the result of academic backstabbing - is reminiscent of the fate suffered by Fleischmann and Pons 20 years ago. Thus, the clear presentation of the scientific facts in this volume becomes all the more crucial in the face of the nonscientific assaults against these novel areas of research.

Immediately following the chapter on bubble nuclear fusion is a chapter by Roger Stringham presenting work that also uses acoustic triggering but that falls within the LENR category.

"Cold fusion" researchers were labeled heretics for their willingness to consider ideas deemed ridiculous by the physics orthodoxy. Many skeptics missed the point: The field did not originate from the speculative theoretical imaginations of Fleischmann and Pons. The field blossomed as the result of empirical studies.

Viable theories may bring comfort to cautious observers and the science orthodoxy, but the LENR phenomena did not arrive replete with such. It is now the job of theoretical physicists, teamed with the experimentalists from a broad variety of disciplines, to develop an understanding of the mechanism or

Downloaded by 89.163.35.42 on June 28, 2012 | http://pubs.acs.org
Publication Date (Web): December 20, 2009 | doi: 10.1021/bk-2009-1029.ch001

mechanisms that will explain the anomalous nuclear-scale energy and nuclear products that will enable this science to progress to a technology.

The careful reader will note two levels of argument represented by the LENR papers. The first argument is for the fundamental establishment of the validity of the research in general. The second argument - more subtle in the case of the experimental work but more obvious in the theoretical work – is for the existence of room-temperature deuterium-deuterium fusion reactions versus the argument for proton addition by way of neutron absorption.

Among the arguments presented for the underlying mechanism or mechanisms of LENR, the reader will find proposed models for fusion, fission and electro-weak processes. Regardless of the outstanding question of the underlying processes, an honest reader will find it difficult to dismiss the fact that a new field of nuclear research has arrived.

Many of the experimentalists assume or speculate that the causative nuclear events are fusion processes, though in many, if not all, cases, the evidence for fusion is far removed from and poorly matches that which is well-understood as the recognized phenomena of thermonuclear fusion. Some LENR researchers interpret their solitary findings of 2.5 MeV neutrons or 3.0 MeV protons as unambiguous proof of deuterium-deuterium fusion. Evidence the findings may be; proof they are not.

The struggle for understanding should not be seen as a distraction from the relevant importance of the overall subject and the legitimate search for answers. No doubt, Nature is showing us something new and, most likely, something significant. Potential applications based on these areas of research are intriguing. However, the immediate opportunity to learn, share and expand scientific knowledge and explore the edge of science is here today.

References

1. Iyengar, P. K.; Srinivasan, M., Eds. *BARC Studies in Cold Fusion, BARC-1500,* Atomic Energy Commission, Government of India: Bombay, 1989; http://www.barc1500report.com
2. Mosier-Boss, P. A.; Szpak, S.; Gordon, F. E.; Forsley, L. P. G. Triple Tracks in CR-39 as the Result of Pd–D Co-Deposition: Evidence of Energetic Neutrons. *Naturwissenschaften* **2008**, *96*, 135-142.

Downloaded by 89.163.35.42 on June 28, 2012 | http://pubs.acs.org
Publication Date (Web): December 20, 2009 | doi: 10.1021/bk-2009-1029.ch001

Downloaded by PENNSYLVANIA STATE UNIV on June 28, 2012 | http://pubs.acs.org
Publication Date (Web): December 20, 2009 | doi: 10.1021/bk-2009-1029.ch002

Chapter 2

Low Energy Nuclear Reactions in Gas Phase: A Comprehensive Review

Jean-Paul Biberian

Département de Physique, Université d'Aix-Marseille, 163 Avenue de Luminy, 13288 Marseille cedex 9, France

Low energy nuclear reactions have been demonstrated experimentally mainly through electrochemical experiments. However, a great deal of work has been performed in gas phase. The existence of anomalous excess heat, production of neutrons, tritium, helium-4 and helium-3 as well as the existence of transmutation of elements has been shown by many experimentalists. This chapter reviews all the work that has been done during the past 20 years in low energy nuclear reactions in gas phase.

Following B. Stanley Pons and Martin Fleischmann's public announcement of "cold fusion" in 1989 (*1*), many scientists started replicating their work by electrochemical techniques. However, a large number of people followed another path. Instead of performing experiments in water-based electrolytes, they developed techniques in gas phase. They used deuterium as well as hydrogen, and various metals like palladium, titanium or nickel. They also did some work with metal oxides. The large number of results obtained with this approach shows that these alternative techniques to electrochemistry are worth pursuing intensively. Future application systems likely will be gas phase-based.

In this review, we will descibe interesting results obtained in gas phase, showing that this way of considering low energy nuclear reactions is very promising. We will focus on the key experiments and describe them in detail. We will also review all the other experiments that have been performed in gas loading.

Excess heat is certainly the Holy Grail of the researchers working in this field. It is well-known now that the effect observed is not chemical and hence is

In Low-Energy Nuclear Reactions and New Energy Technologies Sourcebook Volume 2; Marwan, J., et al.;
ACS Symposium Series; American Chemical Society: Washington, DC, 2010.

most likely of nuclear origin. As we will see in the following sections, neutrons, gamma rays, alpha particles, and transmutations are not the major products of these experiments. What is known now is that anomalous heat production exists, and this is what makes this scientific field so important not only in terms of science but also as a potential source of quasi-unlimited sources of energy. In the following sections, we will review important achievements by the various research teams.

Important Experimental Results

During the past 20 years, a great deal of experimental work has been performed. However, the following four contributions are of specific importance. Gustave Fralick et al. at NASA in 1989 were the first to publish a work showing excess heat in a gas-loading experiment. Yoshiaki Arata and Yue-Chang Zhang in Japan developed a new technology using palladium black, then nano particles of palladium to produce excess heat and helium-4. Yasuhiro Iwamura and co-workers from Mitsubishi Heavy Industries brought the direct proof of transmutations, i.e. appearance of new elements and disappearance of others. In Italy, Francesco Piantelli and co-workers have developed a new way of performing low energy nuclear reactions using the much cheaper nickel-hydrogen couple.

Fralick et al. at NASA in 1989

Following the announcement of the discovery of LENR in March 1989, Fralick et al. (*2*) ran a simple experiment. They loaded a hydrogen purifier consisting of a palladium tube heated at 370°C, and at a pressure of 1.4MPa with deuterium, then hydrogen gases. When they pumped out the gases, in the case of deuterium they observed a temperature rise, wheras with hydrogen, no temperature change was detected. Their initial goal in performing that experiment was to detect neutrons, but no significant effect was observed. Even though this work went unnoticed in the LENR community for many years, this was the first experiment in gas phase showing excess heat production.

Arata and Zhang

A very important contribution in excess heat production and helium detection is the work by Arata and Zhang, who published many papers on this subject (*3, 4, 5, 6, 7, 8, 9, 10, 11, 12, 13, 14, 15, 16, 17, 18, 19, 20, 21*). Their initial work was performed in an electrolytical cell.

Downloaded by PENNSYLVANIA STATE UNIV on June 28, 2012 | http://pubs.acs.org
Publication Date (Web): December 20, 2009 | doi: 10.1021/bk-2009-1029.ch002

Downloaded by PENNSYLVANIA STATE UNIV on June 28, 2012 | http://pubs.acs.org
Publication Date (Web): December 20, 2009 | doi: 10.1021/bk-2009-1029.ch002

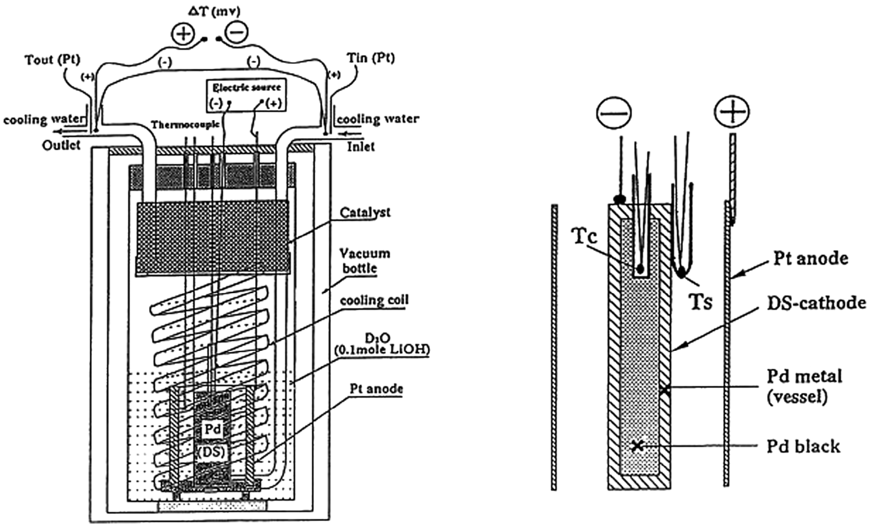
ΔT (mv)
Tout (Pt)
(+)
(-)
(-)
Tin (Pt)
(+)
Electric source
(-)
(+)
cooling water
Outlet
Thermocouple
cooling water
Inlet
Catalyst
Vacuum bottle
cooling coil
D₂O (0.1mole LiOH)
Pt anode
Pd
(DS)
Tc
Ts
Pt anode
DS-cathode
Pd metal (vessel)
Pd black

Figure 1. Arata and Zhang double-structure cathode (right) and mass flow calorimeter (left).

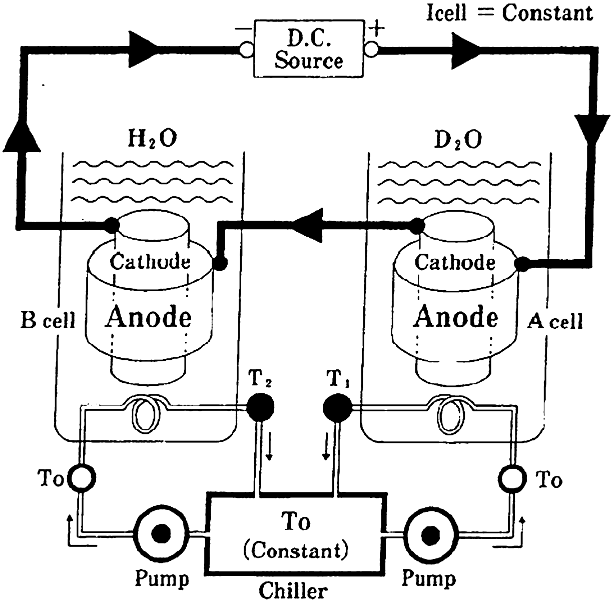
Icell = Constant
D.C. Source
−
+
H₂O
D₂O
Cathode
Anode
B cell
Cathode
Anode
A cell
T₂
T₁
To
To
To (Constant)
Pump
Chiller
Pump

Figure 2. Arata and Zhang system for comparing a cell operating with light water and another one with heavy water. The two cells are placed in a series; therefore, the same current flows in each cell. The input powers are identical for the two cells.

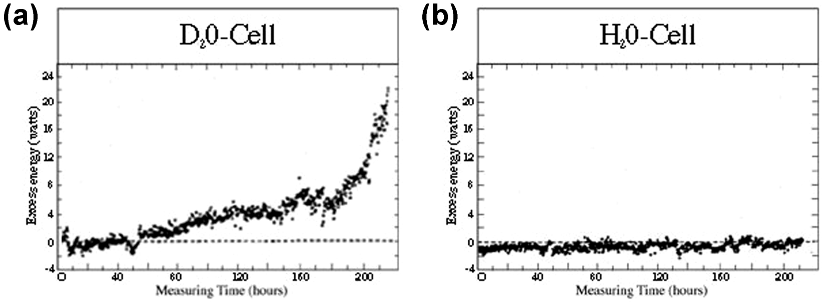

Figure 3. Comparison showing that large amounts of excess heat are produced in the heavy-water cell, while no excess heat is measured in the light-water one. The experiment terminates when the hollow cathode explodes because of the high deuterium pressure build-up in the tube.

However, somehow, this is a gas phase experiment. The reason is that they electrolyzed heavy water with a palladium cathode of unique design. It is the so-called double-structure cathode, composed of a palladium tube filled with palladium black and sealed under vacuum as shown in Figure 1. The initial experiment was a comparison between a cell using D_2O and another one with H_2O, as shown in Figure 2. The two cells are identical, and a direct comparison can be made. The system operates in two steps: First, by electrolysis, water is dissociated, and hydrogen or deuterium enters the palladium walls of the cathode, then diffuses inside the tube, where the palladium powder is placed. The hydrogen or deuterium fills the interior of the tube and loads the palladium powder at high pressure. This is why this approach can be considered a gas-loaded system. Figure 3 shows that the heavy-water device produces excess heat, whereas the light-water one does not. It takes more than two days for the system to produce excess heat because the deuterium atoms must diffuse through the walls of the palladium tube before entering the interior of the tube. The experiment terminates when the gas pressure inside the tube is so high that the tube explodes. The authors also measured production of helium-4. Later, Arata and Zhang (*22, 23*) ran experiments without electrolysis. They directly introduced purified deuterium gas at high pressure inside a cell containing palladium black. In this new design, they used a new form of palladium black: nano particles of palladium imbedded inside a ZrO_2 matrix. The main advantage of this method is that the ZrO_2 matrix prevents sintering of the palladium nano particles. Also, they showed that a loading ratio of three deuterium atoms per palladium is achieved. The high loading, the purity of the deuterium gas and the high pressure of deuterium seem to be important in this system. They also showed production of helium-4.

Downloaded by PENNSYLVANIA STATE UNIV on June 28, 2012 | http://pubs.acs.org
Publication Date (Web): December 20, 2009 | doi: 10.1021/bk-2009-1029.ch002

Iwamura and Co-Workers.

A very important contribution is the one from Iwamura et al. (*24, 25, 26, 27*) from Mitsubishi Heavy Industries in Japan. In their experiment, deuterium gas permeates a specific substrate composed of a 0.1 mm thick palladium foil onto which they deposit five alternative layers of palladium and CaO, as shown in Figure 4.

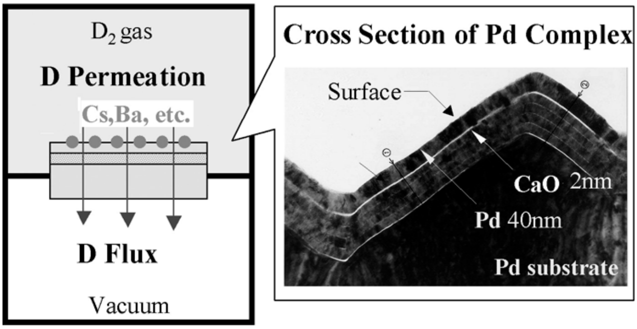
D2 gas
D Permeation
Cs,Ba, etc.
D Flux
Vacuum
Cross Section of Pd Complex
Surface
CaO 2nm
Pd 40nm
Pd substrate

Figure 4. Schematic of the experimental procedure and electron microscope view of the Pd-CaO multi-layer on palladium.

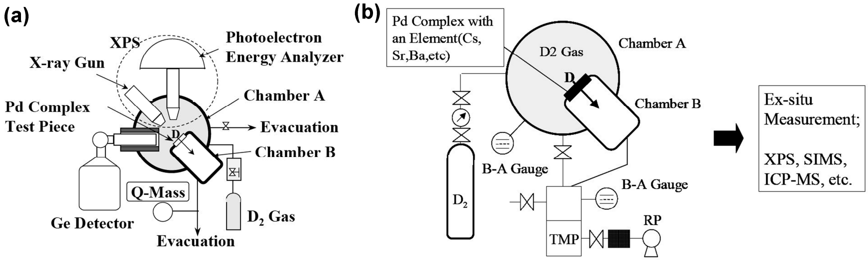
(a)
XPS
X-ray Gun
Photoelectron Energy Analyzer
Chamber A
Pd Complex Test Piece
Evacuation
Chamber B
Q-Mass
Ge Detector
D2 Gas
Evacuation
(b)
Pd Complex with an Element(Cs, Sr,Ba,etc)
D2 Gas
Chamber A
Chamber B
B-A Gauge
B-A Gauge
D2
TMP
RP
Ex-situ Measurement;
XPS, SIMS, ICP-MS, etc.

Figure 5. Schematic of the experimental set-up: a vacuum chamber equipped with a Photoelectron Energy Analyzer and an X-ray source (XPS) for in-situ analysis.

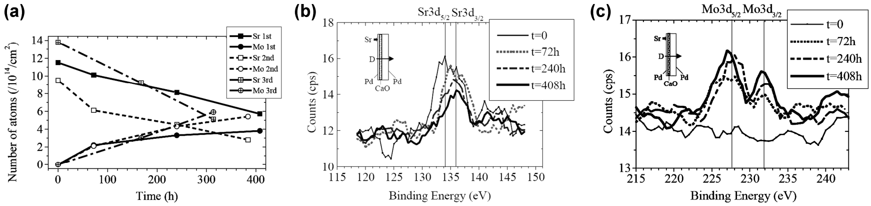

Figure 6(a). Graph showing the disappearance of the strontium and the appearance of molybdenum deduced from the XPS data.
Figure 6(b). XPS spectra of strontium showing its decrease with time.
Figure 6(c). XPS spectra of molybdenum showing its increase with time.

Downloaded by PENNSYLVANIA STATE UNIV on June 28, 2012 | http://pubs.acs.org
Publication Date (Web): December 20, 2009 | doi: 10.1021/bk-2009-1029.ch002

Downloaded by PENNSYLVANIA STATE UNIV on June 28, 2012 | http://pubs.acs.org
Publication Date (Web): December 20, 2009 | doi: 10.1021/bk-2009-1029.ch002

The deuterium gas at about atmospheric pressure is placed on one side of the target and pumped out on the other side; see Figure 5. The chamber where the deuterium gas is placed is an ultra-high vacuum chamber equipped with an X-ray Photo Electron Analyzer. This equipment is a very sensitive analytical tool to perform surface chemical analysis, sensitive to a depth of a few atomic layers. What Iwamura and co-workers have discovered is that, when they add some foreign elements on the surface of the target, they observe a decrease of that element and the apparition of a new one that did not exist before. For instance, when they spice the surface with cesium, they observe the apparition of praseodymium. When strontium is deposited, molybdenum forms; see Figure 6. The analysis is performed in situ by XPS after evacuation of the deuterium gas from the chamber. However, in addition, the authors have performed an ex-situ analysis of the sample by Secondary Ion Mass Spectroscopy, another very surface-sensitive technique that measures mass composition. The molybdenum that has been produced is very different from the natural one, as demonstrated in Figure 7. For these reactions to occur, cesium must gain four deuterons to produce praseodymium. Similarly, strontium must gain four deuterons to produce molybdenum.

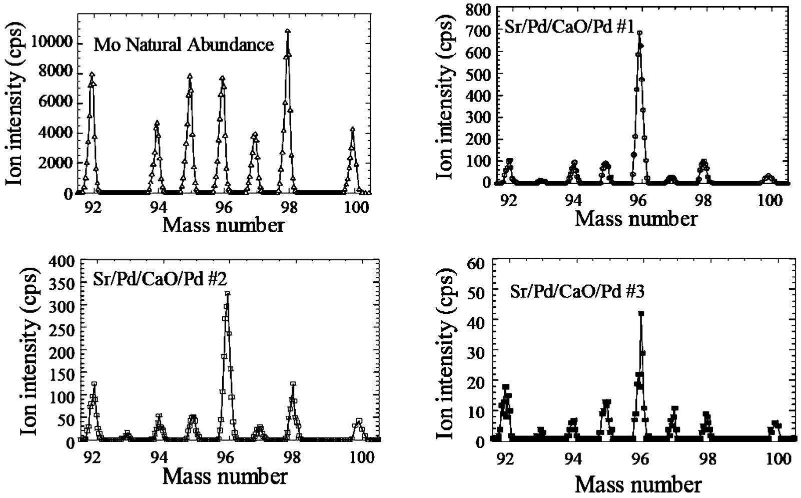

Figure 7. Comparison of secondary ion mass spectra from samples having received deuterium and natural molybdenum.

However, later on, the authors have observed the formation of samarium from barium by an addition of six deuterons (*27*). Figure 8 shows mass spectra of the initial barium, then the appearance of samarium. Interstingly, they used isotopically selected barium. When they deposit Ba-138, they produce Sm-150, whereas when they use Ba-137, they obtain Sm-149. This experiment is another very direct proof of the transmutation effect of deuterated palladium under dynamic conditions.

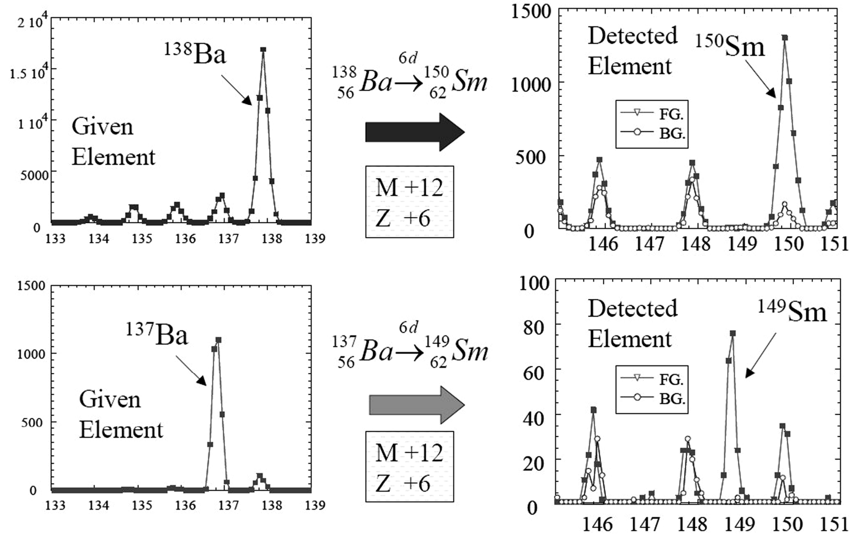

Figure 8. Mass spectra showing the transmutation of baryum into samarium by addition of six deuterons.

Piantelli and Co-Workers

Most of the work in LENR has been produced using the palladium-deuterium system. However, a few authors have used different systems. In particular, Piantelli and co-workers (*28, 29, 30, 31, 32, 33, 34, 35, 36, 37, 38, 39*) from the University of Siena in Italy have used hydrogen gas and nickel. Their unique method deserves special attention, because hydrogen and nickel are a lot more accessible and inexpensive than deuterium and palladium. Figure 9 shows a schematic of the experimental set-up. They have repeatedly produced excess heat. Adriano Battaglia et al. (*35*) have shown the production of neutrons, and Campari et al. (*36, 37*) have shown the production of heat, gamma rays and neutrons. Sergio Focardi et al. (*38*) show the production of heat, particle emission and gamma rays. Campari et al. (*39*) have observed anomalous distribution of elements on a nickel alloy during experiments with hydrogen.

Downloaded by PENNSYLVANIA STATE UNIV on June 28, 2012 | http://pubs.acs.org
Publication Date (Web): December 20, 2009 | doi: 10.1021/bk-2009-1029.ch002

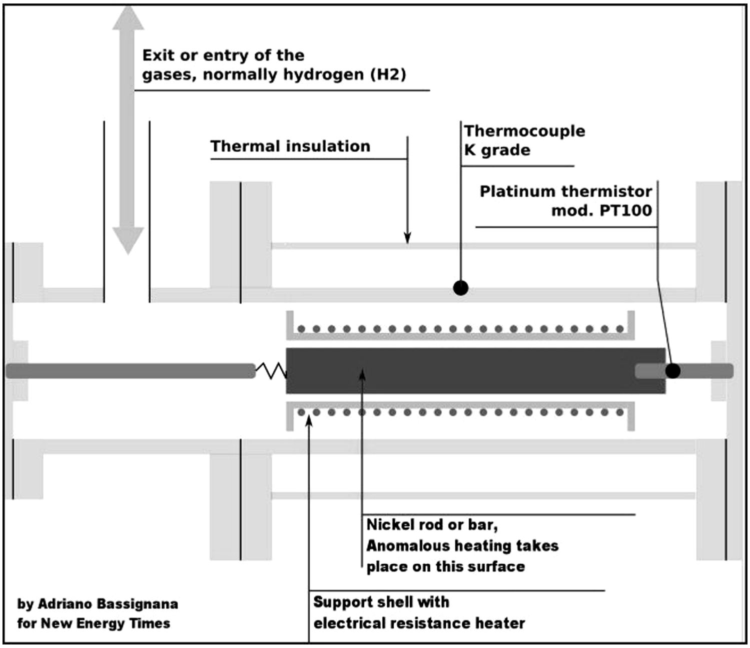
Exit or entry of the gases, normally hydrogen (H2)
Thermal insulation
Thermocouple K grade
Platinum thermistor mod. PT100
Nickel rod or bar, Anomalous heating takes place on this surface
Support shell with electrical resistance heater
by Adriano Bassignana for New Energy Times

Figure 9. Piantelli and co-workers' experimental set-up showing the reaction chamber and, at the center (in grey), the heated nickel rod. The asymmetric attchment of the rod highly conductive on the right side and lightly conductive on the left side creates a temperature gradient that plays a critical role in the success of these experiments.

Downloaded by PENNSYLVANIA STATE UNIV on June 28, 2012 | http://pubs.acs.org
Publication Date (Web): December 20, 2009 | doi: 10.1021/bk-2009-1029.ch002

More Experimental Proofs

The examples shown above are very important in gas-loading experiments. They show unambiguously production of anomalous excess heat, helium and transmutation. However, these groups are not alone in this field, and many more experiments have been carried out confirming the above results and adding more experimental facts. In this section, we will review the work performed by many more groups confirming the above results.

Excess Heat

Vadim Romodanov et al. (*40*) have shown the production of excess heat when deuterium flows through palladium foils. Similar results have been observed by Xing Zhong Li et al. (*41, 42, 43, 44, 45, 46, 47, 48, 49*). In a similar type of experiment, J. Tian et al. (*50*) detected heat after death. Claudio Manduchi et al. (*51*) observed anomalous effects when palladium is cooled from

Downloaded by PENNSYLVANIA STATE UNIV on June 28, 2012 | http://pubs.acs.org
Publication Date (Web): December 20, 2009 | doi: 10.1021/bk-2009-1029.ch002

900°C to room temperature. Kirkinskii et al. (*52-54*) have measured 1 Watt of excess heat per gram of palladium in gas-loaded experiments. However, when palladium powder is heated, sintering occurs, and the original particle size is destroyed. Therefore, it is better to use dispersed palladium in a medium. This is what Arata and Zhang have done using nano particles of palladium in a ZrO_2 matrix. Independently, Case (*55, 56*) tried various palladium catalysts and finally found one that was effective in producing excess heat. Michael McKubre et al. (*57*) successfully replicated this experiment. Marmigi et al. (*58*) showed anomalous excess heat using an oxidized palladium wire. Nassisi et al. (*61, 62, 63*) observed transmutations when irradiating etched palladium samples with an excimer laser.

Early on, Yamaguchi et al. (*64, 65*) observed excess heat when deuterium flows out of a palladium foil covered on one side with gold. Similarly, Liu et al. (*66*) show that excess heat occurs when deuterium flows out of the palladium. The amount of excess heat increases with the deuterium flow. Narita et al. (*67*) have also shown heat production when hydrogen is pumped out of a palladium foil covered on one side with MnOx or gold. Lipson et al. (*68*) showed excess heat while deloading a palladium foil oxidized on one side and covered with gold on the other. Biberian and Armanet (*69, 70*) showed excess heat production when deuterium flows out of a palladium tube. Li et al. (*71*) observed excess heat from palladium wires in deuterium gas. Marmigi et al. (*58*) have shown anomalous excess heat production when a previously oxidized palladium wire is heated in an hydrogen atmosphere. Celani et al. (*59, 60*) showed that large, and stable over time, excess heat was detected when long and thin (50um) Pd wires, coated with nano-materials, underwent the phase transition from beta to alpha phases and large current densities (10-50kAcm^{-2}) were applied along the length of the wire. The power density was up to 400 W/g of palladium. The operating temperature was in the 300-500°C range. The effect happened mainly in pressurized deuterium atmosphere; however, some effect was also observed at a much lower level using hydrogen.

Helium

Arata and Zhang's experiment was duplicated by Clarke et al. (*73*). They confirmed the excess heat as well as the helium-4 production. Possibly helium-4 comes from the fusion of two deuterium atoms. They also showed production of helium-3, which could come from the formation of tritium, which consequently decays into helium-3 by beta emission. Botta et al. (*74, 75*) have detected helium-4 using palladium foils covered on one side with gold and loaded with deuterium. Qiao et al. (*76, 77*) showed production of helium from palladium in deuterium gas. McKubre et al. (*57*) have detected helium-4 in a Case type experiment and showed a temporal and near-quantitative correlation between helium-4 production and excess heat. They calculate from the data shown in Figure 10 that the energy produced is 31 MeV per atom with an uncertainty of +/-13 MeV. They state that this is consistent with a D+D fusion mechanism producing helium-4 and 23 MeV and that the large uncertainty results from the low level of helium produced in the LENR experiment.

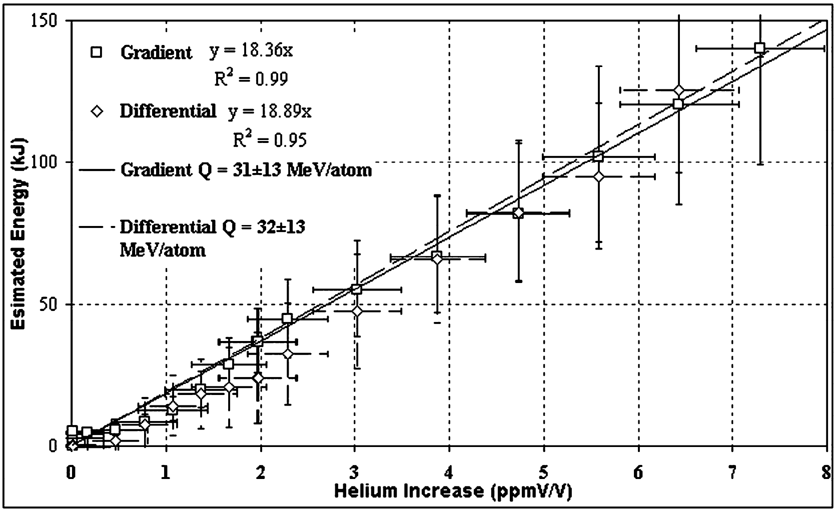

Figure 10. Graph showing a linear correlation between helium-4 production and excess heat.

Neutrons

As early as 1986, Kluev et al. (*78, 79*) discovered the production of neutrons when a strong mechanical action is exerted against heavy ice or LiD. Later, Derjaguin et al. (*80*) showed that neutrons were produced when titanium deuteride chips were subject to mechanical vibrations. Jin et al. (*81*) observed neutrons in a $YBa_2Cu_3O_7$ sample loaded with deuterium. Shioe et al. (*82*) and Shirakawa et al. (*83*) similarly observed neutrons in $LiNbO_3$ fractured in a deuterium atmosphere. Aiello et al. (*84*) have also observed neutrons in palladium loaded with deuterium. De Ninno et al. (*85, 86, 87*) detected neutrons while varying the temperature of titanium foils loaded with deuterium. Menlove et al. (*88, 89, 90, 91*) showed similar results. Fabrizio et al. (*92*) found neutrons the same way. At the same time, Claytor et al. (*93, 94, 95*) and Tuggle et al. (*96*) at the Los Alamos National Laboratory detected neutrons by pulsing currents with palladium electrodes in deuterium gas. Since then, many other scientists have tried to detect neutrons in gas-loading experiments. Bressani et al. (*97, 98, 99*) have measured neutron emission when titanium foils are loaded with deuterium. Yamaguchi et al. (*64, 72*) have demonstrated production of neutrons when deuterium deloads from a palladium foil loaded with deuterium with one face of the palladium covered with gold. Shirakawa et al. (*100*) showed production of neutrons when $LiNbO_3$ is fractured in a deuterium atmosphere. Iwamura et al. (*101*) showed production of neutrons when a palladium foil loaded with deuterium is heated. However, Garg et al. (*102*) in a similar experiment with a palladium wire loaded with deuterium or hydrogen did not detect any neutron. Aoki et al. (*103*) could not detect any neutron above background in a tungsten sodium bronze loaded with deuterium when loading or deloading the material**.** Shinojima et al. (*104*) did not detect neutrons when

Downloaded by PENNSYLVANIA STATE UNIV on June 28, 2012 | http://pubs.acs.org
Publication Date (Web): December 20, 2009 | doi: 10.1021/bk-2009-1029.ch002

flowing deuterium through a palladium foil. However, Lipson et al. (*105, 106*) and Roussetski (*107*) did detect neutrons during exothermic desorption using a Au/Pd/PdO:D sample. Also, Dougar-Jabon et al. (*108*) detected neutrons during alpha/beta phase transition in palladium deuteride. Chicea et al. (*109*) detected neutrons in titanium deuteride when the metal was loaded at high temperature and then the temperature was lowered. Itoh et al. (*110*) observed neutron emission when out-gassing a highly loaded palladium foil.

Tritium and Mass-3

As early as 1990, Iyengar et al. (*111)*, Srinavasan et al. (*112*), Iyengar et al. (*113*), Kauskik et al. (*114*) and Rout et al. (*115, 116*) showed production of tritium in palladium and titanium samples loaded with deuterium. Sankaranarayanan et al. (*117*) reported tritium production with hydrogen in nickel wires. Lamza et al. (*118*) measured tritium in various metals loaded with deuterium. De Ninno et al. (*87*) detected tritium in titanium loaded with deuterium. Yamada et al. (*119*) have shown the production of tritium when deuterium is pumped out of a palladium foil covered on one side with MnOx. Narita et al. (*67*) have observed mass-3 corresponding either to tritium or helium-3 when hydrogen is pumped out of a palladium foil covered on one side with MnOx or gold. Similarly, Wei et al. (*120*) have observed mass-3 when deuterium flows through a palladium foil. Claytor et al. (*95, 121*) measured tritium with Pd-Si electrodes in deuterium gas. Clarke et al. (*122*) detected tritium in titanium loaded with deuterium and later (*73*) observed production of tritium in a cell similar to Arata and Zhang's. Romodanov et al. (*42, 122*) have also detected tritium. Lipson et al. (*124*) detected significant amounts of tritium when cooling $YBa_2Cu_3O_7D_?$, to its Curie temperature (88-93K) in deuterium gas.

Charged Particles

Mo et al. (*125, 126*), Wang et al. (*127*), Jin et al. (*128*), Li et al. (*129*) and Dong et al. (*130*) showed evidence of charged particles emission from deuterated palladium. Cecil et al. (*131*) have observed charged particles in deuterated titanium. By a coincidental method, Jones et al. (*132, 133*) showed that energetic protons and tritons are produced in non-equilibrium conditions in titanium deuteride samples. Roussetski et al. (*134*) have also detected charged particles from titanium hydrides and deuterides triggered by a pico-second powerful laser beam. Cecil et al. (*135*) have also measured charged particles from palladium deuterides. Lipson et al. (*136*) observed beta emission from deuterated titanium.

Downloaded by PENNSYLVANIA STATE UNIV on June 28, 2012 | http://pubs.acs.org
Publication Date (Web): December 20, 2009 | doi: 10.1021/bk-2009-1029.ch002

Transmutations

Kong et al. (*137*) and Qiao et al. (*138*) have detected several new metals on palladium in a deuterium atmosphere. Several groups have reproduced Iwamura's work. In a similar experiment, Higashiyama et al. (*139*) have shown that the praseodymium formation is a function of the flow rate of deuterium through the sample. Minari et al. (*140*) and Hioki et al. (141) have also observed the formation of molybdenum from stronstium and praseodymium from cesium. Yamada et al. (*142, 143*) and Kitamura et al. (*144*) have also observed transmutation. Castellano et al. (*145*) have shown that new elements are found on a deuterated palladium foil irradiated with a laser beam. Tian et al. (*146*) have irradiated hydrogenated palladium wires with a YAG laser; they observed some excess heat and formation of new elements. Di Giulio et al. (*147*) have deposited thin films of palladium on silicon wafers. After laser irradiation, they observe several transmutations products. Wei et al. (*148*) observed new elements (Gd, Tb, Nd) after diffusion of deuterium through a palladium foil.

Conclusion

As we have shown above, during the past 20 years a large number of experimental proofs have been brought up in favor of nuclear reactions in condensed matter. The use of gas phase instead of the original electrochemical system is certainly the future of the field. Effectively, this method has many advantages. On one hand, there is no longer the low-temperature operational limitation as exists with electrolysis in water. On the other hand, the gas phase is a much cleaner environment that permits better control of the materials. Therefore, the first application devices likely will be in gas phase systems.

So far, most of the work has been done in the expensive deuterium-palladium system. This is certainly an interesting choice from the research point of view but not very applicable to practical devices. The fact that some limited experiments have been performed with titanium instead of palladium is encouraging. However, I believe that the most interesting system is the nickel-hydrogen pair. Piantelli's research team has performed wonderful work in this area, and other groups have also obtained interesting results. Early on, Sankaranarayanan et al. (*149*) reported tritium production with hydrogen in nickel wires. Cammarota et al. (*150*) have reproduced the excess heat measurements of Piantelli and co-workers. A different approach has been developed by Mastromatteo (*151*). He used a silicon-based hydrogen source to load a nickel film in a small device. He observed anomalous melting of the nickel film.

Surprisingly, no work has been published regarding the iron-hydrogen or iron-deuterium systems. Iron is an interesting metal because, at low temperature, its crystallographic structure is centered cubic, and above 920°C, it becomes face-centered cubic. Maybe this rare structural change has potential interest.

In any case, the future of LENR in gas phase is bright, and hopefully soon, the first application devices will be available.

Downloaded by PENNSYLVANIA STATE UNIV on June 28, 2012 | http://pubs.acs.org
Publication Date (Web): December 20, 2009 | doi: 10.1021/bk-2009-1029.ch002

References

1. Fleischmann, M.; Pons, S. Electrochemically induced nuclear fusion of deuterium. *J. Electroanal. Chem.* **1989**, *261*, 301.
2. Fralick, G. C.; Decker, A. J.; Blue, J. W. Results of an attempt to measure increased rates of the reaction $2D+2D \rightarrow {}^3He+n$ in a nonelectrochemical cold fusion experiment; *NASA Technical Memorandum 102430*, 1989.
3. Arata, Y.; Zhang, Y. C. Cold fusion in a complex cathode. In *Frontiers of Cold Fusion: Proceedings of the Third International Conference on Cold Fusion,* Nagoya, Japan, Oct. 21-25, 1992; Ikegami, H., Ed.; Universal Academy Press: Tokyo, Japan, 1993.
4. Arata, Y.; Zhang, Y. C. Cold fusion caused by a weak "on-off effect." *Proc. Jpn. Acad., Ser. B.* **1992**, *66*, 33.
5. Arata, Y.; Zhang, Y. C. Reproducible "cold" fusion reaction using a complex cathode. *Fusion Technol.*, **1992**, *22*, 287.
6. Arata, Y.; Zhang, Y. C. A new energy caused by "spillover-deuterium." *Proc. Jpn. Acad., Ser. B,* **1994**, *70*, 106.
7. Arata, Y.; Zhang, Y. C. Achievement of solid-state plasma fusion ("cold fusion"). *Proc. Jpn. Acad., Ser. B,* **1995**, *71*, 98.
8. Arata, Y.; Zhang, Y. C. Excess heat and mechanism in cold fusion reaction. In *Proceedings of the Fifth International Conference on Cold Fusion,* Monte Carlo, Monaco, 1995. Pons, B. S., Ed.; IMRA Europe: Sophia Antipolis, Valbonne, France; p 483.
9. Arata, Y.; Zhang, Y. C. Achievement of solid-state plasma fusion ("Cold Fusion"). *Progress in New Hydrogen Energy: Proceedings of the Sixth International Conference on Cold Fusion*, Lake Toya, Hokkaido, Japan, Oct. 13-18, 1996. Okamoto, M., Ed.; New Energy and Industrial Technology Development Organization, Tokyo Institute of Technology: Tokyo, 1996; p 129.
10. Arata, Y.; Zhang, Y. C. Deuterium nuclear reaction process within solid. *Proc. Jpn. Acad., Ser. B,* **1996**, *72*, 179.
11. Arata, Y.; Zhang, Y. C. Solid-state plasma fusion ('cold fusion'). *J. High Temp. Soc.*, **1997**, *23*, 1.
12. Arata, Y.; Zhang, Y. C. Anomalous "deuterium-reaction energies" within solid. *Proc. Jpn. Acad., Ser. B,* **1998**, *74*, 155.
13. Arata, Y.; Zhang, Y. C. Observation of anomalous heat release and helium-4 production from highly deuterated fine particles. *Jpn. J. Appl. Phys.* **1999**, *38*, L774.
14. Arata, Y.; Zhang, Y. C. Anomalous difference between reaction energies generated within D_2O-cell and H_2O-cell. *Jpn. J. Appl. Phys. Part 2,* **1998**, *37*, L1274.
15. Arata, Y.; Zhang, Y. C. Critical condition to induce 'excess energy' within [DS-H20] cell. *Proc. Jpn. Acad., Ser. B,* **1999**, *75*, 76.
16. Arata, Y.; Zhang, Y. C. Definite difference between [DS-D_2O] and [Bulk-D_2O] cells in deuterium-reaction. *Proc. Jpn. Acad., Ser. B,* **1999**, *75*, 71.
17. Arata, Y.; Zhang, Y. C. Definite difference among [DS-D_2O], [DS-H_2O] and [Bulk-D_2O] cells in the deuterization and deuterium reaction. In *Proceedings of the Eighth International Conference on Cold Fusion*, Lerici

Downloaded by PENNSYLVANIA STATE UNIV on June 28, 2012 | http://pubs.acs.org
Publication Date (Web): December 20, 2009 | doi: 10.1021/bk-2009-1029.ch002

(La Spezia), Italy, May 21, 26, 2000; Scaramuzzi, F., Ed.; Italian Physical Scoiety: Bologna, Italy, 2000; p 11.

18. Arata, Y.; Zhang, Y. C. Picnonuclear fusion generated in "lattice-reactor" of a metallic deuterium lattice within metal atom-clusters. In *Condensed Matter Nuclear Science: Proceedings of the Ninth International Conference on Cold Fusion,* Beijing, China, May 19, 24, 2002; Li, X. Z., Ed.; Tsinghua University Press: Beijing, 2002; p 5.
19. Arata, Y.; Zhang, Y. C. Development of compact nuclear fusion reactor using solid pycnodeuterium as "nuclear fuel." In *Condensed Matter Nuclear Science: Tenth International Conference on Cold Fusion,* Cambridge, MA, Aug. 24-29, 2003; Hagelstein, P. L.; Chubb, S. R., Eds.; World Scientific Publishing Co.: Singapore, 2006; p 139.
20. Arata, Y.; Zhang, Y. C. The establishment of solid nuclear fusion reactor. *J. High Temp. Soc.,* **2008**, *34(2)*, 85.
21. Arata, Y.; Zhang, Y. C. Discovery of solid deuterium nuclear fusion of pycnodeuterium-lumps solidified locally within nano-Pd particles. *High Temp. Soc. Japan,* **2003**, *29*, 1.
22. Arata, Y. Zhang, Y. C. Development of "DS-Reactor" as the practical reactor of "Cold Fusion" based on the DS-cell" with "DS-cathode." In *Condensed Matter Nuclear Science: Proceedings of the Twelfth International Conference on Cold Fusion*, Yokohama, Japan, Nov. 27-Dec. 2, 2005; Takahashi, A.; Ota, K.; Iramura, Y. Eds.; World Scientific Publishing Co.: 2006; p 44.
23. Arata, Y.; Zhang Y. C. "Solid fusion" reactor with zero input energy. *Fourteenth International Conference on Cold Fusion,* Aug. 17-21, 2008, Washington, DC.
24. Iwamura, Y.; Sakano, M.; Itoh, T. Elemental analysis of Pd complexes: effects of D_2 gas permeation. *Jpn. J. Appl. Phys.;* **2002**, *41*, 4642.
25. Iwamura, Y.; Itoh, T.; Sakano, M.; Sakai, S.; Kuribayashi, S. Low energy nuclear transmutation in condensed matter induced by D_2 gas permeation through Pd complexes: correlation between deuterium flux and nuclear products. In *Condensed Matter Nuclear Science: Tenth International Conference on Cold Fusion,* Cambridge, MA, Aug. 24-29, 2003; Hagelstein, P. L.; Chubb, S. R., Eds.; World Scientific Publishing Co.: Singapore, 2006; p 435.
26. Iwamura, Y.; Itoh, T.; Sakano, M.; Yamazaki, N.; Kuribayashi, S.; Terada, Y.; Ishikawa, T. Observation of surface distribution of products by X-ray fluorescence spectrometry during D_2 gas permeation through Pd complexes*;* In *Condensed Matter Nuclear Science: Proceedings of the Twelfth International Conference on Cold Fusion*, Yokohama, Japan, Nov. 27-Dec. 2, 2005; Takahashi, A.; Ota, K.; Iramura, Y. Eds.; World Scientific Publishing Co.: 2006; p 178.

27 Iwamura, Y.; Itoh, T.; Sakano, M.; Yamazaki, N.; Kuribayashi, S.; Terada, Y.; Ishikawa, T.; Kasagi, J. Observation of nuclear transmutation reactions induced by D_2 gas permeation through Pd complexes*;* In *Condensed Matter Nuclear Science: Proceedings of the Eleventh International Conference on Cold Fusion,* Marseilles, France, Oct. 31-Nov. 5, 2004; Biberian, J-P., Ed.; World Scientific Publishing Co.: 2006; p 339.

Downloaded by PENNSYLVANIA STATE UNIV on June 28, 2012 | http://pubs.acs.org
Publication Date (Web): December 20, 2009 | doi: 10.1021/bk-2009-1029.ch002

28. Focardi, S.; Habel, R.; Piantelli, F. Anomalous heat production in Ni-H systems*; Nuovo Cimento A* **1994**, *107*, 163.
29. Focardi, S.; Gabbani, V.; Montalbano, V.; Piantelli, F.; Veronesi, S. Overview of H-Ni systems: old experiments and new setup. *Atti Accad. Fisioc., Serie XV, XV* **1996**, *109*.
30. Focardi, S.; Gabbani, V.; Montalbano, V.; Piantelli, F.; Veronese S. Large excess heat production in Ni-H systems. *Il Nuovo Cimento* **1998**, *111*, 1233.
31. Focardi, S.; Gabbani, V.; Montalbano, V.; Piantelli, F.; Veronesi, S. On the Ni-H system. *Proceedings Asti Workshop on Hydrogen/Deuterium loaded metals;* Collis, W. J. M. F., Ed.; **1999**, *64*, 35.
32. Focardi, S.; Gabbani, V.; Montalbano, V.; Piantelli, F.; Veronesi, S. On the Ni-H system. *Atti Accad. Fisioc., Serie XV, XVIII* **1999**, *109*.
33. Focardi, S.; Gabbani, V.; Montalbano, V.; Piantelli, F.; Veronesi, S. Surface analysis of hydrogen-loaded nickel alloys. In *Condensed Matter Nuclear Science: Proceedings of the Eleventh International Conference on Cold Fusion,* Marseilles, France, Oct. 31-Nov. 5, 2004; Biberian, J-P., Ed.; World Scientific Publishing Co.: 2006; p 414.
34. Focardi, S.; Gabbani, V.; Montalbano, V.; Piantelli, F.; Veronesi, S. On the Ni-H system. *Asti Workshop on Anomalies in Hydrogen/Deuterium Loaded Metals,*Villa Riccardi, Italy, 1997; p 35.
35. Battaglia, A.; Daddi, L.; Focardi, S.; Gabbani, V.; Montalbano, V.; Piantelli, F.; Sona, P. G.; Veronesi S. Neutron emission in Ni-H systems *Nuovo Cimento A* **1999**, *112*, 921
36. Campari, E.; Focardi, S.; Gabbani, V.; Montalbano, V.; Piantelli, F.; Porcu, E.; Tosti, E.; Veronesi, S. Ni-H systems. In *Proceedings of the Eighth International Conference on Cold Fusion*, Lerici (La Spezia), Italy, May 21, 26, 2000; Scaramuzzi, F., Ed.; Italian Physical Scoiety: Bologna, Italy, 2000; p 69.
37. Campari, E.; Fasano, G.; Focardi, S.; Lorusso, G.; Gabbani, V.; Montalbano, V.; Piantelli, F.; Stanghini, C.; Veronesi, S. Photon and particle emission, heat production and surface transformation in Ni-H system. In *Condensed Matter Nuclear Science: Proceedings of the Eleventh International Conference on Cold Fusion,* Marseilles, France, Oct. 31-Nov. 5, 2004; Biberian, J-P., Ed.; World Scientific Publishing Co.: 2006; p 405.
38. Focardi, S.; Gabbani, V.; Montalbano, V.; Piantelli, F.; Veronesi, S. Evidence of electromagnetic radiation from Ni-H systems. In *Condensed Matter Nuclear Science: Proceedings of the Eleventh International Conference on Cold Fusion,* Marseilles, France, Oct. 31-Nov. 5, 2004; Biberian, J-P., Ed.; World Scientific Publishing Co.: 2006; p 70.
39. Campari, E.; Focardi, S.; Gabbani, V.; Montalbano, V.; Piantelli, F.; Stanghini, C. Nuclear reactions in Ni-H systems. *Progress in New Hydrogen Energy: Proceedings of the Sixth International Conference on Cold Fusion*, Lake Toya, Hokkaido, Japan, Oct. 13-18, 1996. Okamoto, M., Ed.; New Energy and Industrial Technology Development Organization, Tokyo Institute of Technology: Tokyo, 1996; p.
40. Romodanov, V. A.; Khokhlov, N. I.; Pokrovsky, A. K. Generation of tritium from deuterium interaction with metals. In *Proceedings of the Eighth International Conference on Cold Fusion*, Lerici (La Spezia), Italy,

Downloaded by PENNSYLVANIA STATE UNIV on June 28, 2012 | http://pubs.acs.org
Publication Date (Web): December 20, 2009 | doi: 10.1021/bk-2009-1029.ch002

May 21, 26, 2000; Scaramuzzi, F., Ed.; Italian Physical Scoiety: Bologna, Italy, 2000; p 259.

41. Li, X. Z.; Mo, D. W.; Zhang, L.; Wang, S. C.; Kang, T. S.; Wang, J. Anomalous nuclear phenomena and solid state nuclear track detector. *Nucl. Tracks Radiat. Meas.* **1993**, *22*, 599.
42. Li, X. Z.; Liu, B.; Tian, J.; Wei, Q. M.; Zhou, R.; Yu, Z. W. Correlation between abnormal deuterium flux and heat flow in a D/Pd system. *J. Phys. D: Appl. Phys*. **2003**, *36*, 3095.
43. Li, X. Z.; Liu, B.; Cai, N. N.; Wei, Q. M.; Tian, J.; Cao, D. X. Progress in gas-loading D/Pd system. The feasibility of a self-sustaining heat generator. In *Condensed Matter Nuclear Science: Tenth International Conference on Cold Fusion,* Cambridge, MA, Aug. 24-29, 2003; Hagelstein, P. L.; Chubb, S. R., Eds.; World Scientific Publishing Co.: Singapore, 2006; p 113.
44. Li, X. Z.; Liu, B.; Ren, X. Z.; Tian, J.; Cao, D. X.; Chen, S.; Pan, G. H.; Ho, D. L.; Deng, Y. "Super-absorption" – correlation between deuterium flux and excess heat. In *Condensed Matter Nuclear Science: Proceedings of the Ninth International Conference on Cold Fusion,* Beijing, China, May 19, 24, 2002; Li, X. Z., Ed.; Tsinghua University Press: Beijing, 2002; p 202.
45. Li, X. Z.; Liu, B.; Ren, X. Z.; Tian, J.; Yu, W. Z.; Cao, D. X.; Chen, S.; Pan, G. H.; Zheng, S. X. New measurements of excess heat in a gas loaded D-Pd system. In *Proceedings of the Seventh International Conference on Cold Fusion,* Vancouver, Canada, April 19-24, 1998; Jaeger, F., Ed.; ENECO, Inc., Salt Lake City, UT, 1998; p 197.
46. Wu, W.; Li, X. Z.; Du, J. H.; Tian, J.; Hao, J. Z.; Ma, B.; Chen, J. P.; Liu, B.; Lei, S. Y. "Pumping effect" – Reproducible excess heat in a gas-loading D/Pd system. In *Condensed Matter Nuclear Science: Proceedings of the Ninth International Conference on Cold Fusion,* Beijing, China, May 19, 24, 2002; Li, X. Z., Ed.; Tsinghua University Press: Beijing, 2002; p 412.
47. Liu, B.; Li, X. Z.; Wei, Q. M.; Mueller, N; Schoch, P.; Oehre, H. Multiple scattering of deuteron wave function near surface of palladium lattice. In *Condensed Matter Nuclear Science: Proceedings of the Twelfth International Conference on Cold Fusion*, Yokohama, Japan, Nov. 27-Dec. 2, 2005; Takahashi, A.; Ota, K.; Iramura, Y. Eds.; World Scientific Publishing Co.: 2006; p 75.
48. Tian, J.; Li, X. Z.; Liu, W. Z.; Cao, D. X.; Zhou, R.; Yu, Z. W.; Jiang, Z. F.; Liu, Y.; He, J. T.; Zhou, R. X. Anomalous heat flow and its correlation with deuterium flux in a gas-loading deuterium-palladium system. In *Condensed Matter Nuclear Science: Proceedings of the Ninth International Conference on Cold Fusion,* Beijing, China, May 19, 24, 2002; Li, X. Z., Ed.; Tsinghua University Press: Beijing, 2002; p 353.
49. Li, X. Z.; Yue, W. Z.; Huang, G. S.; Shi, H.; Gao, L.; Liu, M. L.; Bu, F. S. "Excess heat" measurement in gas-loading D/Pd system. *J. New Energy* **1996**, *1(4)*, 34.
50. Tian, J.; Li, X. Z.; Yu, W. Z.; Mei, M. Y.; Cao, D. X.; Li, A. L.; Li, J.; Zhao, Y. J.; Zhang, C. "Excess heat" and "heat after death" in a gas loading hydrogen/palladium system. In *Condensed Matter Nuclear Science: Proceedings of the Ninth International Conference on Cold Fusion,* Beijing,

Downloaded by PENNSYLVANIA STATE UNIV on June 28, 2012 | http://pubs.acs.org
Publication Date (Web): December 20, 2009 | doi: 10.1021/bk-2009-1029.ch002

China, May 19, 24, 2002; Li, X. Z., Ed.; Tsinghua University Press: Beijing, 2002; p 360.

51. Manduchi, C.; Zannoni, G.; Milli, E.; Riccardi, L.; Mengoli, G.; Fabrizio, M.; Buffa, A. Anomalous effects during the interaction of subatmospheric $D_2(H_2)$ with Pd from 900°C to room temperature. *Nuovo Cimento A* **1994**, *107(2)*, 171.
52. Kirkinskii, V. A.; Drebushchak, V. A.; Khmelnikov, A. I. Experimental evidence of excess heat output during deuterium sorption-desorption in palladium deuteride. In *Condensed Matter Nuclear Science: Proceedings of the Ninth International Conference on Cold Fusion,* Beijing, China, May 19, 24, 2002; Li, X. Z., Ed.; Tsinghua University Press: Beijing, 2002; p 170.
53. Kirkinskii, V. A.; Drebushchak, V. A.; Khmelnikov, A. I. Excess heat release during sorption-desorption by finely powdered palladium deuteride. *Europhys. Lett.* **2002**, *58(3)*, 462.
54. Kirkinskii, V. A.; Khmelnikov, A. I. Setup for measuring of energy balance at interaction of metals and hydrogen isotopes gas at high temperatures and pressures. In *Condensed Matter Nuclear Science: Proceedings of the Thirteenth International Conference on Condensed Matter Nuclear Science*, Sochi, Russia, 25 June-1 July, 2007; Bazhutov, Y., Ed.; Publisher Center MATI: Moscow, 2008, p 43.
55. Case, L. C. The reality of "cold fusion." *Fusion Technol.* **1991**, *20*, 478.
56. Case, L. C. Catalytic fusion of deuterium into helium-4. In *Proceedings of the Seventh International Conference on Cold Fusion,* Vancouver, Canada, April 19-24, 1998; Jaeger, F., Ed.; ENECO, Inc., Salt Lake City, UT, 1998; p 48.
57. McKubre, M.; Tanzella, F.; Tripodi, P.; Hagelstein, P. The emergence of a coherent explanation for anomalies observed in D/Pd and H/Pd systems: evidence for ^{4}He and ^{3}He production. In *Proceedings of the Eighth International Conference on Cold Fusion*, Lerici (La Spezia), Italy, May 21, 26, 2000; Scaramuzzi, F., Ed.; Italian Physical Scoiety: Bologna, Italy, 2000; p 3.
58. Marmingi, A.; Spallone, A.; Celani, F.; Marini, P.; Di Stefano, V. Anomalous heat generation by surface oxidized Pd wires in a hydrogen atmosphere. In *Proceedings of Eighth International Workshop on Anomalies in Hydrogen/Deuterium Loaded Metals*, 13-18 October 2007, Catania, Italy; Rothwell, J.; Mobberley, P., Eds.; The International Society for Condensed Matter Nuclear Science, 2008, p 224.
59. Celani, F.; Spallone, A.; Righi, E.; Trenta, G.; Andreasi, V.; Marmigi, A.; Quercia, P.; Cappuccio, G.; Hampi, D.; Marini, P.; Di Stefano, V.; Nakamura, M.; Todarello, F.; Purchi, E.; Mancini, A.; Mastromatteo, U.; Falcioni, F.; Marchesini, M.; Di Biagio, P.; Sona, P.G; Fontana, F.; Gamberale, L.; Garbelli, D. Electrochemical D loading of palladium wires by heavy ethyl-alcohol and water electrolyte, related to Ralstonia bacteria problematics. In *Condensed Matter Nuclear Science: Proceedings of the Thirteenth International Conference on Condensed Matter Nuclear Science*, Sochi, Russia, 25 June-1 July, 2007; Bazhutov, Y., Ed.; Publisher Center MATI: Moscow, 2008, p 181.

Downloaded by PENNSYLVANIA STATE UNIV on June 28, 2012 | http://pubs.acs.org
Publication Date (Web): December 20, 2009 | doi: 10.1021/bk-2009-1029.ch002

Downloaded by PENNSYLVANIA STATE UNIV on June 28, 2012 | http://pubs.acs.org
Publication Date (Web): December 20, 2009 | doi: 10.1021/bk-2009-1029.ch002

60. Celani, F.; Spallone, A.; Righi, E.; Trenta, G.; Andreasi, V.; Marmigi, A.; Cappuccio, G.; Hampi, D.; Marini, P.; Di Stefano, V.; Nakamura, M.; Todarello, F.; Purchi, E.; Mastromatteo, U.; Mancini, A.; Falcioni, F.; Marchesini, M.; Di Biagio, P.; Martini, U.; Sona, P.G.; Fontana, F.; Gamberale, L.; Garbelli, D. Deuterons electromigration in thin Pd wires coated with nano-particles: evidence for ultra fast deuterium loading and anomalous, large, thermal effects. *Fourteenth International Conference on Cold Fusion,* Aug. 17-21, 2008, Washington, DC.
61. Nassisi, V.; Longo, M. L. Experimental results of transmutation of elements observed in etched palladium samples by an excimer laser. *Fusion Technol.* **2000**, *37*, 247.
62. Nassisi, V. Incandescent Pd and anomalous distribution of elements in deuterated samples processed by an excimer laser. *J. New Energy* **1997**, *2(3/4)*, 14.
63. Nassisi, V. Transmutation of elements in saturated palladuim hydrides by an XeCl excimer laser. *Fusion Technol.* **1998**, *33*, 468.
64. Yamaguchi, E.; Nishioka, T. Cold nuclear fusion induced by controlled out-diffusion of deuterons in palladium. *Jpn. J. Appl. Phys. Part 2* **1990**, *29*, L666.
65. Yamaguchi, E.; Sugiura, H. Excess heat and nuclear products from Pd:D/Au heterostructures by the ‘in-vacuo’ method. In *Proceedings of the Seventh International Conference on Cold Fusion,* Vancouver, Canada, April 19-24, 1998; Jaeger, F., Ed.; ENECO, Inc., Salt Lake City, UT, 1998; p.
66. Liu, B.; Li, X. Z.; Wei, Q. M.; Zheng, S. X. Selective resonant tunneling through Coulomb barrier by confined particles in lattice well. In *Proceedings of Eighth International Workshop on Anomalies in Hydrogen/Deuterium Loaded Metals*, 13-18 October 2007, Catania, Italy; Rothwell, J.; Mobberley, P., Eds.; The International Society for Condensed Matter Nuclear Science, 2008; p 204.
67. Narita, S.; Yamada, H.; Monma, H.; Onodera, H.; Tanaka, N.; Tateishi, T.; Baba, M.; Yamaguchi, E. Anomalous heat evolution for palladium hydride in controlled gas out-diffusion. In *Condensed Matter Nuclear Science: Proceedings of the Ninth International Conference on Cold Fusion,* Beijing, China, May 19, 24, 2002; Li, X. Z., Ed.; Tsinghua University Press: Beijing, 2002; p 280.
68. Lipson, A. G.; Lyakhov, B. F.; Rousstesky, A. S.; Asami, N. Evidence for DD-reaction and a long-range alpha emission in Au/Pd/PdO:D heterostructure as a result of exothermic deuterium deposition. In *Proceedings of the Eighth International Conference on Cold Fusion*, Lerici (La Spezia), Italy, May 21, 26, 2000; Scaramuzzi, F., Ed.; Italian Physical Scoiety: Bologna, Italy, 2000; p 231.
69. Biberian, J. P.; Armanet, N. Excess heat production during D_2 diffusion through palladium. *Thirteen International Conference on Condensed Matter Nuclear Science*, Russia; 2006, p 170.
70. Biberian, J. P.; Armanet, N. Excess heat during diffusion of deuterium through palladium. In *Proceedings of Eighth International Workshop on Anomalies in Hydrogen/Deuterium Loaded Metals*, 13-18 October 2007,

Catania, Italy; Rothwell, J.; Mobberley, P., Eds.; The International Society for Condensed Matter Nuclear Science, 2008; p 19.

71. Li, X. Z.; Yue, W. Z.; Huang, G. S.; Shi, H.; Gao, L.; Liu, M. L.; Bu, F. S. "Excess heat" measurement in gas-loading D/Pd system. *Progress in New Hydrogen Energy: Proceedings of the Sixth International Conference on Cold Fusion*, Lake Toya, Hokkaido, Japan, Oct. 13-18, 1996. Okamoto, M., Ed.; New Energy and Industrial Technology Development Organization, Tokyo Institute of Technology: Tokyo, 1996; p 455.
72. Yamaguchi, E.; Nishioka, T. Direct evidence for nuclear fusion reactions in deuterated palladium. *Frontiers of Cold Fusion: Proceedings of the Third International Conference on Cold Fusion,* Nagoya, Japan, Oct. 21-25, 1992; Ikegami, H., Ed.; Universal Academy Press: Tokyo, Japan, 1993; p.
73. Clarke, B. W.; Oliver, B.; McKubre, M.; Tanzella, F.; Tripodi, P. Search for ^{3}He in Arata style palladium cathodes II: evidence for tritium production. *Fusion Sci. and Technol.* **2001**, *40*, 152.
74. Botta, E.; Bracco, R.; Bressani, T.; Calvo, D.; Cela, V.; Fanara, C.; Ferracin, U.; Iazzi, F. Search for ^{4}He production from Pd/D_2 systems in gas phase. In *Proceedings of the Fifth International Conference on Cold Fusion,* Monte Carlo, Monaco, 1995. Pons, B. S., Ed.; IMRA Europe: Sophia Antipolis, Valbonne, France, p 233.
75. Botta, E.; Bressani, T.; Calvo, D.; Fanara, C.; lazzi, F. Measurement of ^{4}He production from D_2 gas-loaded Pd samples. *Progress in New Hydrogen Energy: Proceedings of the Sixth International Conference on Cold Fusion*, Lake Toya, Hokkaido, Japan, Oct. 13-18, 1996. Okamoto, M., Ed.; New Energy and Industrial Technology Development Organization, Tokyo Institute of Technology: Tokyo, 1996; p 29.
76. Qiao, G. S.; Han, X. L.; Kong, L. C.; Zheng, S. X.; Huang, H. F.; Yan, Y. J.; Wu, Q. L.; Deng, Y.; Lei, S. L.; Li, X. Z. Nuclear products in a gas-loading D/Pd and H/Pd system. In *Proceedings of the Seventh International Conference on Cold Fusion,* Vancouver, Canada, April 19-24, 1998; Jaeger, F., Ed.; ENECO, Inc., Salt Lake City, UT, 1998; p 314.
77. Qiao, G. S.; Han, X. M.; Kong, L. C.; Li, X. Z. J. Nuclear transmutation in a gas-loading system. *New Energy* **1997**, *2(2)*, 48.
78. Kluev, V. A.; Lipson, A. G.; Toporov, Y. P.; Deryagin, B. V.; Lushchikov, V. I.; Strelkov, A. V.; Shabalin, E. P. High-energy processes accompanying the fracture of solids. *Sov. Tech. Phys. Lett.* **1986**, *12*, 551.
79. Kluev, V. A.; Lipson, A. G.; Topornov, Y. P.; Derjaguin, B.; Lushikov, V. I.; Strelkov, A. V.; Shabalin, E. P. High-energy processes accompanying the fracture of solids. *J. Sov Tech Physics Lett* **1986**, *12*, 1333.
80. Derjaguin, B. V.; Lipson, A. G.; Kluev, V. A.; Sakov, D. M.; Topporov, Y. P. Titanium fracture yields neutrons? *Nature* **1989**, *341*, 492.
81. Jin, S. X.; Zhan, F. X.; Liu, Y. Z. Deuterium absorbability and anomalous nuclear effect of YbaCuO high temperature superconductor. In *Condensed Matter Nuclear Science: Fourth International Conference on Cold Fusion*, Dec. 6-9, 1993, Maui, HI, 1994; Passell, T. O., Ed.; Electric Power Research Institute: Palo Alto, CA, 1995; Vol. 3, p 4-1.
82. Shioe, Y.; Mondal, N. N.; Chiba, M.; Hirose, T.; Fujii, M.; Nakahara, H.; Sueki, K.; Shirakawa, T.; Utsumi, M. Measurement of neutron production

Downloaded by PENNSYLVANIA STATE UNIV on June 28, 2012 | http://pubs.acs.org
Publication Date (Web): December 20, 2009 | doi: 10.1021/bk-2009-1029.ch002

rate regarding the quantity of $LiNbO_3$ in the fracturing process under D_2 atmosphere. *Nuovo Cimento A*, **1999**, *112*, 1059.

83. Shirakawa, T.; Chiba, M.; Fujii, M.; Sueki, K.; Miyamoto, S.; Nakamitu, Y.; Toriumi, H.; Uehara, T.; Miura, H.; Watanabe, T.; Fukushima, K.; Hirose, T.; Seimiya, T; Nakahara, H. A. Neutron emission from lithium niobate fracture. *Chem. Lett.* **1993**, *22*, 897.
84. Aiello, S.; De Filippo, E.; Lanzano, G.; Lo Nigro, S.; Pagano, A. Nuclear fusion experiment in palladium charged by deuterium gas. *Fusion Technol.* **1990**, *18*, 115.
85. De Ninno, A.; Frattolillo, A.; Lollobattista, G.; Martinis, L.; Martone, M.; Mori, L.; Podda, S.; Scaramuzzi, F. Emission of neutrons as a consequence of titanium-deuterium interactions. *Nuovo Cimento,* note brevi **1989**, *101*, 841.
86. De Ninno, A.; Frattolillo, A.; Lollobattista, G.; Martinis, L.; Martone, M.; Mori, L.; Podda, S.; Scaramuzzi, F. Evidence of emission of neutrons from a titanium-deuterium system. *Europhysics Letters* **1989**, *9(3)*, 221.
87. De Ninno, A.; Scaramuzzi, F.; Frattolillo, A.; Migliori, S.; Lanza, F.; Scaglione, S.; Zeppa, P.; Pontorieri, C. The production of neutrons and tritium in the deuterium gas-titanium interaction. In *Proceedings of the Second Annual Conference on Cold Fusion,* Como, Italy, 1991; Bressani, T.; Del Giudice, E.; Preparata, G., Eds.; Societa Italiana di Fisica: Bologna, Italy, 1991; p 129.
88. Menlove, H. O.; Fowler, M. M.; Garcia, E.; Mayer, A.; Miller, M. C.; Ryan, R. R. Measurement of neutron emission from cylinders containing titanium with pressurized deuterium gas. *Workshop on Cold Fusion Phenomena*, Santa Fe, NM; 1989.
89. Menlove, H. O.; Paciotti, M. A.; Claytor, T. N.; Maltrud, H. R.; Rivera, O. M.; Tuggle, D. G.; Jones, S. E. Tritium and neutron measurements from deuterated Pd-Si; Anomalous Nuclear Effects in Deuterium/Solid Systems. *AIP Conference Proceedings 228*, 1990; p 467.
90. Menlove, H. O.; Fowler, M. M.; Garcia, E.; Miller, M. C.; Paciotti, M. A.; Ryan, R. R.; Jones, S. E. Measurement of neutron emission from Ti and Pd in pressurized D_2 gas and D_2O electrolysis cells. *J. Fusion Energy* **1990**, *9(4)*, 495.

91 Menlove, H. O.; Paciotti, M. A.; Claytor, T. N.; Tuggle, D. G. Tritium generation and neutron measurements in Pd-Si under high deuterium gas pressure. In *Proceedings of the Second Annual Conference on Cold Fusion,* Como, Italy, 1991; Bressani, T.; Del Giudice, E.; Preparata, G., Eds.; Societa Italiana di Fisica: Bologna, Italy, 1991; p 395.

92. Fabrizio, M.; Manduchi, C.; Mengoli, G.; Milli, E.; Zannoni, G. Rome Emissione di neutroni dall'interazione di deuterio gassoso con titanio e con leghe a base di palladio. *Workshop on the Status of Cold Fusion in Italy,* University of Rome III, 1993; p 74.
93. Claytor, T. N.; Seeger, P.; Rohwer, R. K.; Tuggle, D. G.; Doty, W. R. Tritium and neutron measurements of a solid state cell. *NSF/EPRI Workshop on Anomalous Effects in Deuterated Materials,* Washington, DC., 1989.

Downloaded by PENNSYLVANIA STATE UNIV on June 28, 2012 | http://pubs.acs.org
Publication Date (Web): December 20, 2009 | doi: 10.1021/bk-2009-1029.ch002

94. Claytor, T. N.; Jackson, D. D.; Tuggle, D. G. Tritium production from low voltage deuterium discharge on palladium and other metals. *Infinite Energy* **1996**, *2(7)*, 39.
95. Claytor, T. N.; Tuggle, D. G.; Menlove, H. O. Tritium generation and neutron measurements in Pd-Si under high deuterium gas pressure. In *Proceedings of the Second Annual Conference on Cold Fusion,* Como, Italy, 1991; Bressani, T.; Del Giudice, E.; Preparata, G., Eds.; Societa Italiana di Fisica: Bologna, Italy, 1991; p 395.
96. Tuggle, D. G.; Claytor, T. N.; Taylor, S. F. Tritium evolution from various morphologies of palladium. *Trans. Fusion Technol.* **1994**, *26(4T)*, 221.
97. Bressani, T.; Calvo, D.; Feliciello, A.; Lamberti, C.; Iazzi, F.; Minetti, B.; Cherubini, R.; Haque, Z. M. I.; Ricci, R. A. Studies of electrolytic and gas phase loading of palladium with deuterium. In *Proceedings of the Second Annual Conference on Cold Fusion,* Como, Italy, 1991; Bressani, T.; Del Giudice, E.; Preparata, G., Eds.; Societa Italiana di Fisica: Bologna, Italy, 1991; p 373.
98. Bressani, T.; Calvo, D.; Feliciello, A.; Lamberti, C.; Iazzi, F.; Minetti, B.; Cherubini, R.; Haque, Z. M. I.; Ricci, R. A. Observation of 2.5 MeV neutrons emitted from a titanium-deuterium system. *Nuovo Cimento Soc. Ital. Fis. A* **1991**, *104*, 1413.
99. Botta, E.; Bressani, T.; Calvo, D.; Feliciello, A.; Gianotti, P.; Lamberti, C.; Agnello, M.; Iazzi, F.; Minetti, B.; Zecchina, A. Measurement of 2.5 MeV neutron emission from Ti/D and Pd/D systems. *Nuovo Cimento A* **1992**, *105*, 1663.
100. Shirakawa, T.; Fujii, M.; Chiba, M.; Sueki, K.; Ikebe, T.; Yamaoka, S.; Miura, H.; Watanabe, T.; Hirose, T.; Nakahara, H.; Utsumi, M. Particle acceleration and neutron emission in a fracture process of a piezoelectric material. In *Condensed Matter Nuclear Science: Fourth International Conference on Cold Fusion*, Dec. 6-9, 1993, Maui, HI, 1994; Passell, T. O., Ed.; Electric Power Research Institute: Palo Alto, CA, 1995; Vol. 3, p 6-1.
101. Iwamura, Y.; Itoh, T.; Toyoda, I. Observation of anomalous nuclear effects in D_2-Pd system. In *Condensed Matter Nuclear Science: Fourth International Conference on Cold Fusion*, Dec. 6-9, 1993, Maui, HI, 1994; Passell, T. O., Ed.; Electric Power Research Institute: Palo Alto, CA, 1995; Vol. 3, p 12-1.
102. Garg, A. B.; Rout, R. K.; Srinavasan, M.; Sankarnarayanan, T. K.; Shyam, A.; Kulkarni, L. V. Protocol for controlled and rapid loading/unloading of H_2/D_2 gas in self heated Pd wides to trigger nuclear events. In *Proceedings of the Fifth International Conference on Cold Fusion,* Monte Carlo, Monaco, 1995. Pons, B. S., Ed.; IMRA Europe: Sophia Antipolis, Valbonne, France, p 461.
103. Aoki, T.; Kurata, Y.; Ebihara, H. Search for neutrons emitted from sodium tungsten bronzes. *Progress in New Hydrogen Energy: Proceedings of the Sixth International Conference on Cold Fusion*, Lake Toya, Hokkaido, Japan, Oct. 13-18, 1996. Okamoto, M., Ed.; New Energy and Industrial Technology Development Organization, Tokyo Institute of Technology: Tokyo, 1996; p 291.

Downloaded by PENNSYLVANIA STATE UNIV on June 28, 2012 | http://pubs.acs.org
Publication Date (Web): December 20, 2009 | doi: 10.1021/bk-2009-1029.ch002

104. Shinojima, H.; Takahashi, N.; Koji, S.; Hiroshi, Detection for nuclear products in transport experiments of deuterium through palladium metals. *Progress in New Hydrogen Energy: Proceedings of the Sixth International Conference on Cold Fusion*, Lake Toya, Hokkaido, Japan, Oct. 13-18, 1996. Okamoto, M., Ed.; New Energy and Industrial Technology Development Organization, Tokyo Institute of Technology: Tokyo, 1996; p 351.
105. Lipson, A. G.; Lyakhov, B. F.; Rousstesky, A. S.; Asami, N. Evidence for DD-reaction and a long-range alpha emission in Au/Pd/PdO:D heterostructure as a result of exothermic deuterium deposition. In *Proceedings of the Eighth International Conference on Cold Fusion*, Lerici (La Spezia), Italy, May 21, 26, 2000; Scaramuzzi, F., Ed.; Italian Physical Scoiety: Bologna, Italy, 2000; p 231.
106. Lipson, A. G.; Lyakhov, B. F.; Roussetski, A. S.; Akimoto, T.; Mizuno, T.; Asami, N.; Shimada, R.; Miyashita, S.; Takahashi, A. Evidence for low-intensity D-D reaction as a result of exothermic deuterium desorption from Au/Pd/PdO:D heterostructure. *Fusion Technol.* **2000**, *38*, 238.
107. Roussetski, A. S. Investigation of nuclear emissions in the process of D(H) escaping from deuterized (hydrogenised) PdO-Pd-PdO and PdO-Ag samples. *Progress in New Hydrogen Energy: Proceedings of the Sixth International Conference on Cold Fusion*, Lake Toya, Hokkaido, Japan, Oct. 13-18, 1996. Okamoto, M., Ed.; New Energy and Industrial Technology Development Organization, Tokyo Institute of Technology: Tokyo, 1996; p 345.
108. Dougar-Jabon, V. D.; Kariaka, V. I.; Samsonenko, N. V. Study of the neutron and g-emission from the palladium-deuterium system in the process of the transformation of the crystalline structure. In *Proceedings of the Eighth International Conference on Cold Fusion*, Lerici (La Spezia), Italy, May 21, 26, 2000; Scaramuzzi, F., Ed.; Italian Physical Scoiety: Bologna, Italy, 2000; p 219.
109. Chicea, D.; Stoicescu, D. Experimental evidence of nuclear reactions in deuterated titanium samples under non-equilibrium conditions induced by temperature variation. In *Proceedings of the Eighth International Conference on Cold Fusion*, Lerici (La Spezia), Italy, May 21, 26, 2000; Scaramuzzi, F., Ed.; Italian Physical Scoiety: Bologna, Italy, 2000; p 247.
110. Itoh, T.; Iwamura, Y.; Gotoh, N.; Toyoda, I. Observation of nuclear products under vacuum conditions from deuterated palladium with high loading ratio. In *Proceedings of the Fifth International Conference on Cold Fusion,* Monte Carlo, Monaco, 1995. Pons, B. S., Ed.; IMRA Europe: Sophia Antipolis, Valbonne, France, p 189.
111. Iyengar, P. K.; Srinavasan, M. Overview of BARC studies in Cold Fusion. In *The First Annual Conference on Cold Fusion,* March 28-31, 1990, Salt Lake City, Utah. National Cold Fusion Institute: University of Utah Research Park, Salt Lake City, Utah, 1990; p 62.
112. Srinivasan, M.; Shyam, A.; Kaushik, T. C.; Rout, R. K.; Kulkarni, L. V.; Krishnan, M. S.; Malhotra, S. K.; Nagvenkar, V. G.; Iyengar, P. K. Observation of tritium in gas/plasma loaded titanium samples. *AIP Conference Proceedings 228,* 1990; p 514.

Downloaded by PENNSYLVANIA STATE UNIV on June 28, 2012 | http://pubs.acs.org
Publication Date (Web): December 20, 2009 | doi: 10.1021/bk-2009-1029.ch002

113. Iyengar, P. K.; Srinivasan, M.; Sikka, S. K.; Shyam, A.; Chitra, V.; Kulkarni, L. V.; Rout, R. K.; Krishnan, M. S.; Malhotra, S. K.; Gaonkar, D. G.; Sadhukhan, H. K.; Nagvenkar, V. B.; Nayar, M. G.; Mitra, S. K.; Raghunathan, P.; Degwekar, S. B.; Radhakrishnan, T. P.; Sundaresan, R.; Arunachalam, J.; Raju, V. S.; Kalyanaraman, R.; Gangadharan, S.; Venkateswaran, G.; Moorthy, P. N.; Venkateswarlu, K. S.; Yuvaraju, B.; Kishore, K.; Guha, S. N.; Panajkar, M. S.; Rao, K. A.; Raj, P.; Suryanarayana, P.; Sathyamoorthy, A.; Datta, T; Bose, H.; Prabhu, L. H.; Sankaranarayanan, S.; Shetiya, R. S.; Veeraraghavan, N.; Murthy, T. S.; Sen, B. K.; Joshi, P. V.; Sharma, K. G. B.; Joseph, T. B.; Iyengar, T. S.; Shrikhande, V. K.; Mittal, K. C.; Misra, S. C.; Lal, M.; Rao, P. S. Bhabha Atomic Research Centre studies on cold fusion. *Fusion Technol.* **1990**, *18*, 32.

114. Kaushik, T. C.; Shyam, A.; Srinivasan, M.; Rout, R. K.; Kulkarni, L. V.; Krishnan, M. S.; Nagvenkar, V. B. Preliminary report on direct measurement of tritium in liquid nitrogen treated TiDx chips. *Indian J. Technol.* **1990**, *28*, 667.

115. Rout, R. K.; Shyam, A.; Srinivasan, M.; Garg, A. B.; Shrikhande, V. K. Reproducible anomalous emissions from palladium deuteride/hydride. *Fusion Technol.* **1996**, *30*, 273.

116. Rout, R. K.; Shyam, A.; Srinivasan, M.; Garg, A. B. Phenomenon of low energy emission from hydrogen/deuterium loaded palladium. *Frontiers of Cold Fusion: Proceedings of the Third International Conference on Cold Fusion,* Nagoya, Japan, Oct. 21-25, 1992; Ikegami, H., Ed.; Universal Academy Press: Tokyo, Japan, 1993; p 547.

117. Sankaranarayanan, T. K.; Srinavasan, M.; Bajpai, M. B.; Gupta, D. S. Evidence for tritium generation in self-heated nickel wires subjected to hydrogen gas absorption/desorption cycles. In *Proceedings of the Fifth International Conference on Cold Fusion,* Monte Carlo, Monaco, 1995. Pons, B. S., Ed.; IMRA Europe: Sophia Antipolis, Valbonne, France, p 173.

118. Lanza, F; Bertolini, G.; Vocino, V.; Parnisari, E.; Ronsecco, C. Tritium production resulting from deuteration of different metals and alloys. In *Proceedings of the Second Annual Conference on Cold Fusion,* Como, Italy, 1991; Bressani, T.; Del Giudice, E.; Preparata, G., Eds.; Societa Italiana di Fisica: Bologna, Italy, 1991; p 151.

119. Yamada, H.; Narita, S.; Inamura, I.; Nakai, M.; Iwasaki, K.; Baba, M. Tritium production in palladium deuteride/hydride in evacuated chamber. In *Proceedings of the Eighth International Conference on Cold Fusion*, Lerici (La Spezia), Italy, May 21, 26, 2000; Scaramuzzi, F., Ed.; Italian Physical Scoiety: Bologna, Italy, 2000; p 241.

120. Wei, Q. M.; Li, X. Z.; Liu, B.; Mueller, N; Schochi, P.; Oehre, H. High resolution mass spectrum for $D_2(H_2)$ gas permeating palladium film. In *Condensed Matter Nuclear Science: Proceedings of the Twelfth International Conference on Cold Fusion*, Yokohama, Japan, Nov. 27-Dec. 2, 2005; Takahashi, A.; Ota, K.; Iramura, Y. Eds.; World Scientific Publishing Co.: 2006; p 278.

Downloaded by PENNSYLVANIA STATE UNIV on June 28, 2012 | http://pubs.acs.org
Publication Date (Web): December 20, 2009 | doi: 10.1021/bk-2009-1029.ch002

121. Claytor, T. N.; Jackson, D. D.; Tuggle, D. G. J. Tritium production from low voltage deuterium discharge of palladium and other metals. *New Energy* **1996**, *1(1)*, 111.

122. Clarke, B. W.; Clarke, R. M. Search for ^{3}H, ^{3}He, and ^{4}He in D_2-loaded titanium. *Fusion Technol.* **1992**, *21*, 170.

123. Romodanov, V. A.; Savin, V.; Skuratnik, Y.; Yuriev, M. Nuclear reactions in condensed media and X-ray. In *Proceedings of the Seventh International Conference on Cold Fusion,* Vancouver, Canada, April 19-24, 1998; Jaeger, F., Ed.; ENECO, Inc., Salt Lake City, UT, 1998; p 330.

124. Lipson, A. G.; Sakov, D. M.; Lyakhov, B. F.; Saunin, E. I.; Deryagin, B. V. Generation of the products of DD nuclear fusion in high-temperature superconductors $YBa_2Cu_3O_7$-Dy near the superconducting phase transition. *Tech. Phys.* **1995**, *40*, 839.

125. Mo, D. W.; Zhang, L.; Chen, B. X.; Liu, Y. S.; Doing, S. Y.; Yao, M. Y.; Zhou, L. Y.; Huang, H. G.; Li, X. Z.; Shen, X. D.; Wang, S. C.; Kang, T. S.; Huang, N. Z. Real time measurements of the charged particles and the loading ratio (D/Pd). *Frontiers of Cold Fusion: Proceedings of the Third International Conference on Cold Fusion,* Nagoya, Japan, Oct. 21-25, 1992; Ikegami, H., Ed.; Universal Academy Press: Tokyo, Japan, 1993; p 535.

126. Mo, D. W.; Liu, Y. S.; Zhou, L. Y.; Dong, S. Y.; Wang, K. L.; Wang, S. C.; Li, X. Z. Search for precursor and charged particles in “cold fusion.” In *Proceedings of the Second Annual Conference on Cold Fusion,* Como, Italy, 1991; Bressani, T.; Del Giudice, E.; Preparata, G., Eds.; Societa Italiana di Fisica: Bologna, Italy, 1991; p 123.

127. Wang, C.; Kang, T. S.; Wang, K. L.; Dong, S. Y.; Feng, Y. Y.; Mo, D. W.; Li, X. Z. Identification of the energetic charged particles in gas-loading experiment of “cold fusion” using CR-39 plastic track detector. In *Proceedings of the Second Annual Conference on Cold Fusion,* Como, Italy, 1991; Bressani, T.; Del Giudice, E.; Preparata, G., Eds.; Societa Italiana di Fisica: Bologna, Italy, 1991; p 169.

128. Jin, S.; Zhang, F.; Yao, D.; Wu, B. Anomalous nuclear events in deuterium palladium systems. In *Proceedings of the Second Annual Conference on Cold Fusion,* Como, Italy, 1991; Bressani, T.; Del Giudice, E.; Preparata, G., Eds.; Societa Italiana di Fisica: Bologna, Italy, 1991; p 145.

129. Li, X. Z.; Dong, S. Y.; Wang, K. L.; Feng, Y. Y.; Luo, C.; Hu, R.; Zhou, P.; Mo, D. W.; Zhu, Y.; Song, C.; Chen, Y.; Yao, M.; Ren, C.; Chen, Q. The precursor of “cold fusion” phenomenon in deuterium/solid systems*;* Anomalous Nuclear Effects in Deuterium/Solid Systems. *AIP Conference Proceedings 228,* 1990; p 419.

130. Dong, S. Y.; Wang, K. L.; Feng, Y. Y.; Chang, L.; Luo, C. M.; Hu, R. Y.; Zhou, P. L.; Mo, D. W.; Zhu, Y. F.; Song, C. L.; Chen, Y. T.; Yao, M. Y.; Ren, C.; Chen, Q. K.; Li, X. Z. Precursors to “cold fusion” phenomenon and the detection of energetics charged particles in deuterium/solid systems. *Fusion Technol.* **1991**, *20*, 330.

131. Cecil, F. E.; Liu, H.; Beddingfield, D. H.; Galovich, C. S. Observation of charged-particle bursts from deuterium-loaded thin-titanim foils. *AIP Conference Proceedings 228*, 1990; p 375.

Downloaded by PENNSYLVANIA STATE UNIV on June 28, 2012 | http://pubs.acs.org
Publication Date (Web): December 20, 2009 | doi: 10.1021/bk-2009-1029.ch002

132. Jones, S. E.; Bartlett, T. K.; Buehler, D. B.; Czirr, J. B.; Jensen, G. L.; Wang, J. C. Preliminary results from the BYU charged-particle spectrometer. *AIP Conference Proceedings 228,* 1990; p 397.
133. Jones, S. E.; Keeney, F. W.; Johnson, A. C.; Buehler, D. B.; Cecil, F. E.; Hubler, G.; Hagelstein, P. L.; Ellsworth, J. E.; Scott, M. R. Charged-particle emissions from metal deuterides. In *Condensed Matter Nuclear Science: Tenth International Conference on Cold Fusion,* Cambridge, MA, Aug. 24-29, 2003; Hagelstein, P. L.; Chubb, S. R., Eds.; World Scientific Publishing Co.: Singapore, 2006; p 509.
134. Roussetski, A. S.; Lipson, A. G.; Andreanov, V. P. Nuclear emissions from titanium hydride/deuteride, induced by powerful picosecond laser beam. In *Condensed Matter Nuclear Science: Tenth International Conference on Cold Fusion,* Cambridge, MA, Aug. 24-29, 2003; Hagelstein, P. L.; Chubb, S. R., Eds.; World Scientific Publishing Co.: Singapore, 2006; p 559.
135. Cecil, F. E.; Liu, H.; Beddingfield, D.; Galovich, C. S. Energetic charged particles from deuterium metal systems. In *Condensed Matter Nuclear Science: Tenth International Conference on Cold Fusion,* Cambridge, MA, Aug. 24-29, 2003; Hagelstein, P. L.; Chubb, S. R., Eds.; World Scientific Publishing Co.: Singapore, 2006; p 535.
136. Lipson, A. G.; Klyuev, V. A.; Deryagin, B. V.; Toporov, Y. P.; Sakov, D. M. Anomalous beta activity of products of mechanical working of a titanium-deuterated material. *Sov. Tech. Phys. Lett.* **1989**, *15(10)*, 783.
137. Kong, L. C.; Han, X. L.; Zheng, S. X.; Huang, H. F.; Yan, Y. J.; Wu, Q. L.; Deng, Y.; Lei, S. L.; Li, C. X.; Li, X. Z. Nuclear products and transmutation in a gas-loading D/Pd and H/Pd system. *J. New Energy* **1998**, *1*, 20.
138. Qiao, G. S.; Han, X. L.; Kong, L. C.; Zheng, S. X.; Huang, H. F.; Yan, Y. J.; Wu, Q. L.; Deng, Y.; Lei, S. L.; Li, X. Z. Nuclear products in a gas-loading D/Pd and H/Pd system. In *Proceedings of the Seventh International Conference on Cold Fusion,* Vancouver, Canada, April 19-24, 1998; Jaeger, F., Ed.; ENECO, Inc., Salt Lake City, UT, 1998; p 314.
139. Higashiyama, T.; Sakano, M.; Miyamaru, H.; Takahashi, A. Replication of MHI transmutation experiment by D gas permeation through Pd complex. In *Condensed Matter Nuclear Science: Tenth International Conference on Cold Fusion,* Cambridge, MA, Aug. 24-29, 2003; Hagelstein, P. L.; Chubb, S. R., Eds.; World Scientific Publishing Co.: Singapore, 2006; p 447.
140. Minari, T.; Nishio, R.; Taniike, A.; Furuyama, Y.; Kitamura, A. Experiments on condensed matter nuclear events in Kobe University. In *Condensed Matter Nuclear Science: Tenth International Conference on Cold Fusion,* Cambridge, MA, Aug. 24-29, 2003; Hagelstein, P. L.; Chubb, S. R., Eds.; World Scientific Publishing Co.: Singapore, 2006; p 218.
141. Hioki, T.; Takahashi, N.; Motohiro, T. XPS study on surface layer elements of Pd/CaO multilayer complex with and without deuterium permeation. In *Condensed Matter Nuclear Science: Proceedings of the Thirteenth International Conference on Condensed Matter Nuclear Science*, Sochi, Russia, 25 June-1 July, 2007; Bazhutov, Y., Ed.; Publisher Center MATI: Moscow, 2008, p 518.
142. Yamada, H.; Narita, S.; Taniguchi, S.; Ushirozawa, T.; Kurihara, S.; Higashizawa, M.; Sawada, H.; Itagaki, M.; Odashima, T. Producing

Downloaded by PENNSYLVANIA STATE UNIV on June 28, 2012 | http://pubs.acs.org
Publication Date (Web): December 20, 2009 | doi: 10.1021/bk-2009-1029.ch002

Downloaded by PENNSYLVANIA STATE UNIV on June 28, 2012 | http://pubs.acs.org
Publication Date (Web): December 20, 2009 | doi: 10.1021/bk-2009-1029.ch002

transmutation elements on plain Pd-foil by permeation of highly pressurized deuterium gas. In *Condensed Matter Nuclear Science: Proceedings of the Twelfth International Conference on Cold Fusion*, Yokohama, Japan, Nov. 27-Dec. 2, 2005; Takahashi, A.; Ota, K.; Iramura, Y. Eds.; World Scientific Publishing Co.: 2006; p 196.

143. Yamada, H.; Narita, S.; Onodera, H.; Suzuki, H.; Tanaka, N.; Nyui, T.; Ushi, T. Analysis by time-of-flight secondary mass spectroscopy for nuclear products, in hydrogen penetration through palladium. In *Condensed Matter Nuclear Science: Tenth International Conference on Cold Fusion,* Cambridge, MA, Aug. 24-29, 2003; Hagelstein, P. L.; Chubb, S. R., Eds.; World Scientific Publishing Co.: Singapore, 2006; p 455.
144. Kitamura, A.; Nishio, R.; Iwai, H.; Satoh, R.; Tanike, A.; Furuyama, Y. In situ accelerator analysis of palladium complex under deuterium permeation. In *Condensed Matter Nuclear Science: Proceedings of the Twelfth International Conference on Cold Fusion*, Yokohama, Japan, Nov. 27-Dec. 2, 2005; Takahashi, A.; Ota, K.; Iramura, Y. Eds.; World Scientific Publishing Co.: 2006; p 272.
145. Castellano, M.; Di Giulio, M.; Dinescu, M.; Nassisi, V.; Conte, A. Pompa, P. P. Nuclear transmutation in deuterated Pd films irradiated by an UV laser. In *Proceedings of the Eighth International Conference on Cold Fusion*, Lerici (La Spezia), Italy, May 21, 26, 2000; Scaramuzzi, F., Ed.; Italian Physical Society: Bologna, Italy, 2000; p 287.
146. Tian, J.; Jin, L. H.; Shen, B. J.; Wang, Q. S.; Dash, J. Heat measurements and surface studies of Pd wires after being exposed to a H_2 gas-loading system irradiated with a YAG frequency doubling laser. In *Condensed Matter Nuclear Science, Proceedings of the Thirteenth International Conference on Condensed Matter Nuclear Science*, Sochi, Russia, 25 June-1 July, 2007; Bazhutov, Y., Ed.; Publisher Center MATI: Moscow, 2008, p 217.
147. Di Giulio, M.; Filippo, E.; Manno, D.; Nassisi, V. Analysis of nuclear transmutations observed in D- and H- loaded films. *J. Hydrogen Eng.* **2002**, *27*, 527.
148. Wei, Q. M.; Rao, Y. C.; Tao, S. T.; Luo, D. L.; Li, X. Z. Element analysis of the surface layer on the Pd and Pd-Y alloy after deuterium permeation. *Conference on Eighth International Workshop on Anomalies in Hydrogen/Deuterium Loaded Metals*, 13-18 October 2007, Catania, Italy.
149. Sankaranarayanan, T. K.; Srinavasan, M.; Bajpai, M. B.; Gupta, D. S. Evidence for tritium generation in self-heated nickel wires subjected to hydrogen gas absorption/desorption cycles. In *Proceedings of the Fifth International Conference on Cold Fusion,* Monte Carlo, Monaco, 1995. Pons, B. S., Ed.; IMRA Europe: Sophia Antipolis, Valbonne, France, p 173.
150. Cammarota, G.; Collis, W.; Rizzo, A.; Stremmenos, C. A flow calorimetry study of the Ni/H system. *Conference on Anomalies in Hydrogen / Deuterium Loaded Metals*, Bologna, Italy, 1999.
151. Mastromatteo, U. An energy amplifier device. *Eighth International Conference on Cold Fusion,* Lerici, Italy, 2000; p 81.

Downloaded by UNIV OF DELAWARE MORRIS LIB on June 28, 2012 | http://pubs.acs.org
Publication Date (Web): December 20, 2009 | doi: 10.1021/bk-2009-1029.ch003

Chapter 3

Wide-Ranging Studies on the Emission of Neutrons and Tritium by LENR Configurations: An Historical Review of the Early BARC Results

Mahadeva Srinivasan

Formerly Associate Director, Physics Group,
Bhabha Atomic Research Centre (BARC)
Trombay, Mumbai 400 085, India

On receipt of news of the Fleischmann-Pons announcement in March 1989, scientists loaded samples of Pd and Ti metal with deuterium using both electrolytic methods and gas/plasma-based absorption techniques. Twelve research groups and 50 scientists were involved in this massive effort. Clear evidence was accumulated for the generation of neutrons and tritium. Not only was the rate of neutron emission measured, but also, in some cases, a sophisticated analysis of the stastistical characteristics of neutron emission was carried out. The most important findings were: (a) Tritium production is much more probable than neutrons, with the neutron to tritium yield ratio being ~ 10^{-7}; (b) A fraction of the neutrons released is in the form of bursts of tens to hundreds of simultaneously emitted neutrons; and (c) The nuclear reactions responsible for the production of these seem to be occurring in highly localized hot spots in the host metal. These results strongly suggest the possible occurrence of some type of micro-nuclear explosions in selected lattice sites.

In Low-Energy Nuclear Reactions and New Energy Technologies Sourcebook Volume 2; Marwan, J., et al.;
ACS Symposium Series; American Chemical Society: Washington, DC, 2010.

Introduction

A four-line news item on the historic Martin Fleischmann and Stanley Pons (F&P) announcement carried by the 24 March 1989 issue of the Times of India newspaper triggered a flurry of activity at the Bhabha Atomic Research Centre (BARC) in Mumbai. Within days, groups with expertise in diverse disciplines such as hydriding of metals, electrochemistry, isotope exchange processes in upgrading heavy water, fusion plasma experiments and neutron and tritium measurements set up a variety of electrolytic cells with widely different geometrical configurations in order to verify the extraordinary claims of F&P. The objective of the onslaught was to establish whether the F&P effect had any nuclear dimension to it. At that time, BARC was more interested in confirming the possible occurrence of nuclear fusion reactions at room temperature than the excess-heat aspect. Because neutrons and tritium were the commonly expected products of fusion reactions, these were the signatures that our experiments sought.

BARC, being the foremost nuclear research and development centre in India, with more than 50 divisions and 3,500 scientists and engineers, had the expertise and equipment readily available for study of almost every aspect of nuclear technology. Details of the various cell setups and the results of the neutron and tritium measurements carried out in the early years are documented in references (*1, 2, 3, 4*). The first publication on the confirmation of generation of neutrons and tritium in the BARC LENR experiments was presented at the Fifth International Conference on Emerging Nuclear Energy Systems (ICENES), held in Karlsruhe during July 1989 (*1*). A comprehensive Technical Note with 50 authors, published in the August 1990 issue of Fusion Technology (*4*), describes in great detail the LENR experiments conducted at BARC during the first eight months following the F&P announcement, inclusive of the gas/plasma-loaded Ti samples studies (*5*). An interim progress report, “BARC Studies in Cold Fusion,” covering the period April to September 1989 (*2*) unambiguously confirming the occurrence of nuclear reactions at room temperature in deuterided Pd and Ti samples was published around the same time as the highly negative findings of the report of the Energy Research Advisory Board Cold Fusion Panel set up by the U.S. Department of Energy (*6*) and played a key role in helping keep interest in the subject alive. During 1992-95, some experiments were carried out with Ni-H systems, which also indicated the production of tritium (*7, 8, 9*).

Unfortunately, following global trends of that era, LENR work at BARC fell victim to the highly skeptical view of the subject that gained credence, and studies in this controversial area of research were terminated by the mid-’90s. However, following a one-day brainstorming workshop held in January 2008 at the National Institute of Advanced Studies (NIAS) in Bangalore (*10*), which took stock of the new developments in the field, interest in LENR studies has revived once again in India. In the present paper, we revisit the forgotten BARC results of the early years and examine what lessons, if any, can be drawn from them two decades on, in the light of the new developments in the field.

Downloaded by UNIV OF DELAWARE MORRIS LIB on June 28, 2012 | http://pubs.acs.org
Publication Date (Web): December 20, 2009 | doi: 10.1021/bk-2009-1029.ch003

Electrolytic Cells and Neutron Measurements (*1, 2, 3, 4*)

The Neutron Physics Division had a head start in the BARC LENR campaign because, coincidentally, a large cathode surface area (300 cm^2) Pd-D_2O electrolytic cell with 5M NaOD electrolyte was all set and ready to be switched on on 24 March 1989! This off-the-shelf, ultra-pure hydrogen generator with 16 Pd-Ag alloy tubular cathodes arranged along a circle (inner and outer nickel cylinders constituted the anode) had been procured from Milton Roy Co. of Ireland for generating oxygen-free deuterium for plasma-focus hot fusion experiments. On receipt of the F&P announcement, researchers installed neutron monitors on either side of the cell, and electrolysis began. A NE 102A plastic scintillator fast neutron detector and a bank of three BF_3 counters embedded in a paraffin assembly constituted two independent foreground neutron monitors, while a similar He^3 counter bank in paraffin served as background monitor. Fig. 1 presents the first evidence of neutron production obtained, on 21 April 1989. Both the neutron monitors detected a dozen coincident peaks of varying magnitude.

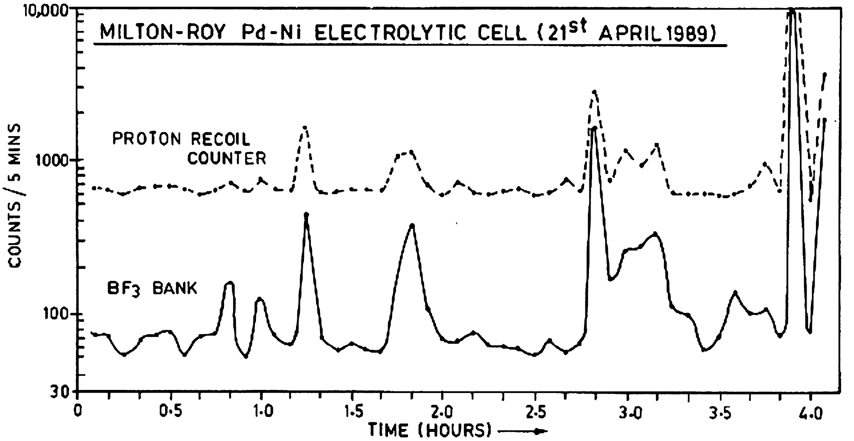

Figure 1. Neutron counts variation during run 1 of Milton Roy cell. (Reproduced from reference 2 Copyright 2008 Bhabha Atomic Research Centre)

One of the questions that intrigued the BARC investigators even at that early stage was whether these neutrons were being generated one at a time in a random fashion following Poisson statistics or in bursts of 2, 5, 10 or even more, as in a spontaneous fission neutron source. Because the multiplicity distribution of neutron emission could throw much light on the mechanism responsible for neutron generation, a sophisticated statistical analysis of the neutron output from several LENR devices was carried out (*1, 2, 3, 4*). These neutron multiplicity measurements are discussed later in this paper.

Engineers of the Desalination Division set up a large cathode area (780 cm^2) five module bipolar electrolyzer with Pd-Ag alloy cathode plates and alternating porous nickel plate anodes. Fig. 2 is a schematic of this electrolyzer; the total

Downloaded by UNIV OF DELAWARE MORRIS LIB on June 28, 2012 | http://pubs.acs.org
Publication Date (Web): December 20, 2009 | doi: 10.1021/bk-2009-1029.ch003

volume of the NaOD electrolyte in this cell was 1 liter, and the maximum current capacity was 78 amps.

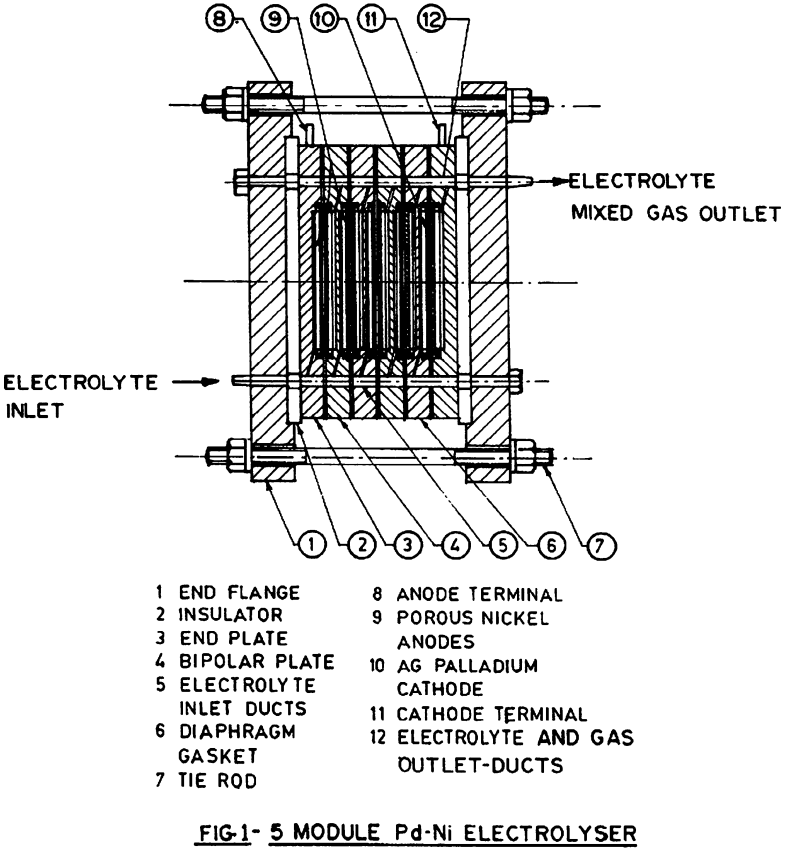
⑧
⑨
⑩
⑪
⑫
ELECTROLYTE
MIXED GAS OUTLET
ELECTROLYTE
INLET
①
②
③
④
⑤
⑥
⑦
1 END FLANGE
2 INSULATOR
3 END PLATE
4 BIPOLAR PLATE
5 ELECTROLYTE INLET DUCTS
6 DIAPHRAGM GASKET
7 TIE ROD
8 ANODE TERMINAL
9 POROUS NICKEL ANODES
10 AG PALLADIUM CATHODE
11 CATHODE TERMINAL
12 ELECTROLYTE AND GAS OUTLET-DUCTS
FIG-1- 5 MODULE Pd-Ni ELECTROLYSER

Figure 2. Five module Pd – Ni electrolizer. (Reproduced from reference 2. Copyright 2008 Bhabha Atomic Research Centre)

The Neutron Physics Division assisted with the neutron measurements, using He3 detectors and a NE 102A plastic fast neutron monitor. Within a few hours of the start of cell operation, a large spike of neutron emission lasting about two minutes was recorded by both the foreground neutron channels, whereas the background monitor did not show any change in count rate.

Many groups used cathode samples with minimal pretreatment, using only normal cleaning agents readily available in a laboratory. The chemists, however, vacuum-annealed the cathode materials before deployment in the cells. The Analytical Chemistry Division set up several cells using a variety of cathode configurations, including hollow Pd cylinder, Pd ring, and nickel-titanium alloy. Neutrons produced by two of their cells were detected via the 1186 Kev neutron capture gamma ray emitted by a sheet of gadolinium placed in front of a large Na(I) gamma detector. Fig. 3 shows three large neutron spikes emitted by one of their cells.

Downloaded by UNIV OF DELAWARE MORRIS LIB on June 28, 2012 | http://pubs.acs.org
Publication Date (Web): December 20, 2009 | doi: 10.1021/bk-2009-1029.ch003

Downloaded by UNIV OF DELAWARE MORRIS LIB on June 28, 2012 | http://pubs.acs.org
Publication Date (Web): December 20, 2009 | doi: 10.1021/bk-2009-1029.ch003

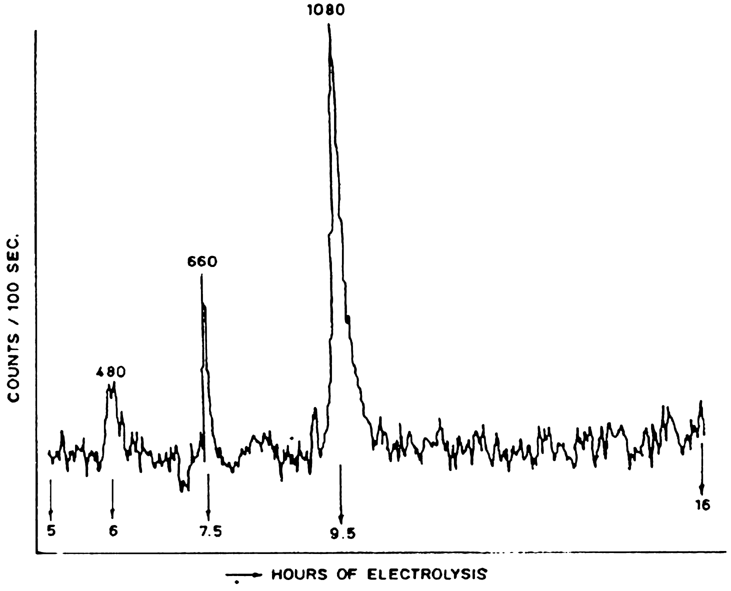

FIG. 7 COUNTS OF 1186 keV CAPTURE γ - RAY OF GADOLINIUM
NaI(Tl) DETECTOR

Figure 3. Time variation of 1186 kev Gd capture gamma ray counts (Anal. Chem. divn cell). (Reproduced from reference 2. Copyright 2008 Bhabha Atomic Research Centre)

Table I (adapted from ref 3) summarizes details of the eight electrolysis experiments in which both neutron and tritium production was observed. (The last cell in the continuation table is from the Indira Gandhi Centre for Atomic Research (IGCAR) at Kalpakkam near the city of Chennai, which is a sister institution of BARC). Six groups reported observation of the first neutron emission on the first day. The neutron emission observed from the cells using Pd or Pd alloy cathodes in the 1989 experiments was generally in the form of spikes superimposed on a steady background. In contrast, the Ti cathode cell set up by the Desalination Division indicated continuous neutron production, in the range of 50 percent to 100 percent above the background level.

Downloaded by UNIV OF DELAWARE MORRIS LIB on June 28, 2012 | http://pubs.acs.org
Publication Date (Web): December 20, 2009 | doi: 10.1021/bk-2009-1029.ch003

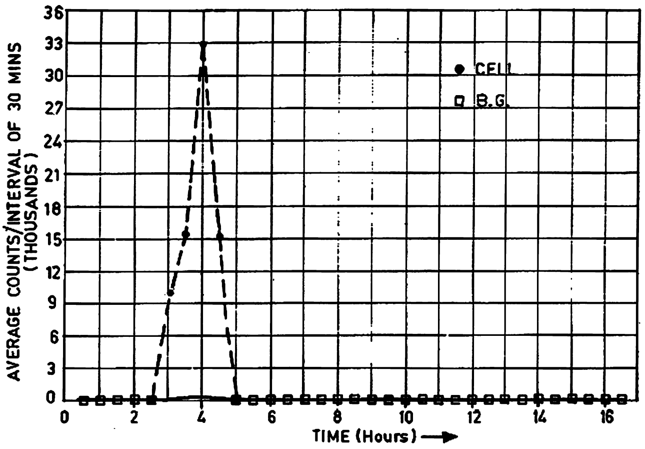

FIG.3 NEUTRON YIELD VARIATION DURING THE BURST OF 16th JUNE 89

Figure 4. Neutron output of quiescent Milton Roy Cell: 16 June 1989. (Reproduced from reference 2. Copyright 2008 Bhabha Atomic Research Centre)

On several occasions, neutron emission was also observed from electrolytic cells hours or days after the cell current had been switched off. Fig. 4 depicts one such neutron output episode from a quiescent Milton Roy cell.

Neutron measurements carried out in 1994 (*11*) on a newly procured Milton Roy cell (Pd-Ag alloy cathodes) indicated a steady but low rate of neutron production ~ 9 percent above background levels throughout a one-month period as shown in Fig. 5. This cell, however, employed 1M LiOD as electrolyte rather than 5M NaOD, used by the earlier Milton Roy cell. Neutron production by the new cell was independently confirmed by the neutron multiplicity measurements carried out throughout the one-month period as discussed in the multiplicity measurements section of this paper.

Downloaded by UNIV OF DELAWARE MORRIS LIB on June 28, 2012 | http://pubs.acs.org
Publication Date (Web): December 20, 2009 | doi: 10.1021/bk-2009-1029.ch003

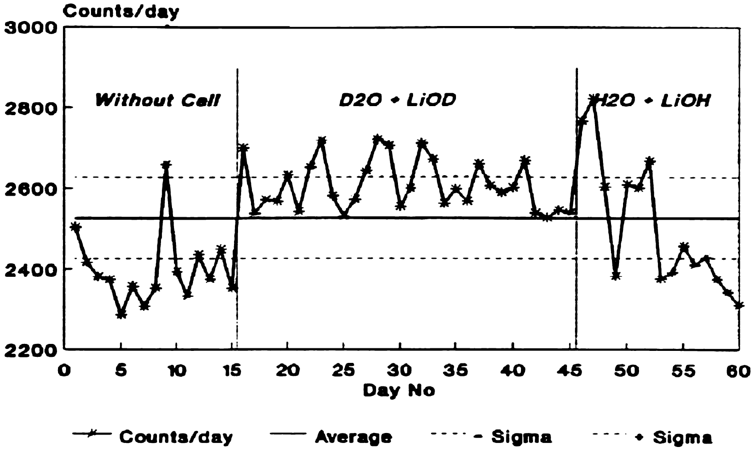

Figure 5. Steady neutron production by New Milton Roy cell: 1994 results. (Reproduced from reference 2. Copyright 2008 Bhabha Atomic Research Centre)

Neutron emission in the form of distinct spikes above background level was also observed from an unperturbed titanium deuteride disc just sitting on the table (see Fig. 6). Statistical analysis of this event also was carried out. Emission of neutrons from a shutdown cell or undisturbed TiD disc is analogous to the heat-after-death episodes observed during calorimetric measurements by other workers in the LENR field.

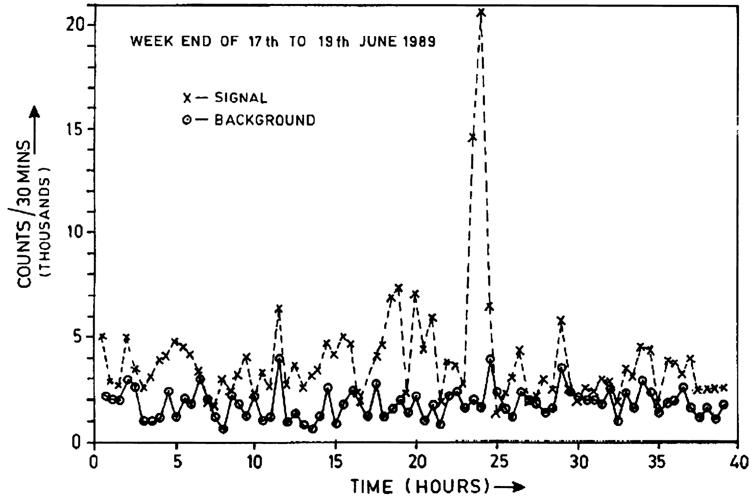

FIG.1: NEUTRON COUNTS VARIATION FROM DEUTERATED Ti DISC

Figure 6. Neutron emission from TiD disc (Reproduced from reference 2. Copyright 2008 Bhabha Atomic Research Centre)

Measurement of Tritium Levels in Electrolyte Samples

The tritium levels in the electrolyte samples collected after operating the cells for some time were measured by specialist groups of the Isotope and Health Physics divisions of BARC using well-known liquid scintillation counting techniques applicable for low-energy beta emitters, taking the following precautions: (a) 40K free counting vials were employed to minimize background counts; (b) For higher count rate cases, 0.1 to 2 ml of sample was added to the scintillator, while for low count rate samples, ≈ 10 ml was used. In the higher-concentration samples, pH was reduced by diluting them with double distilled water, in order to minimize chemiluminescence as well as quenching effects. If warranted, microdistillation of the test samples was carried out before the addition of scintillation cocktail. Independently, whenever possible, the measured tritium values were cross-checked with results obtained after chemiluminescence cooling; and (c) Commercially available Instagel scintillation cocktail was preferred over Dioxane as a solvent to minimize chemiluminescence interference effects. Samples of the initial electrolyte saved before the start of electrolysis were counted, along with the test samples drawn from the operating electrolysis cells.

To compute the excess tritium produced in each run, the following points were considered: (a) Initial tritium concentration in the stock D_2O. This was measured before every experiment and was typically a few Bq/ml; (b) To be on the conservative side, the tritium carried away by the D_2 gas stream during electrolysis was neglected even though it is known that, above 20°C, the (T/D) ratio in the gas stream is comparable to that in the liquid phase; and (c) Dilution effects from the periodic make-up of D_2O were also taken into consideration. Sec. 9 of ref. (*2*) describes in detail the procedures and precautions adopted while carrying out the tritium measurements. The quantum of tritium observed in the electrolytes of 11 additional electrolytic cells, besides the eight cells of Table I in which neutrons, too, were measured, are summarized in Table II of ref. (*3*). The quantum of tritium generated in the various BARC cells (22 cells in all) was in the range of a few KBq to a few MBqs. The maximum tritium concentration attained in the electrlolyte of any cell was 55.6 KBq/ml, corresponding to a total tritium yield of 13.9 MBq; this was observed in the large cathode area Milton Roy cell soon after the 21 April 1989 event described earlier.

Downloaded by UNIV OF DELAWARE MORRIS LIB on June 28, 2012 | http://pubs.acs.org
Publication Date (Web): December 20, 2009 | doi: 10.1021/bk-2009-1029.ch003

Downloaded by UNIV OF DELAWARE MORRIS LIB on June 28, 2012 | http://pubs.acs.org
Publication Date (Web): December 20, 2009 | doi: 10.1021/bk-2009-1029.ch003

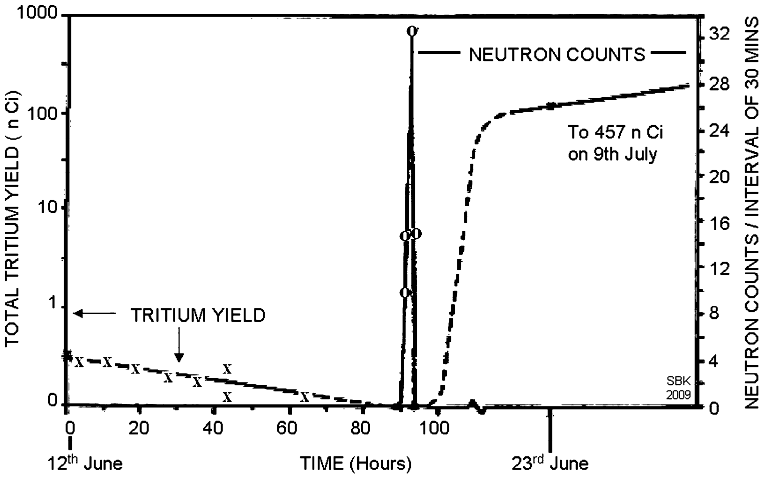

Figure 7. Concomitant generation of neutrons and tritium run 2 of Milton Roy cell. (Reproduced from reference 2. Copyright 2008 Bhabha Atomic Research Centre)

Although neutrons are measured online as and when they are emitted, tritium is measured off-line periodically, whenever electrolyte samples are drawn, as a cumulative post-run quantity. Figs. 7 and 8, which give the time variation of neutrons and tritium observed in two of the BARC cells, suggest that neutrons and tritium are both probably generated concomitantly. Most research groups collected electrolyte samples every few days, and these invariably showed the presence of tritium only in samples collected after a neutron emission was recorded.

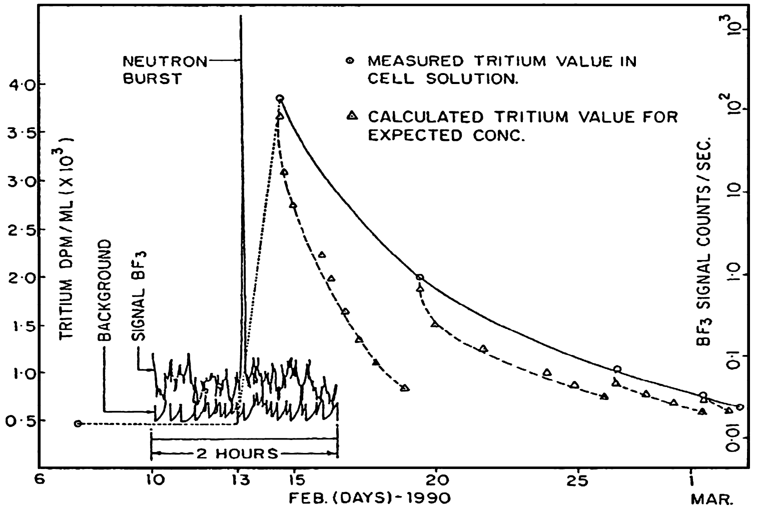

Figure 8. Increase of tritium in electrolyte following neutron burst: ROMG cell. (Reproduced from reference 2. Copyright 2008 Bhabha Atomic Research Centre)

The bottom row of Table I, which summarizes results from those cells in which both neutrons and tritium were observed, displays the neutron-to-tritium yield ratio. This ratio is seen to be in the region of 10^{-7}. Because the neutron-to-tritium yield ratio for the two main branches of d-d fusion reaction is unity, as per conventional nuclear physics data, in LENR devices this ratio is clearly off by seven orders of magnitude; this experimentally observed anomaly has come to be known as the branching ratio anomaly in LENR literature. BARC results were among the first to establish this anomaly as a characteristic signature of the physics of LENR devices.

Table 1a. Electrolysis Experiments with Neutron and Tritium Generation

DIVISION	***HWD***	***NtPD***	***NtPD***	***DD***
Cell ID	**Ti-SS**	**MR-1**	**MR-2**	**5 Module**
Cathode	**Ti Rod**	**Pd-Ag Tubes**	**Pd-Ag Tubes**	**Pd-Ag Discs**
Area (cm2)	**104**	**300**	**300**	**78**
Anode	**SS Pipe**	**Ni Pipes**	**Ni Pipes**	**Porous Ni**
Electrolyte	**5M NaOD**	**5M NaOD**	**5M NaOD**	**5M NaOD**
Switch on tim	**~ 3 hrs**	**~ 5 hrs**	**~ 0.5 hrs**	**~ 4 hrs**
Neutron yld	**3.0×10^7**	**4.0×10^7**	**9.0×10^7**	**5.0×10^6**
T yld (atoms)	**1.4×10^{14}**	**8.0×10^{15}**	**1.9×10^{15}**	**4.0×10^{15}**
(n/T) ratio	**2.0×10^{-7}**	**0.5×10^{-8}**	**0.5×10^{-8}**	**1.2×10^{-9}**

Downloaded by UNIV OF DELAWARE MORRIS LIB on June 28, 2012 | http://pubs.acs.org
Publication Date (Web): December 20, 2009 | doi: 10.1021/bk-2009-1029.ch003

Downloaded by UNIV OF DELAWARE MORRIS LIB on June 28, 2012 | http://pubs.acs.org
Publication Date (Web): December 20, 2009 | doi: 10.1021/bk-2009-1029.ch003

Table 1b. Electrolysis Experiments with Neutron and Tritium Generation

DIVISION	***AnCD***	***ROMG***	***ROMG***	***IGCAR***
Cell ID	**PDC-1**	**RSC-11**	**RCS-19**	**RCP-II**
Cathode	**Pd Tube**	**Pd Cube**	**Pd Pellet**	**Pd Button**
Area (cm2)	**5.9**	**6.0**	**5.7**	**8.0**
Anode	**Pt Mesh**	**Pt Mesh**	**Pt Mesh**	**Pt Mesh**
Electrolyte	**0.1M LiOD**	**0.1M LiOD**	**0.1M LiOD**	**0.1M LiOD**
Switch on time	**~9 hrs**	**~24 hrs**	**~930 hrs**	**~300 hrs**
Neutron yld	**3.0×10^6**	**1.4×10^6**	**3.0×10^6**	**2.4×10^6**
T yld (atoms)	**7.2×10^{13}**	**6.7×10^{11}**	**4.0×10^{12}**	**3.5×10^{12}**
(n/T) ratio	**4.0×10^{-6}**	**1.7×10^{-6}**	**1.0×10^{-6}**	**7.0×10^{-7}**

SOURCE : This is an abridged version of Table 1 of reference 3.

Studies on Deuterium Gas/Plasma-Loaded Ti Samples (5)

Five types of gas/plasma-loading approaches were adopted at BARC for loading deuterium into titanium samples. Presence of tritium, if any, on the surface of these samples was established subsequently through autoradiography and direct counting of the beta particles emitted by the tritium as well as through the Ti k-alpha x-rays. A very fortuitous characteristic of titanium is that the betas emitted by tritium which have energy up to 18 Kev are able to excite the 4.3 Kev k-alpha x-ray line of Ti, which can be identified easily by standard x-ray detectors (*2, 5, 12*).

(a) In the first approach, which used standard procedures for gas loading, titanium samples were thoroughly cleaned using acids, then vacuum-annealed, degassed and heated to 800 °C using a resistance furnace, then allowed to cool in D2 gas atmosphere. In the lathe shavings (or chips) experiment described in ref. (*5, 12*), deuterium loading was carried out by this procedure. In this experiment, after loading, the deuterated chips were dropped directly into liquid nitrogen;

subsequent measurements indicated presence of large amounts of tritium (tens of MBqs) in four of about a thousand chips! The autoradiograph of these four chips showed several remarkable hot spots that could be radiographed repeatedly over several months (*12*). Fig. 9 shows the beautiful image given by chip no. Z4, which was found to contain 424 KBq of tritium using a windowless flow proportional beta counter (*12*). The chips belonging to the control lot, which was not loaded with deuterium nor treated in liquid nitrogen, did not indicate presence of any tritium.

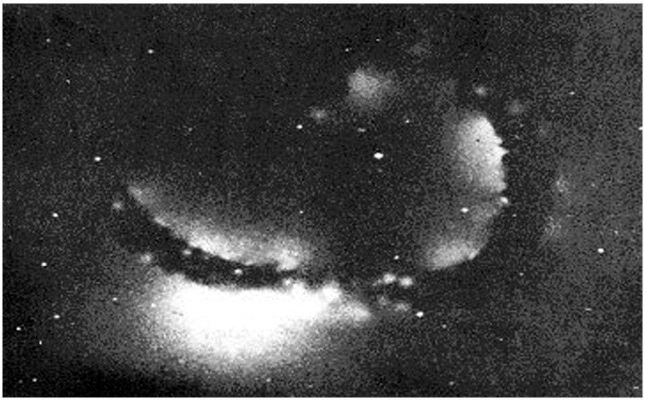

Figure 9. Autoradiograph of a deuterated Ti chip showing tritium containing hot spots. (Reproduced from reference 5. Copyright 2008 Bhabha Atomic Research Centre)

(b) In the second approach, machined Ti electrode samples (discs and cones) were heated in deuterium gas using an induction heater. Some of these subsequently gave characteristic spotty autoradiographs. Measurements using x-ray detectors confirmed the presence of tritium in the spotty regions, especially along the edges, which displayed a nice ring of dots along the periphery in the case of a disc and, in the case of a cone, an intense hot spot corresponding to the tip of the cone. (Refs. *1, 2, 3, 4, 5* reproduce their autoradiographic images.)

(c) The third method of deuterium loading was through a DC plasma glow discharge between a pair of titanium electrodes, which leads to absorption of deuterium by the cathode.

(d) The fourth method employed a high-voltage (40Kv) discharge shot in a plasma focus device, in which a large Ti rod served as the central anode. In this method, during the electrical discharge, a very hot and high-density deuterium plasma focus is formed just above the top of the rod, following a Z-pinch initiated magnetic compression phenomenon in the gas. During this process, the anode is subject to transient but intense magnetic and electric fields, and its top surface gets very effectively cleaned, resulting in efficient absorption of deuterium on the surface region, in spite of the fact that the rod is positively biased during the discharge transient. Because the electromagnetic fields last hardly a microsecond, the anode rod, which remains exposed to the gas in the chamber after each discharge shot, gets deuterated on the surface. One Ti rod

Downloaded by UNIV OF DELAWARE MORRIS LIB on June 28, 2012 | http://pubs.acs.org
Publication Date (Web): December 20, 2009 | doi: 10.1021/bk-2009-1029.ch003

that was subjected to 50 such plasma focus shots was later found to contain 14.5 MBq of tritium, which remained entrenched on the surface for almost five years (*13*)! Fig. 10 depicts the very impressive autoradiographic image of the top surface of this rod.

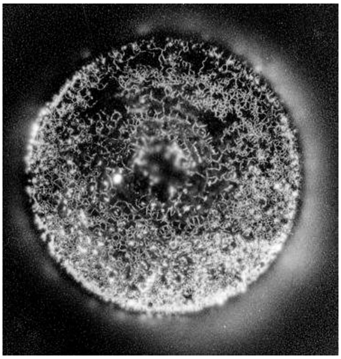

Figure 10. Autoradiograph of Ti plasma focus electrode after 50 discharges. Reproduced from reference 2. Copyright 2008 Bhabha Atomic Research Centre)

Downloaded by UNIV OF DELAWARE MORRIS LIB on June 28, 2012 | http://pubs.acs.org
Publication Date (Web): December 20, 2009 | doi: 10.1021/bk-2009-1029.ch003

(e) In the so-called aged-TiD-targets study, anomalously large amounts of tritium (varying from a fraction of a MBq to a couple of hundred MBqs) were detected on the surface of all 12 of 12 TiD targets, which had been manufactured several (nine to 19) years earlier by loading deuterium onto thin Ti films coated on copper backings, for use as targets in accelerator experiments. The presence of tritium was confirmed through five measurement techniques including autoradiography. Every one of the 12 aged targets gave a very impressive coin-like round image. But, interestingly, the images were quite uniform, not spotty as in the deuterated Ti samples discussed above. We postulate that the tritium could have been produced by LENR processes in the TiD thin films even while merely sitting in the drawer over the years! The possibility that tritium could have entered as contamination during the manufacturing stage of the TiD targets at the suppliers' end (nine were from M/s Amersham company of UK, and three had been fabricated at BARC by the Isotope Division) has been ruled out after discussions with the manufacturers. Further details regarding this study are available in sec. 5 of ref. (*3*).

Ni Hydrogen Experiments (*7, 8, 9*)

Experiments were initiated with light-water electrolytic cells using Ni cathodes and K_2CO_3 solutions as electrolyte, following reports of observation of excess heat in such systems by Mills and Kneizys (*14*) and other groups in the early '90s. Although observation of excess heat in open electrolysis cells with Ni cathodes and K_2CO_3 electrolyte was reported by us at ICCF 3 in Nagoya in 1992 (*7*), we have since come to the conclusion that the apparent excess heat reported at that time can be attributed to hydrogen-oxygen recombination effects within the open cell.

BARC groups were, however, probably the first to report observation of tritium in light-water cells. At Nagoya, we reported that 18 of 29 cells indicated tritium levels in the range of 46 Bq/ml to 3390 Bq/ml after a few weeks of cell operation. The high value of 3,390 Bq/ml was produced in a cell in which D_2O to the extent of 25 percent was added, but three other identical cells with 25 percent D_2O did not give any tritium. One cell with enriched (54 percent enriched in Li6) Li_2CO_3 in H_2O gave 1,454 Bq/ml, whereas two others with the same type of cathode and electrolyte gave no tritium whatsoever. Cell no. OM-3 even showed a steady increase of tritium level, reaching a comfortable value of 224 Bq/ml over four weeks (see Fig. 8 of ref. (*7*)).

Some skepticism was expressed even within BARC circles regarding the reliability of low-level tritium measurements in light-water cells – suspicions that the result could have been either from cross-contamination at the tritium measurements lab, where samples from different research groups were handled, or from “tritium in the BARC atmospheric air.” Hence, starting in June 1993, a completely new set of Ni light-water cells was set up and studied at two sites over three months; six cells were set up at the Chemical Engineering Division, and 17 cells (five at a given time) at the Process Instrumentation Division, specifically for the purpose of verifying tritium production. This time, a new captive liquid scintillation counting facility was installed in the Chemical Engineering Division, and extra caution was observed to avoid any possible external contamination. All electrolyte samples were micro-distilled, with researchers taking care to avoid alkali carryover before mixing with scintillation cocktail for counting. With this equipment, tritium levels down to 0.5 Bq/ml could be measured. Details regarding these repeat measurements are presented in ref. (*8*). In all, 10 of 23 of the new cells showed low levels of tritium in the 0.5 to 4.8 Bq/ml range. In three of the Chemical Engineering Division cells, from which electrolyte samples could be drawn online without disturbing cell operation, an intriguing saw-tooth oscillatory variation of tritium levels of the electrolyte was observed. Ref. (*8*) discusses this observation, pointing out, with cross references, that such oscillatory behaviour of tritium levels in electrolyte has been observed by other laboratories in Pd-D_2O cells also.

During 1994-95, some experiments were also conducted with self-heated thin Ni wires in a hydrogen gas atmosphere by subjecting the wires to several cycles of hydrogen absorption – desorption. The wires were then cut into 1 cm bits and analyzed for tritium content after dissolution. The results again showed, as in the case of titanium, a non-uniform production of tritium along the length of the wire, with some sections showing no tritium and others containing significant amounts; one bit had as much as 2,333 Bq. Details are published in ref. (*9*).

Downloaded by UNIV OF DELAWARE MORRIS LIB on June 28, 2012 | http://pubs.acs.org
Publication Date (Web): December 20, 2009 | doi: 10.1021/bk-2009-1029.ch003

Neutron Multiplicity Measurements

Principle of Statistical Analysis of Neutron Output

As mentioned earlier, the objective of carrying out a statistical analysis of the neutron output is to ascertain whether the neutrons produced by LENR devices are emitted in bunches of two, five, 20 or even several hundreds. If a large number of neutrons enter a neutron detector and simultaneously cause nuclear events in it, the detector and its electronics register only a huge-sized pulse, but the event is not time-resolved and does not get registered as individual neutron pulses. This limitation can be surmounted by exploiting the statistical time spread (typically 25 μs) that occurs during the slowing-down process when a bunch of simultaneously produced fast neutrons impinges on a large hydrogenous moderator assembly. Thermal neutron detectors, such as BF_3 or He^3 gas proportional counters, embedded in the moderator block can register these neutrons individually and sequentially.

Two techniques were used to determine the statistical characteristics of the pulse train issuing from the BF_3 or He^3 neutron counter banks (*15*). In the first method, the frequency distribution of counts in 20 ms time bins was recorded (Sec. 4 of ref. (*2*)). In each sweep of the pulse train, there were 1,000 such bins, with a 280 ms separation between the 20 ms bins (as required by the data acquisition system), consuming in all a real-time duration of five minutes per a 1,000 bin sweep.

The second approach to measuring the statistical characteristics of the pulse train was an adaptation of the artificial dead time method (*15, 16, 17*) developed originally for investigating neutron density fluctuations in experimental fission reactors (reactor noise analysis) as well as for the passive neutron assay of plutonium in the safeguards field. When more than one neutron from a neutron burst is registered by the bank of BF_3 or He^3 detectors, the corresponding cluster of electronic pulses is all time-correlated and closely spaced within a span of about 100 μs. In such events, the second, third and subsequent pulses of the family of pulses are diverted by a 100 μs wide artificial dead-time gate into a separate burst counts analyzer, while the leading pulses are totalized separately.

Downloaded by UNIV OF DELAWARE MORRIS LIB on June 28, 2012 | http://pubs.acs.org
Publication Date (Web): December 20, 2009 | doi: 10.1021/bk-2009-1029.ch003

Theoretical Considerations

For a purely random (Poisson) pulse series wherein N_0 is the average count rate and τ is the counting time interval (in this case 20 ms) and for the case when $N_0\tau$ is << 1, the probability of registering one count in a single 20 ms interval is $N_0\tau$; $[(N_0\tau)^2]/2!)$ gives the probability of getting doubles, $[(N_0\tau)^3]/3!)$ that of getting a multiplicity of three counts and so on. Note that the probability of getting higher-order multiplicity counts steadily decreases.

If now there are ϵ burst events per sec generating υ neutrons each superimposed on the random background, and the neutron detection efficiency is ϵ, then the contribution of the burst events to the overall count rate would be $\varsigma\upsilon\epsilon$. The probability of getting r counts in time τ from burst events is governed by a binomial distribution. Table I of Sec. A4 in ref. (*2*) summarizes the expressions for the contribution to the various orders of multiplicity counts from random and burst events. Table II of the same paper gives numerical examples with typical parameters for the expected frequency distribution of counts for random and bunched neutronic events. The main point brought out is that, whereas, for random events and low count rates, the probability of getting doubles, triples, etc. is extremely small, in the case of burst events these probabilities are non-negligible. Interestingly, for burst events, the peak of the multiplicity distribution actually shifts to higher multiplicity values as the product $\upsilon\epsilon$ increases. Thus, when the product $\upsilon\epsilon$ exceeds unity (as for example when a bunch of 100 neutrons is emitted in a single event and detection efficiency e is 10 percent), the probability of registering three or four counts per interval could be even higher than that of singles or doubles counts!

Frequency Spectrum Measurements (1989)

Several frequency spectrum measurement runs were carried out during May-June 1989, both with a Milton Roy electrolytic cell and a couple of deuterium gas-loaded titanium targets. In these measurements, one of the thermal neutron detector banks was used for monitoring the test LENR device, while the other, placed at a distance of 1.5 m from the device, served as a background neutron monitor. The efficiency of detection for neutrons emanating from the LENR source range from 0.5 percent to 1.5 percent.

The statistical characteristics of background counts was first studied to ensure that the equipment was functioning properly. This was done both in the presence of (overnight run of 26/27 May) and absence of (2 to 5 June) the Milton Roy cell. During the latter 63-hour background study, not even once, in ~750,000 trials, did either of the detector banks register three or more counts in any 20 ms time bin, confirming that the equipment was functioning very satisfactorily and that no high-multiplicity neutron burst events were in the background. The average background count rate during this campaign was ~0.023 cps in the BF_3 bank and ~0.43 cps in the He^3 bank, and the frequency spectrum of counts recorded corresponded strictly to a Poisson distribution.

In the quiescent Milton Roy cell study (electrolytic current not on) conducted earlier (26/27 May), the BF_3 counter bank monitored the electrolytic cell while a plastic scintillator (NE 102A) biased to register only neutrons of energy > 9 MeV monitored cosmic ray background events. To our surprise, a few very high-multiplicity events, even as high as 10 to 15 neutrons, were registered in some of the 20 ms bins (unlike the background-only study discussed above). However, there were no high-multiplicity counts whenever the plastic scintillator also recorded a very high-energy neutron event in coincidence with a BF_3 bank count. This indicated that the source of the high neutron multiplicity events was the quiescent Milton Roy cell, not cosmic rays.

Frequency distribution measurement runs with an operating Milton Roy cell began on 12 June. The first neutron emission episode lasting ~ five minutes duration occurred 30 minutes after the start of electrolysis. Two more such episodes were observed about an hour later. The cell current was then switched

Downloaded by UNIV OF DELAWARE MORRIS LIB on June 28, 2012 | http://pubs.acs.org
Publication Date (Web): December 20, 2009 | doi: 10.1021/bk-2009-1029.ch003

off (evening of 14 June), but surprisingly three additional short neutron emission episodes occurred within a few hours of electrolysis being terminated. During these episodes, the neutron count rates were in the range of ~0.5 to 1.7 cps, which corresponded to four to 14 times that of the background value of ~0.12 cps. In four of the above six episodes, count multiplicities of two, three, four, five, and even 10 were recorded at least once each. Throughout this period, lasting several days, the background counter did not register any noticeable increase in count rate; nor were there any multiple-counts events.

As mentioned earlier and evident from Fig. 4, on the evening of 16 June, an extended 2.5-hour neutron emission episode took place, in spite of the cells not having been operated for 52 hours before that. The count rate during this wide neutron emission episode attained a value as high as 20 cps at the peak. Even the background neutron monitor, which was 1.5 m away, indicated a small increase in count rate, commensurate with its efficiency for neutrons emanating from the Milton Roy cell. Although the frequency distribution of counts measured during this long episode generally corresponded to a Poisson distribution, multiplicities of five or more were registered several times. Close to the peak of the emission episode, for example, more than 20 such high-multiplicity cascade events occurred within five minutes (Table VII of ref. (9)).

Downloaded by UNIV OF DELAWARE MORRIS LIB on June 28, 2012 | http://pubs.acs.org
Publication Date (Web): December 20, 2009 | doi: 10.1021/bk-2009-1029.ch003

Frequency Spectrum Measurements With TiD_2 Targets

A 15 g sample of Ti-ZrD_2 was monitored over the weekend of 9-11 June 1989. The He^3 detector bank was the foreground counter, while the BF_3 detector was the background monitor. Even though there was no statistically significant increase in average neutron count rate relative to the no-target case (0.42 cps), in the presence of the deuterated target the foreground counter (He^3 bank) recorded several high-multiplicity events (three counts and four counts per 20 ms bin), whereas the background counter did not register any events beyond doubles.

During the weekend of 17-19 June, a deuterated Ti metal disc target was monitored. An 85-minute neutron emission episode occurred as mentioned (see Fig. 6), during which it is estimated to have emitted 5×10^5 neutrons in all. Here, too, several high-multiplicity events were registered, whereas the corresponding background counter did not record any high-multiplicity counts.

In general, the frequency spectrum of counts follows Poisson distribution for low-multiplicity events, but the spectrum has a distinct tendency to show a slight peak between the multiplicities of four and six. If we assume that this peak results from the superposition of bunched neutronic events on a Poisson background, the value of ς is 400 to 600. This follows from the fact, noted earlier, that the peak of the binomial distribution occurs at the multiplicity value corresponding to the product $\upsilon\epsilon$ and ϵ values in the above experiments was in the region of ~0.01.

Burst Neutron Measurements Using the Dead-Time Method

Experiments deploying the artificial dead-time technique were conducted (*17*) during a 60-day period in the summer of 1994 using a second Milton Roy electrolytic cell, procured in 1991. A noteworthy difference between the 1989 experiments and the 1994 runs, both of which used Milton Roy cells, was that the electrolyte used in the later tests was LiOD (LiOH for control runs) instead of the earlier NaOD. Also, this time the test cell was mounted inside the central tube of an annular neutron detector setup employing 16 numbers of 50 mm dia x 300 mm long BF_3 neutron counters located inside a plexiglass assembly. The neutron detection efficiency in this setup was ~10 percent, thereby significantly increasing the probability of detecting more than one neutron from a bunch of simultaneously emitted neutrons.

Data acquisition was carried out under three conditions. During the first 15 days, only background counts were acquired; the average background rate was ~ 0.048 cps. During the next 30 days, the Milton Roy cell was housed inside the central tube of the annular neutron detector assembly, and electrolysis was performed. The last 15 days were meant to be a control run, in which the cell was operated with LiOH electrolyte. Fig. 5 shows a plot of the daily average countrate over the two months of the experiment.

Discussion of Dead-Time Method Results

The total neutron counts per day with the D_2O cell can be seen to be consistently ~ 9 percent above the background level throughout the month-long run. However, in the case of the H_2O run, which was conducted immediately after the 30-day D_2O run, the average daily count rate steadily decreased to background level, suggesting the slow replacement of D by H within the Pd cathodes over time. Although there was no characteristic spiked neutron emission episode throughout the 30-day duration, there were several events with multiplicities of six and even seven counts in the burst counts data, in the case of both D_2O and H_2O cells. On the whole, however, the number of burst events was very few, the average values being 7.6, 3.8 and 1.7 bursts per day for the cases of D_2O cell, H_2O cell and background runs, respectively.

In these experiments, because the overall neutron detection efficiency was ~ 10 percent, approximately 10 neutrons are emitted by the electrolytic cell for every neutron detected. Likewise, a multiplicity of four counts during a 100 μs interval implies emission of a burst of roughly 40 neutrons by the cell. Of the 2,608 neutrons detected per day in presence of the Pd-D_2O cell, after subtracting the background of 2,386, the balance of 222 counts/day can be attributed to the cell. Of this, about 14.5 counts per day can be attributed to high-multiplicity (>20) burst neutron emission events. The overall conclusion of the 1994 experiments is that about 6.5 percent of the neutrons produced by the Milton Roy electrolytic cell can be attributed to high-multiplicity (> 20 neutrons/burst) events, and the balance, 93.5 percent, is produced either as single neutrons (with Poisson distribution) or with multiplicities of < 20 neutrons.

Downloaded by UNIV OF DELAWARE MORRIS LIB on June 28, 2012 | http://pubs.acs.org
Publication Date (Web): December 20, 2009 | doi: 10.1021/bk-2009-1029.ch003

An attempt was made again to replicate the 1994 neutron multiplicity measurements with the same Milton Roy cell and the same counting equipment during 1997. But the authors who carried out the new attempt have reported (*17*) they did not obtain any conclusive evidence for neutron emission from the cell this time.

Conclusions of the Statistical Analysis Measurements

- On the whole, there is unmistakable evidence that, in the presence of LENR sources, there are significant numbers of high-multiplicty neutron emission events. Throughout both the 1989 and 1994 campaigns, the background counters never registered multiplicities beyond doubles in any interval, and the background data adhered strictly to Poisson distribution. There was never any contribution to the higher-multiplicity counts from random (Poisson) sources. This very satisfactory behavior gives us confidence that our multiplicity measurements in the presence of LENR sources are trustworthy.
- Quoting a single number for the magnitude of the neutron bursts may not be appropriate, especially because not all the bursts may have the same magnitude. In the 1989 experiments, when there were many large spike neutron emission episodes, perhaps the burst size may have been in the region of several hundreds of neutrons. However, in the 1994 experiments, in which there were no characteristic spike neutron emission episodes but the Milton Roy cell seems to have emitted neutrons steadily throughout a one-month period, we estimate that approximately 6.5 percent of these neutrons were in the form of bursts, but of a smaller size, possibly of 20 to 100 neutrons per burst.
- The dead-time technique is clearly superior and a great improvement because the analysis interval is only 100 µs as compared to the 20 ms interval used earlier. Also, in the dead-time method, every burst event is captured, unlike the multi-channel time analyzer method of 1989, in which there was a large unused time gap between intervals.
- In the context of neutron multiplicity measurements, the following general comment is relevant: If the neutron detection efficiency ϵ is, say, 1 percent and one neutron count is registered, it could still have resulted from a single burst of 100 neutrons because of the 1 percent detection efficiency! If 10 counts are registered during a one-minute interval, it could imply either that there were 1,000 events in which 1 neutron each was emitted (single neutron events) or there were 10 burst events, each of which emitted 100 neutrons each!

Downloaded by UNIV OF DELAWARE MORRIS LIB on June 28, 2012 | http://pubs.acs.org
Publication Date (Web): December 20, 2009 | doi: 10.1021/bk-2009-1029.ch003

Overall Conclusions, Comments and Speculations

- The fact that a dozen groups of novices set up cells using Pd samples lying about in the laboratory, yet detected neutrons and tritium within the first day itself is noteworthy. Table I, which tabulates the switch-on time for each of the electrolysis experiments, shows that six of the 11 cells listed detected the first neutron signal within nine hours, one within 24 hours. However, all these cells stopped yielding any more neutron signals on continued electrolysis, telling us something about the crucial role of poisoning effects during electrolysis, which has been noted by others.
- Of course, several other cells did not produce any neutrons or tritium. Thus, like most other workers in the LENR field, the BARC groups also could not replicate the results.
- BARC results clearly demonstrated that, for neutron emission to take place in LENR configurations, one does not need the high degree of deuterium loading that seems to be a prerequisite for excess-heat production. Other workers in the LENR field have come to a similar conclusion.
- In the case of titanium, tritium was observed in localized hot spots in three types of gas/plasma-loading experiments. All these used machined cold-worked targets, and careful scrutiny of the autoradiographic images indicates that tritium is found to a maximum extent where there has been severe cold-work-caused lattice defects. Somehow, cold working seems to have been responsible for creating the nuclear active environment (NAE) sites that Storms has postulated (*18*). In contrast, the tritium in the thin film Ti targets of the aged-targets study is uniformly distributed.
- Why do we see spots in which tritium is concentrated only in titanium, not in Pd? The answer to this is possibly given by the reproducibility of the autoradiographic images, up to several years in the case of titanium LENR samples, but never in Pd. This means tritium is very immobile in Ti but not so in Pd. Possibly, at the time of formation, tritium is being generated in local hot spots (the NAEs) in Pd. Also, but soon after that, the tritium diffuses in the Pd lattice and gets redistributed in the sample. The live observation of thermal hot spots on the Pd cathode during electrolysis reported by some groups, such as the SPAWAR group and Swartz et al., reinforces our contention.
- In hindsight, we should have looked for transmutation products at these hot-spot sites in titanium; but in those early days, none of us thought of the occurrence of transmutation as a possibility in LENR devices!
- It is instructive to examine in an integrated fashion the following four separate findings that have emerged from the BARC studies: (a) simultaneous production of neutrons and tritium (mainly in Pd electrolysis experiments); (b) branching ratio anomaly, namely (n/T) ~10^{-7}; at least one Ti cathode cell also has given rise to this anomalous branching ratio; (c) the spotty nature of tritium containing sites in titanium targets; and (d) production of neutrons sometimes in bursts of tens to hundreds of neutrons.

Downloaded by UNIV OF DELAWARE MORRIS LIB on June 28, 2012 | http://pubs.acs.org
Publication Date (Web): December 20, 2009 | doi: 10.1021/bk-2009-1029.ch003

- If the indication of simultaneous production of n and T is viewed in the light of burst neutron emission, tens of millions of tritium nuclei could be produced along with a few tens to hundreds of neutrons in a local hot spot or NAE (possibly in less than a nanosecond). We thus speculate that, once an NAE is formed, a rapid cascade of several hundred million tritium-producing nuclear reactions takes place in rapid succession in a local region, maybe even within a single nanoparticle – a sort of chain or cascade event – during which process on average, for every 10 million tritium nuclei generated, one neutron is also emitted as a very low-probability offshoot side reaction event!
- One criticism of this line of argument is that one component of the evidence (simultaneous emission of n and T) is from electrolysis experiments with Pd cathodes while the other component (namely spotty nature of tritium bearing sites) is with gas-loaded Ti targets. A limited number of results, however, do overlap the two broad classes of experiments.
- The evidence for the chain-reaction scenario is not watertight, but such a speculative line of thought may be worth pursuing, if only to see where it leads! Perhaps one could design and carry out specific experiments to eliminate or confirm individual components of this highly speculative scenario. What could be the mechanism responsible for the production of such neutron bursts? In view of the importance of understanding the mechanism responsible for producing neutron bursts and the related question of chain nuclear events, experiments involving statistical analysis of neutron emission warrant attempts at replication.
- Also, in situations in which the absolute rate of neutron emission by the LENR source is extremely small in comparison to the background count rate, measurement of high-multiplicity events can establish the occurrence of neutron emission in an unambiguous manner. This advantage of neutron multiplicity measurements has not been adequately appreciated, even by the LENR community, during the last two decades!
- Interestingly, nickel, too, has given evidence of non-uniform behavior. Here again, the tritium-bearing localized regions are possible because hydrogen (and tritium) are less mobile in Ni than in Pd.
- Last, production of tritium in nickel light-water cells is very intriguing and deserves attempts at replication, especially because the design and operation of such light-water electrolysis cells is very simple and inexpensive; students at universities can repeat it easily, but one does need access to a qualified lab where samples can be sent for tritium measurements. To the best of our knowledge, nobody has reported observing neutrons from a Ni light-water electrolyitic cell. It would be worth looking for neutrons from such LENR systems, also. ·

Downloaded by UNIV OF DELAWARE MORRIS LIB on June 28, 2012 | http://pubs.acs.org
Publication Date (Web): December 20, 2009 | doi: 10.1021/bk-2009-1029.ch003

Acknowledgements

I wish to place on record my sincere thanks to Dr. P.K. Iyengar who was a tremendous source of inspiration. I also wish to thank the many co-authors of the various papers cited herein who have contributed significantly to the work discussed in this review paper. Many of these authors many have since retired from BARC.

References

1. Iyengar, P. K. Cold Fusion Results in BARC Experiments. In *Proc. Fifth Int. Conf. on Emerging Nucl. Energy Systems,* Karlsruhe, Germany, July 1989; p 291.
2. Iyengar, P. K.; Srinivasan, M., Eds.; *BARC Studies in Cold Fusion, BARC-1500,* Atomic Energy Commission, Government of India: Bombay, 1989.
3. Iyengar, P. K.; Srinivasan, M. Overview of BARC Studies in Cold Fusion. In *The First Annual Conference on Cold Fusion, Salt Lake City,Utah.* National Cold Fusion Institute: University of Utah Research Park, Salt Lake City, Utah, 1990.
4. lyengar, P. K. et al. Bhabha Atomic Research Centre Studies in Cold Fusion. *Fusion Technol.,* August **1990,** *18,* 32.
5. Srinivasan, M. et al. Observation of Tritium in Gas/Plasma-Loaded Titanium Samples. In *Proc. Int. Workshop on Anomalous Nuclear Effects in Deuterium/Solid Systems, Brigham Young University, Provo, Utah, 1990*. American Institute of Physics: New York, 1991; pp 519-534.
6. Final Report of the ERAB Cold Fusion Panel, Department of Energy, Washington, DC, Nov. 8, 1989.
7. Srinivasan, M. et al. Tritium and Excess-Heat Generation During Electrolysis of Aqueous Solutions of Alkali Salts With Nickel Cathode. In *Frontiers of Cold Fusion: Third International Conference on Cold Fusion, Nagoya, Japan*, *1992.* Ikegami, H., Ed.; Universal Academy Press: Tokyo, Japan, 1992; p 123.
8. Sankaranarayanan, T. K. et al. Investigation of Low-level Tritium Generation in Ni-H2O Electrolytic Cells. *Fusion Technol*. **1996,** *30,* 349.
9. Sankaranarayanan, T. K. et al. Evidence for Tritium Generation in Self-Heated Nickel Wires Subjected to Hydrogen Gas Absorption/Desorption Cycles. In *Proceedings of the 5th International Conference on Cold Fusion,* Monte Carlo, Monaco, 1995; Pons, B. S., Ed.; IMRA Europe: Sophia Antipolis, Valbonne, France; p 173.
10. Srinivasan, M. Meeting Report on “Energy Concepts for the 21st Century.” *Current Science* April 10, **2008**, *94(7)*, 842.
11. Shyam, A. et al. Observation of High-Multiplicity Bursts of Neutrons During Electrolysis of Heavy Water With Palladium Cathode Using the Dead-Time Filtering Technique. In *Proceedings of the 5th International*

Downloaded by UNIV OF DELAWARE MORRIS LIB on June 28, 2012 | http://pubs.acs.org
Publication Date (Web): December 20, 2009 | doi: 10.1021/bk-2009-1029.ch003

Conference on Cold Fusion, Monte Carlo, Monaco, 1995; Pons, B. S., Ed.; IMRA Europe: Sophia Antipolis, Valbonne, France; p 181.

12. Kaushik, T. C. et al. Preliminary report on direct measurement of tritium in liquid nitrogen treated TiDx chips. *Ind. J. Technol.*, **1990**, *28*, 667.
13. Rout, R. K. et al. Detection of High Tritium Activity on the Central Titanium Electrode of Plasma Focus Device. *Fusion Technol.* **1991**, *19*, 391.
14. Mills, R. L.; Kneizys, K. Excess Heat Production by the Electrolysis of an Aqueous Potassium Carbonate Electrolyte and the Implications for Cold Fusion. *Fusion Technol.* **1991**, *20*, 65.
15. Srinivasan, M. et al. Statistical Analysis of Neutron Emission in Cold Fusion Experiments. In *The First Annual Conference on Cold Fusion, Salt Lake City,Utah.* Will, F., Ed.; National Cold Fusion Institute: University of Utah Research Park, Salt Lake City, Utah, 1990, p 175.

16 Degwekar, D. G.; Srinivasan, M. A Simple Dead-Time Method for Measuring the Fraction of Bunched Neutronic Emission in Cold Fusion Experiments. *Ann. Nucl. Energy* **1990,** *17*, 583.

17. Shyam, A.; Kaushik, T. C. Absence of Neutron Emission During Interaction of Deuterium With Metal at Low Energies. *Pramana* **1998,** *50,* 75.
18. Storms, E. *The Science of Low Energy Nuclear Reaction.* World Scientific Publishing Co.: Singapore, 2007.

Downloaded by UNIV OF DELAWARE MORRIS LIB on June 28, 2012 | http://pubs.acs.org
Publication Date (Web): December 20, 2009 | doi: 10.1021/bk-2009-1029.ch003

Downloaded by COLUMBIA UNIV on June 28, 2012 | http://pubs.acs.org
Publication Date (Web): December 20, 2009 | doi: 10.1021/bk-2009-1029.ch004

Chapter 4

Excess Heat and Anomalous Isotopes and Isotopic Ratios From the Interaction of Palladium With Hydrogen Isotopes

J. Dash, Q. Wang, and D. S. Silver

Low Energy Nuclear Laboratory
Portland State University, Portland, Oregon 97207

Surface studies of 40 μm thick Pd foils after electrolysis in D_2O / H_2SO_4 electrolyte for six minutes found inversions in isotopic ratios. Anomalous isotopes and isotopic ratios were also found on the surface of a 350 μm thick Pd foil which produced excess heat during electrolysis in a similar electrolyte. Further research is necessary to establish the reproducibility of these results.

Our 1994 publication *(1)* presented evidence of localized, microscopic surface concentrations of gold and silver on palladium cathodes which had been electrolyzed in an electrolyte containing either H_2SO_4 and D_2O or H_2SO_4 and H_2O. The unique capabilities of a scanning electron microscope (SEM) equipped with an energy-dispersive spectrometer (EDS) made it possible to locate concentrations of these elements on a microscopic scale. Our experiments included the detection of excess heat. We suggested that the excess heat and unexpected elements could be explained by the energy released during transmutation of platinum to gold and palladium to silver in the presence of thermal neutrons.

A previous study by another group also reported elemental anomalies on the surface of palladium after electrochemical loading of deuterium *(2)*. A near-surface enrichment of rhenium and silver was detected by x-ray photoelectron microscopy (XPS). These elements are present as impurities in the starting palladium at levels (50 ppm Rh and 100 ppm Ag), well below the XPS detection limit. It is not clear why nickel, which is present before electrolysis as an impurity at the 200-300 ppm level, was not similarly enriched to a concentration

In Low-Energy Nuclear Reactions and New Energy Technologies Sourcebook Volume 2; Marwan, J., et al.;
ACS Symposium Series; American Chemical Society: Washington, DC, 2010.

which could be detected by XPS. This report does not include a bulk analysis of a Pd cathode after electrolysis. The authors concluded that surface segregation of Rh and Ag impurities most likely results from the forcing current and time during long-term electrolysis.

In another study by the same group *(3)*, time-of-flight secondary ion mass spectroscopy (TOF-SIMS) measurements of the Pd blank (no electrolysis) and Pd electrolyzed in H_2O gave the natural abundances of the stable Pd isotopes. However, two samples electrolyzed in D_2O had more than 20 percent increases in 106 Pd intensities and decreases in 105 Pd intensities. These researchers suggested the possibility that 105 Pd obtained a neutron and became 106 Pd. Although this SIMS research seemed promising, it was not mentioned in a later publication from this group *(2)*. Apparently, this research was terminated.

In 1994, we also published a report on the changes in surface topography and microcomposition of a palladium cathode caused by electrolysis in acidified light water *(4)*. A thin palladium cathode became bent and torn during electrolysis in acidified light water. Localized changes in composition, including the possibility of the formation of silver by neutron absorption, were reported.

Results of our SIMS study of Pd foils before and after electrolysis were presented in 1996 *(5)*. We found an isotopic inversion on the surface of a Pd foil cathode which had been electrolyzed in acidified heavy water. In the spectrum from the control (unelectrolyzed Pd foil), the signal from 106 Pd (natural abundance 27.33 at.%) was slightly greater than the signal from 108 Pd (natural abundance 26.46 at.%). However, a SIMS spectrum from an electrolyzed Pd foil had a more intense signal from 108 Pd than from 106 Pd. The difference between these two abundances decreases with increasing sputtering time. After sputtering for 50 minutes to a depth of about 0.3 μm, these two isotopes have the same abundance.

The same report included data on excess thermal power (0.3 W maximum) which was observed from electrolysis of acidified heavy water with a Pd foil cathode, compared with an identical cell containing a Pt cathode. After about 70 hours of electrolysis and a dormant period of 75 days, the cells were again electrolyzed. In five consecutive experiments totaling 20 hours over two weeks, the cell with the Pt cathode produced as much as 0.3 W excess thermal power compared with the cell containing a Pd cathode.

In 1997, we published the results of electrolysis experiments with titanium cathodes *(6)*. One experiment produced about 1 W excess thermal power compared with a control. Geiger-Mueller counters used to monitor radiation emitted by the cells showed no significant difference compared to background. LiF chips sealed in plastic and placed inside the cells before electrolysis also showed no significant difference compared to background. The Ti cathodes were examined before and after electrolysis, using SEM and EDS. A new microscopic feature on a cathode after electrolysis contained appreciable vanadium, one atomic number higher than titanium, just as silver is one atomic number higher than palladium and gold is one atomic number higher than platinum.

In the same publication *(6)*, we presented evidence of microscopic, time-dependent changes in fibers on the surface of a Pd cathode which had been electrolyzed about six months earlier. Distinct changes in the morphology of one

Downloaded by COLUMBIA UNIV on June 28, 2012 | http://pubs.acs.org
Publication Date (Web): December 20, 2009 | doi: 10.1021/bk-2009-1029.ch004

of the fibers occurred in two days during storage at room temperature and atmospheric pressure. An EDS spectrum of a new, oval-shaped feature showed that it contained an appreciable amount of silver. A spectrum from the same spot one month later suggested that silver was changing to cadmium, which is one atomic number greater than silver. This is further evidence for the possibility of transmutation.

Experimental Methods I

Palladium (AESAR stock #11514) was cold-rolled from 500 to 40 μm thickness. Each cathode was prepared from a piece of this foil 2 cm long and 0.8 cm wide which was spot-welded to a Pt lead wire. The anodes were prepared in the same way, using Pt foil spot-welded to a Pt lead wire.

The electrolyte contained 20 ml D_2O and 3.5 ml H_2SO_4 (sp. g. 1.84) in one cell. A second cell contained 20 ml deionized H_2O and 3.5 ml H_2SO_4.. The heavy-water and light-water cells were connected in series, Fig. 1.

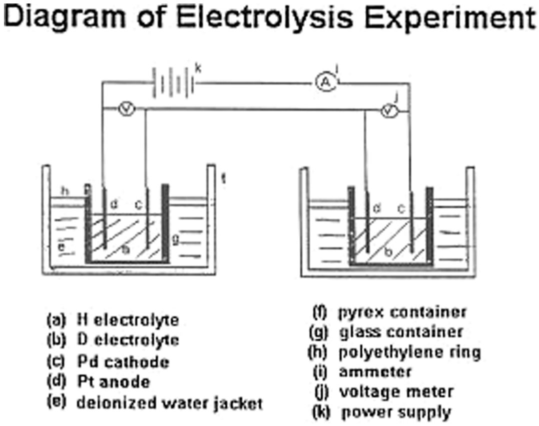
Diagram of Electrolysis Experiment
k
i
A
V
j
h
a
d
c
f
g
e
b
(a) H electrolyte
(b) D electrolyte
(c) Pd cathode
(d) Pt anode
(e) deionized water jacket
(f) pyrex container
(g) glass container
(h) polyethylene ring
(i) ammeter
(j) voltage meter
(k) power supply

Fig. 1. The heavy-water and light-water cells are connected in a series. Each cell has a Pd cathode and a Pt anode. All heavy-water cathodes bent toward their anodes 45 to 90 degrees, but the light-water cathodes bent toward their anodes only slightly.

In one experiment, the time of electrolysis was six minutes at a current density of about 0.25 A per cm^2. After microscopy of the electrodes was completed, SIMS analysis was performed on a control (no electrolysis) Pd foil from the same cold-rolled strip and on the Pd cathodes from the light-water and heavy-water cells.

The instrument used for these analyses was a PHI II SIMS, Model 3500, linked to a General Balzer 16 mm rod quadrupole mass spectrometer. Each sample was bombarded with a 3 KV Cs ion beam, which scanned an area of about 1.4 mm x 1mm. Pd was sputtered from the cathode at the rate of about 0.1

Downloaded by COLUMBIA UNIV on June 28, 2012 | http://pubs.acs.org
Publication Date (Web): December 20, 2009 | doi: 10.1021/bk-2009-1029.ch004

nm per second. Sputtering for long times obtained the relative abundances of the isotopes versus depth.

Results and Discussion I

Figure 2a gives the signal intensities for the three most abundant Pd isotopes as a function of sputtering time for the control (no electrolysis) foil. As expected, 106 Pd gives the highest signal intensity (counts per second, CPS), 108 Pd is next, and 105 Pd gives the lowest signal intensity. There is no significant change in signal intensity with increasing sputter time, i.e., with increasing depth into the sample. This is similar to the three other depth profiles taken from other locations on the unelectrolyzed control foil.

The SIMS results for the Pd foil which was electrolyzed for six minutes in H_2O electrolyte are given in Fig. 2b. After sputtering for five minutes, the relative intensities are in proportion to their natural isotopic abundances, i.e., 27.3 percent for 106 Pd, 26.5 percent for 108 Pd, and 22.3 percent for 105 Pd. After 12 minutes of sputtering, the signal intensities are almost constant for all three isotopes until sputtering was stopped after 25 minutes. Four other regions on the same sample gave very similar depth.

Downloaded by COLUMBIA UNIV on June 28, 2012 | http://pubs.acs.org
Publication Date (Web): December 20, 2009 | doi: 10.1021/bk-2009-1029.ch004

Downloaded by COLUMBIA UNIV on June 28, 2012 | http://pubs.acs.org
Publication Date (Web): December 20, 2009 | doi: 10.1021/bk-2009-1029.ch004

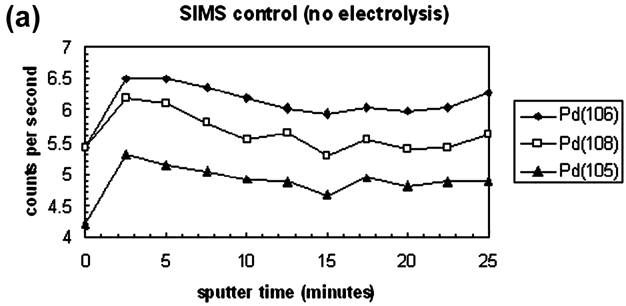

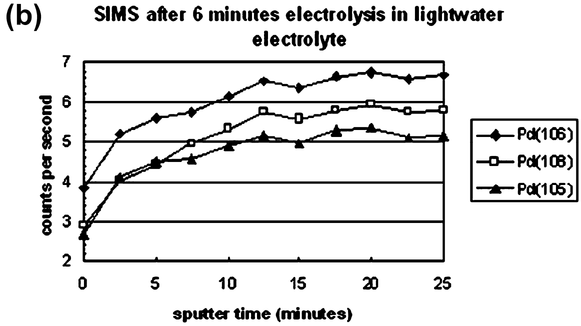

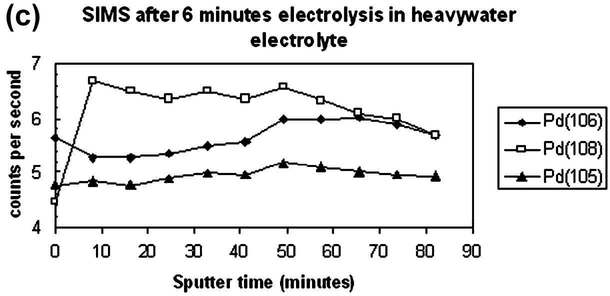

Fig. 2a. Depth profiles for the most abundant Pd isotopes: control (no electrolysis)
Fig. 2b. Depth profiles for the most abundant Pd isotopes: after H_2O electrolysis
Fig. 2c. Depth profiles for the most abundant Pd isotopes: after D_2O electrolysis

SIMS profiles were taken from nine different regions of the Pd foil which was electrolyzed in D_2O electrolyte. Fig. 2c shows a typical profile. Sputtering for about 10 minutes clearly shows an inversion in signal intensity: 108 Pd now has greater signal intensity than 106 Pd, whereas the opposite is expected, based on natural abundances. All nine of the depth profiles from this foil show this inversion. This suggests the possibility that 106 Pd absorbs a neutron and becomes 107 Pd, which beta decays to produce 107 Ag, a stable isotope. Another possibility is that 106 PdD forms during electrolysis. This would appear in the SIMS spectrum as mass 108, thus increasing the 108 Pd signal and diminishing the Pd 106 signal.

Fig. 2c shows that the difference in signal intensities of 106 Pd and 108 Pd diminishes with increasing sputtering time. After 65 minutes, corresponding to a depth of about 0.4 µm, the signals from these two isotopes are identical. The process which caused the changes in signal intensities appears confined to the outermost layers of the cathode surface. This is not surprising because the electrolysis time of only six minutes would be insufficient to achieve uniform bulk composition.

Fig. 3 shows a SIMS depth profile from a different area of the same Pd cathode after electrolysis for six minutes in D_2O electrolyte. The signal from 106 Pd is far less than expected. It coincides with the signal from 105 Pd, which has a natural abundance 5 at.% less than 106 Pd. The signal from 108 Pd is consistently greater than that from 105 Pd and 106 Pd throughout the 81-minute sputtering time. There is no tendency for merger of the 106 Pd and 108 Pd signals, such as that shown in the bottom graph, Fig. 2.

SIMS profiles for eight of the nine analyzed areas of the heavy-water electrolyzed Pd cathode show that there is also an inversion in the abundance of 104 Pd (11.14 at.% natural abundance) and 110 Pd (11.72 at.% natural abundance). Data for the control and for the light-water and heavy-water electrolyzed Pd cathodes are given in Fig. 4.

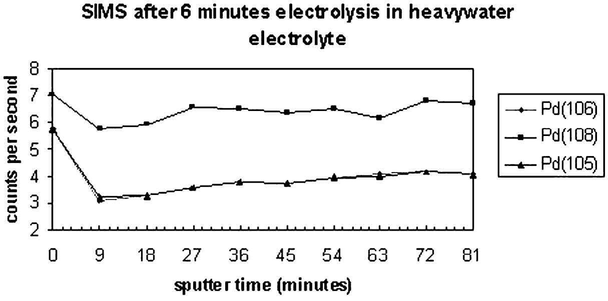

Fig. 3. SIMS depth profile from a different area of the same Pd cathode.

The signal from 110 Pd is greater than the signal from 104 Pd throughout 25 minutes of sputtering, both for the control (upper graph) and for the six-minute H_2O electrolyzed Pd cathode (center graph). The lower graph gives data for the Pd cathode after electrolysis for six minutes in D_2O electrolyte. It shows that the signal from Pd 110 is only about half the intensity of the signal for this isotope in the upper two graphs, whereas the signal from Pd 104 for this cathode is only slightly less than that in the upper two graphs. The inversion is almost constant throughout the 81-minute sputtering time. Its cause may have a similar explanation to those suggested above for the 106/108 inversion. For example, if 110 PdH and / or 110 PdD form preferentially, the SIMS spectrum would have diminished intensity at mass 110. Further research is necessary to determine the reasons for the inversions and the reproducibility of these results.

Downloaded by COLUMBIA UNIV on June 28, 2012 | http://pubs.acs.org
Publication Date (Web): December 20, 2009 | doi: 10.1021/bk-2009-1029.ch004

Experimental Methods II

During electrolysis of D_2O-H_2SO_4 electrolyte with a Ti cathode and a Pt anode, Ti erodes from the cathode and dissolves in the electrolyte *(7)*. When this electrolyte containing dissolved Ti was used for electrolysis with a Pd cathode and a Pt anode, enhanced excess heat was observed. Also, localized concentrations of unexpected elements were found on the surface of the Pd cathode.

(a)

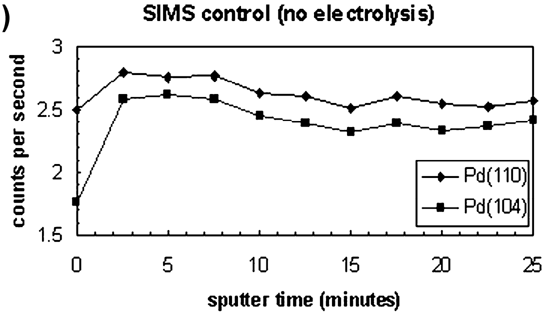

(b)

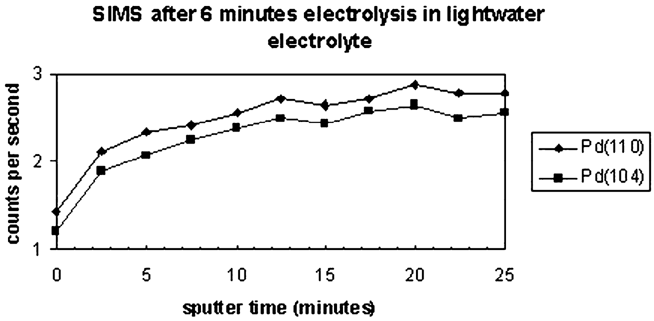

(c)

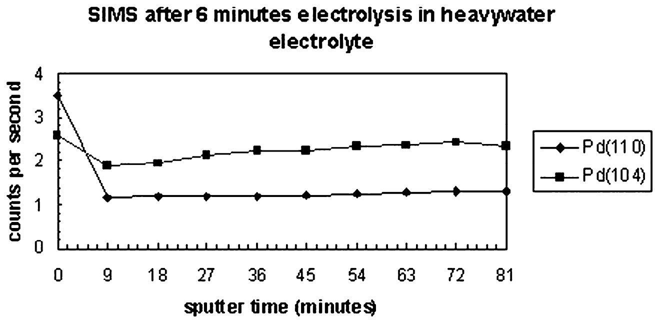

Fig. 4a,b, c. SIMS depth profiles for Pd 104 and Pd 110.

Downloaded by COLUMBIA UNIV on June 28, 2012 | http://pubs.acs.org
Publication Date (Web): December 20, 2009 | doi: 10.1021/bk-2009-1029.ch004

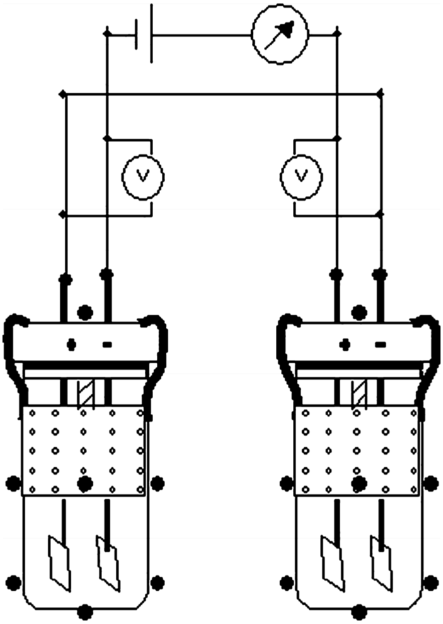

Fig. 5. Circuit containing a constant current DC power supply and a control cell in a series with an experimental cell. The black circles indicate the locations of eight thermocouples attached to the outside of each cell. The output of the thermocouples and the cell voltages were monitored with a computer. The cell temperature was then calculated as the arithmetic average of these eight readings.

This report contains data on the variation of excess heat production with concentration of Ti in the electrolyte and on the variation of the magnitude of the excess thermal power over 16 days. Data on the distribution of elements on the Pd cathode is also presented.

Fig. 5 shows the circuit diagram used for electrolysis. A control cell with two Pt foil electrodes is connected in series with an experimental cell containing a Pt foil anode and a Pd foil (0.35 mm thick) cathode. The Pd was Alfa Aesar stock number 11514, 99.9% Pd (metals basis). The as-received thickness was 0.5 mm. It was cold-rolled to 0.35 mm thickness, then sheared to produce a cathode 23 × 25 mm. A 1 mm diameter Pt lead wire was then crimped to the Pd cathode through a hole which was punched in one end of the Pd. One mm diameter Pt lead wires were crimped to the Pt electrodes in the same way. The electrolyte in the control cell contained concentrated H_2SO_4 and deionized H_2O in the ratio 1:12.3. The experimental cell electrolyte contained the same stock of concentrated H_2SO_4 and Aldrich D_2O (catalog number 34,716-7) in the ratio 1:6.7. The average current density on the Pd cathode was about 0.3 A/cm^2.

Downloaded by COLUMBIA UNIV on June 28, 2012 | http://pubs.acs.org
Publication Date (Web): December 20, 2009 | doi: 10.1021/bk-2009-1029.ch004

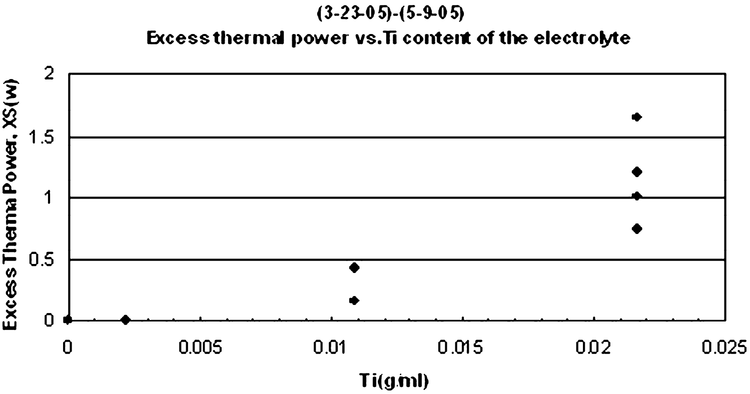

Fig. 6. Excess heat approximately doubled after Ti content of the electrolyte was increased from 0.011 g/ml to 0.022 g/ml. At higher concentrations of Ti, a Ti compound deposited on the cell wall.

Results and Discussion II

Fig. 6 shows the effect of Ti additions to the experimental cell electrolyte on excess thermal power. Data points with no added Ti and with 0.002 g/ml added Ti show that no excess heat was produced. After we increased the Ti content to 0.011 g/ml, two consecutive runs gave significant (0.2 and 0.4 W) excess thermal power. At 0.022 g/ml Ti concentration, three runs gave 1.2, 0.7, and 1.0 W excess thermal power. At higher concentrations of Ti, a Ti compound deposits on the cell wall.

Pd from the same stock was cold-rolled from 0.5 to 0.35 mm thickness. A cathode 25 x 23 x 0.35 mm ^{3} was prepared from this. Electrolyte was prepared containing 6.7 g D_2O: 1 g H_2SO_4 and about 0.02 g Ti per ml of solution. An identical cell (control cell) without Ti was constructed. Each cell had eight thermocouples attached for temperature measurements, which were used for excess heat calculations. The cells were connected in series in the circuit shown in Fig. 5.

Electrolysis was performed for about six hours per day for eight days. Excess power compared to a control cell was observed for every run. It ranged from 0.5 to 2.6 W. The average was 1.8 W.

Downloaded by COLUMBIA UNIV on June 28, 2012 | http://pubs.acs.org
Publication Date (Web): December 20, 2009 | doi: 10.1021/bk-2009-1029.ch004

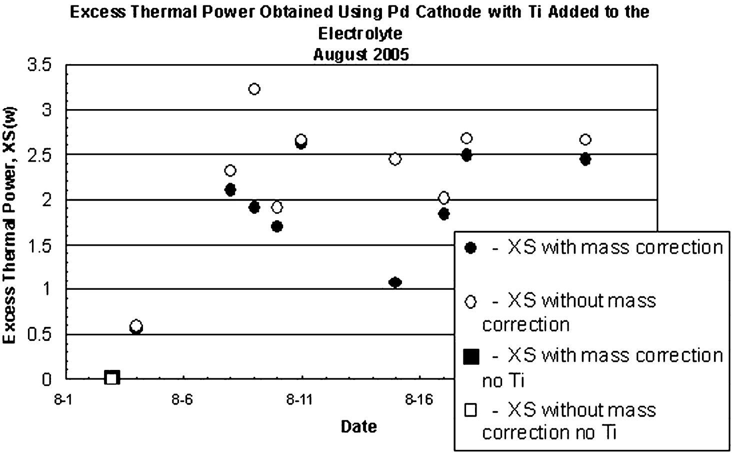

Fig. 7. Excess thermal power with and without mass correction. Average excess is 1.8 W. Mass correction was calculated in order to account for the loss of recombination heat because of the escape of gases from the cells.

Fig. 7 gives the excess heat results for eight consecutive runs with a new batch of electrolyte containing heavy water and sulfuric acid in the same ratio as before and with 0.024 g/ml Ti added.

The data in Fig. 7 for six of the eight runs show that the calculated excess thermal power assuming no mass loss is almost the same as the results obtained when the mass loss is included in the calculations. For the 8/9 and 8/15 data, the control cell lost ~ 1 g more mass than the experimental cell, and the calculated excess thermal power is not accurate. For the other runs, both cells lost less than 0.5 g, and the calculated excess thermal power is thought to be accurate.

The Pd electrode used for the data in Fig. 7 was examined with a scanning electron microscope equipped with an energy-dispersive spectrometer. Characteristic x-ray spectra were taken from each of the rectangles, on both the concave and the convex sides shown in Figs. 8a and 8b.

Downloaded by COLUMBIA UNIV on June 28, 2012 | http://pubs.acs.org
Publication Date (Web): December 20, 2009 | doi: 10.1021/bk-2009-1029.ch004

Downloaded by COLUMBIA UNIV on June 28, 2012 | http://pubs.acs.org
Publication Date (Web): December 20, 2009 | doi: 10.1021/bk-2009-1029.ch004

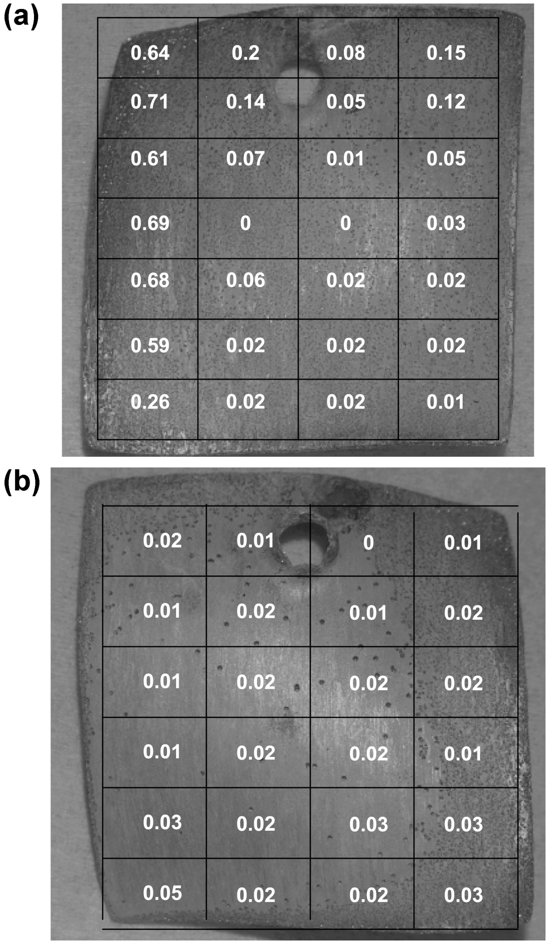

(a)

0.64	0.2	0.08	0.15
0.71	0.14	0.05	0.12
0.61	0.07	0.01	0.05
0.69	0	0	0.03
0.68	0.06	0.02	0.02
0.59	0.02	0.02	0.02
0.26	0.02	0.02	0.01

(b)

0.02	0.01	0	0.01
0.01	0.02	0.01	0.02
0.01	0.02	0.02	0.02
0.01	0.02	0.02	0.01
0.03	0.02	0.03	0.03
0.05	0.02	0.02	0.03

Fig.8a. Side facing anode (concave).
Fig.8b. Back side (convex).

The spectrum shown in Fig. 9a was taken from the rectangle on the left of center in Fig. 8a, and the spectrum shown in Fig. 9b, was taken from the rectangle in the upper left corner of Fig. 8a. Both spectra have predominant Pd Lα peaks at 2.84 keV, but the Pd Lβ peak at 2.99 keV is far more intense in the Fig. 9b than in the Fig.9a spectrum. The expected intensity ratio, Pd Lβ/Lα, is 0.42 *(8)*, whereas this ratio in Fig. 9a is 0.43, and it is 0.97 in Fig. 9b. A possible explanation for this difference is that Ag, which has its Lα peak at 2.98 keV, is present at some locations on the Pd cathode

Downloaded by COLUMBIA UNIV on June 28, 2012 | http://pubs.acs.org
Publication Date (Web): December 20, 2009 | doi: 10.1021/bk-2009-1029.ch004

(a)

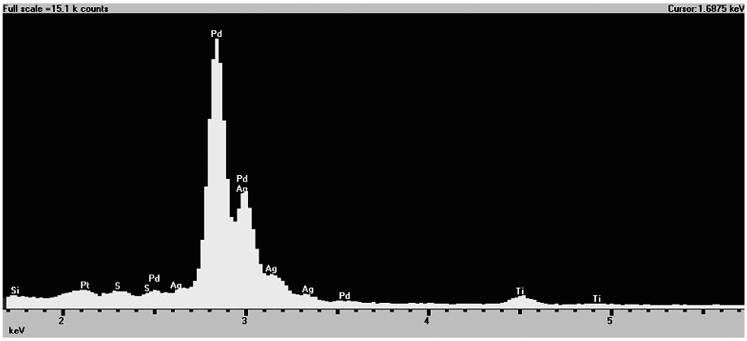

(b)

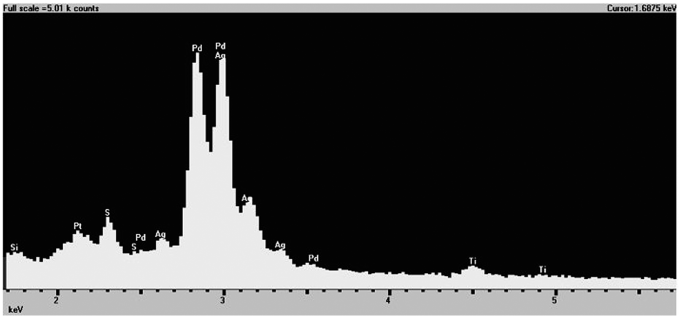

Fig. 9a. This spectrum was taken from the rectangle on the left side of center in Fig. 8a.

Fig. 9b. This spectrum was taken from the rectangle in the upper left corner of Fig. 8a.

after electrolysis, as proposed previously *(1)*. Further evidence to support this suggestion is that the AgL1 peak at 2.63 keV, the Ag Lβ peak at 3.15 keV and the AgLß$_2$ peak at 3.35 keV are fully developed in the Fig. 9b. These peaks are not prominent in Fig. 9a.

ISIS deconvolution software was used to determine the ratio Ag/Pd for each of the rectangles in Fig. 8. This ratio was 0.64 for the Fig. 9b spectrum and zero for the Fig. 9a spectrum. The number on each rectangle is the ratio Ag/Pd for that area. For example, the number 0.64 for upper left corner, concave side, tells us that the number of Ag atoms is 64 percent of the number of Pd atoms in that area. The concave side faced the anode during electrolysis. The silver is concentrated near the left edge of the concave side. Ag was not detected in two rectangles near the center of the concave side. No high concentrations of Ag were found on the convex side of the Pd cathode.

The addition of about 0.02 g/ml of Ti to the electrolyte appears to enhance the output of excess thermal power and to improve reproducibility. The mechanisms which produce these effects are not known. However, Ti is known to have catalytic properties *(9)*. It may be that a complex of Ti deposits on the Pd cathode and activates sites which would otherwise remain dormant. The spectra in Fig. 9 both have small Ti peaks, which probably result from the deposition of a Ti complex. In addition to Pd, Ag, and Ti, the Fig. 9b spectrum contains appreciable amounts of S, Fe, Ni, and Pt. These elements are not detected in the

Fig. 9a. S and Pt most likely are deposited from the electrolyte. The origin of Fe and Ni is not known. It is unlikely that these elements were present in appreciable amounts in the electrolyte before electrolysis.

The lower left quadrant of the Pd cathode in Fig. 8a was examined blind, on both the concave and convex sides, by National Renewable Energy Laboratory (NREL) scientists. The analyses included SIMS, SEM, and Auger Electron Spectroscopy.

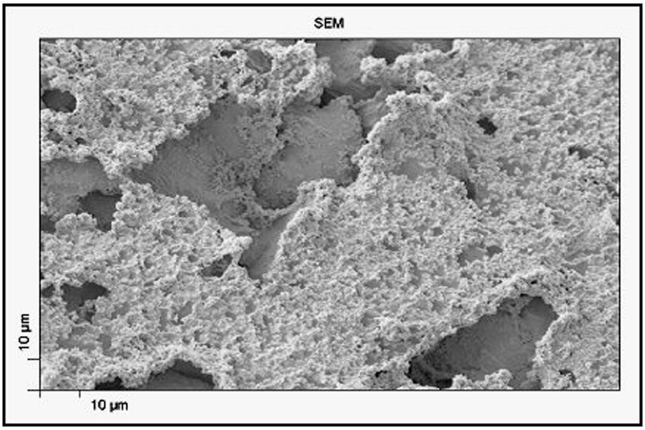

Fig. 10. SEM photo of the concave side of the Pd cathode. AES analyses were taken from the two large dark gray areas and from the light gray area.

Table 1. AES analyses (at.%) of dark gray and light gray areas in Fig. 5. The dark gray areas have large concentrations of C, O, and N before and after sputtering. These elements were also found on the light gray area as received but not after sputtering.

Dark gray	C	O	S	N	Pd	Pt
As-received	48.5	21.6	2.3	12.4	12.0	3.1
20 sec sputter	45.9	14.6	3.3	13.1	21.2	1.9

Light gray	C	O	S	N	Pd	Pt
As-received	54.2	17.4	1.9	10.3	6.4	9.9
20 sec sputter			2.6		79.0	18.4

Dark gray	C	O	S	N	Pd	Pt
As-received	54.3	16.9	2.9	12.6	10.3	3.0
20 sec sputter	45.5	14.8	4.0	13.9	15.5	6.3

Downloaded by COLUMBIA UNIV on June 28, 2012 | http://pubs.acs.org
Publication Date (Web): December 20, 2009 | doi: 10.1021/bk-2009-1029.ch004

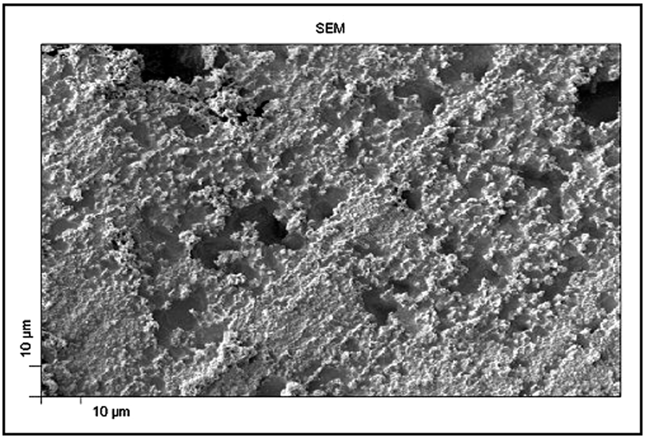

Fig. 11. SEM photo of the convex side of the Pd cathode after electrolysis.

Table 2. AES analyses (at.%) of the convex side of the Pd cathode after electrolysis. Carbon was not detected on this side of the cathode. After sputtering, oxygen and nitrogen were not detected. Chlorine was detected on both light and dark gray areas.

Dark gray	Cl	O	S	N	Pd	Pt
As-received	2.4	13.9	2.2	11.3	68.0	2.1
20 sec sputter	1.1	9.8	3.3	9.8	73.5	2.6

Light gray	Cl	O	S	N	Pd	Pt
As-received	3.0	9.8	1.1	8.3	75.0	2.8
20 sec sputter	0.7		0.6		94.5	4.2

Figs. 10 and 11 show that both sides of the Pd cathode contain a mixture of smooth, dark gray areas in a matrix of mottled, light gray areas. The outermost layers of the concave side of the Pd cathode contain about 50 at.% C, but C was not detected on the convex side. It is difficult to accept that this difference could be caused by contamination. The main difference between the two sides is that the concave side had higher current density during electrolysis. If C was deposited on the concave side, it should have also been deposited on the convex side but to a lesser extent.

The origin of the Cl on only the convex side is also puzzling. Again, contamination or deposition during electrolysis is expected to affect both sides.

The SIMS data on the same Pd cathode after electrolysis does not contain any inversions of isotopic abundance such as those in Figs. 2-4, but there are significant differences compared with the control, a pure (99.999 percent) Pd

Downloaded by COLUMBIA UNIV on June 28, 2012 | http://pubs.acs.org
Publication Date (Web): December 20, 2009 | doi: 10.1021/bk-2009-1029.ch004

Downloaded by COLUMBIA UNIV on June 28, 2012 | http://pubs.acs.org
Publication Date (Web): December 20, 2009 | doi: 10.1021/bk-2009-1029.ch004

foil which had not been electrolyzed. For example, there are no changes in isotopic abundance in the depth profiles for the control. Fig. 12 shows the count rate for masses 107 and 109 for the convex side of the unelectrolyzed control Pd foil. The average count rate is about 22 counts per second for both mass 107 and mass 109. However, the graph in Fig. 13 shows that convex side of the electrolyzed Pd cathode has about 50 percent greater signal from mass 107 compared with mass 109.

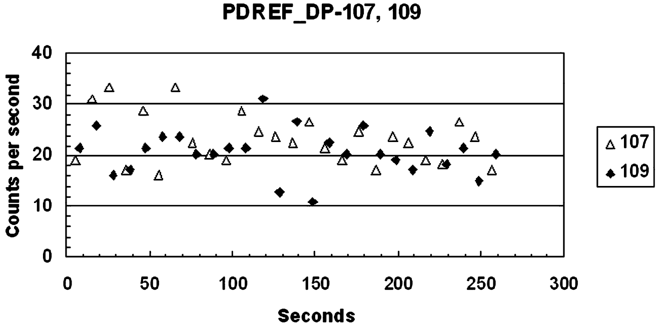

Fig. 12. Counts per second for the control Pd foil from masses 107 and 109. The count rate does not change with increasing depth into the foil. The average count per second is about 22 for both masses.

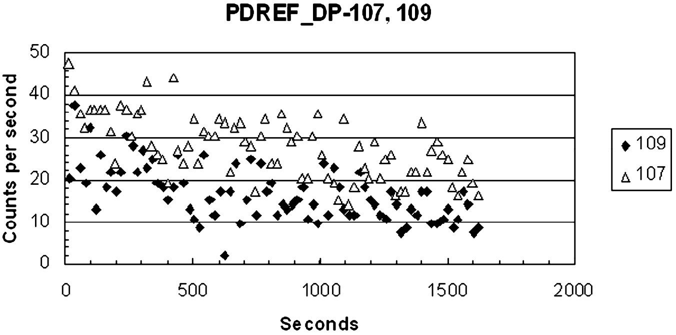

Fig. 13. Counts per second versus sputtering time (seconds) for the convex side of the electrolyzed Pd foil, which faced away from the anode during electrolysis. Compared with the control, there is less overlap of the data for mass 107 (yellow) with the data for mass 109 (blue). The average count per second is about 30 for mass 107 and 20 for mass 109.

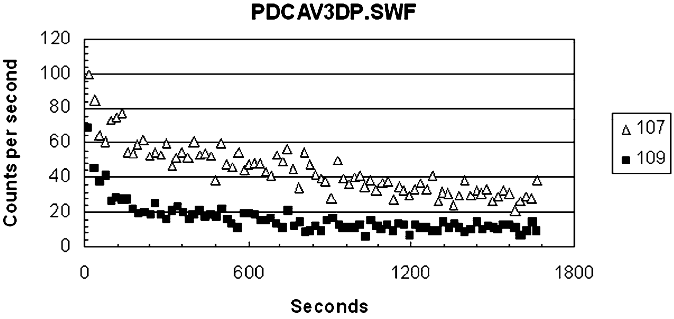

Fig. 14. Depth profile of the signals from masses 107 and 109 for the Pd cathode after electrolysis (concave side).

The SIMS depth profiles for masses 107 and 109 from the concave side of the electrolyzed Pd cathode are shown in Fig. 14.

Here, it is apparent that the count rates for both 107 and 109 decrease with increasing sputtering time, and the count rate for for mass 107 is about double that for mass 109 throughout 1,700 seconds of sputtering. There is no overlap of the count rates from these two masses. At the start of sputtering, the signal from mass 107 is about 90 cps, and this falls to about 35 cps at the end of sputtering. The signal from mass 109 falls from about 75 cps to about 15 cps during the same period.

Masses 107 and 109 are stable isotopes of Ag, so transmutation of Pd by absorption of thermal neutrons is one possible explanation for the presence of these isotopes. The EDS data (Fig. 9b) clearly shows that Ag is present on the concave surface of the 0.35 mm thick Pd cathode after electrolysis. This conclusion is supported by previous observations *(1, 4, 6)*. Another possibility is that PdH and PdD are formed. Then, 105 PdH would appear at mass 106, 106 PdH would appear at mass 107, and 108 PdH would appear at mass 109. Also, 105 PdD would appear at mass 107, 106 PdD would appear at mass 108, and 108 PdD would appear at mass 110. Thus, it seems likely that the mass 107 and 109 signals in Fig. 14 result from a combination of both transmutation of Pd to Ag and PdH and PdD formation.

Summary and Conclusions

SIMS spectra from 40 μm thick Pd foil cathodes after electrolysis in H_2O/H_2SO_4 electrolyte for six minutes show no significant changes in isotopic abundance compared with the control, which was not electrolyzed. However, Pd foil cathodes electrolyzed in D_2O/H_2SO_4 electrolyte had inversions in which the 108 Pd signal exceeded the 106 Pd signal and the 104 Pd signal exceeded the 110 Pd signal. These inversions may have been caused by the formation of PdD and PdH. For example, 106 PdD would appear at 108, thus increasing the abundance of 108 Pd. Also, 102 PdD would appear at 104, thus increasing the

Downloaded by COLUMBIA UNIV on June 28, 2012 | http://pubs.acs.org
Publication Date (Web): December 20, 2009 | doi: 10.1021/bk-2009-1029.ch004

abundance of 104 Pd. Another possibility is that transmutation to Ag occurred. This would require the presence of thermal neutrons *(10, 11, 12)*.

A much thicker Pd foil (350 µm thick) electrolyzed for 74 hours in D_2O/H_2SO_4 electrolyte did not show inversions of isotopic abundance, but it did show significant differences in the SIMS spectra compared with the control. The occurrence of weak signals of almost the same intensity from the control at masses 107 and 109 suggests that Ag is present as an impurity in the control. The SIMS spectrum from the concave side of the electrolyzed Pd foil has about twice the intensity of the signal at mass 107 compared with mass 109. Based on natural abundance, the ratio of the signals should be 107/109 ~ 1.1, instead of the observed 2. Any attempt to explain these results should include the effects of PdH and PdD which are formed during electrolysis. PdH would appear in the SIMS spectrum at 107 and 109, but their ratio should be ~ 1, not the observed 2. Another possibility is that transmutation to Ag occurred. Ag was detected by EDS in localized concentrations on both sides of this Pd cathode after electrolysis. Large concentrations of C on the concave side were detected by EDS studies, in agreement with the AES results. EDS also detected C on the convex side of the Pd cathode, but at much lower concentrations. This suggests that the C content is related to the current density during electrolysis. The high C content is on the concave surface which faced the Pt foil anode and therefore had much higher current density than the convex surface, which faced away from the anode. The changes in the SIMS spectra are also much greater on the concave side. Fig. 9 shows one example. There are others, too numerous to present in this report.

As noted above, interpretation of the SIMS spectra requires consideration of the presence of hydrogen and deuterium, which form at the Pd cathode during electrolysis. These elements bond with palladium to form the compounds PdH and PdD. Now, consider the most abundant Pd isotopes, 106 Pd and 108 Pd:

(1) 106 Pd + H → 107 PdH.

PdH would appear in its SIMS spectrum as mass 107, which is the mass of a stable silver isotope. In the same manner, 108 Pd would appear as mass 109, which is the mass of the second stable silver isotope. In Fig. 14, the intensity ratio I_{107} / I_{109} is about 2, whereas the natural abundance ratio of these two silver isotopes is about 1.1. There must be other factors which enhance the intensity at mass 107. For example,

(2) 105 Pd + D → 107 PdD.

There are many other possibilities. Also, we know from the EDS data in Fig. 9 that silver is present, especially on the left edge of the concave side of the 0.35 mm thick cathode. We believe that this silver is the result of transmutation in the presence of thermal neutrons:

(3) $^{106}Pd_{46}$ + neutron → $^{107}Ag_{47}$ + electron.

Downloaded by COLUMBIA UNIV on June 28, 2012 | http://pubs.acs.org
Publication Date (Web): December 20, 2009 | doi: 10.1021/bk-2009-1029.ch004

Equation (3) is an exothermic reaction, producing 3 x 10^4 eV *(13)*. Thus, it could contribute to the observed excess heat.

Anomalous thermal neutron capture and sub-surface Pd isotope separation in cold-worked palladium foils as a result of deuterium loading has been reported *(14)*. During deuterium loading, the probability of thermal neutron absorption in a cold-worked Pd foil, similar to the cold-rolled Pd foils used in our research, is increased by a factor of eight compaired to a Pd foil which has not been cold-worked. This type of research appears to be an important contribution in explaining our results.

Since 1989, there have been many other reports of anomalous elements resulting from the interaction of metals with hydrogen isotopes *(13, 14, 15, 16, 17, 18, 19)*. The results reported here add to that growing body of evidence.

Downloaded by COLUMBIA UNIV on June 28, 2012 | http://pubs.acs.org
Publication Date (Web): December 20, 2009 | doi: 10.1021/bk-2009-1029.ch004

Acknowledgements

We are grateful for the financial support received during the past 20 years from Portland State University, the U.S. Army Research Office, the Drexler Foundation, the New Energy Foundation, and the New York Community Trust. We are also grateful to NREL scientists who performed the SEM, AES, and SIMS analyses on the 0.35 mm thick Pd cathode.

Figures 1-4 and 10- 14 were originally published in the proceedings of the 13th International Conference on Condensed Matter Nuclear Science, pp. 462-475, 2008. We thank Yuri Bazhutov, editor, for permission to reproduce these here. Figures 5-9 were originally published in proceedings of the 12th International Conference on Condensed Matter Nuclear Science, pp. 140-144, World Scientific Publishing Co., 2006. Ning Tu kindly granted permission to publish these figures here.

References

1. Dash, J. J.; Noble, J. J.; Diman, J. Surface Morphology and Microcomposition of Palladium Cathodes after Electrolysis in Acidified Light and Heavy Water: Correlation With Excess Heat. *Trans. of Fusion Technology* **1994**, *26,* 299.
2. Rolison, D.; O'Grady, W. Observation of elemental anomalies at the surface of palladium after electrochemical loading of deuterium or hydrogen. *Anal. Chem.* **1991***, 63*, 1697.
3. Rolison, D.; O'Grady, W.; Doyle, Jr, R.; Trzaskoma, P. Anomalies in the surface analysis of deuterated palladium. In *The First Annual Conference on Cold Fusion,* March 28-31, 1990, Salt Lake City, Utah. National Cold Fusion Institute: University of Utah Research Park, Salt Lake City, Utah, 1990; p 272.
4. Dash, J.; Noble, G.; Diman, J. Changes in surface topography and microcomposition of a palladium cathode caused by electrolysis in acidified

light water. *Cold Fusion Source Book;* Fox, H., Ed.; Fusion Information Center: Salt Lake City, Utah; p 172.

5. Dash, J. Chemical changes and excess heat caused by electrolysis with H_2SO_4 – D_2O electrolyte. *Progress in New Hydrogen Energy: Proceedings of the Sixth International Conference on Cold Fusion*, Lake Toya, Hokkaido, Japan, Oct. 13-18, 1996. Okamoto, M., Ed.; New Energy and Industrial Technology Development Organization, Tokyo Institute of Technology: Tokyo, 1996; p 477.
6. Dash, J.; Kopecek, R.; Miguet, S. Excess heat and unexpected elements from aqueous electrolysis with titanium and palladium cathodes. *Proceedings of the 32nd Intersociety Energy Conversion Engineering Conference,* Honolulu, HI, July 27-Aug. 1, 1997; **1997**, 2, 1350.
7. Warner J.; Dash, J. Heat produced during the electrolysis of D_2O with titanium cathodes. In *Proceedings of the Eighth International Conference on Cold Fusion*, Lerici (La Spezia), Italy, May 21, 26, 2000; Scaramuzzi, F., Ed.; Italian Physical Scoiety: Bologna, Italy, 2000; p 161.
8. Johnson, Jr., G. G.; White, E. W. X-ray emission wavelengths and keV tables for nondiffractive analysis. *American Society for Testing and Materials Data Series DS* 46, 1970.
9. Liu, J.; Yu, Y.; Li, Y.; He, H.; Tan, H.; Xu, K. Shock activation of titanium oxide and its photocatalytic activity. *Chemical Abstracts* **1999**, *131(8)*, 1303.
10. Kozima, H. *The Science of the Cold Fusion Phenomenon*. Elsevier: San Diego, CA, 2006.
11. Fisher, J. C. Theory of low temperature particle showers. In *Condensed Matter Nuclear Science: Tenth International Conference on Cold Fusion,* Cambridge, MA, Aug. 24-29, 2003; Hagelstein, P. L.; Chubb, S. R., Eds.; World Scientific Publishing Co.: Singapore, 2006; p 915.
12. Widom, A.; Larsen, L. Ultra low momentum neutron catalyzed nuclear reactions on metallic hydride surfaces. *Eur. Phys. J. C.* **2006**, *46*, 107.
13. *Handbook of Chemistry and Physics.* Lide, D. R., Ed.; CRC Press: 1993; pp 11-64.
14. Lipson, A. G.; Kuznetsov, V. A.; Saunin, E. I.; Miley, G. H. Anomalous thermal neutron capture and sub-surface Pd-isotopes separation in cold-worked palladium foils as a result of deuterium loading, In *Condensed Matter Nuclear Science: Proceedings of the Ninth International Conference on Cold Fusion,* Beijing, China, May 19, 24, 2002; Li, X. Z., Ed.; Tsinghua University Press: Beijing, 2002; p 213.
15. Notoya, R. Cold fusion by electrolysis in a light water-potassium carbonate solution with a nickel electrode. *Fusion Technology* **1993**, *24*, 202.
16. Will, F.; Cedzynska, K.; Linton, D. Tritium generation in palladium cathodes with high deuterium loading. *Trans. of Fusion Technology* **1994**, *26*, 209.
17. Bush, R.; Eagleton, R. Evidence for electrolytically induced transmutation and radioactivity correlated with excess heat in electrolytic cells with light water rubidium salt electrolytes. *Trans. of Fusion Technology* **1994**, *26*, 344.

Downloaded by COLUMBIA UNIV on June 28, 2012 | http://pubs.acs.org
Publication Date (Web): December 20, 2009 | doi: 10.1021/bk-2009-1029.ch004

18. Miley, G. H.; Narne, G.; Williams, M. J.; Patterson, J. A.; Nix, J.; Cravens, D.; Hora, H. Quantitative observation of transmutation products occurring in thin-film coated microspheres during electrolysis. *Progress in New Hydrogen Energy: Proceedings of the Sixth International Conference on Cold Fusion*, Lake Toya, Hokkaido, Japan, Oct. 13-18, 1996. Okamoto, M., Ed.; New Energy and Industrial Technology Development Organization, Tokyo Institute of Technology: Tokyo, 1996; p 629.
19. Savvatimova, I.; Kucherov, Y. R.; Karabut, A. B. Cathode material change after deuterium glow discharge experiments. In *Condensed Matter Nuclear Science: Fourth International Conference on Cold Fusion*, Dec. 6-9, 1993, Maui, HI, 1994; Passell, T. O., Ed.; Electric Power Research Institute: Palo Alto, CA, 1995; p 389.
20. Chicea, D. Comment on carbon production in deuterium-metal systems. In *Condensed Matter Nuclear Science: Tenth International Conference on Cold Fusion,* Cambridge, MA, Aug. 24-29, 2003; Hagelstein, P. L.; Chubb, S. R., Eds.; World Scientific Publishing Co.: Singapore, 2006; p 475.

Downloaded by COLUMBIA UNIV on June 28, 2012 | http://pubs.acs.org
Publication Date (Web): December 20, 2009 | doi: 10.1021/bk-2009-1029.ch004

Downloaded by UNIV OF GUELPH LIBRARY on June 28, 2012 | http://pubs.acs.org
Publication Date (Web): December 20, 2009 | doi: 10.1021/bk-2009-1029.ch005

Chapter 5

Dual Laser Stimulation and Optical Phonons in Palladium Deuteride

Dennis Letts[1] , Dennis Cravens[2], Peter L. Hagelstein[3]

[1]12015 Ladrido Lane, Austin, TX 78727, [2]Dennis Cravens, Ambridge University, P.O. Box 1317, Cloudcroft, NM 88317, [3]Research Laboratory of Electronics, MIT, Cambridge, MA 02139

In work done in 2007, we observed that two laser beams irradiating a deuterated palladium cathode at a single spot induced significant thermal increases many times larger than those expected from laser heating alone. This effect was observed only when the lasers were tuned to produce a beat frequency near 8 THz, 15 THz and 20 THz. These preliminary experiments support the conjecture that optical phonons are involved in the heat-producing mechanism (THz = 10^{12} Hz).

In recent experiments, results from more than 20 runs appear to confirm the three thermally sensitive frequencies at 8, 15 and 20 THz. Further, the experiments allowed us to produce an initial thermal response spectrum.

Introduction

As is well known by now, Martin Fleischmann, Stanley Pons and Marvin Hawkins first proposed the idea that nuclear reactions might be induced in deuterated palladium on March 23, 1989 *(1)*. The idea was controversial from its inception and was based on unexpected experimental results, not on established nuclear theory. The original experiments of Fleischmann and Pons showed electrode power densities and figures of merit normally associated with nuclear reactions, but with no indication of commensurate energetic particles. Their

In Low-Energy Nuclear Reactions and New Energy Technologies Sourcebook Volume 2; Marwan, J., et al.;
ACS Symposium Series; American Chemical Society: Washington, DC, 2010.

claim for nuclear reactions induced in the solid state at room temperature rested mainly on the fact that known chemistry could not account for the observed power and energy densities. This 1989 nuclear claim took several years to confirm experimentally; subsequently, numerous confirmations of the excess-heat effect have been reported by many groups.

In 1993, Melvin Miles and his collaborators claimed to see ^{4}He in roughly the amount expected from D-D fusion *(2)*. Excess heat correlated with ^{4}He in the outgas was reported by SRI *(3)* and by Apicella et al. in 2004 at ICCF12 *(4)*. In these experiments, most of the helium comes out in the gas, with perhaps 30 percent or so remaining in the metal. In the only two experiments (M4 at SRI, and Laser3 at ENEA) which have been done to date where an effort was made to collect all of the ^{4}He (including the residual helium retained in the cathode), the excess energy per helium atom was found to be 24 MeV to within better than 10 percent.

Downloaded by UNIV OF GUELPH LIBRARY on June 28, 2012 | http://pubs.acs.org
Publication Date (Web): December 20, 2009 | doi: 10.1021/bk-2009-1029.ch005

Theoretical Ideas

From the beginning, Peter Hagelstein pondered the role of phonons in the solid-state fusion of deuterium. His early work proposed a coherent phonon-photon mechanism as described in reference *(5)*, presented at the ASME meeting in December 1989. He proposed that the large nuclear energy release might be radiated into the lattice phonon field “one phonon at a time.” By 2003, Hagelstein modified the details of his phonon theory to favor a phonon exchange process as reported in his ICCF10 conference paper, reference *(6),* but the role of phonon coupling remained an important part of his overall theory. In his conjecture 4, page 847 of reference *(6),* he states, “Anomalies in metal deuterides are stimulated by strong phonon excitation.” In 2007, Hagelstein refined his phonon theory further in reference *(7)*; in this paper, he proposed once again that phonons are involved in the transfer of 24 MeV quanta from the D+D > ^{4}He reaction to the lattice in the form of phonons, leading to heat. The energy exchange is conjectured to be accomplished in large-number, single-phonon exchange processes. Hagelstein suggests that the optical phonon modes are the most likely candidates, especially the modes with low group velocity typically located at the edge of an optical phonon mode. In palladium deuteride, the optical phonon band ranges between 8 and 15-16 THz (*8,9*).

Experimental Support for Theory

The work discussed in this paper began in March 2007 as a series of experiments conducted by Dennis Letts and Dennis Cravens in collaboration with Hagelstein. Our goal was to see whether an experimental connection could be made with the phonon aspects of Hagelstein’s theory. His theory is complex, but our experimental approach was simple: We used dual lasers to create beat frequencies near the known low-momentum optical phonon modes for palladium deuteride. At very high intensity, nonlinear processes can produce a response at the sum or difference frequency of the incident laser beams. Here, the intensity is much lower, but the system seems to respond to the difference in laser frequencies. Figure 1 shown below was our guide for all of the initial experiments and remains in use as more data is accumulated in continuing experiments. Before the experiments were run, Hagelstein predicted that the edges of the optical phonon band would be the best candidates for stimulation to produce excess power. This region is where low group-velocity compressional phonon modes exist. This is consistent with our observations near 8 and 15 THz; but the response near 20 THz requires an alternate explanation. Perhaps the simplest conjecture for this higher-frequency response is proton contamination, which might be expected to produce a zero-group velocity band near 20 THz. Such a conjecture may be confirmed in future experiments in which the proton contamination is better-controlled and from phonon band calculations done for palladium deuteride contaminated with hydrogen.

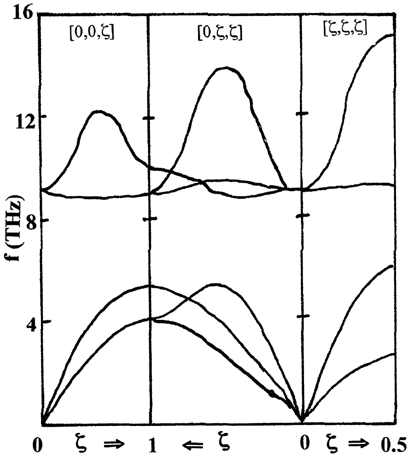

Figure 1 Band diagram for PdD redrawn from Sansores et al. (10). The zero group velocity points can be seen to be near 8.5 THz and 15 THz.

Instrumentation and Calorimetry

This work covers 19 tests from three cells. Two periods are involved: March 2007 to May 2007 and April 2008 to the present. The goal of this work was the creation of a beat frequency versus excess-power graph to determine whether a thermal response could be seen at difference frequencies in the vicinity of the optical phonon modes. If phonon modes are involved with the production of anomalous heat, then such a graph might show elevated excess-power production clustered about the optical phonon frequencies. What we found was a response at three frequencies, the lower two of which seem to match PdD optical

Downloaded by UNIV OF GUELPH LIBRARY on June 28, 2012 | http://pubs.acs.org
Publication Date (Web): December 20, 2009 | doi: 10.1021/bk-2009-1029.ch005

phonon zero group velocity points. These observations are reported in this paper.

All experiments were conducted in Austin, Texas. The experimental setup is shown below in Figure 2. Isoperibolic calorimetry was used on all tests. The lab temperature was fairly stable at 26 +/- 1 C. The temperature enclosure (the black box shown in Figure 2) was controlled by Labview and held at 25 +/- .03 C. The cell power was provided by a digital HP E3632A power supply. The input cell power was held constant by Labview to within 10 mW. This is typically 7 - 10 watts with current up to 1.25 to 1.5 amps (Figure 3).

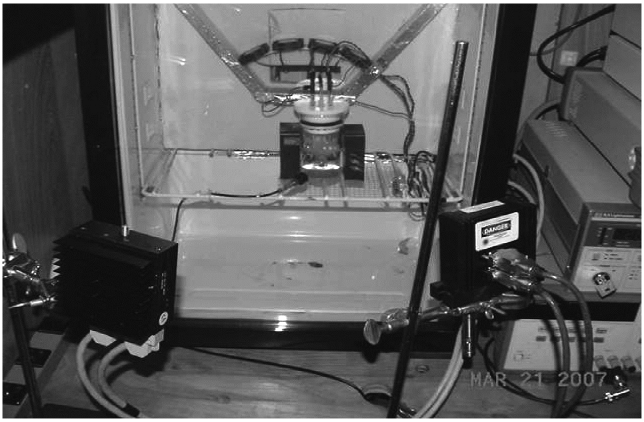

Figure 2 shows cell in temperature-controlled enclosure stimulated by dual lasers. Note optical spectrum analyzer detector in front of cell to check laser calibration during the experiment.

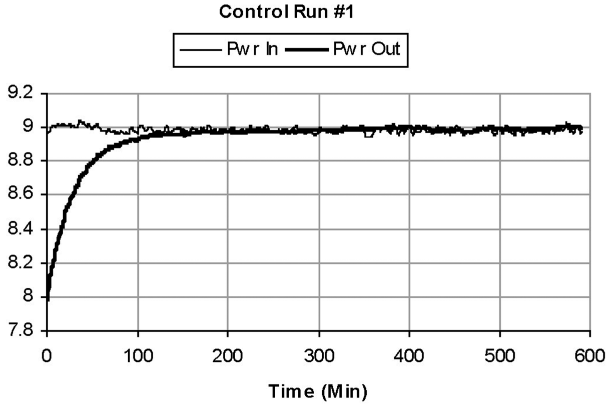

Figure 3 shows that the isoperibolic calorimeter demonstrates good long-term stability when the cell is not producing excess power. Most experiments run for 10 hours or less, so the calorimeter is stable over the time scale of the experiments. The standard deviation of the calorimeter output is 0.01W.

Downloaded by UNIV OF GUELPH LIBRARY on June 28, 2012 | http://pubs.acs.org
Publication Date (Web): December 20, 2009 | doi: 10.1021/bk-2009-1029.ch005

Experimental

A typical cell is shown in Figure 4 below. Two thermistors recorded cell temperature. One probe was placed slightly above the cathode, and one probe was placed slightly below the cathode. The average of the two probes was compared to enclosure temperature in computing excess power. The cell was not mechanically stirred. One hundred grams of 0.5M LIOD was used as electrolyte. Platinum-coated alumina pellets were used as recombiners, providing a closed electrochemical cell.

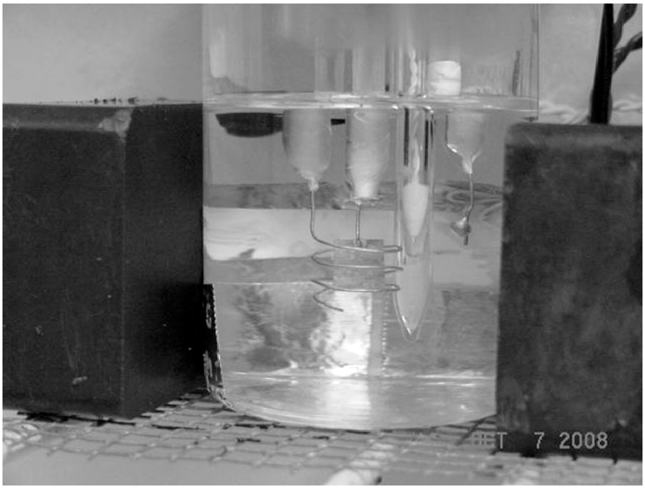

Figure 4 shows typical cell configuration. Magnets as shown provide a 700 gauss field across the cathode face. Air is vigorously stirred within the temperature-controlled enclosure.

The cathode stock was palladium made from a billet provided by Scott Little of Austin, Texas. The palladium was taken from a large palladium target from Texas Nuclear. The target was unused and of unknown purity but thought to be at least 0.995. The cathode was prepared following a 17-step protocol described previously *(11)*. The cathode was cold-rolled using a 90-degree rotation with each pass. This is thought to minimize stress build-up in any one direction. The work reported in this paper began on March 20, 2007, with experiment 662G (see Table I in the appendix below).

Optical Phonon Mode Resonances

After a few scans of the beat frequencies across the three optical phonon mode edges, it became apparent there was a very narrow band that would trigger excess power. It quickly became a goal to determine the spectral response of the

Downloaded by UNIV OF GUELPH LIBRARY on June 28, 2012 | http://pubs.acs.org
Publication Date (Web): December 20, 2009 | doi: 10.1021/bk-2009-1029.ch005

sensitive regions. One example of the left edge of the 20 THz sensitive region is seen in experiment 662t1 shown in Figure 5 below. The strategy was to begin scanning the beat frequency below the suspected left edge of the 20 THz optical phonon mode. In Figure 5, the scan started at 18.31 THz and advanced in steps of 0.16 THz. When the scan reached 18.79 THz, an exothermic cathode response was observed as the cell temperature increased sharply. The edges of the optical phonon bands may vary with loading, cell temperature or other factors not yet known. This particular experiment showed the left edge to be at 18.79 THz. Two experiments tested 21.40 THz and 21.70 THz, and both tests triggered excess power, suggesting that the band edge is above 22 THz. Figure 6 below shows that the right edge of the 20 THz mode appears to be near 22.11 THz.

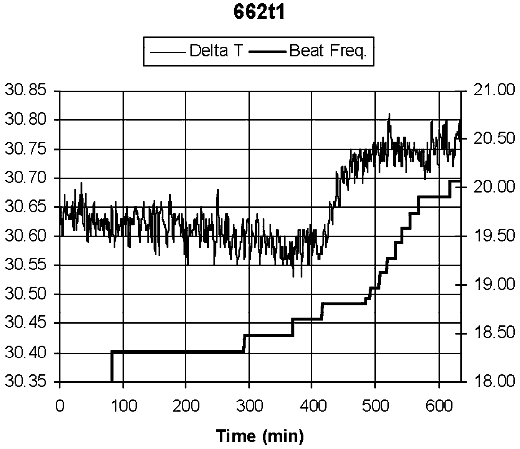

Figure 5 Graph shows the possible left edge of the optical phonon mode that triggers an exothermic reaction in palladium deuteride.

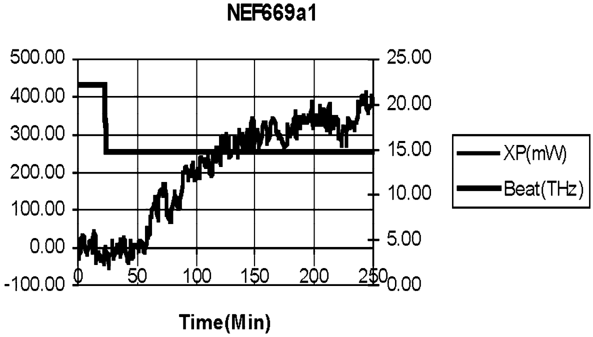

Figure 6 shows that a beat frequency of 22.11 THz does not trigger excess power, suggesting that the right edge is slightly to the right of 22 THz.

Downloaded by UNIV OF GUELPH LIBRARY on June 28, 2012 | http://pubs.acs.org
Publication Date (Web): December 20, 2009 | doi: 10.1021/bk-2009-1029.ch005

Downloaded by UNIV OF GUELPH LIBRARY on June 28, 2012 | http://pubs.acs.org
Publication Date (Web): December 20, 2009 | doi: 10.1021/bk-2009-1029.ch005

Using a similar strategy for the other two optical phonon modes leads to a series of graphs that identified the edges of all three modes for deuterated palladium. Figure 7 below shows a composite graph of all three modes. The mode near 8 THz is centered at 8.3 THz and has a mode width of 0.70 THz. The mode near 15 THz is centered at 15.3 THz and has a mode width of 0.44 THz. The mode near 20 THz is centered at 20.5 THz and has a mode width of 0.68 THz.

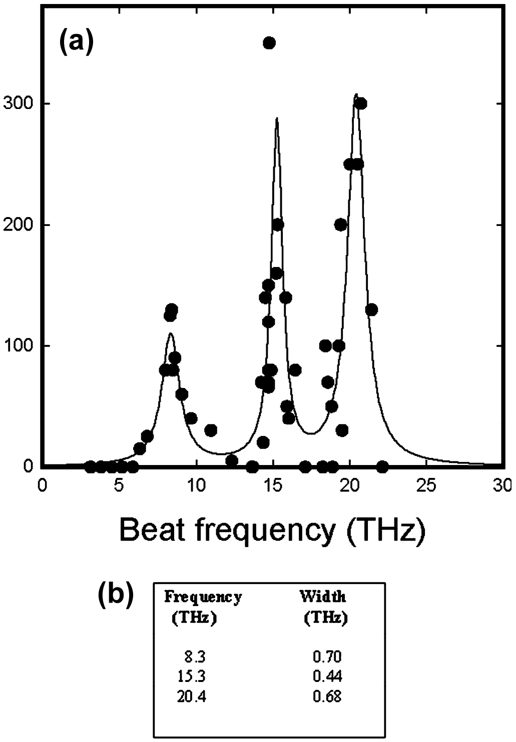

Frequency (THz)	Width (THz)
8.3	0.70
15.3	0.44
20.4	0.68

Figure 7a shows three specific triggering beat frequencies. Vertical scale is XP in mW. Also shown is a curve from a least-squares fit to a sum of three Lorentzians $\Sigma_j c_j/[(f-f_j)^2+\gamma_j^2]$, *where the center frequencies* f_j *and broadening parameters* γ_j *are indicated. Figure 7b shows that the width of the three peaks is fairly consistent and less than 1 THz; the 15 THz peak has the smallest scatter, with a peak width of only 0.44 THz.*

Temperature Dependence

Various researchers have reported that excess-power production can be larger when cell operating temperature is elevated. Our results are generally consistent with this. In Figures 8 and 9, we show an excess-heat event induced by dual laser stimulation at 21 THz; a cell temperature of 63 C resulted in 225 mW of excess power (Figure 8), and a cell temperature of 75 C produced 900 mW of excess power (Figure 9). An increase in the cell operating temperature from 63 C to 75 C resulted in a change in excess-power production from 225 mW to 900 mW, a 400 percent increase. This increase of excess power with temperature is qualitatively consistent with that reported by Storms *(12)* and other researchers.

Downloaded by UNIV OF GUELPH LIBRARY on June 28, 2012 | http://pubs.acs.org
Publication Date (Web): December 20, 2009 | doi: 10.1021/bk-2009-1029.ch005

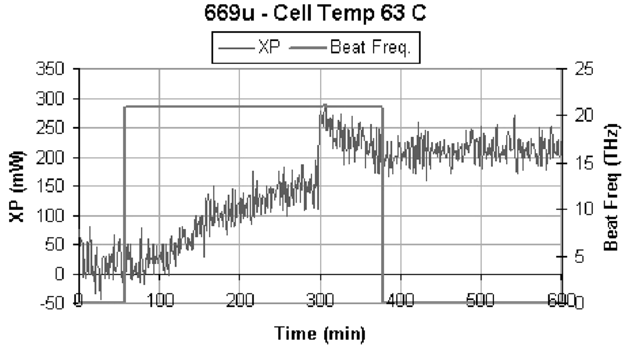

Figure 8 Graph shows that a 21 THz beat frequency triggers excess power of 225 mW at a cell temperature of 63 C.

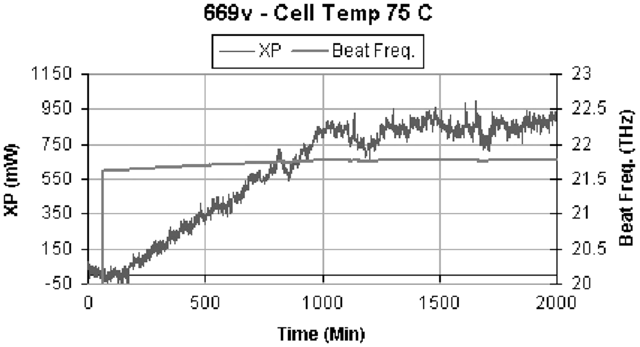

Figure 9 Graph shows that the cell triggers at about the same beat frequency as 669u but the thermal response at 75 C is four times greater than at 63 C.

In previous work, one of us (PLH) had conjectured that the temperature dependence of the excess power came about from the thermodynamics of states with double occupancy (dideuterium formation next to a single-atom host lattice vacancy). A weakness of the argument is that it requires the dideuterium state to lie above the octahedral state energy by the activation energy (670 meV in Storms experiment), which is unlikely. The binding energy of H_2 in σ-bonded $Pd(H_2)$ is less than 100 meV. In addition, if the dideuterium state did have such an elevated energy, then one would see a very steep dependence of dideuterium-state occupation with loading, much steeper than would correspond to observed excess-heat versus loading curves.

In the protocol for the dual laser experiments, a thin layer of gold coats the outer surface of the palladium (conjectured to be effective by virtue of having a plasmon resonance reasonably matched to the laser frequency). One might expect this gold to provide a barrier for helium diffusion. Perhaps the activation energy in gold for single-atom interstitial diffusion is correspondingly higher.

Downloaded by UNIV OF GUELPH LIBRARY on June 28, 2012 | http://pubs.acs.org
Publication Date (Web): December 20, 2009 | doi: 10.1021/bk-2009-1029.ch005

Discussion

Beating experiments using a dual-laser configuration provide a new tool that can be used to study excess heat in Fleischmann-Pons experiments. We have found the dual-laser experiment to be more robust than using a single laser for stimulating excess power. The cathodes appear to respond to the frequency difference between the two lasers, which, as a practical matter, allows us to explore the response of the system in the THz regime, which is otherwise not so accessible. We have found a response at three frequencies: 8, 15 and 20 THz.

The first two of these frequencies correspond to the zero-momentum optical phonon band edges of PdD, while the 20 THz frequency corresponds to the band edge in PdH. It has been conjectured that hydrogen contamination may be responsible for the 20 THz feature, although this has not been verified experimentally. Another possibility is that it may be associated with optical phonons of other metal deuterides or perhaps with weakly deuterated gold.

Why the system should respond to the beat frequency at such low laser intensities is another issue. We would not expect an optical nonlinearity associated with the electromagnetic fields unless the laser intensity were orders of magnitude higher. If so, then perhaps the nonlinearity lies within the coupled plasmon-phonon modes that are weakly stimulated by the laser. Once again, it is hard to understand how a nonlinearity would develop with such low incident power densities. However, under investigation is an excess-power effect, presumed to originate from a new kind of nuclear process. If the reaction energy is communicated to these modes, as would be consistent with theoretical models that have been under investigation for some time, then the internal mode amplitudes may be enhanced by orders of magnitude. If so, then a nonlinear response would not be so difficult to understand.

This scenario suggests that we should not neglect low-momentum acoustical modes near 5 THz. An inspection of the spectrum of Figure 7 indicates that the system does not respond near 5 THz, suggesting that the acoustic modes alone do not participate. However, we might expect down-conversion of 15 THz optical phonon mode energy to 5 THz acoustical mode energy, which suggests that the system may be able to drive the acoustical mode. If so, then perhaps the 20 THz response may involve coupling to a "product mode," where one 15 THz optical phonon and one 5 THz acoustical phonon combine to provide a response at 20 THz. Further research may shed light on these questions.

We have observed that the excess power in two experiments that are very nearly the same except for the cell temperature produces markedly different amounts of excess power. This result is generally consistent with earlier results on Fleischmann-Pons cells, except that the increase that we found was larger than expected. Whether this is true systematically remains to be determined. If the effect is real, then perhaps it may be possible to interpret it in terms of differences in the cathode surface.

Downloaded by UNIV OF GUELPH LIBRARY on June 28, 2012 | http://pubs.acs.org
Publication Date (Web): December 20, 2009 | doi: 10.1021/bk-2009-1029.ch005

Acknowledgement

Thanks to the New Energy Foundation for support of this research.

References

1. Pons, S.; Fleischmann, M.; Hawkins, M. Electrochemically Induced Nuclear Fusion of Deuterium. *J. Electroanal. Chem.* **1989**, *261*, 301-308.
2. Miles, M.; Hollins, R. A.; Bush, B. F.; Lagowski, J. J.; Miles, R. E. Correlation of Excess Power and Helium Production During D_2O and H_2O Electrolysis Using Palladium Cathodes. *J. Electroanal. Chem.* **1993**, *346*, 99-117.
3. McKubre, M. C. H. et al. Energy Production Processes in Deuterated Metals. *EPRI Report TR-107843-V1* **1998**; see also Hagelstein, P. L. et al. New Physical Effects in Metal Deuterides. In *Condensed Matter Nuclear Science: Proceedings of the Eleventh International Conference on Cold Fusion.* Biberian, J.-P., Ed.; Marseille, France, 2004; World Scientific Publishing Co.: 2006; p 23.
4. Apicella, M.; Castagna, E.; Capobianco, L.; D'Aulerio, L.; Mazzitelli, G.; Sarto, F.; Rosada, A.; Santoro, E.; Violante, V.; McKubre, M. C. H.; Tanzella, F.; Sibilia, C. Some Recent Results at ENEA. In *Condensed Matter Nuclear Science: Proceedings of the 12th International Conference on Cold Fusion, Yokohama, Japan, 2005;* Takahashi, A.; Ota, K.; Iwamura, Y., Eds.; World Scientific Publishing Co., 2006; p 117.
5. Hagelstein, P. L. Coherent Fusion Theory. In *Proceedings of ASME winter annual meeting.* San Francisco, CA. 1989; p 1.
6. Hagelstein, P. L. Unified Phonon Coupling SU(N) Models for Anomalies in Metal Deuterides. In *Condensed Matter Nuclear Science: Proceedings of the Tenth International Conference on Cold Fusion*, Cambridge, Mass. 2003; Hagelstein, P. L.; Chubb, S. R., Eds.; World Scientific Publishing Co.: 2006; p 837.

7. Hagelstein, P. L. Progress Toward a Theory for Excess Heat in Metal Deuterides. *Seventh symposium on Current Trends in International Fusion Research: A Review.* Washington, DC, 2007. In *Current Trends in International Fusion Research; Proceedings of the Seventh Symposium.* Panarella, E.; Raman, R., Eds.; NRC Research Press, National Research Council of Canada: Ottawa, 2007.
8. Rowe, J. M.; Rush, J. J.; Smith, H. G.; Mostoller, M.; Flotow, H. E. Lattice Dynamics of a Single Crystal of $PdD_{0.63}$. *Phys. Rev. Lett.* **1974,** *33*, 1297.
9. Glinka, C. J.; Rowe, J. M.; Rush, J. J.; Rahman, A.; Sinha, S. K.; Flotow, H. E. Inelastic-Neutron-Scattering Line Shapes in $PdD_{0.63}$. *Phys. Rev. B.* **1978**, *17*, 488.
10. Sansores, L. E.; Taguena-Martinez, J.; Tahir-Kheli, R. A. Lattice Dynamics of PdDx and PdHx. *J Phys. C: Solid State Phys.* **1982**, *15*, 6907-6917.
11. Letts, D.; Cravens, D. Laser Stimulation of Deuterated Palladium: Past and Present. In *Condensed Matter Nuclear Science: Proceedings of the Tenth International Conference on Cold Fusion*, Cambridge, Mass. 2003; Hagelstein, P. L.; Chubb, S. R., Eds.; World Scientific Publishing Co.: 2006; p 159.
12. Storms, E. Some Characteristics of Heat Production Using the Cold Fusion Effect. In *Condensed Matter Nuclear Science: Proceedings of the Fourth International Conference on Cold Fusion.* Maui, Hawaii. 1993; Passell, T. O., Ed.; Electric Power Research Institute: Palo Alto, CA, 1995; Vol. 2, 4-1.
13. Xia, J. et al. A Comparative Study of Helium Atom Diffusion Via an Interstitial Mechanism in Nickel and Palladium. *Phys. Stat. Sol.* **2006,** *243*, 579.
14. Pons, S.; Fleischmann, M.; Hawkins, M. Electrochemically Induced Nuclear Fusion of Deuterium. *Journal of Electroanalytical Chemistry.* **1989**, *261*, 301-308.
15. Miles, M.; Hollins, R. A.; Bush, B. F.; Lagowski, J. J.; Miles, R. E. Correlation of Excess Power and Helium Production During D_2O and H_2O Electrolysis Using Palladium Cathodes. *Journal of Electroanalytical Chemistry.* **1993**, *346*, 99-117.
16. McKubre, M. C. H. et al. Energy Production Processes in Deuterated Metals. *EPRI Report TR-107843-V1.* **1998**; see also Hagelstein, P. L. et al. New Physical Effects in Metal Deuterides. In *Condensed Matter Nuclear Science: Proceedings of the Eleventh International Conference on Cold Fusion.* Biberian, J.-P., Ed.; Marseille, France, 2004; World Scientific Publishing Co.: 2006; p 23.
17. Apicella, M.; Castagna, E.; Capobianco, L.; D'Aulerio, L.; Mazzitelli, G.; Sarto, F.; Rosada, A.; Santoro, E.; Violante, V.; McKubre, M. C. H.; Tanzella, F.; Sibilia, C. Some Recent Results at ENEA. In *Condensed Matter Nuclear Science: Proceedings of the 12th International Conference on Cold Fusion, Yokohama, Japan, 2005;* Takahashi, A.; Ota, K.; Iramura, Y., Eds.; World Scientific Publishing Co.: 2006; p 117.
18. Hagelstein, P. L. *Coherent Fusion Theory.* ASME winter annual meeting: San Francisco, CA, 1989, p 1.

Downloaded by UNIV OF GUELPH LIBRARY on June 28, 2012 | http://pubs.acs.org
Publication Date (Web): December 20, 2009 | doi: 10.1021/bk-2009-1029.ch005

19. Hagelstein, P. L. Unified Phonon Coupling SU(N) Models for Anomalies in Metal Deuterides. In *Condensed Matter Nuclear Science: Proceedings of the Tenth International Conference on Cold Fusion*, Cambridge, Mass. 2003; Hagelstein, P. L.; Chubb, S. R., Eds.; World Scientific Publishing Co.: 2006; p .
20. Hagelstein, P. L. Progress Toward a Theory for Excess Heat in Metal Deuterides. *Seventh symposium on Current Trends in International Fusion Research: A Review.* Washington, DC, 2007; In *Current Trends in International Fusion Research; Proceedings of the Seventh Symposium.* Panarella, E.; Raman, R., Eds.; NRC Research Press, National Research Council of Canada: Ottawa, 2007.
21. Rowe, J. M.; Rush, J. J.; Smith, H. G.; Mostoller, M.; Flotow, H. E. Lattice Dynamics of a Single Crystal of $PdD_{0.63}$. *Phys. Rev. Lett.* **1974,** *33*, 1297.
22. Glinka, C. J.; Rowe, J. M.; Rush, J. J.; Rahman, A.; Sinha, S. K.; Flotow, H. E. Inelastic-Neutron-Scattering Line Shapes in $PdD_{0.63}$. *Physical Review B.* **1978,** *17*, 488.
23. Sansores, L. E., Taguena-Martinez, J., Tahir-Kheli, R. A. Lattice Dynamics of PdDx and PdHx. *J Phys. C: Solid State Phys.* **1982,** *15*, 6907-6917.
24. Letts, D.; Cravens, D. Laser Stimulation of Deuterated Palladium: Past and Present. In *Condensed Matter Nuclear Science: Proceedings of the Tenth International Conference on Cold Fusion*, Cambridge, Mass. 2003; Hagelstein, P. L.; Chubb, S. R., Eds.; World Scientific Publishing Co.: 2006; p 159.
25. Storms, E. Some Characteristics of Heat Production Using the Cold Fusion Effect. In *Condensed Matter Nuclear Science: Proceedings of the Fourth International Conference on Cold Fusion.* Maui, Hawaii. 1993; Passell, T. O., Ed.; Electric Power Research Institute: Palo Alto, CA, 1995; p 4.
26. Xia, J. et al. A Comparative Study of Helium Atom Diffusion Via an Interstitial Mechanism in Nickel and Palladium. *Phys. Stat. Sol.* **2006,** *243*, 579.

Downloaded by UNIV OF GUELPH LIBRARY on June 28, 2012 | http://pubs.acs.org
Publication Date (Web): December 20, 2009 | doi: 10.1021/bk-2009-1029.ch005

Appendix

Table I. Shows 49 data points from 19 experiments taken from three cells tested in 2007 and 2008. Cells in Table I were tested at ~ 50-60 C.

No.	*Experiment*	*Date*	*Freq. (THz)*	*XP(mW)*
1	662n	3/25/2007	3.12	0
2	662n	3/25/2007	3.81	0
3	662n	3/25/2007	4.50	0
4	662n	3/25/2007	5.18	0
5	662n	3/25/2007	5.86	0
6	662n	3/25/2007	6.33	15
7	662n	3/25/2007	6.80	25
8	662i	3/21/2007	8.00	80
9	662g	3/20/2007	8.30	125
10	662k	3/22/2007	8.40	130
11	662i(2)	3/21/2007	8.48	80
12	662i(2)	3/21/2007	8.61	90
13	662i(2)	3/21/2007	9.06	60
14	662i(2)	3/21/2007	9.65	40
15	662i(2)	3/21/2007	10.95	30
16	662i(2)	3/21/2007	12.31	40
17	662i	3/21/2007	13.62	0
18	662i(2)	3/21/2007	13.68	20
19	662i	3/21/2007	14.23	70
20	662i(2)	3/21/2007	14.36	20
21	662f1	4/13/2007	14.50	140
22	662j1	4/15/2007	14.70	70
23	662w	3/31/2007	14.70	70
24	662y	4/2/2007	14.70	120
25	662a1	4/4/2007	14.70	80
26	662j1	4/15/2007	14.70	150
27	662s1	4/23/2007	14.70	66
28	669a1	5/8/2008	14.75	350
29	662i(2)	3/21/2007	14.88	80
30	662f1	4/13/2007	15.20	160
31	662a1	4/4/2007	15.30	200
32	662f1	4/13/2007	15.82	140
33	662b2	5/5/2007	15.90	50
34	662w	3/31/2007	16.02	40
35	662f1	4/13/2007	16.45	80
36	662f1	4/13/2007	17.09	0
37	662i2	3/21/2007	18.23	0
38	662c2	5/5/2007	18.40	100
39	662w	3/31/2007	18.56	70
40	662t1	4/25/2007	18.80	50
41	662i2	3/21/2007	18.87	0
42	670a	6/6/2008	19.28	100
43	662o	3/25/2007	19.40	200
44	662i2	3/21/2007	19.50	30
45	669u	4/30/2008	20.00	250
46	662x1	4/29/2007	20.50	250
47	662o2	5/17/2007	20.70	300
48	662i2	3/21/2007	21.40	130
49	669a1	5/8/2008	22.11	0

Downloaded by UNIV OF GUELPH LIBRARY on June 28, 2012 | http://pubs.acs.org
Publication Date (Web): December 20, 2009 | doi: 10.1021/bk-2009-1029.ch005

Downloaded by CORNELL UNIV on June 28, 2012 | http://pubs.acs.org
Publication Date (Web): December 20, 2009 | doi: 10.1021/bk-2009-1029.ch006

Chapter 6

Hot Deuteron Generation and Charged Particle Emissions on Excitation of Deuterium Subsystem in Metal Deuterides

Andrei Lipson[1], Ivan Chernov[2], Alexei Roussetski[3], Yuri Cherdantsev[2], Aslan Tsivadze[1], Boris Lyakhov[1], Eugeny Saunin[1] and Michael Melich[4]

[1] A.N. Frumkin Institute of Physical Chemistry and Electrochemistry, Russian Academy of Sciences, 119991 Moscow, Russia
[2] Tomsk Polytechnic University, 634050 Tomsk, Russia
[3] P. N. Lebedev Physics Insitute, Russian Academy of Sciences, 119991 Moscow, Russia
[4] Naval Postgraduate School, Monterey, CA 93943-5000 USA

Statistically significant emissions of DD-reaction products, 3 MeV protons and high-energy alpha particles (11-20 MeV) were observed in specially prepared Pd/PdO:D_x and TiD_x targets in vacuum, stimulated by electron beam ($J \sim 0.6$ mA/cm^2, $U = 30$ keV). These charge particles' energies and identities were determined using a set of CR-39 detectors covered with various metal foils. In contrast, the Pd/PdO:D_x and the TiD_x samples show no sign of nuclear emissions in vacuum without e-beam stimulation. Extrapolation of both DD-reaction cross section and the enhancement factor (consistent with a calculated screening potential $U_e = 750$ eV) to very low deuteron energy satisfactorily describes the detected DD-reaction yield in Pd/PdO:D_x targets, under the assumption of hot deuteron ($<E_d> \sim 3.0$ eV) generation under e-beam bombardment. This result strongly supports the theoretical prediction *(1, 2)* for electron excitation of the D-subsystem in Pd- deuterides.

In Low-Energy Nuclear Reactions and New Energy Technologies Sourcebook Volume 2; Marwan, J., et al.;
ACS Symposium Series; American Chemical Society: Washington, DC, 2010.

Introduction

Studies of the radiation absorption properties of metal hydrides by the Tomsk group *(1, 2)* have shown that a localized excitation produces a global release of hydrogen. For example, an electron beam or x-ray beam area about 40 mm^2, impinging on a 1 cm^2 foil, rapidly releases mostly atomic, not molecular, hydrogen over the entire foil surface. This surprising experimental result can be described in terms of a three-component model: the electrons, the protium/deturium, and the metal matrix. Each component responds differently to the excitation energy of the impinging beams. These original Tomsk experiments do not provide the energy spectrum of the released atomic hydrogen.

Lipson and colleagues *(3, 4, 5, 6, 7, 8, 9)*, using CR-39 detectors, have detected the emission of charged particles with MeV-level energies when deuterated metals are allowed to warm up from liquid-nitrogen temperature to room temperature. Using accelerator beams to calibrate the energy and identify the charged particles plus other techniques to rule out background and other sources of error, they have developed reliable methods for detecting low count rates (hundreds of counts) over experiments lasting about 10 hours.

The work reported here joins the stimulated-foil experiment of the Tomsk group, along with the group's theoretical understanding of its results, to the composite thin films, the desorption experiments, the CR-39 detection methods, and models of DD scattering at low energies of Lipson and colleagues. We have found that electron-beam stimulation appears to induce a D-desorption process from specially prepared Pd/PdO:Dx and TiDx targets. This apparently is caused by a statistically significant emission of DD-reaction product (involving 3 MeV protons), as well as additional emission of higher-energy alpha particles. It is important that the same Pd/PdO:Dx and TiDx samples show no sign of nuclear emissions in vacuum without e-beam stimulation. Extrapolation of both DD-reaction cross section and the enhancement factor (consistent with calculated screening potential U_e = 750 eV) to very low deuteron energy (E_d ~ 1.0 eV) allowed us to describe in a satisfactory manner our results for the detected DD-reaction yield in Pd/PdO:D_x target under e-beam excitation. This result appears to support the theoretical suggestion *(1, 2)* that electron excitation of a D-subsystem in Pd/PdO deuteride can result in significant changes in the associated dynamics.

Experimental

The Pd-based samples were prepared from Nilaco (Japan) Pd foil (99.95 percent purity) of 50 μm thick with dimensions S = 30 × 10 mm^2. The TiD_x samples were prepared from technical purity titanium foil of 30 and 300 μm thick. The Pd/PdO heterostructure samples served as cathodes during their electrochemical loading in 0.3 M-LiOD solution in D_2O with a Pt anode. The loading was carried out at electrolytic current density, j = 10 mA/cm^{2,} at ~ 280 K (below room temperature) in a special electrolytic cell with split cathode and

Downloaded by CORNELL UNIV on June 28, 2012 | http://pubs.acs.org
Publication Date (Web): December 20, 2009 | doi: 10.1021/bk-2009-1029.ch006

anodic spaces. After loading was complete, up to x = D/Pd ~ 0.73 (about 40 min required), the samples were rinsed in pure D_2O and then put in a Dewar to cool them to T =77 K. Those cooled samples were then rapidly mounted (< 1 min) in the sample holder. The sample was then in front of two or three CR-39 detectors covered with various metal foils (filters) when it was put into the SEM vacuum chamber using a special handle-manipulator (Fig. 1).

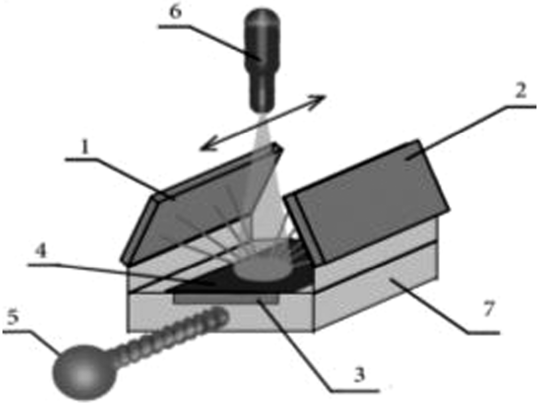

Figure 1. Experimental sample-detector holder mounted in the SEM vacuum chamber (p = 10-6 torr) and irradiated by collimated electron beam of EDS electron gun (J = 100-300 nA, E = 30 keV), where 1,2 and 3 – are the CR-39 detectors covered with the 11 µm Al (1), 25 µm Cu (2) and 33 µm Al (3) foil filters, respectively, 4 – is the deuterated sample. 5-manipulator, 6-electron gun, 7- stainless steel support.

In the first series of experiments, the e-beam spot bombarded the sample in one fixed position at foil center (the automatic scanning has been carried out within the beam spot). In the second series of experiment, the e-beam was positioned on the sample surface at three fixed positions, with 15 minutes of irradiation at each position. The mean fraction of the deuterium desorbed from the sample during e-beam irradiation in vacuum has been determined by anodic polarization of the samples, after termination of e-beam with the sample removed from the vacuum chamber. This measurement showed about 10 percent of residual deuterium remaining in the Pd/PdO:D_x sample after its about 50 min in 30 keV e-beam irradiation with current density J= 0.6 µA/cm2. This desorption rate is consistent with a mean D+ desorption current from the Pd/PdOD_x sample during e-beam action of $J_D \sim 3.3 \times 10^{15}$ D/s-cm^2. This number of desorbed deuterons is consistent with the rate of D-desorption in air at ambient conditions (Fig. 2).

Downloaded by CORNELL UNIV on June 28, 2012 | http://pubs.acs.org
Publication Date (Web): December 20, 2009 | doi: 10.1021/bk-2009-1029.ch006

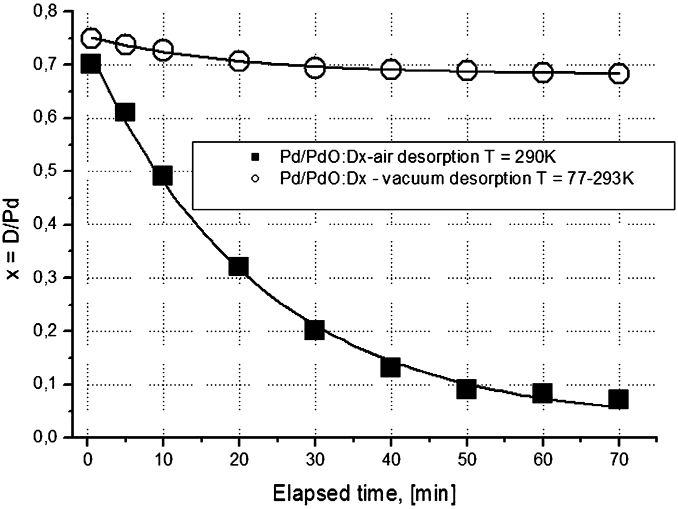

Figure 2. D-desorption rate from the Pd/PdO:Dx samples in vacuum (electrolysis at T=280 K with cooling down to T = 77K after electrolysis termination)) and in air at ambient conditions (electrolysis at T=290K).

In contrast to Pd/PdO samples, the Ti samples have been loaded in a 1 M solution of D_2SO_4 in D_2O for time = 35 hr at J = 30 mA/cm^2, in order to dissolve the TiO_2 oxide layer at the Ti-surface and to provide D-penetration. This technique is able to provide a several-microns-thick TiD_1 compound formation at the Ti cathode surface layer. The average loading was determined by weighing the sample in a balance before and after e-beam irradiation. It was found that the D-desorption rate in case of TiD irradiation is consistent with the $J_D \sim 1.0 \times 10^{14}$ D/s-cm^2. The TiD_1 compound is very stable and does not lose deuterium below T = 400 C. Thus, all desorbed deuterons in TiD result from e-beam irradiation.

A set of noiseless (non-electronic) plastic track detectors detected the charged particles emitted by the deuterated samples when under electron irradiation. The identity and energy of the emitted particles were determined by simultaneously using two or three CR-39 detectors covered with various foils of known stopping range (this arrangement can be considered the simplest dE-E detector without time converter). Reference experiments were performed at the Frumkin Institute. These were carried out in vacuum with open and Cu-covered CR-39 detectors, but with no electron-beam excitation.

The desorbed deuterium and generated charged particles reach the detectors from the spot produced by e-beam with area S = 8x6 mm^2 (Fig. 1) The effective distance between the center of the spot and detectors 1 and 2 is about $<R_{eff}>$ = 12 mm. The background counts are always taken from the rear side of CR-39 (opposite to the side directed to the sample's surface). The foreground counts have been read out from the CR-39 surface of detectors 1, 2 and 3 that face the sample, and the background counts that will be subtracted come from the rear side of the same detector. Thus, the background estimate comes from the detector face that sees the vacuum chamber *(1, 2)* or to the stainless support *(3)*.

Downloaded by CORNELL UNIV on June 28, 2012 | http://pubs.acs.org
Publication Date (Web): December 20, 2009 | doi: 10.1021/bk-2009-1029.ch006

Downloaded by CORNELL UNIV on June 28, 2012 | http://pubs.acs.org
Publication Date (Web): December 20, 2009 | doi: 10.1021/bk-2009-1029.ch006

The resulting counts caused by charged particle emission from the sample are computed by subtracting the background read-out data (rear side) from the foreground (front side facing the sample) of the same CR-39 detector. Subtraction of the rear side reading data could provide more information when the CR-39 detector was irradiated by fast neutrons. Unfortunately, this batch of the CR-39 track detectors was probably irradiated by a weak fast neutron flux enroute to Moscow from the United States at an airport security facility. As a result, the background level in the track diameter range of interest (4-8 μm) was found to be four-to-five times above the usual 4-8 μm track diameter background, which is normally $N < 10$ track/cm^2.

We thus considered only tracks close to the normal incidence with respect to the CR-39 surface, such that incidence angle Θ with respect to the perpendicular to the detector's surface would be $-10° < \Theta < 10°$. During the experiments reported here, the effective read-out area of the CR-39 detector chips with dimensions 2x1 cm^2 was reduced to about 1 cm^2 (to avoid severely defective sites on the detector's edge). In such a condition, the effective geometrical efficiency of detectors 1 and 2 was calculated as following: $\varepsilon_g = 1/4\pi\langle R_{eff}\rangle^2 S = 2.6\text{x}10^{-2}$, where $S = 0.48$ cm^2 is the effective area of the irradiated spot at the surface of the sample, which is taken equal to the area of the e-beam. From previous reported work, the efficiency of the detectors in tight contact with the sample (the #3 detector) is calculated as $\varepsilon \cong ½(1-\cos\Theta_c)$, where Θ_c – is the critical angle for charged particle of the given type and energy, the pre-factor $a \sim 1/2$ is the numerical coefficient that accounts for the non-circular tracks (that is, the tracks with the small deviations from their circular shape). The detectors were etched in 6N NaOH at t = 70 C with the rate of ~ 1.3 μ/hr.

The negative results showing absence of the charged particle emissions in the background measurements in a vacuum chamber are shown in Fig 3. a, b.

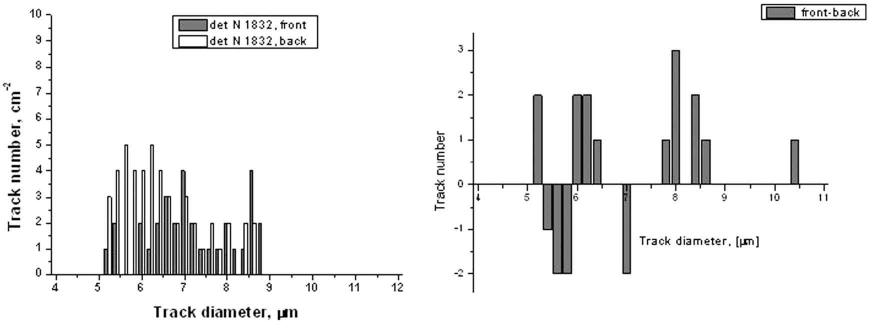

Figure 3 (a,b) The background in the vacuum chamber (Tomsk); the front and the back sides counts (a); the differential spectrum: the front minus back (i.e. opposite the front one) sides of this CR-39 detector (b). As seen, in the diameter range of interest (5-8 μm), the deviation of track number difference between the front and the rear side of the detector is about ± 2. The tracks at the detector's surface are from a weak fast neutron irradiation and radon exposure (see the "maximum" at Æ = 8 μm).

Experimental Results

Experimental Results: Pd/PdO:D$_x$

In order to evaluate the contribution of the electron-beam stimulation, it was important to carry out CR-39 measurements in the spontaneous vacuum D-desorption mode at T=290 K (upper curve in Fig. 1). To increase efficiency of measurements, the detection here has been performed using two detectors (one open, another filtered with 25 µm thick Cu-foil) attached to the Pd/PdOD$_x$ samples from both sides. The results presented in Fig. 4 (a-d) show a null effect. Indeed, differential spectra obtained by subtracting the background data (the tracks from the rear side of the detectors, which is opposite the front side facing the sample) from the foreground one (tracks at the front side of the same detector) within the standard deviation of ± 3 counts doesn't produce any peak in the total track diameter range of interest (4-12 µm). Notice that these null-effect data were obtained for both open (Fig. 4 a, b) and 25 µm Cu covered CR-39 (Fig. 4 c, d). These results definitely indicate that no charged particle emission occurs during low rate (Fig. 1) spontaneous vacuum deuterium desorption from the Pd/PdO:Dx heterostructure. Thus, the electron beam is critical for vacuum desorption.

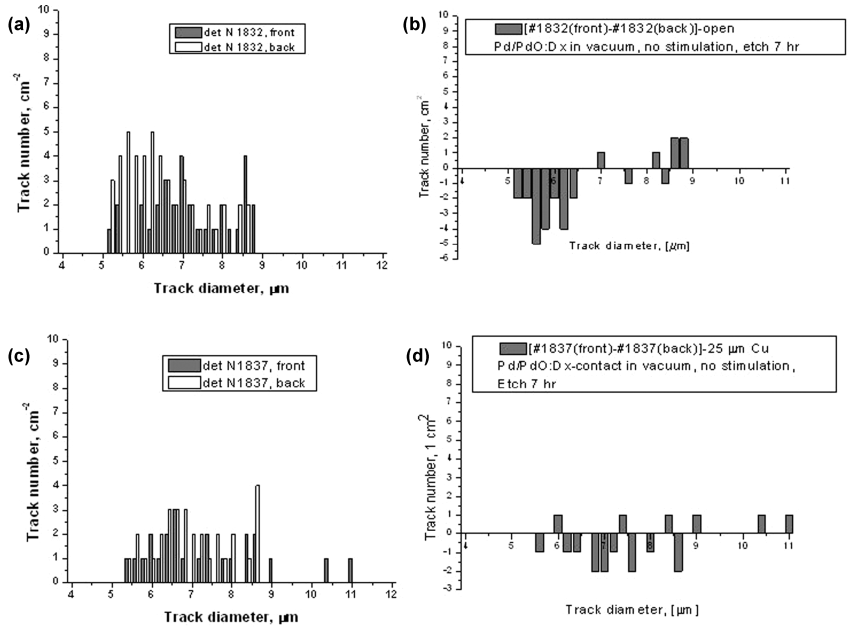

Figure 4 (a-d): Open detector result: the front and the back sides counts (a); the difference between the front (attached to the sample) and back (i.e. opposite the front one) sides of the CR-39 detector (b); 25 µm Cu covered CR-39 detector results: the front and the back sides counts (c); 25 µm Cu covered CR-39 detector; the difference between the front (attached to the sample) and back sides of the CR-39 detector.

Downloaded by CORNELL UNIV on June 28, 2012 | http://pubs.acs.org
Publication Date (Web): December 20, 2009 | doi: 10.1021/bk-2009-1029.ch006

Preliminary Electron Beam Irradiation Results: $Pd/PdO/Pd:D_x$

In contrast to the spontaneous vacuum D-desorption experiment, statistically useful results have been obtained in two separate series of experiments with $Pd/PdO/Pd:D_x$ samples consisting of 16 and 20 runs, respectively, exposed in vacuum under electron-beam stimulation. In these experiments, we used three CR-39 detectors in each series (as shown in Fig. 1). Two of them (covered with 11 μm Al and 25 μm Cu foils) have been placed under the free face of the sample irradiated by e-beam; the third detector (covered with 33 μm Al) has been placed at the rear side of the sample that has not been irradiated by electrons.

Total differential spectra (track number vs. track diameter) obtained for detectors 1, 2 and 3 in 36 runs of e-beam stimulated D-desorption with duration of 50 minutes each (total time of exposure is $\Sigma t = 1{,}800$ minutes) are shown in Figs 5-7, respectively. These figures contain summary results (the read-out data from 2 cm^2 area of the CR-39 detectors, in total) of the first series (16 consecutive runs with the 4 $Pd/PdO:D_x$ samples irradiated by 30 keV electron beam ($J = 0.3$ μA/cm^2) and the second series (20 consecutive runs with another set of six freshly prepared $Pd/PdO:D_x$ samples). As seen from the figures, the CR-39 spectra for each detector 1,2,3 consist of two statistically significant peaks: peak I (of lower track diameter) and peak II (of larger track diameter).

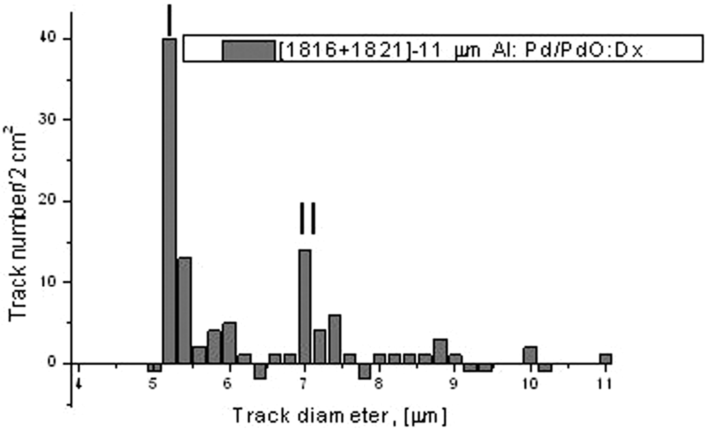

Figure 5. Summary differential spectrum of the 11 μm Al covered CR-39 detector. The sum obtained in both first (16 runs) and second (20 runs) series of experiments. Total time of 1+2 series is t = 1,800 min, using 10 similar Pd/PdO:Dx. As seen, both highly statistically significant 2.75 MeV proton (5.2-5.4 μm track diameter, peal I) and 11-20 MeV alphas (7.0-7.6 μm track diameter "peak" II) bands appear.

Downloaded by CORNELL UNIV on June 28, 2012 | http://pubs.acs.org
Publication Date (Web): December 20, 2009 | doi: 10.1021/bk-2009-1029.ch006

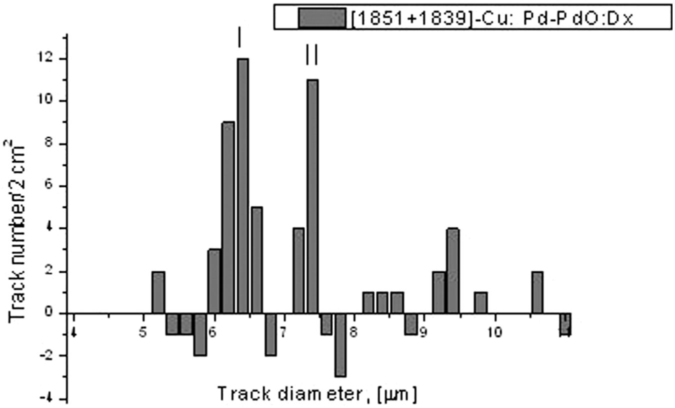

Figure 6. Summary differential spectrum of the 25 μm Cu covered CR-39 detector (position 2 in Figure 2) obtained in both first (16 runs) and second (20 runs) series of experiments. Total time of 1+2 series is t = 1,800 min, using 10 similar Pd/PdO:Dx. The statistically significant bands of 1.4 MeV protons (track diameter in the range of 6.0-6.6 μm, peak I), consistent with the 3 MeV proton losses in 25 μm Cu foil) and 12-20 MeV alphas (track diameter near 7.4 μm, consistent with ~ 19 MeV alpha losses in 25 μm Cu foil, peak II) appear in the spectrum. Peak IIa is consistent with incident ~ 11 MeV alpha emission.

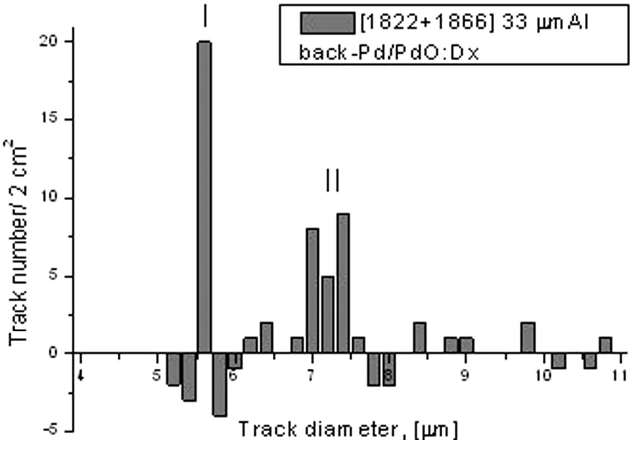

Figure 7. Summary differential spectrum of the 33 μm Al covered CR-39 detector placed below the rear (non-irradiated by e-beam) side of the Pd/PdO:Dx sample (position #3 in Figure 2) obtained in both first (16 runs) and second (20 runs) series of experiments (b). Total time of 1+2 series is t = 1,800 min, using 10 similar Pd/PdO:Dx. The statistically significant bands of 2.1 MeV protons (track diameter near 5.6 μm, consistent with 3 MeV proton losses in 33 μm Al foil, peak I) and alphas (track diameter 7-7,4 μm, consistent with ~ 14-19 MeV alpha losses in 33 μm Al foil, peak II) appear in the spectrum.

Downloaded by CORNELL UNIV on June 28, 2012 | http://pubs.acs.org
Publication Date (Web): December 20, 2009 | doi: 10.1021/bk-2009-1029.ch006

According to the accelerator calibration data, the lower track diameter peak I can be ascribed to 3MeV proton emission. Indeed, taking into account proton energy losses in the metal foils covering detectors 1, 2 and 3, one can estimate that the final energy of incident 3 MeV proton passing the foils (11 μm Al – detector 1, 25 μm Cu – detector 2 and 33 μm Al – detector 3) would be 2.75, 1,40 and 2.0 MeV, respectively. The track diameters, consistent with these energetic protons, are 5.25, 6.4 and 5.8 μm, respectively. These track diameters are consistent with the position of peak I for detectors 1, 2 and 3, showing an average track diameter d = 5.3±0.2, 6.4 ±0.3 and 5.7±0.2 μm, respectively.

The position of peak II and the appropriate change in the average track diameter, corresponding to peak II in detectors 1, 2 and 3, are inconsistent with the proton emission. As shown earlier, the tracks located near 7.0-7.6 μm diameter range (in 11 μm Al foil-covered Landauer CR-39 etched during seven hours) can be ascribed to energetic alpha particles with a broad spectrum in the range of 11-20 MeV. Indeed, after passage through the 25 μm Cu foil, covering detector 2 (which cut off all alphas with energies below ~ 10 MeV), the spectrum of peak II, corresponding to detector 1 (Fig. 5), changes its position. The maximum of peak II in Fig. 6 (detector 2) is shifted from d = 7.0 μm (Fig. 5) to 7.2 μm (Fig. 6). The similar maximum in detector 3 is spread in the range of 7.0-7.6 μm (after passage of 33 μm Al). Moreover, a larger track diameter component (which is not observed in detector 1) also appeared in detector 2 (d ~ 9.2-9.4 μm), indicating splitting of the alpha spectrum into the higher and lower energy components. More detailed information on the energy spectra of emitted alpha particles has been extracted using a sequential etching procedure applied to detectors 1 and 2 and described in the next section of the paper.

Thus, in contrast to the spontaneous vacuum D- desorption experimental series, the summary results obtained with seven-hours-etched CR-39 detectors 1, 2 and 3 showed statistically significant signatures of 3 MeV proton and energetic alpha emission (Figs. 5-7) observed during stimulation of D-desorption from electrochemically loaded Pd/PdO:D_x heterostructure by 30 keV electron-beam irradiation.

Sequential Etching of Detectors 1 and 2

In order to get unambiguous proof that emissions of DD-reaction product (3 MeV protons) and energetic alphas have really been observed in our experiments with e-beam stimulation, we performed a sequential etching of detectors 1 (11 μm Al foil-covered, #1816) and 2 (25 μm Cu foil-covered, #1851) facing the open surface of the sample (Fig. 2) in the second series of experiments. This procedure included 14-, 21- and 28-hour etching and analysis (in addition to the analysis of the same detectors etched during seven hours, shown in the previous section). The diameters obtained during sequential etching diameters of tracks of peaks I and II have been compared with those of proton and alpha tracks extracted from similarly etched calibration detectors. The sequential etching data for p and α accelerator bombardment are presented in Ref. *(6)*.

Downloaded by CORNELL UNIV on June 28, 2012 | http://pubs.acs.org
Publication Date (Web): December 20, 2009 | doi: 10.1021/bk-2009-1029.ch006

The sequential etching data (Figs.11-14), including track diameter fit shown in Fig. 15 presents additional unambiguous evidence for 3 MeV proton emission during vacuum electron-beam bombardment of the Pd/PdO:Dx heterostructure. Indeed, the shift of tracks in a main (lower-diameter track) peak to the larger diameter for detectors 1 and 2 (Figs. 12 and 14) is consistent (within the standard deviation) with those shifts obtained for 2.75 and 1.4 MeV normal incidence proton tracks, respectively (Fig. 15). Notice that these chosen proton energies of 2.75 and 1. 4 MeV are associated with the 3.0 MeV protons from DD-reaction, passed through the 11 μm thick Al and 25 μm thick Cu foils, respectively. These are the foils that were used as filters in detectors 1 and 2, respectively.

Downloaded by CORNELL UNIV on June 28, 2012 | http://pubs.acs.org
Publication Date (Web): December 20, 2009 | doi: 10.1021/bk-2009-1029.ch006

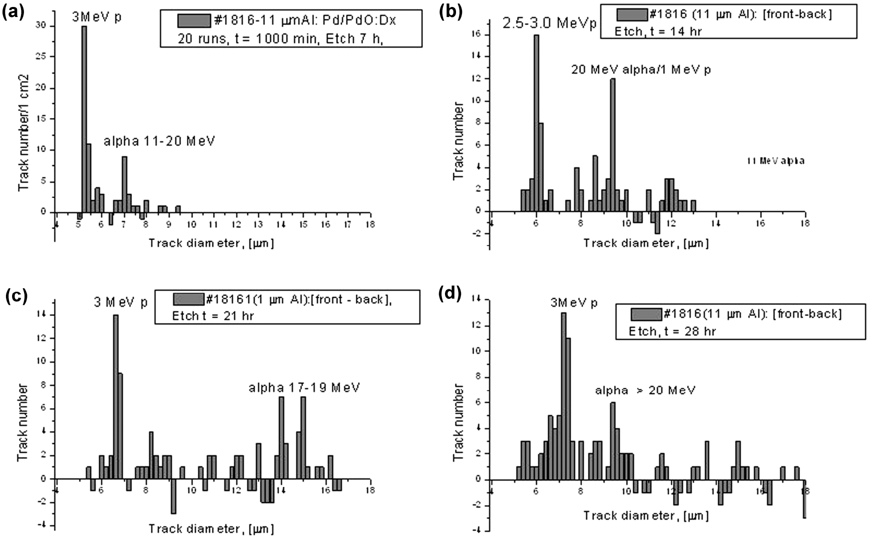

Figure 8 (a-d). Differential spectra (with subtracting of the background at the rear detector's face) of #1816 CR-39 detector (#1) exposed during e-beam irradiation of 6 Pd/PdO:Dx samples during 1,000 min) after the etching during 7 (a), 14(b), 21(c) and 28(d) hours. The shift of the peaks in a larger track diameter side with increase in etching time is very clear.

Downloaded by CORNELL UNIV on June 28, 2012 | http://pubs.acs.org
Publication Date (Web): December 20, 2009 | doi: 10.1021/bk-2009-1029.ch006

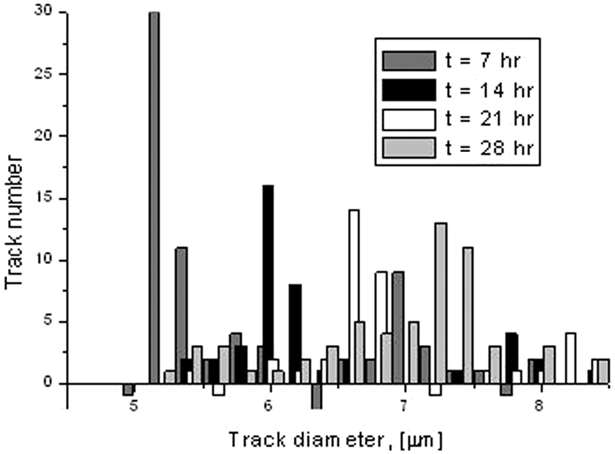

Figure 9. Shift in track diameter for the main peak I (3 MeV protons) obtained during sequential etching of #1816 detector covered with 11 μm thick Al foil.

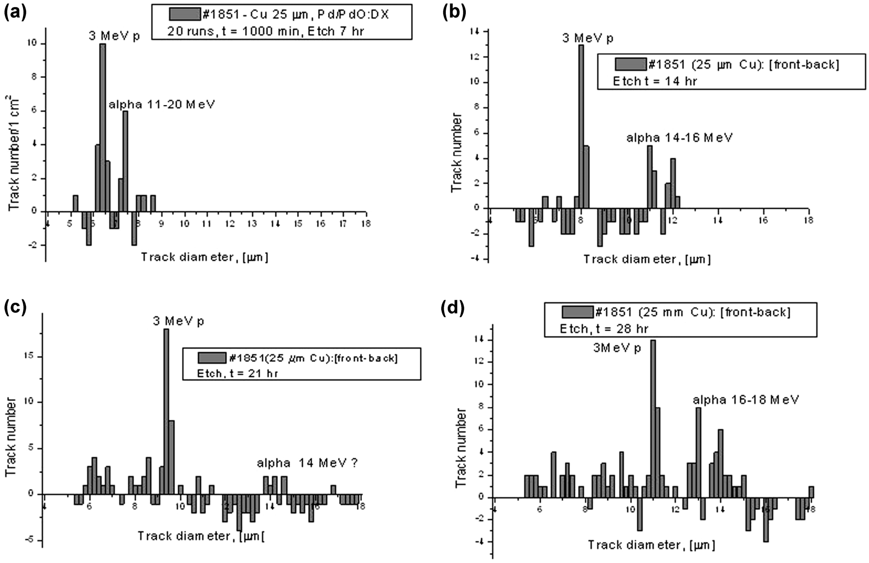

Figure 10 (a-d). Differential spectra (with subtracting of the rear face background results) of #1851 (detector #2) CR-39 detector (exposed in front of the free surface of the 6 Pd/PdO:Dx samples during their e-beam irradiation during 1,000 min) after its etching during 7 (a), 14(b), 21(c) and 28(d) hours. The shift of the peaks in a larger track diameter side with increase in etching time is very clear.

Downloaded by CORNELL UNIV on June 28, 2012 | http://pubs.acs.org
Publication Date (Web): December 20, 2009 | doi: 10.1021/bk-2009-1029.ch006

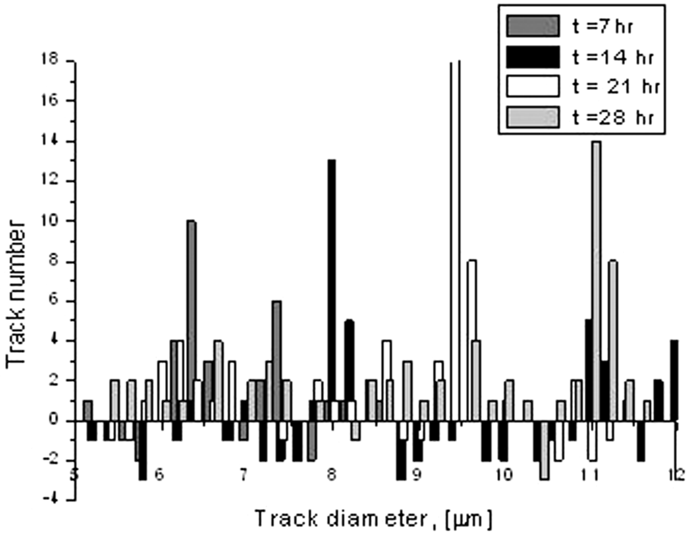

Figure 11. Sift in main peak I track diameter (1.4 MeV protons) following by sequential etching of #1816 detector covered with 25 μm thick Cu foil.

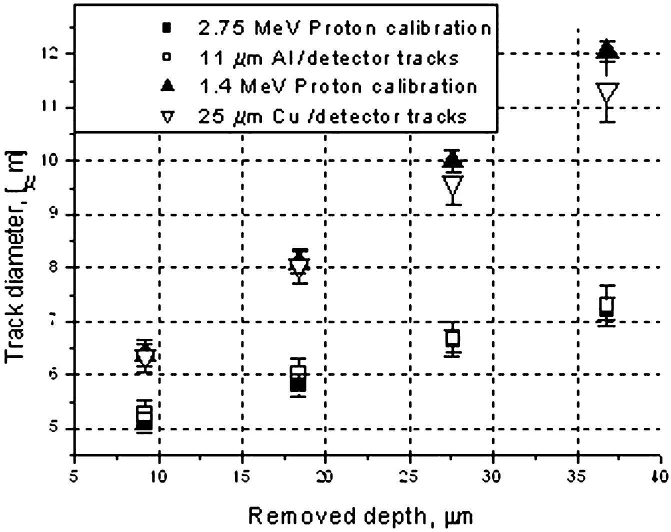

Figure 12. Track diameter vs. removed depth (d(h)) dependences for proton tracks detected during sequential etching of detectors 1 and 2, respectively. The black squares and triangles represent the fit of experimental tracks from detectors 1 and 2 (empty squares and triangles, respectively) with d(h) functions obtained using normal incidence accelerator CR-39 bombardment at proton energies 2.75 (consistent with 3 MeV proton after its passage through 11 μm thick Al foil) and 1.4 (consistent with 3 MeV proton after its passage through the 25 μm thick Cu foil) MeV, respectively.

Downloaded by CORNELL UNIV on June 28, 2012 | http://pubs.acs.org
Publication Date (Web): December 20, 2009 | doi: 10.1021/bk-2009-1029.ch006

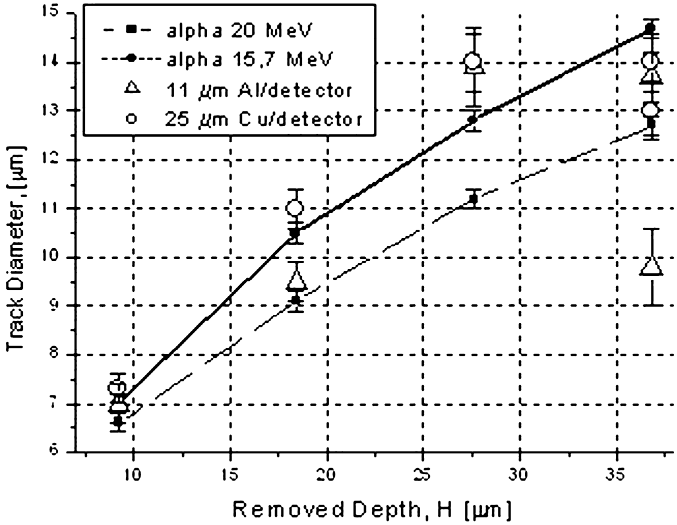

Figure 13. Track diameter vs. removed depth (d(h)) dependences for alpha tracks detected during sequential etching of detectors 1 and 2, respectively. The dashed and dotted lines represent fits of experimental tracks from detectors 1 and 2 with d(h) functions obtained using normal incidence accelerator CR-39 bombardment at alpha energies 20 and 15.7 (corresponding to 20 MeV alpha after its passage through the 25 μm thick Cu foil) MeV, respectively.

Because of lower statistics, the sequential etching data (shown in Figs. 11 and 13) obtained for the second main peak (located at d ~ 7.0-7.6 μm track diameter at etch time t = 7 hr) and their fit with normal incidence accelerator alpha beams of 20 and 15.7 MeV energies (Fig.16) are less impressive than those shown in Fig. 15 for 3.0 MeV protons. The lower statistics of energetic alphas is reflected in the large track spread at the larger diameters during CR-39 etching in depth leading to the spread of the second peak. The last circumstance results mainly because the emitted alphas are not a monoenergetic beam, in contrast to DD- protons. The spread is larger at the larger track diameter, making it impossible to identify alphas with energy located near 11 MeV.

Despite larger statistical errors (especially for detector 1 covered with 11 μm thick Al foil) than those for 3 MeV protons, this data eventually confirms the emission of high-energy alphas. Indeed, the track diameter vs. removed depth function d(h) for detector 2 is satisfactorily fitted with the d(h) function of 15.7 MeV alphas (Fig. 16 dashed line). At the same time, expecting that alpha particles with mean incident energy of ~ 20 MeV will pass through the 25 μm thick Cu foil, the energy losses in this foil would be of 4.3 MeV, such that the energy of the alpha particle decreases to 15.7 MeV. Note that the detector 1 data presented in Fig. 16 also could be fitted with a 1.2 MeV proton curve. However, in this case, one would expect that the Pd/PdO:Dx sample would emit 1.6 MeV protons that are detected by the CR-39 alongside the 3.0 MeV particles. This, however, is not the case, because the 25 μm thick Cu foil covering detector 2 will stop all protons with the energies E < 2.4 MeV. This is why the tracks obtained in the second main peak should be considered only as high-energy alpha particles in the range of 11-20 MeV and cannot be ascribed to 1-2 MeV protons.

Thus, the sequential etching data shows that, during e-beam irradiation of the Pd/PdO:D_x heterostructure, the 3 MeV protons and high-energy alphas (in the range, roughly, of 11-20 MeV) have been really emitted.

Charged Particle Emission Rate in the Pd/PdO:D_x

The results for the e-beam irradiated face of the Pd/PdO:Dx heterostructure sample, obtained by averaging 11 µm Al and 25 µm Cu data, taken for detectors 1 and 2, respectively, in 36 runs (t = 1,800 min) follow:

- **a.** For 3 MeV protons $\langle \Delta N_p \rangle = (3.71 \pm 0.48) \times 10^{-4}$ cps/cm^2 of CR-39 or taking into account total efficiency of the detection ($\varepsilon = 0.026$) $N_p = (1.39 \pm 0.18) \times 10^{-2}$ p/s-cm^2 of Pd/PdO:Dx sample. (The significance level above the background is $L = 7.7\ \sigma$.)
- **b.** For alpha particles with energy in the range of 11-20 MeV. $\langle \Delta N_\alpha \rangle = (1.87 \pm 0.32) \times 10^{-4}$ cps/cm^2 of CR-39 or taking into account total efficiency of the detection ($\varepsilon = 0.026$), $N_\alpha = (0.71 \pm 0.12) \times 10^{-2}$ α/s-cm^2 of Pd/PdO:Dx sample. (The significance level is $L = 6.0\ \sigma$.)

The yield of DD-reaction in the Pd/PdO:Dx target under e-beam bombardment, taken only for movable deuterons (the desorbed flux $J_d = 3x10^{15}$ D/s-cm2), is found to be $\lambda_{DD} \sim 3.3x10^{-18}$ p/D.

For the detector in position 3 (Fig. 2) placed under the rear (non-irradiated by e-beam) side of the Pd/PdO:Dx sample, the average result in 36 runs (t = 1,800 min) during e-beam irradiation of the front side of the Pd/PdO:Dx, the results follow:

- **a.** For 3 MeV protons $\langle \Delta N_p \rangle = (1.81 \pm 0.40)x\ 10^{-4}$ cps/cm^2 of CR-39 or taking into account total efficiency of the track detection for 1.9 MeV protons after permeation of 3 MeV p through 33 µm Al ($\varepsilon = 0.11$), $N_p = (1.68 \pm 0{,}37) \times 10^{-3}$ p/s-cm^2 of the Pd/PdO:Dx sample. (The significance level is $L = 4.5\ \sigma$.)
- **b.** For alpha particles with the energy in the range of 11-19 MeV $\langle \Delta N_\alpha \rangle = (2{,}49 \pm 0.45) \times 10^{-4}$ cps/cm^2 of CR-39 or taking into account total efficiency of the track detection for high energy (> 11 MeV) alphas ($\varepsilon = 0.17$) $N_\alpha = (1.46 \pm 0.27) \times 10^{-3}$ α/s-cm^2 of the Pd/PdO:Dx sample. (The significance level is $L = 5.5\ \sigma$.)

The count rate calculation shows that the front side of the sample irradiated by the electron beam provides an excess (5-8 times) in the absolute intensity of the proton and alpha emissions compared to that detected at the rear side of the sample, which has not been irradiated directly. At the same time, both the front and the rear sides of the Pd/PdO:Dx sample under e-beam stimulation show a large excess in the proton and alpha emission bands, compared to the same Pd/PdO:D_x target that has been run in a vacuum without excitation of their D-subsystem (that is, in the spontaneous D-desorption mode). Observation of

Downloaded by CORNELL UNIV on June 28, 2012 | http://pubs.acs.org
Publication Date (Web): December 20, 2009 | doi: 10.1021/bk-2009-1029.ch006

nuclear emissions from the rear side of the target under e-beam irradiation indicates some D-desorption enhancement from the rear side caused by e-beam interaction with the front side of Pd/PdO:D_x sample.

Experimental Results: TiD_x

Experiments with the **TiD_x** samples have been carried out similarly to that performed with Pd/PdO:Dx. In contrast to the Pd/PdO heterostructure, ready-to-use Ti deuteride samples were put in a vacuum chamber. One surface of the samples was scanned by an electron beam (E= 30 keV, J = 0.6 µA/cm2). Then, in another run, the sample was turned over, and the other surface of the TiDx was scanned. Twenty-six runs, with a duration of 50 minutes each, were made. (The total foreground time is 1,300 minutes, including 300 minutes (six runs) in the first series and 1,000 minutes (20 runs) in a second series). Three CR-39 detectors (with 11 and 33 µm Al filters and with a 26 µm Cu filter), according to the diagram depicted in Fig. 2, were employed in each series of experiments with the TiD_x.

Downloaded by CORNELL UNIV on June 28, 2012 | http://pubs.acs.org
Publication Date (Web): December 20, 2009 | doi: 10.1021/bk-2009-1029.ch006

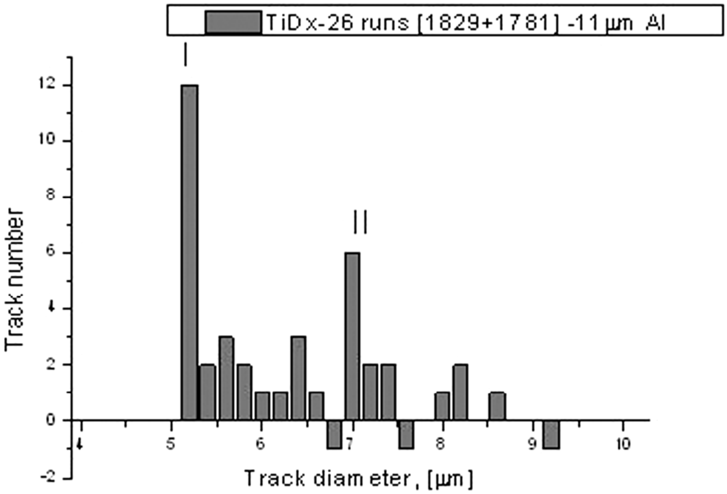

Figure 14. Summary differential spectrum of the 11 µm Al covered CR-39 detector (position 1 in Figure 2) obtained in both first (6 runs) and second (20 runs) series of experiments (c). Total time of 1+2 series is t = 1,300 min, using 10 similar TiDx samples. As seen from the data (c), both statistically significant 3 MeV proton (5.2-5.4 µm track diameter) and 11-19 MeV alphas (7.0-7.6 µm track diameter) bands appear from the electron beam excited face of the TiDx sample.

Downloaded by CORNELL UNIV on June 28, 2012 | http://pubs.acs.org
Publication Date (Web): December 20, 2009 | doi: 10.1021/bk-2009-1029.ch006

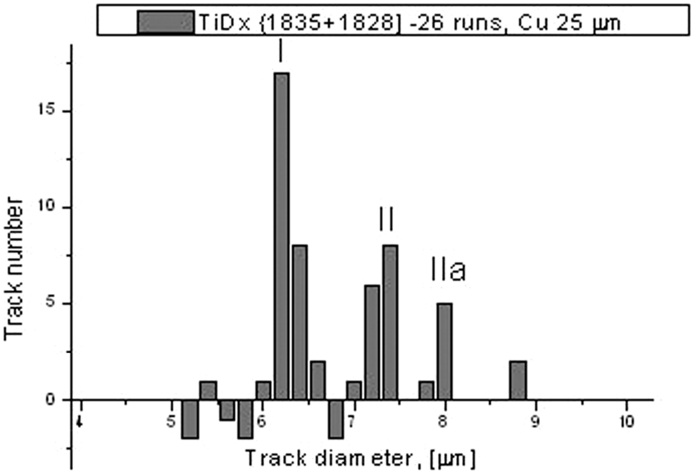

Figure 15. Summary differential spectrum of the 26 µm Cu covered CR-39 detector (position 2 in Figure 2) obtained in total 26 runs with the TiDx samples. The statistically significant bands of 1.4 MeV protons (track diameter in the range of 6.0-6.6 µm, consistent with the 3 MeV proton losses in 26 µm Cu foil, peak I) and 14 MeV alphas (track diameter near 7.4 µm, consistent with ~ 17-20 MeV alpha losses in 26 µm Cu foil,peak II) appear in the spectrum. Peak IIa is consistent with incident ~ 11 MeV alpha emission.

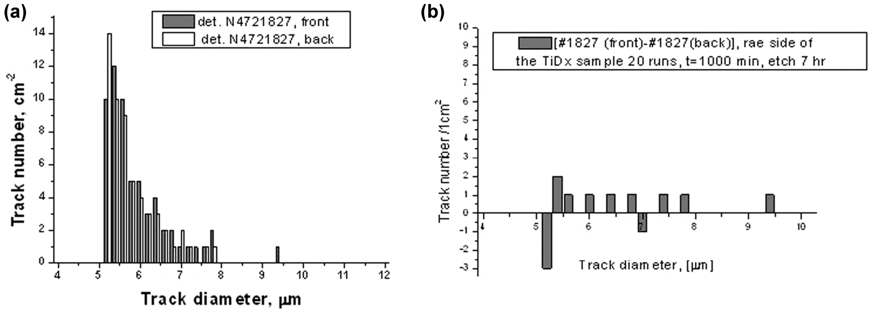

Figure 16 a,b. Summary foreground and the background spectra (a) and the differential spectrum (b) of the 33 µm Al covered CR-39 detector placed below the rear (non-irradiated by e-beam) side of the TiDx sample (the detector with position #3 in Figure 2) obtained in the second series (20 runs) of experiments with the 5 TiDx samples. No statistically significant results have been found over all differential spectrum (b) of the rear side of the TiDx sample.

The results on nuclear particle detection for CR-39 covered with Al and Cu filters are shown in Figs. 14-16. As seen from Figs. 14 and 15, representing differential spectra of the charged particles emitted from the free surface of the TiDx sample (facing the front side of detectors 1 and 2 in Fig. 2), the track diameter distributions obtained at 11μm Al covered detector 1 and 25 μm Cu covered detector 2 are similar to the spectra of the Pd/PdO:Dx and show the two-peak system. The position of both peaks obtained with detectors 1 and 2 during TiDx exposure under the electron beam are the same as obtained for Pd/PdO:Dx samples under electron bombardment (Figs. 5 and 6). Because of those similarities, we ascribe peaks I and II generated by TiDx samples under electron bombardment to 3 MeV(DD) proton and energetic alpha emissions, respectively. Notice that the rear side of the sample (attached to detector 3, Fig. 2), which is opposite the electron-irradiated free surface of TiDx, does not demonstrate nuclear tracks above the background (Fig. 16 a, b). This is caused by absence of the deuterium desorption from the TiDx at room temperature without e-beam stimulation.

The results for the e-beam irradiated face of the TiDx sample, obtained by averaging 11 μm Al and 25 μm Cu data, taken for detectors 1 and 2, respectively, in 26 runs (t = 1,300 min) follow:

a. For 3 MeV protons $<\Delta N_p> = (2.87 \pm 0.61) \times 10^{-4}$ cps/cm^2 of CR-39 or taking into account total efficiency of the detector ($\varepsilon = 0.026$) $N_p = (1.10 \pm 0.23) \times 10^{-2}$ p/s-cm^2 of TiDx sample. (The significance level of the result above the background is $L = 4.74\ \sigma$.)

b. For alpha particles with the energy in the range of 11-19 MeV $<\Delta N_\alpha> = (1.60 \pm 0.38) \times 10^{-4}$ cps/cm^2 of CR-39 or taking into account the total efficiency of the detector ($\varepsilon = 0.026$), $N_\alpha = (0.61 \pm 0.15) \times 10^{-2}$ α/s-cm^2 of the TiDx sample. (The significance level is $L = 4.3\ \sigma$.)

In contrast to the Pd/PdOD$_x$ sample (with high D-diffusivity), the faces of the TiDx sample that were not irradiated by the e-beam show no signatures of nuclear emission. The yield of DD-reaction in the TiDx target under e-beam bombardment, taken only for mobile deuterons (the desorbed flux $J_d = 10^{14}$ D/s-cm^2), is found to be $\lambda_{DD} \sim 1.1\text{x}10^{-16}$ p/D.

Thus, the e-beam excitation of the TiDx samples results in generation of a DD-reaction (producing 3 MeV protons) as well as high-energy alpha particles. The intensity of the nuclear emissions is quite comparable to that of the Pd/PdO:Dx samples but provides lower statistical significance. In contrast to the Pd/PdO:Dx system, the TiDx samples show no emissions from the face opposite the e-beam irradiated side. This is evidence that no nuclear emissions occur without D-desorption from the rear face of the TiDx samples, and the Pd/PdO:Dx heterostructure provides weak spontaneous D-desorption from its rear side. Such a desorption could be partially stimulated by e-beam interaction with the front (irradiated) face of the Pd/PdO:D$_x$ sample.

Downloaded by CORNELL UNIV on June 28, 2012 | http://pubs.acs.org
Publication Date (Web): December 20, 2009 | doi: 10.1021/bk-2009-1029.ch006

Discussion

Thus, we have shown experimentally that charged particle emission in Pd/PdO:D_x and TiD_x in a vacuum can be stimulated by a relatively weak (J< 1 μA/cm2, E=30 keV) electron beam. We found that e-beam excitation of the D-subsystem in those deuterides with a high affinity to hydrogen generates a DD-reaction (3 MeV proton emission) as well as energetic alpha particles with energy in the range of 11-19 MeV. The yield of DD-reaction for Pd/PdO:Dx and TiDx targets taken per movable (desorbed) deuteron is found to be 10^{-18}-10^{-16} per deuteron pair. This figure is about five to seven orders of magnitude above the so-called Jones level.

The alpha particle emission effect has been observed previously in experiments on D-desorption from the Pd/PdO:Dx *(7, 8, 9)* system and high-current deuterium glow discharge bombardment of the Ti cathode *(5)*. The origin of energetic alphas remains puzzling (though some ideas discussed consider a multi-body (3D) fusion origin of these energetic alpha particles *(8)*), and further experiments are required in order to shed light on the mechanism of high-energy alpha emission in deuterated solids. In this work, we did not consider the alpha emission mechanism. Instead, we are going to discuss possible factors of the DD-reaction enhancement, providing measurable 3 MeV proton yield.

In this connection, below we show that extrapolation of both the DD-reaction cross section and the enhancement factor to very low deuteron energy (E_d ~ 3.0 eV) with a reasonable screening potential U_e = 750 eV allows a satisfactory accounting of the detected DD-reaction yield in the Pd/PdO:Dx target under e-beam excitation. This result strongly supports the theoretical prediction *(1, 2)* of electron excitation of hydrogen subsystem in Pd deuteride.

In order to estimate the DD-reaction rate in the Pd/PdO:Dx target under electron bombardment, we use a simple model of the process, taking into account that D-desorption stimulated by e-beam results in deuterium flux moving toward the Pd/PdO:Dx surface. Thus, the moving deuteron flux can be considered as a low-energy projectile or deuteron beam, and the deuterated surface of the Pd/PdO sample as a deuterated target. The deuteron (D^+) current, estimated through D-desorption rate (see Experimental part) would be J_d = 0.5 mA/cm^2, and the mean concentration of deuterons at the surface corresponds to a mean D/Pd ratio during e-beam bombardment (<x> ~ 0.15 or $N_d = 1.1\text{x}10^{22}$ cm^{-3}).

In order to estimate the DD-reaction rate, we use a so-called thick target yield expression, normally employed in accelerator physics *(3, 4, 5)*, recently developed and modified for lower energy applications *(10):*

$$Y_{DD} = J_d N_{eff}(T) \times \int_0^{E_d} f(E)\sigma_{DD}(E)(dx/dE)dE \qquad (1),$$

where J_d – is the deuteron current on target, i.e. in our case, the desorbed deuteron flux from the surface of the Pd/PdO:$D_{<x>}$; $N_{eff}(T) = N_0\exp(-\varepsilon_d \Delta T/k_B T T_0)$ is the effective deuteron concentration in the target (here N_0 – is

Downloaded by CORNELL UNIV on June 28, 2012 | http://pubs.acs.org
Publication Date (Web): December 20, 2009 | doi: 10.1021/bk-2009-1029.ch006

Downloaded by CORNELL UNIV on June 28, 2012 | http://pubs.acs.org
Publication Date (Web): December 20, 2009 | doi: 10.1021/bk-2009-1029.ch006

the bound deuteron concentration in the target, i.e. at the Pd/PdO:Dx surface, corresponding to the <x> = D/Pd ~ 0.15±0.05 at T_0 = 290 K, T – is the real target temperature, $\Delta T = T - T_0$, ε_d - is the activation energy of deuteron escape from the target, here ε_d = 0.2 eV= the activation energy of D-diffusion in Pd); $\sigma_{DD}(E)$ – is the bare cross section of DD-reaction (for example, without any enhancement) and dE/dx – is the deuteron stopping power in the target (here in the Pd); the f(E) - is the enhancement factor, derived from the following equation:

$$f(E) = Y_{exp}(E)/Y_b(E) = \exp[\pi\eta(E)U_e/E] \qquad (2),$$

where $Y_{exp}(E)$ – is the total experimental DD-reaction yield at deuteron energy E, taken in the center-of-mass system, $Y_b(E)$ – is the yield deduced with the standard cross-section approximation of Bosch and Halle *(11)* or bare yield (without taking into account the electron screening in the target); $2\pi\eta(E) = 31.29\, Z^2(\mu/E)^{1/2}$ – is the Sommerfeld parameter (Z – is the charge of the particle, μ- is the reduced mass) and U_e – is the electron screening potential of deuterons in the target. Based on analysis of screening potentials for 60 elements of the periodic table *(8)*, it was shown that U_e depends on the diffusivity of deuterons in the target and could be determined by a semi-empirical formula *(10)*:

$$U_e = (T/T_0)^{-1/2}[a \ln(y) + b] \qquad (3),$$

where a = 145.3 and b=71.2 – are the numerical constants and $y = k \times y_0(J_d/J_0)$, (here $k = \exp(-\varepsilon_d \Delta T/k_B T T_0)$ y_0 = Pd/D at T_0 = 290 K and J_0 = 0.03 mA/cm^2). Substitution of J_d = 0.5 mA/cm^2, T=290 K and <Pd/D> = 6.7 in eq. (3) gives U_e = 750±50 eV. Notice that this screening value falls roughly into the interval bounded by Kasagi's (600 eV) [3,4] and Raiola's (800 eV) [12-14] estimates of U_e deduced from the 2.5-10 keV deuteron bombardment results of the Pd/PdO and the Pd targets, respectively.

In order to estimate the DD-reaction yield in the Pd/PDO:DX under e-bombardment, we extrapolate directly to lower energies both the integral I(E) = $\int_0^{E_d} \sigma_{DD}(E)(dx/dE)dE$, (containing linear combination of the bare cross section and stopping power), and the enhancement factor, determined by eq (2) with the U_e ~ 750 eV (Fig. 17).

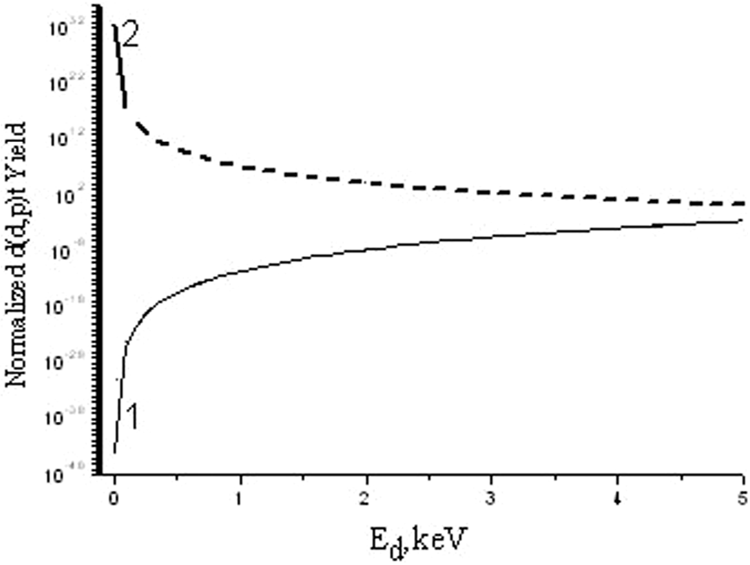

Figure 17. Extrapolation of the bare DD-reaction yield (assuming no enhancement) in Pd/PdO target normalized to that at Ed = 10 keV – (curve 1) and of the enhancement factor (see eq. (2) at screening potential value Ue = 750 eV) - (curve 2), respectively, to very low deuteron energy (Ed ® 1.0 eV).

These extrapolations, as well as substitution of the deuteron flux and effective D-concentration values in eq. (1), allow us to conclude that the DD-reaction rate of ~ 0.01 p/s-cm^2 in 4π steradian could be reached in the Pd/PdO:Dx target (with the U_e ~ 750 eV) only if the mean kinetic energy of the desorbing deuterons would be of the order of E_d ~ 3-4 eV (that is, two orders of magnitude above the kT).

Thus, straight extrapolation of the DD-cross-section and enhancement factor to very low deuteron energy necessitates a hot deuteron flux in the eV range desorbed from the Pd/PdODx target in order to provide an experimentally measured DD-yield in a vacuum under electron-beam irradiation. This result strongly supports the theoretical prediction *(1, 2)* of electron excitation of hydrogen subsystem in Pd deuteride. Indeed, the d(d,p)t reaction rate with the deduced 3-4 eV deuteron flux is strong evidence of a strong electric field (F ~ 10^8 V/cm) generation within a distance comparable to the lattice parameter (a_0 = 0.39 nm) caused by plasmon formation at the Pd/PdO:Dx surface during e-beam interaction with the D-subsystem of the deuteride.

In contrast to Pd/PdO:Dx data, the results obtained for the TiDx target under similar electron irradiation cannot be easy explained by eV deuteron kinetic energies, taking into account only the low-energy extrapolation of the linear combination of the DD-reaction cross section and the enhancement factor. The problem is that, because of very low D- diffusivity in Ti, the screening potential at the surface of TiDx would also be quite low. Indeed, using eq. (3) with J_d = 0.015 mA/cm^2 and y_0 ~ 2.0 (assuming that at the surface the D-

Downloaded by CORNELL UNIV on June 28, 2012 | http://pubs.acs.org
Publication Date (Web): December 20, 2009 | doi: 10.1021/bk-2009-1029.ch006

concentration is x = D//Ti ~ 0.5 during e-bombardment), one can obtain U_e ~ 70 eV (close to Kasagi's value *(4)*). At this small screening potential, in order to produce DD-reaction rate of the order of ~ 0.01 p/s-cm^2 , the kinetic energy of deuteron flux (in a laboratory system) has to be rather higher, exceeding the value E_d = 1 keV. The situation could be improved, assuming that the main fraction of desorbed deuterium in TiD_x under e-beam irradiation would escape directly from the surface layer (of 1-2 lattice parameter thick), but not from the total 2-4 μm thick area of D-localization. (This means that the energy transferred the by electron beam would be effectively redistributed to the deuterons located over the top of the TiD_x target - sort of inverse population.) If, in this case, at the same D-flux J_d = 0.015 mA/cm^2, the mean residual deuterium concentration at the surface would be x = D/Ti < 0.1, then at E_d ~ 5-10 eV and the screening potential $U_e \geq 600$, the deuteron yield, according to eq. (1), becomes similar to that in Pd/PdO:Dx derived above. It is also possible to speculate that a thin TiO_2 strong dielectric layer (in contrast to semi-metallic PdO) always existing on top of the TiDx target can be negatively charged under the electron bombardment. This macroscopic electric field would accelerate D+ ions passing through the surface, thus increasing their kinetic energy from several to hundreds eV. Such a process could certainly increase the yield of a DD-reaction in the TiDx target. In order to make clear the mechanism of a high DD-reaction yield in the TiDx target under electron bombardment, further experimental and theoretical studies are required.

Conclusions

- Taking into consideration the totality of our experimental data, including vacuum experiments with and without e-beam irradiation, we conclude that electron beam (J ~ 100-300 nA, E = 30 keV) stimulation of the Pd and Ti based deuteride targets (cathodes) surface can enhance the intensity of the emissions of nuclear charged particles.
- Both products of DD-reaction (3 MeV protons) and high-energy alphas (11-20 MeV) are clearly distinguished in the e-beam stimulation experiment with the Pd/PdO:D_x and TiD_x targets.
- Signatures of 3 MeV and energetic alphas appear simultaneously at the surface of all (two or three) independent detectors used in the same experiment and covered by metallic foil filters with different stopping ranges/powers. To increase the accuracy of measurements, the rear-detector-side background results have been subtracted from the foreground data obtained at the CR-39 side facing the sample's surface.
- Sequential etching of detectors 1 and 2 during 7, 14, 21 and 28 hours show an appropriate track diameter shift (increase), in accordance with the calibration curves obtained by CR-39 proton and alpha accelerator bombardment. This powerful technique allows us to identify unambiguously the emission of 3 MeV protons from DD-reaction as well as indicate the presence of energetic alpha particles with energies in the range 11-20 MeV.
- Total statistics obtained in experiments with the Pd/PdO:Dx heterostructure under e-beam irradiation show 3MeV/DD proton emission intensity in 4 π ster.:

Downloaded by CORNELL UNIV on June 28, 2012 | http://pubs.acs.org
Publication Date (Web): December 20, 2009 | doi: 10.1021/bk-2009-1029.ch006

N_p = (1.39 ± 0.18) × 10^{-2} p/s-cm^2 of the Pd/PdO:Dx sample, with the significance level above the background L = 7.7 σ. The intensity of energetic alphas is found to be: N_α = (0.71 ± 0.12) × 10^{-2} α/s-cm^2 of Pd/PdO:Dx sample (the significance level is L = 6.0 σ). The yield of DD-reaction in the Pd/PdO:Dx target under e-beam bombardment, taken only for movable deuterons (the desorbed flux $J_d = 3 \times 10^{15}$ D/s-cm^2) is found to be $\lambda_{DD} \sim 3.3x10^{-18}$ p/D.

- Total statistics obtained in experiments with the TiD_x foils under e-beam irradiation show 3MeV/DD proton emission intensity in 4 π ster. : N_p = (1.10 ± 0.23) × 10^{-2} p/s-cm^2 of the TiDx sample. (The significance level above the background is L = 4.74 σ.) And alpha intensity_N_α = (0.61 ± 0.15) × 10^{-2} α/s-cm^2 of the TiD_x sample. (The significance level is L = 4.3 σ.)
- The yield of the DD-reaction in the TiDx target under e-beam bombardment, taken only for movable deuterons (the desorbed flux $J_d = 10^{14}$ D/s-cm^2), is found to be $\lambda_{DD} \sim 1.1x10^{-16}$ p/D.
- No signatures of nuclear emissions have been found in the case of Pd/PdO:D_x and TiD_x samples exposed in a vacuum at T=290K in the absence of e-beam stimulation.
- The rear side of the Pd/PdO:Dx sample (opposite the e-beam irradiated side) shows N_p = (1.68 ± 0,37) × 10^{-3} p/s-cm^2 of the Pd/PdO:Dx sample. (The significance level is L = 4.5 σ.) And N_α = (1.46 ± 0.27) × 10^{-3} α/s-cm^2 of the Pd/PdO:Dx sample. (The significance level is L = 5.5 σ.) These values are five to eight times less than the charged particle emissions' intensities from the e-beam bombarded side.
- Data analysis has been performed for the Pd/PdO:Dx target. Extrapolation of both the DD-reaction cross section and the enhancement factor to very low deuteron energy ($E_d \sim 1.0$ eV) with a reasonable screening potential $U_e = 750$ eV allows a satisfactory accounting for the detected DD-reaction yield in the Pd/PdO:Dx target, assuming hot (E_d ~3-4 eV) deuteron generation under e-beam excitation. This result strongly supports the theoretical prediction *(1, 2)* for electron excitation of the hydrogen subsystem in the Pd deuteride.

Downloaded by CORNELL UNIV on June 28, 2012 | http://pubs.acs.org
Publication Date (Web): December 20, 2009 | doi: 10.1021/bk-2009-1029.ch006

References

1. Tyurin, Y.; Chernov, I. Non-equilibrium release of atomic hydrogen from metals under irradiation. *Int. J. Hydrogen Energy* **2002,** *27*, 829.
2. Silikin, V.; Chernov I. et al. Influence of hydrogen absorption on low-energy electronic collective excitations in palladium. *Phys. Rev. B*, **2007,** *76*, 245105.
3. Yuki, H.; Kasagi, J.; Lipson, A. G. et al. Anomalous enhancement of *DD* reaction in Pd and Au/Pd/PdO heterostructure targets under low-energy deuteron bombardment. *J. Exp. Theor. Phys. Lett*, **1998,** *68(11)*, 785.
4. Kasagi, J.; Yuki, H.; Lipson, A. G. et al. Strongly Enhanced DD Fusion Reaction in Metals Observed for keV D^+ Bombardment. *J. Phys. Soc. Jpn.*, **2002,** *71(12)*, 2881.
5. Lipson, A. G.; Roussetski, A. S.; Karabut, A. B; Miley, G. H. Strong Enhancement of DD-reaction and X-ray Generation in High Current Pulsed

Glow Discharge in Deuterium with the Ti Cathode. *J. Exp. Theor. Phys.*, **2005,** *100,* 1175.

6. Lipson, A. G.; Roussetski, A. S.; Saunin, E. I. Analysis of #2 W. Williams's detector after SPAWAR/Galileo type electrolysis experiment. *Eighth International Workshop on Anomalies in Hydrogen/Deuterium Loaded Metals*, 13-18 October 2007, Catania, Italy.
7. Lipson, A. G.; Roussetski, A. S. et al. Observation of long-range alpha-particles during deuterium/hydrogen desorption from Au/Pd/PdO:D(H) heterostructure. *Bulletin of the Lebedev Physical Institute (Russian Academy of Sciences)* **2001,** *10*, p 22-29.
8. Lipson, A. G.; Miley, G. H.; Roussetski, A.S. Energetic alpha and proton emissions on the electrolysis of thin-Pd films. *Trans. Amer. Nuclear. Soc.*. **2003,** *88*, 638.
9. Lipson, A. G. et al. Reproducible Nuclear Emissions and X-ray Generation From Pd/PdO:Dx Heterostructure During Exothermic Deuterium Desorption. In *Condensed Matter Nuclear Science: Proceedings of the 12th International Conference on Cold Fusion, Yokohama, Japan, 2005*, Takahashi, K.; Ota, K.; Iramura, Y., Eds.; World Scientific Publishing Co., 2006; p 293.
10. Lipson, A. G. et al. Edge effects caused by enhancement of DD/DT fusion reactions in metals at low energy of projectile particles in an ITER-type fusion reactor. *High Energy Chemistry*, **2008,** *42(4)*, 361.
11. Bosch, H. S.; Halle, G. M. Improved formulas for fusion cross-section and thermal reactivities. *Nuclear Fusion* **1992,** *32*, 611.
12. Raiola, F.; Migliardi, P.; Gang, L. et al. Electron screening in d(d,t)p for deuterated metals and the periodic table. *Phys. Lett B* **2002,** *547*, 193.
13. Raiola, F.; Gang, L.; Bonomo, C. et al. Enhanced electron screening in d(d,t)p for deuterated metals. *Europhys. J.A* **2004,** *19*, 283.
14. Raiola, F. et al. Enhanced d(d,p)t fusion reaction in metals. *Europhys. J.A* **2006,** *27*, 79.

Downloaded by CORNELL UNIV on June 28, 2012 | http://pubs.acs.org
Publication Date (Web): December 20, 2009 | doi: 10.1021/bk-2009-1029.ch006

Downloaded by CORNELL UNIV on June 28, 2012 | http://pubs.acs.org
Publication Date (Web): December 20, 2009 | doi: 10.1021/bk-2009-1029.ch007

Chapter 7

Characterization of Energetic Particles Emitted During Pd/D Co-Deposition for Use in a Radioisotope Thermoelectric Generator (RTG)

Pamela A. Mosier-Boss[1], Frank E. Gordon[1], and Lawrence P.G. Forsley[2]

[1]SPAWAR Systems Center Pacific, Code 71730, San Diego, CA 92152
[2]JWK International Corp., Annandale, VA 22003

CR-39 is a solid-state nuclear-track etch detector. Using these detectors in Pd/D co-deposition experiments, researchers have detected energetic particles and neutrons. The source of these particles and neutrons is the cathode. In this communication, spacer experiments and track modeling are done to characterize the energetic particles emitted. The potential use of these energetic particles to power a RTG is discussed.

Introduction

A radioisotope thermoelectric generator (RTG) is a simple electrical generator which obtains its power from radioactive decay by the Seebeck effect using an array of thermocouples. Figure 1 shows a schematic of an RTG that has been used on the Cassini probe. The main component of the RTG is a container that holds the radioactive material (fuel). An array of thermocouples is placed in the walls of the container. The outer end of each thermocouple is connected to a heat sink. As the fuel undergoes radioactive decay, heat is produced and flows through the thermocouples to the heat sink, generating electricity in the process.

In Low-Energy Nuclear Reactions and New Energy Technologies Sourcebook Volume 2; Marwan, J., et al.;
ACS Symposium Series; American Chemical Society: Washington, DC, 2010.

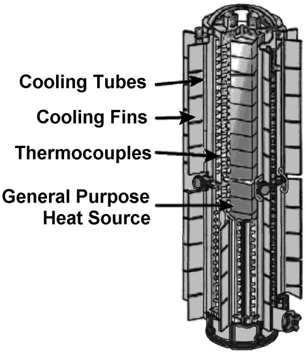

Figure 1. Schematic of an RTG used in the Cassini probe (1).

Downloaded by CORNELL UNIV on June 28, 2012 | http://pubs.acs.org
Publication Date (Web): December 20, 2009 | doi: 10.1021/bk-2009-1029.ch007

In order to be used to power an RTG, the fuel needs to have a half-life long enough to produce energy at a relatively continuous rate for a reasonable time. At the same time, the half-life needs to be short enough so that it decays sufficiently quickly to generate a usable amount of heat. It would be desirable for the fuel to produce high energy radiation that has low penetration. If there are size considerations, the fuel must produce a large amount of energy per mass and volume. Based on these criteria, alpha radiation is the preferred fuel because it is easier to shield against than other forms of radioactive decay. The properties of sources commonly used in RTGs are summarized in Table 1. Radioactive sources typically used in these devices include ^{238}Pu, ^{90}Sr, and ^{210}Po. Although ^{238}Pu has a long half-life, reasonable energy density, and exceptionally low gamma and neutron radiation levels, it is not naturally occurring. ^{238}Pu is usually prepared by the irradiation of ^{237}Np. Consequently, ^{238}Pu is expensive. ^{90}Sr has a shorter half-life and much lower energy density and produces gamma radiation, but it is cheaper. Although ^{210}Po has a high energy density, it has limited use because of its very short half-life and significant gamma ray production.

The Pd/D system is another source of energetic particles that potentially could be used in RTGs. Using CR-39, researchers have detected the emission of particles in experiments using bulk palladium in both gas permeation (*2*) and electrolysis (*3, 4, 5*). Recently, particle emission has been reported using electrodes prepared by the Pd/D co-deposition process (*6, 7*). The Pd/D system has the following advantages over traditional radioactive alpha sources: (i) the rate of energetic particle production can be controlled by manipulating the experimental parameters and (ii) the rate of gamma emissions is low (*7, 8*). However, in order to use the particles generated as the result of Pd/D co-deposition, researchers need to know the particles' energies. To determine the energies of these particles, researchers conducted the following experiments: placement of spacers between the CR-39 detector and cathode, sequential etching of the CR-39 detector, and track modeling. The results of these experiments are discussed in this communication.

Table 1. Properties of sources commonly used in RTGs.

Isotope	Emission Half-Life	W/g (thermal) $/W (thermal)	Comments
^{238}Pu	5.5 MeV α 86.8 y	0.55 3000	Exceptionally low γ and neutron radiation levels, <2.5 mm Pb shielding required
^{242}Cm	6.1 MeV α 0.445 y	120 495	Requires heavy shielding from γ and neutron radiation
^{90}Sr	0.2 MeV β 28 y	0.93 250	γ radiation; lifetime three times shorter and has a lower density than ^{238}Pu; main advantage is that it is inexpensive
^{144}Cs	46 keV β 0.781 y	25 15	Short half-life; weak beta emitter
^{210}Po	5.3 MeV α 0.378 y	141 570	Phenomenal energy density but short half-life and significant γ ray production

Experimental Procedure

Cell assembly and experimental procedures have been described elsewhere (*6, 7*). The CR-39 detectors were not pre-etched before use. Blanks showed that the number of latent tracks from environmental radiation was <85 cm.^{2} Although the response of CR-39 is non-homogeneous, it has no impact on the results obtained during Pd/D co-deposition. In these experiments, Pd is plated out from a $PdCl_2$-LiCl-D_2O solution onto a metal substrate. In one set of experiments, the cathode substrate is in contact with the CR-39 detector (Fukuvi), and both the cathode and CR-39 are immersed in the plating solution. Cathode materials that have been used include Ni screen and Ag/Au/Pt wires. After the Pd is completely plated out onto the cathode, the external electric or magnetic field is applied, and the cell current is ramped up in a step-wise fashion, to a final applied current of -100 mA. A regulated high-voltage source (EMCO model 4330) is used to apply 6000 V DC (and has a ~6% AC component) across two Cu plates taped to the sides of the cell. Two NdFeB magnets are used to apply the magnetic field. The strength of the magnetic field is 2500 Gauss. In the spacer experiments, a 6 μm thick Mylar film is placed between the cathode and the CR-39 detector, Figure 2a. The magnets are used to hold the CR-39 detector in place. In these experiments, a magnetic field is present throughout the plating and electrolysis phases. Placing the cathode close to the detector optimizes the geometry to detect any energetic particles emitted during the Pd/D co-deposition. At the completion of an experiment, the cell is disassembled, and the CR-39 detector is etched in a 6.5 N NaOH solution. Etching conditions are indicated in the figure captions. After etching, the CR-39 detector is subjected to microscopic examination and is scanned using an automated track analysis system. The automated scanning system measures the

Downloaded by CORNELL UNIV on June 28, 2012 | http://pubs.acs.org
Publication Date (Web): December 20, 2009 | doi: 10.1021/bk-2009-1029.ch007

track length and diameter, optical density (average image contrast), and image symmetry.

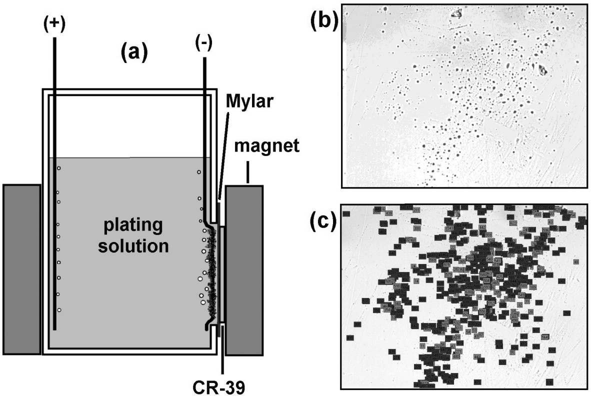

Figure 2. (a) Schematic of the electrochemical cell used in a spacer experiment. (b) Tracks obtained in the CR-39 detector as a result of a spacer experiment using 6 µm Mylar. Magnification is 200X. Detector etched in 6.5 M NaOH at 62 °C for two h. (c) Results of computer analysis. Light rectangles indicate positively identified tracks.

Results and Discussion

Summary of Control Experiments

When a charged particle passes through CR-39, it leaves behind an ionization trail that is more sensitive to chemical etching than the bulk. After chemical etching, conical tracks remain as holes or pits when viewed from the surface (9). The tracks are either elliptical or spherical and are dark. Microscopic examination of the bottom of the track shows a bright spot resulting from the tip of the track cone. When backlit, the tip of the cone acts like a lens and causes the bright spot inside the pit. These features are diagnostic of a nuclear-generated track. These same features are observed for pits in the CR-39 detectors that have been used in a Pd/D co-deposition experiment (*7*).

A series of control experiments showed that the pits in CR-39 obtained as a result of Pd/D co-deposition experiments were not the result of chemical or mechanical damage (*7*). The CR-39 was placed in contact with the cell components. No pits were observed in the CR-39, indicating that the pits are not the result of radioactive contamination of the cell components, i.e. electrodes, polyethylene supports, heat shrink, cell body, and plating solution. No pits were observed in the CR-39 when the $PdCl_2$ was replaced with $CuCl_2$. For both sets of $PdCl_2$ and $CuCl_2$ experiments, the same electrochemical reactions are occurring. At the cathode, a metal is plating out in the presence of D_2. At the anode, O_2 and

Downloaded by CORNELL UNIV on June 28, 2012 | http://pubs.acs.org
Publication Date (Web): December 20, 2009 | doi: 10.1021/bk-2009-1029.ch007

Cl_2 gases are evolved. The only difference is that Pd absorbs D and Cu does not. The $CuCl_2$ experiments indicate that the pits are not the result of chemical reaction of the CR-39 with D_2, O_2, or Cl_2 gases. Nor are they the result of the impingement of D_2 bubbles on the surface of the CR-39, the metal dendrites piercing into the detector or a corona or electrostatic discharge. A significant decrease in pits, at least four orders of magnitude, was observed when D_2O was replaced with H_2O. Because light water does contain some deuterium, the tracks observed in the light-water experiments may be from Pd/D interactions.

The results of sequential etching of the CR-39 detectors provide additional support that the pits observed as a result of Pd/D co-deposition are nuclear in origin. Before running a Pd/D co-deposition experiment, researchers exposed a back corner of the CR-39 detector to an ^{241}Am source. On completion of the experiment, the chip was etched for 9, 12, 16, and 20 h. After each etching, the detector was subjected to microscopic analysis. Images were taken of both the ^{241}Am and Pd/D pits. Both sets of pits got larger and shallower the longer they were etched (*7*). Because the ^{241}Am and Pd/D pits were on the same CR-39 detector, both sets of pits experienced identical etching conditions. The diameters of an ^{241}Am- and a Pd/D-generated pit were measured as a function of etch time. Although the ^{241}Am pit is elliptical and the Pd/D pit is circular in shape, their etch rates can be compared because the track etch rate along the particle trajectory is independent of the angle at which the particle entered the detector (*10*). Figure 3 shows plots of the diameters of the ^{241}Am- and Pd/D-generated pits as a function of etch time. As can be seen, the plots have similar slopes, indicating that the ^{241}Am- and Pd/D-generated pits have identical etching rates. This would be expected if the Pd/D pits were nuclear in origin.

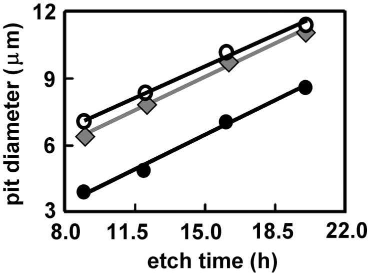

Figure 3. Plots of the major (♦) and minor (●) axis diameters of ^{241}Am- and Pd/D(○-)-generated pits as a function of etch time. The microphotographs are found in the supplementary material of (7). The slopes of the lines are 0.444± 0.028 and 0.434±0.038 for the ^{241}Am minor and major axis, respectively, and 0.404± 0.028 for the Pd/D-generated pit.

Downloaded by CORNELL UNIV on June 28, 2012 | http://pubs.acs.org
Publication Date (Web): December 20, 2009 | doi: 10.1021/bk-2009-1029.ch007

Summary of External Field Experiments

The Pd deposit formed as a result of Pd/D co-deposition has a uniform cauliflower-like morphology comprising aggregates of spherical micro-globules. When researchers subjected the deposit to an external electric field, the formation of branches, dendritic growths, craters, rods, wires, and folded thin films was observed (*11*). In contrast, star-like features are observed when the Pd deposit is subjected to an external magnetic field (*7*).

Experiments were conducted to determine whether the presence of an external magnetic/electric field affected particle generation in the Pd/D co-deposition process (*7*). It was found that the presence of an external field had no impact when Ag, Au, or Pt wires were used as the cathode substrate. When Pd was plated on these substrates, tracks were obtained in both the presence and absence of an external field. This was not true when a Ni screen was used as the cathode substrate. Tracks were observed in the CR-39 detectors when the Ni/Pd/D cathode was subjected to an external magnetic/electric field. In the absence of a field, the impression of the Ni screen was observed on the surface of the detector. This damage is suggestive of X-ray and/or γ-ray emission.

Downloaded by CORNELL UNIV on June 28, 2012 | http://pubs.acs.org
Publication Date (Web): December 20, 2009 | doi: 10.1021/bk-2009-1029.ch007

Results of Spacer Experiments

The primary and secondary fusion reactions that occur in a hot plasma are (*12*):

$$D + D \rightarrow T\ (1.01\ \text{MeV}) + p\ (3.02\ \text{MeV}) \qquad (1)$$
$$D + D \rightarrow n\ (2.45\ \text{MeV}) + {}^{3}\text{He}\ (0.82\ \text{MeV}) \qquad (2)$$
$$D + T\ (\leq 1.01\ \text{MeV}) \rightarrow \alpha\ (6.7\text{-}1.4\ \text{MeV}) + n\ (11.9\text{-}17.2\ \text{MeV}) \qquad (3)$$
$$D + {}^{3}\text{He}\ (\leq 0.82\ \text{MeV}) \rightarrow \alpha\ (6.6\text{-}1.7\ \text{MeV}) + p(12.6\text{-}17.5\ \text{MeV}) \qquad (4)$$

If these reactions occur in the Pd/D lattice, the energetic particles (protons, tritons, alphas, and ^{3}He) formed in the primary and secondary reactions will leave tracks on the front surface of the CR-39 detector that is in contact with the cathode. The size of the pit created by the energetic particle in the CR-39 depends on the particle's size, energy, and charge. In principle, the particles could be differentiated from one another using a calibration curve like the one shown in Figure 4a (*9)*. However, this calibration curve was obtained under controlled conditions, using cyclotron-generated monoenergetic particle beams, and implies that it would be relatively easy to differentiate the energetic particles. In reality, particles emitted from a nuclear source exhibit a range of sizes as shown in Figure 4b. This size distribution is the result of scattering of the particles and is a function of the distance between the source and the detector. The greater the distance between the source and the detector, the greater the energy loss. This results in larger-diameter tracks as well as elliptical tracks.

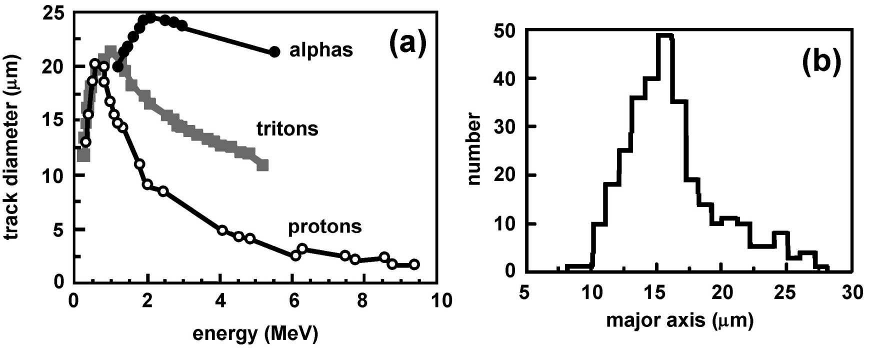

Figure 4. (a) An example of a CR-39 calibration curve for alphas, tritons, and protons (9). (b) Size distribution of tracks obtained for CR-39 exposed to an ^{241}Am alpha aource.

The particles produced during Pd-D co-deposition also exhibit a size distribution. An additional complication in speciation is that the particles have to traverse a layer of water before they reach the CR-39 detector. The presence of water slows the particles, which result in a loss of energy. Linear energy transfer (LET) curves were used to determine the resultant decrease in energy. Figure 5a shows the LET curves, as a function of water thickness, for alphas, ^{3}He, tritons, and protons. Another complication for Pd/D co-deposition is that the thickness of the water layer the particles need to traverse varies. As shown in Figure 5b, the metal deposit formed as a result of Pd/D co-deposition has a cauliflower structure. Consequently, nooks and crannies in the deposit trap pockets of water. Because of the cauliflower structure of the Pd deposit, the thickness of the water film between the CR-39 detector and the Pd deposit varies, which in turn causes an increase in the range of particle sizes.

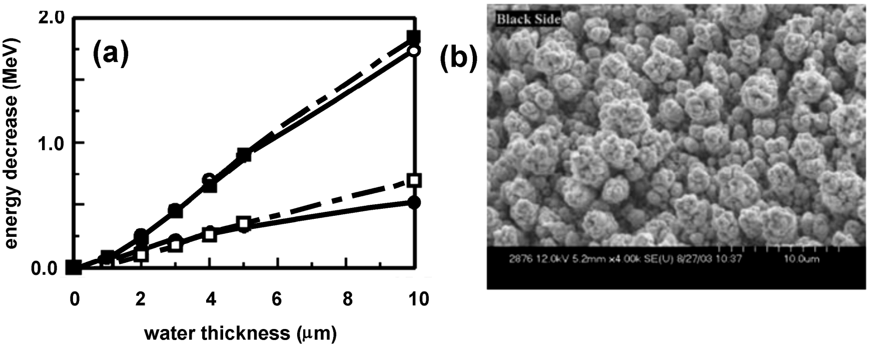

Figure 5. (a) LET curves showing the decrease in energy as a function of thickness of the water film for alphas (■), ^{3}He (○), tritons (□), and protons (●). (b) SEM of the Pd deposit formed as a result of Pd/D co-deposition.

Downloaded by CORNELL UNIV on June 28, 2012 | http://pubs.acs.org
Publication Date (Web): December 20, 2009 | doi: 10.1021/bk-2009-1029.ch007

Downloaded by CORNELL UNIV on June 28, 2012 | http://pubs.acs.org
Publication Date (Web): December 20, 2009 | doi: 10.1021/bk-2009-1029.ch007

Because of these complications, there will be significant overlap between the size distributions of the different energetic particles produced during Pd/D co-deposition. As a result of these complications, a calibration curve like the one shown in Figure 4a cannot be used to identify the energetic particles or to determine their energies. Placing spacer materials between the cathode and the CR-39 detector provides a better means of characterizing the energetic particles. Experiments were conducted in which a 6 μm thick Mylar film was placed between the CR-39 detector and cathode, as shown in Figure 2a. In these experiments, a ~90 percent decrease in the number of tracks is observed. Figure 2b shows tracks observed in the CR-39, and Figure 2c shows the results of the computer analysis of those tracks. Based on the measured properties of a feature, the software of the automated scanning system determines whether those feature properties are consistent with those of an energetic particle. If the optical properties of the feature are consistant, then the software indicates that the feature is an energetic particle. It should be noted that the software ignores overlapping tracks. Consequently, in areas of high track density, the software underestimates the number of tracks.

The software of the automated scanning system can neither identify the energetic particle nor determine the energy of the particles. Fortunately, LET curves can be used to aid in speciation and to determine particle energetics. The LET curves indicate that 6 μm thick Mylar cuts off < 0.45 MeV protons and < 1.45 MeV alphas. However, this is the energy of the particle when it reaches the CR-39 detector – after it has traversed the water layer and the 6 μm Mylar. Knowing the LET curves for water and 6 μm Mylar allows the conclusion that the majority of the particles formed as a result of Pd/D co-deposition are < 0.45-0.97 MeV protons and < 1.45-3.30 MeV alphas.

Results of Track Modeling

The 6 μm thick Mylar spacer experiments indicate that the majority of the particles formed as a result of Pd/D co-deposition have energies on the order of 1 MeV. This energy estimate is supported by computer modeling of the tracks. The ionization trail created by the energetic particle traversing the CR-39 is more sensitive to chemical etching than the rest of the bulk is, i.e., $V_t > V_b$ where V_t and V_b refer to the rates of etching the track and the bulk, respectively. Figure 6a shows a schematic of the geometry of a track that forms in a detector as it is etched (*13*). In this schematic, I is the initial detector surface, I' is the surface after the etching, V_t is the etch rate along the particle trajectory (track etch rate), V_b is the etch rate of the undamaged regions of the detector (bulk etch rate), O is the entrance point and E is the end point of a particle in the detector material, and $OE=R$ is the particle range in the detector material. The distance between I and I' is equal to h, the thickness of the layer removed by etching. In Figure 6a, L' is the total distance traveled by the etching solution along the particle track, and L is the track depth. Etching progresses in all directions with the rate V_b except along the particle path, where the etching goes with the rate V_t. In three dimensions, the track is a cone with the developing angle δ. The circle A represents the revolution of a point on the track wall around the particle path.

During etching, the track wall moves parallel to itself. A thorough discussion on the formation and growth of tracks as a function of etching time can be found in a review written by Nikezic and Yu (*13*).

Nikezic and Yu have developed a computer program, TRACK_TEST, that is used to calculate parameters and plot profiles for etch pits in nuclear track materials (*14, 15, 16*). The executable program is freeware and can be downloaded from the City University of Hong Kong Trackology Research Web site (*17*). The input parameters are particle energy, incident angle, etch rate, and etch time. There are three forms of the V function for the CR-39 detector available, and the user chooses the one that best describes the etching behavior of his/her detectors. For the Fukuvi CR-39 detectors used in these experiments, the optimum V function was found to be:

$$V_T = V_B\left(e^{(-a_1x+a_4)} - e^{(-a_2x+a_3)} + e^{a_3} - e^{a_4} + 1\right) \tag{5}$$

where x is the residual range of the alpha particle and a_1=0.1, a_2=1, a_3=1.27, and a_4=1 (*18*). The outputs of the calculations are the lengths of the major and minor axes, the track depth, and the track profile showing the end point of the particle that entered the detector. This end point corresponds to the bright spot observed inside the pits.

Figure 6b shows two photomicrographs obtained for a CR-39 detector that has been used in a Pd/D co-deposition experiment. These images were taken in an area where the track density is relatively low. In these areas, the number of latent tracks is low and does not impact the measurements of track lengths. The top microphotograph was taken with the focus on the surface of the CR-39 detector. The bottom microphotograph in Figure 6b is an overlay of two images. One image was taken with the focus on the surface of the detector, and the other image is focused on the bottom of the pits. Using the above equation, researchers computer-analyzed the track indicated by an arrow in Figure 6b. This track has an elliptical shape indicating that the particle has entered the surface of the CR-39 detector at an angle. The bright spot indicates the location of the end point of the particle that entered the detector. Computer modeling shows that a 1.3 MeV alpha particle hitting the surface of the CR-39 at a 35° angle causes a track with a similar elliptical shape, Figure 6c. Figure 6d is an enlargement of the pit indicated in Figure 6b. The major and minor axis were measured for the Pd/D pit, Figure 6d, and the computer-generated track, Figure 6c. The ratio of the minor vs. major axis of the pit shown in Figure 6d is 0.88. This matches the ratio (0.89) of the computer-generated track, Figure 6c. In Figures 6c and 6d, d_2 is the length of the major axis, and d_1 is the distance between the bright spot (particle end point) and the back edge of the pit/track. The ratios, d_1/d_2, for the Pd/D pit and the computer-generated track are also in agreement.

Downloaded by CORNELL UNIV on June 28, 2012 | http://pubs.acs.org
Publication Date (Web): December 20, 2009 | doi: 10.1021/bk-2009-1029.ch007

Downloaded by CORNELL UNIV on June 28, 2012 | http://pubs.acs.org
Publication Date (Web): December 20, 2009 | doi: 10.1021/bk-2009-1029.ch007

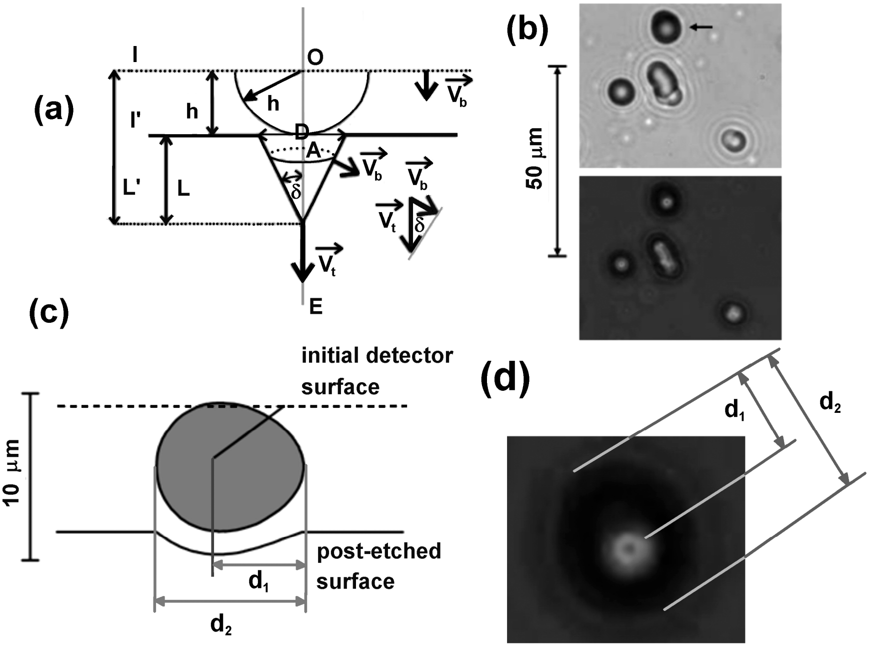

Figure 6. (a) Schematic illustrating the geometry of the track development, adapted from Nikezic and Yu (13). Images of pits in CR-39 created as the result of a Pd/D co-deposition reaction. Ag wire, no external field experiment, 1000× magnification. The CR-39 detector was etched for 6 h at 62 °C. (b) For the top image the focus is on the surface of the CR-39. The bottom image is an overlay of two images taken at two different focal lengths (surface and the bottom of the pits). (c) Results of computer modeling the track indicated by an arrow in (b). This is the shape of the track obtained for a 1.3 MeV alpha particle hitting the CR-39 detector at a 35° angle after six hours of etching at an etch rate of 1.25 μm hr^{-1}. The ratio, d_1/d_2, is 0.6. (d) Enlarged image of the pit indicated in Figure 6b. The ratio, d_1/d_2, is 0.57.

Other Radiation Emissions

As discussed *vide supra*, for use in an RTG, it is desirable for the fuel to produce high energy radiation that has low penetration. It is, therefore, of interest to determine what other kinds of radiation are emitted in the Pd/D system. To measure these other radiation emissions, researchers have used constant integrating detectors such as photographic film and CR-39 as well as electronic detectors such as Si(Li) with a Be window, HPGe with an Al window, and liquid scintillators.

A series of experiments were conducted to measure tritium generation in cathodes prepared by Pd/D co-deposition. In these experiments, the D_2 and O_2 gases were recombined in a separate chamber. The tritium content in the liquid and gas phases was measured daily using a liquid scintillator. The measured data were analyzed using the following mass balance expression:

$$f(t) = f(0)\left(\frac{m(0)-r(i)t}{m(0)}\right)^{S-1} + \frac{q}{(S-1)r(i)} \bullet \left\{1-\left[\frac{m(0)-r(i)t}{m(0)}\right]^{S-1}\right\} \qquad (6)$$

where f is the tritium mass fraction, *m* is the mass of the electrolyte phase, *r(i)* denoted the rate of change associated with the cell current, *q* is the rate at which tritium is added/removed, and *s* is the isotopic separation factor (*19*). Five Pd/D co-deposition experiments were done (*20*). Two gave perfect mass balances for tritium, and three showed excess tritium. In the three experiments that showed excess tritium, the production of tritium occurred in bursts and sporadically. During a burst, the rate of tritium production was estimated to be 10^3 to 10^4 atoms s^{-1}. Tritium is a beta emitter, and its emission occurs at 0.01859 MeV. Although it is not dangerous externally, it is a radiation hazard when inhaled, ingested through food or water, or absorbed through the skin. With regard to an RTG, minimal shielding is required to block the betas emitted by tritium. Consequently, tritium is not a concern for an RTG.

Figure 7 summarizes results obtained using three kinds of detectors that indicate that X-rays and γ-ray emissions are occurring in the Pd/D system. Figure 7a shows fogging of photographic film after a Pd/D co-deposition experiment conducted on the Ag disk of a piezoelectric crystal (*7*). A thin plastic film was placed between the Pd/D deposit and the photographic film to prevent any reactions between the silver salts of the film and the D_2 outgassing from the cathode. Like CR-39, photographic film is an example of an integrating detector. When an event occurs, it gets permanently stamped in the emulsion of the film. The advantages with an integrating detector are that nothing gets lost or averaged away and the spatial distribution of the events can be determined. The disadvantage is that it is not known when the events occurred. As can be seen in Figure 7a, the circular shape of the cathode is apparent on the film. The fogging pattern observed on the film indicates that the emission of X-rays is not homogeneous. It also indicates that some sites are more active than others.

Downloaded by CORNELL UNIV on June 28, 2012 | http://pubs.acs.org
Publication Date (Web): December 20, 2009 | doi: 10.1021/bk-2009-1029.ch007

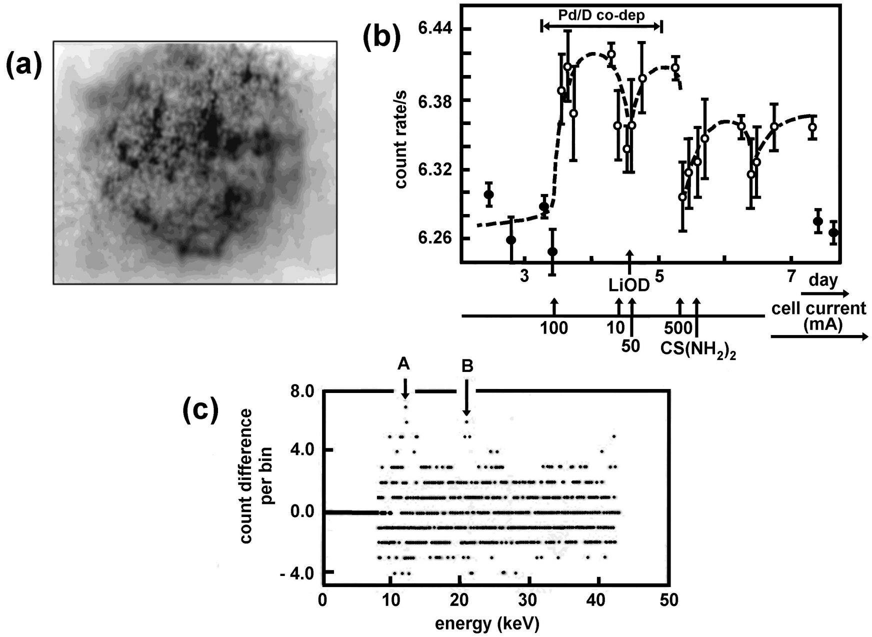

Figure 7. (a) Fogging of photographic film after three days' exposure to Pd deposited on a Ag disk electrode. A thin plastic sheet separated the photographic film and the cathode. (b) X-ray and/or γ-ray flux measured during Pd/D co-deposition. Measurements were made using a HPGe detector, spectral range 15-3000 keV. Pd is plated from a 0.003 M $PdCl_2$ -0.3 M LiCl solution in D_2O onto a Cu/Ag/Pd electrode. Applied cell currents and addition of LiOD and thiourea to the electrolyte are indicated: (●) background (○) operating cell. (c) Background subtracted X-ray spectrum measured during cathodic polarization of the Pd/D system. The cathode is a Ni screen pressed against a thin acrylic window. The spectrum was obtained using a Si(Li) detector. Weak lines at 8-12 (A) and 20 (B) keV are indicated.

Temporal measurements of X-rays and/or γ-rays were made using HPGe and Si(Li) detectors (*8*). The spectral ranges of these detectors were 15-3000 keV for the HPGe and 7-40 keV for the Si(Li). All measurements were made inside Pb caves to minimize the background. A separate NaI detector in another Pb cave was used to monitor the background. No fluctuations in the background were observed in the course of these experiments. In the HPGe experiment, summarized in Figure 7b, Pd/D co-deposition was done on a Cu/Ag/Pd electrode. To prepare the cathode, Ag was plated onto the Cu substrate using a silver-cyanide solution. A Pd bright layer was then plated on top of the Ag layer using a $Pd(NH_2)_4^{2+}$ plating solution. As shown in Figure 7b, the background count is 6.272±0.019 cps. When the cell was activated, the count rate was observed to increase. The average count rate between days 3 and 5 is

Downloaded by CORNELL UNIV on June 28, 2012 | http://pubs.acs.org
Publication Date (Web): December 20, 2009 | doi: 10.1021/bk-2009-1029.ch007

6.383±0.027 cps. On day 5, a decrease in the count rate was observed. The addition of thiourea resulted in an increase in the count rate. Thiourea is an additive that retards the rate of gaseous hydrogen evolution from the cathode surface. This results in an enhancement of the net D-loading rate. When the cell was turned off, the count rate dropped back down to 6.27 cps. On subtraction of the background, no discernable peaks were observed in the 15-3000 keV spectral window. Figure 7c shows a background-subtracted spectrum typically obtained during Pd/D co-deposition using the Si(Li) detector (*8*). An increase in the baseline is observed, and weak peaks at 8-12 and 20 keV are observed. The increase in the baseline is attributed to the Bremsstrahlung arising from the oscillating plasma of the cathodically polarized Pd/D system. The 8-12 keV peak results either from a Ni K line or a Pt L line. The peak at 20 keV is attributed to the Pd K_α line. Additional experiments with both the HPGe and Si(Li) detectors showed that the emission of X-rays and γ-rays was sporadic and of limited duration. It is therefore expected that this level of radiation from the Pd/D system can easily be shielded in an RTG.

Besides energetic particles, CR-39 detectors also interact with neutrons (*21, 22*). Depending on the energy of the neutron, three types of interactions with CR-39 are possible. The energies of DD and DT hot fusion neutrons are 2.45 MeV and 11.9-17.2 MeV, respectively. Both DD and DT neutrons can scatter elastically producing recoil protons, carbons, and oxygens in the forward direction. But the more energetic DT neutrons can also undergo two inelastic (n,p and n,α) reactions with carbon or oxygen. These inelastic reactions result in charged particles that can produce tracks on both the front and back sides of the CR-39 detector. The CR-39 detectors used in Pd/D co-deposition experiments show tracks on both the front and back surfaces (*23*). The size distribution of the tracks on the backside of the CR-39 detectors range between 8 and 40 μm. This size distribution is consistent with neutrons (*22*). The neutron recoil reactions also occur inside the CR-39 detector. Further etching of the CR-39 detector used in the Pd/D co-deposition experiments reveals tracks from these recoil reactions inside the detector (*23*). Three-pronged stars, or triple tracks such as those shown in Figure 8a, provide further evidence of the production of energetic neutrons in Pd/D co-deposition. If the energy of the neutron is greater than 9.6 MeV (*24*), the inelastic n,α interaction can cause the carbon atom to shatter into three α particles. The residuals of the reaction can be viewed in the CR-39 detector as a three-pronged star, where each prong represents each charged particle that occurs in the decay. Figure 8b shows a three-pronged star observed in a CR-39 detector that was exposed to DT neutrons (*25*). On the surface, the triple track shows three overlapping tracks, top images of Figure 8b. Inside the triple track, the lobes of the triple track are splitting apart from a center point. The latter is also observed in the triple tracks resulting from Pd/D co-deposition, bottom images of Figure 8a. For an RTG, neutrons can be problematic. Neutrons cannot be shielded. However, they can be thermalized using hydrogenated material, which will add mass to the RTG.

Downloaded by CORNELL UNIV on June 28, 2012 | http://pubs.acs.org
Publication Date (Web): December 20, 2009 | doi: 10.1021/bk-2009-1029.ch007

Downloaded by CORNELL UNIV on June 28, 2012 | http://pubs.acs.org
Publication Date (Web): December 20, 2009 | doi: 10.1021/bk-2009-1029.ch007

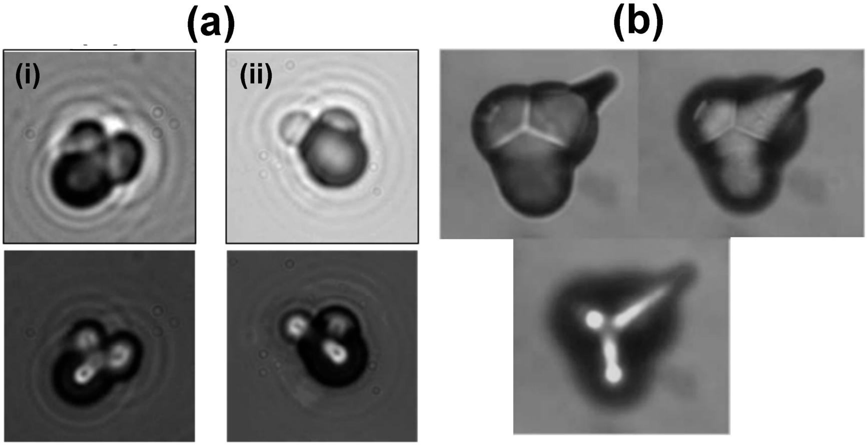

Figure 8. (a) Photomicrographs of triple tracks observed in CR-39 detectors used in Pd/D co-deposition reactions. A 60 μm polyethylene film separated the detector and the cathode. Etching conditions are 62 °C for 6 h, (i), and 10 h,(ii). Images obtained using 1,000X magnification. In the top images, the focus is on the surface of the CR-39 detector. Bottom images are an overlay of two images taken at two different focal lengths (surface and bottom of the pit). (b) A triple track observed in a CR-39 detector that has been exposed to DT neutrons. The micro-photographs were taken by J. K. Pálfalvi, Atomic Energy Research Institute (AERI), Budapest, Hungary, and first presented at the 8th Workshop on Radiation Monitoring on the International Space Station (WRMISS), LBNL Berkeley (San Francisco), USA, 3-5 September, 2003.

Conclusions

Earlier, it was shown that pits are formed on the surface of CR-39 detectors during the Pd/D co-deposition process. The Pd cathode is the source of these pits. The size distribution and ellipticity of the tracks were consistent with those obtained for energetic particles. Use of the particles generated as the result of Pd/D co-deposition as a source to power RTGs was evaluated. The production of these particles occurs in bursts, and their generation is sporadic. Experiments conducted by placing a 6 μm thick Mylar film between the cathode and the CR-39 detector indicate that the majority of the particles have energies on the order of 1 MeV. This conclusion is supported by track modeling of the pits. Low-energy radiation emission has been observed in Pd/D co-deposition. The cathodically polarized Pd/D system emits X-rays with a broad energy distribution (Bremsstrauhlung), with the occassional emergence of recognizable peaks (20 keV from Pd Kα and 8-12 keV from either Ni or Pt). Like the particle emissions, the emission of radiation is sporadic and of limited duration. On the back surface of the CR-39 detectors, tracks are observed. The size distribution and ellipticity of the tracks suggest that the tracks were caused by knock-ons from neutrons. Triple tracks, diagnostic of the carbon break-up reaction, have been observed in the CR-39 detectors. The threshold energy of the neutron to initiate the carbon break-up reaction is 9.6 MeV. These results indicate that, for use to power an RTG, the Pd/D co-deposition operational parameters need to be optimized for particle generation. In particular, the flux of particles needs to be increased, and the radiation/neutron emissions need to be minimized.

Acknowledgements

The effort was funded by the SSC-Pacific ILIR program and JWK Corporation. The authors would like to thank Dr. Gary Phillips, nuclear physicist, retired Naval Research Laboratory, U.S. Navy, Radiation Effects Branch, for valuable discussions in interpreting the data. The authors acknowledge the contributions of Dr. Stanislaw Szpak, retired from SPAWAR Systems Center Pacific, who pioneered the Pd/D co-deposition process. We also wish to thank Dr. Jay W. Khim, chief executive officer of JWK Corporation, for funding Project GeNiE at JWK International and for his valuable discussions about experiments and data analysis.

Downloaded by CORNELL UNIV on June 28, 2012 | http://pubs.acs.org
Publication Date (Web): December 20, 2009 | doi: 10.1021/bk-2009-1029.ch007

References

1. Frazier, T. A. *Summary Draft Environmental Impact Statementfor the Proposed Consolidation of Nuclear Operations Related to Production of Radioisotope Power Systems,* June 2005; DOE/EIS-0373D.
2. Li, X. Z. The Precursor of Cold Fusion Phenomenon in Deuterium/Solid Systems in Anomalous Nuclear Effects in Deuterium/Solid Systems. In *AIP Conference Proceedings,* Brigham Young Univ., Provo, UT: American Institute of Physics: New York, 1990; 228-232.
3. Oriani, R. A.; Fisher, F. C. Generation of Nuclear Tracks During Electrolysis. *Jpn. J. Appl. Phys.* **2002**, *41,* 6180-6183.
4. Lipson, A. G.; Roussetski, A. S.; Miley, G. H.; Castano, C. H. In-Situ Charged Particles and X-ray Detection in Pd Thin Film-Cathodes During Electrolysis in Li_2SO_4 /H_2O. In *Condensed Matter Nuclear Science: Proceedings of the Ninth International Conference on Cold Fusion*, Beijing, China, May 19-24, 2002; Li, X. Z., Ed.; Tsinghua Univ. Press: Beijing, 2002; 218-223.
5. Lipson, A. G.; Roussetski, A. S.; Miley, G. H.; Saunin, E. I. Phenomenon of an Energetic Charged Particle Emission from Hydrogen/Deuterium Loaded Metals. In *Condensed Matter Nuclear Science: Proceedings of the Tenth International Conference on Cold Fusion*, Cambridge, MA, Aug. 24-29, 2003; Hagelstein, P. L.; Chubb, S. R., Eds.; World Scientific Publishing Co.: Singapore, 2006; 539-558.
6. Szpak, S.; Mosier-Boss, P. A.; Gordon, F. E. Further Evidence of Nuclear Reactions in the Pd Lattice: Emission of Charged Particles. *Naturwissenschaften,* **2007**, *94*, 511-514.

7. Mosier-Boss, P. A.; Szpak, S.; Gordon, F. E.; Forsley, L. P. G. Use of CR-39 in Pd/D Co-Deposition Experiments. *Eur. Phys. J. Appl. Phys.*, **2007**, *40*, 293-303.
8. Szpak, S.; Mosier-Boss, P. A.; Smith, J. J. On the Behavior of the Cathodically Polarized Pd/D System: Search for Emanating Radiation. *Phys. Lett. A,* **1996**, *210*, 382-390.
9. Yoshioka, T.; Tsuruta, T.; Iwano, H.; Danhara, T. Spontaneous Fission Decay Constant of ^{238}U Determined by SSNTD Method Using CR-39 and DAP Plates. *Nucl. Instr. and Meth. in Phys. Res. A.*, **2005**, *555*, 386-395.
10. Dörschel, B.; Hermsdorf, D.; Reichelt, U.; Starke, S,; Wang, Y. 3D Computation of the Shape of Etched Tracks in CR-39 for Oblique Particle Incidence and Comparison with Experimental Results. *Radiat. Meas.*, **2003**, *37*, 563-571.
11. Szpak, S.; Mosier-Boss, P. A.; Gordon, F. E.; Forsley, L. P. G. The Effect of an External Electric Field on Surface Morphologgy of Co-Deposited Pd/D Films. *J. Electroanal. Chem.*, **2005**, *580*, 284-290.
12. Séguin, F. H.; Frenje, J. A.; Li, C. K.; Hicks, D. G.; Kurebayashi, S.; Rygg, J. R.; Schwartz, B.-E.; Petrasso, R. D.; Roberts, S.; Soures, J. M.; Meyerhofer, D. D.; Sangster, T. C.; Knauer, J. P.; Sorce, C.; Glebov, V. Y.; Stoeckl, C.; Phillips, T. W.; Leeper, R. J.; Fletcher, K.; Padalino, S. Spectrometry of Charged Particles from Inertial-Confinement-Fusion Plasmas. *Rev. Sci. Instrum*. **2003**, *74*, 975-995.
13. Nikezic, D.; Yu, K. N. Formation and Growth of Tracks in Nuclear Track Materials. *Mat. Sci. Eng. R.* **2004**, *46*, 51-123.
14. Nikezic, D.; Yu, K. N. Computer Program TRACK_TEST for Calculating Parameters and Plotting Profiles for Etch Pits in Nuclear Track Materials. *Comp. Phys. Commun.* **2006**, *174*, 160-165.
15. Nikezic, D.; Ng, F. M. F.; Yip, C. W. Y.; Yu, K. N. Application of the Ray Tracing Method in Studying α Tracks in SSNTDs. *Radiat. Meas*. **2005**, *40*, 375-379.
16. Nikezic, D.; Yu, K. N. Three-Dimensional Analytical Detrmination of the Track Parameters: Over-Etched Tracks. *Radiat. Meas*. **2003**, *37*, 39-45.
17. http://www.cityu.edu.hk/ap/nru/test.htm.
18. Brun C.; Fromm, M.; Meyer, P.; Groetz, J. E.; Abel, F.; Chambaudet, A.; Dörschel, B.; Hermsdorf, D.; Bretschneider, R.; Kadner, K.; Kühne, H. Intercomparative Study of the Detection Characteristics of the CR-39 SSNTD for Light Ions: Present Status of the Besancon-Dresden Approaches. *Radiat. Meas*. **1999**, *31*, 89-98.
19. Szpak, S.; Mosier-Boss, P. A.; Boss, R. D.; Smith, J. J. Comments on the Analysis of Tritium Content in Electrochemical Cells. *J. Electroanal. Chem*. **1994**, *373*, 1-9.
20. Szpak, S.; Mosier-Boss, P. A.; Boss, R. D.; Smith, J. J. On the Behavior of the Pd/D System: Evidence for Tritium Production. *Fus. Technol*. **1998**, *33,* 38-51.
21. Frenje, J. A.; Li, C. K.; Séguin, F. H.; Hicks, D. G.; Kurebayashi, S.; Petrasso, R. D.; Roberts, S.; Glebov, V. Y.; Meyerhofer, D. D.; Sangster, T. C.; Soures, J. M.; Stoeckl, C.; Schmid, G. J.; Lerche, R. A. Absolute Measurements of Neutron Yields From DD and DT Implosions at the

Downloaded by CORNELL UNIV on June 28, 2012 | http://pubs.acs.org
Publication Date (Web): December 20, 2009 | doi: 10.1021/bk-2009-1029.ch007

OMEGA Laser Facility Using CR-39 Track Detectors. *Rev. Sci. Instrum.* **2002**, *73*, 2597-2605.

22. Phillips, G. W.; Spann, J. E.; Bogard, J. S.; VoDinh, T.; Emfietzoglou, D.; Devine, R. T.; Moscovitch, M. Neutron Spectrometry Using CR-39 Track Etch Detectors. *Radiat. Prot. Dosim.* **2006**, *120*, 457-460.
23. Mosier-Boss, P. A.; Szpak, S.; Gordon, F. E.; Forsley, L. P. G. Detection of Energetic Particles and Neutrons Emitted During Pd/D Co-Deposition. *Low-Energy Nuclear Reactions Sourcebook;* Marwan, J.; Krivit, S., Eds.; American Chemical Society, Oxford University Press: Washington DC, 2008.
24. Al-Najjar, S. A. R.; Abddel-Naby, A.; Durrani, S. A. Fast-Neutron Spectrometry Using the Triple-α Reaction on the XR-39 Detector. *Nuclear Tracks* **1986**, *12*, 611-615.
25. Pálfalvi, J. K.; Akatov, Y.; Szabó, J.; Sajó-Bohus, L.; Eördögh, I. Evaluation of SSNTD Stacks Exposed on the ISS. *Radiation Protection Dosimetry* **2004**, *110*, 393-397.

Downloaded by CORNELL UNIV on June 28, 2012 | http://pubs.acs.org
Publication Date (Web): December 20, 2009 | doi: 10.1021/bk-2009-1029.ch007

Downloaded by DUKE UNIV on June 28, 2012 | http://pubs.acs.org
Publication Date (Web): December 20, 2009 | doi: 10.1021/bk-2009-1029.ch008

Chapter 8

Recent Advances and Results in Acoustic Inertial Confinement Bubble Nuclear Fusion

R. P. Taleyarkhan[1*], C. D. West[2], R. T. Lahey, Jr.[3], R. I. Nigmatulin[4], R. C. Block[3], J. S. Cho[5], and Y. Xu[6]

[1]Purdue University, W. Lafayette, IN 47905, USA
[2]University of Tennessee, Knoxville, TN, USA (retd., ORNL, TN, USA)
[3]Rensselaer Polytechnic Institute, Troy, NY 12181, USA
[4]Russian Academy of Sciences, Moscow, Russia
[5]FNC Technology Inc. (locn., Seoul National University), Seoul, S.Korea
[6]Westinghouse Electric Company, Pittsburgh, PA 15235, USA
(*) - Corresponding Author: rusi@purdue.edu

This paper provides an update on developments since the first announcement of the discovery in 2002 of acoustic inertial confinement (*a.k.a* bubble) nuclear fusion. A theoretical foundation for the supercompression of acoustically driven deuterated bubble clusters has been developed and published. Initially, bubble fusion experiments used external neutron sources for nucleating bubble clusters, and despite compelling evidence, lingering doubts remained because of the use of external neutrons to maintain neutron production. This was overcome using a self-nucleation method. In those novel experiments, seeding of nanometer bubbles was accomplished using nuclear-decay recoils from dissolved uranyl nitrate. Bubble fusion experiments have been replicated successfully, and confirmatory results were reported at least five times since 2005. Moreover, speculations and controversies about the discovery related to our bubble fusion experiments have now been conclusively addressed, rebutted, and dismissed.

In Low-Energy Nuclear Reactions and New Energy Technologies Sourcebook Volume 2; Marwan, J., et al.;
ACS Symposium Series; American Chemical Society: Washington, DC, 2010.

Introduction

It is well-known *(3, 4)* that the intense implosive collapse of bubbles, including acoustic cavitation bubbles, can lead to extremely high compression-induced pressures and temperatures from shock heating and to the generation of the light flashes known as sonoluminescence (SL). In addition, the violent implosions of bubble clusters produce audible shock waves.

In a typical bubble fusion experiment, a nuclear particle (e.g., fast neutrons or nuclear decay recoils) can cause bubble nucleation when the test liquid is in an acoustically tensioned metastable state whereby the cavitation bubbles' radius increases from an initial radius (R_o) of tens of nanometers to a maximum radius (R_m), which is in the millimeter range.

The liquid's kinetic energy, which is accumulated during the implosion stage, and is subsequently converted to internal energy in and around the bubble, is about $E = p_m R_m^3$. In typical sonofusion experiments (*1-4*), p_m = 15 bar, R_m = 500 to 800 μm, which leads to 10^4 to 10^5 times more liquid phase kinetic energy, E, than in typical single bubble sonoluminescence (SBSL) experiments (i.e., where p_m = 1.5 bar, R_m = 50 μm); therefore, a vastly higher potential for bubble compression exists.

Experimental System

Figure 1 shows typical components used in different bubble fusion experiments. The test liquid is placed in a cylindrical glass test section and driven harmonically with a lead-zirconate-titanate (PZT) piezoelectric driver ring attached around the outside surface of the test section. This induces an acoustic standing wave in the test section which has a pressure antinode of maximum amplitude ~15 bar. Test-cell design and operational aspects have been described elsewhere *(1, 2, 3)*. Up to four independent nuclear particle detection systems were used in our various reported studies. They included use of a long-established passive track-edge fast neutron detector (CR-39^{TM} plastic detector from Landauer, Inc.) that is insensitive to γ rays but detects neutrons, a lithium iodide (LiI) thermal neutron detector (TND), a fast rise-time liquid scintillation (LS) detector to ascertain the energy and quantity of any emitted neutrons, and a NaI γ ray spectrum detector.

Downloaded by DUKE UNIV on June 28, 2012 | http://pubs.acs.org
Publication Date (Web): December 20, 2009 | doi: 10.1021/bk-2009-1029.ch008

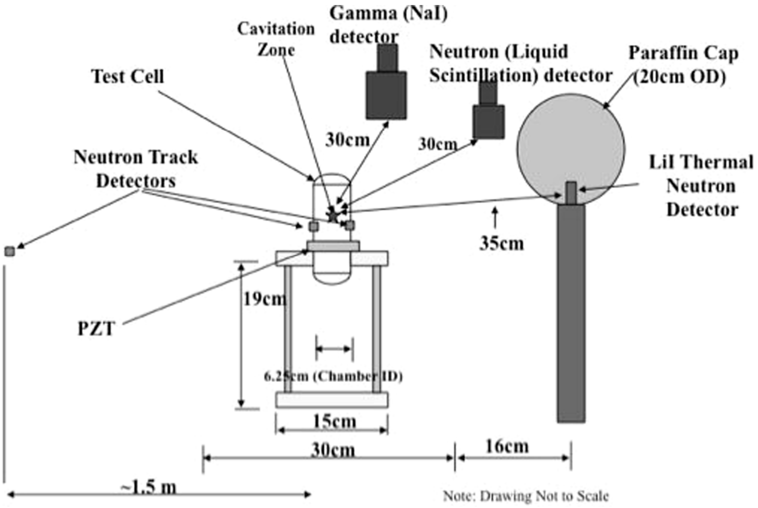
Gamma (NaI) detector
Cavitation Zone
Test Cell
Neutron (Liquid Scintillation) detector
Paraffin Cap (20cm OD)
30cm
30cm
Neutron Track Detectors
LiI Thermal Neutron Detector
35cm
19cm
PZT
6.25cm (Chamber ID)
15cm
30cm
16cm
~1.5 m
Note: Drawing Not to Scale

Fig. 1. Schematic representation of a typical bubble fusion experimental setup (5).

Results From Bubble Fusion Experiments

We previously presented compelling evidence (*1, 2, 3, 4*) for ≤ 2.45 MeV neutron emissions and tritium production during external neutron-seeded cavitation experiments with chilled deuterated acetone (C_3D_6O). Figure 2 shows typical results for tritium production. The tritium emission rate was measured to be in the vicinity of ~ 3-4 x 10^5 T/s with about ~ 4 to 5 standard deviation (SD) statistical significance. A typical neutron emission time spectrum is shown in Fig. 3 where neutron counts were obtained using a LS detector from the start of nucleation (i.e., around t = 0-15 μs) of the bubbles using a pulse neutron generator (PNG), to ~ 5,000 μs, the time required for the bubbles to exit the acoustic antinode and condense back into the test liquid. These results indicate that the neutrons from bubble fusion are well-separated in time and intensity from those neutrons used for seeding the bubbles, and the overall emission rate was between ~10^5 n/s to 5x10^5 n/s, with an overwhelming ~30 to 60 SD statistical significance. Significantly, the neutron emission rate is consistent with the tritium production rate. The energy of the neutrons was found to be ≤ 2.45 MeV, as would be expected from D-D fusion, and found to be time-correlated *(2)* with sonoluminescence (SL) flashes of light, indicating that the neutron emissions were taking place during energetic bubble implosions. In contrast, gamma ray emissions were not time-correlated with the neutron bursts, but they occurred subsequent to the neutron bursts, as expected. This is because fast (≤ 2.45 MeV) neutrons must be thermalized before they can be absorbed in shielding and detector materials containing hydrogen before gamma rays can be emitted.

Downloaded by DUKE UNIV on June 28, 2012 | http://pubs.acs.org
Publication Date (Web): December 20, 2009 | doi: 10.1021/bk-2009-1029.ch008

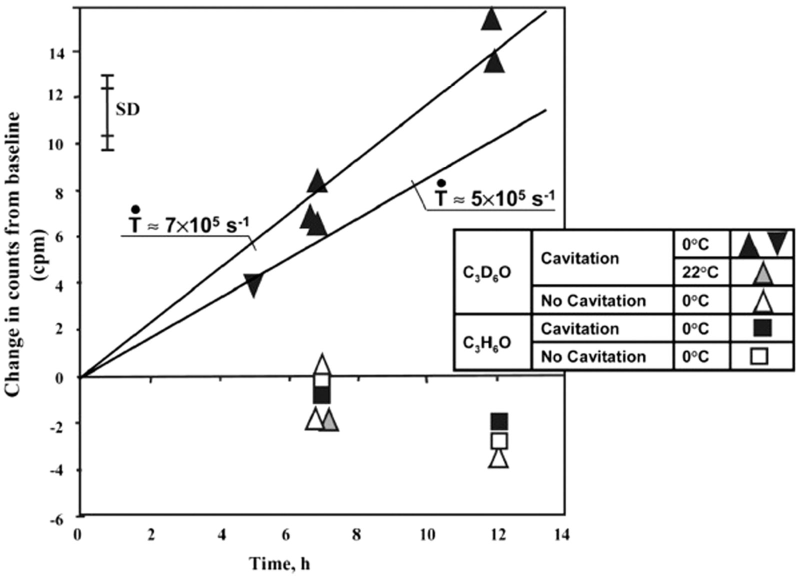

Fig. 2. Tritium emission during neutron-seeded acoustic cavitation (1).

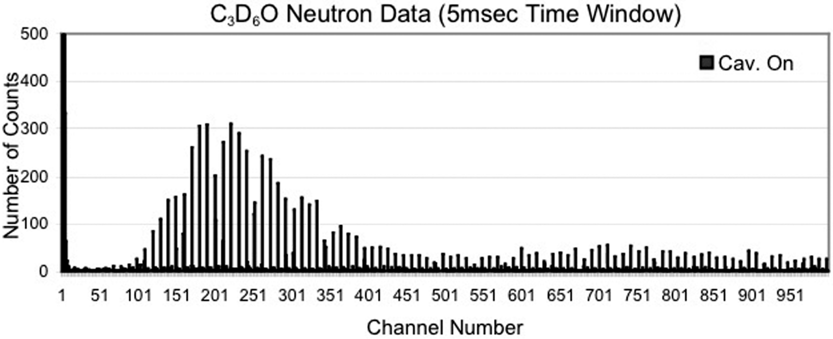

Fig. 3. Evolution of neutrons during bubble fusion experiments (Y axis represents neutron counts; X axis represents time from start of PNG neutron burst; each channel represents 5 μs of time) (2).

Downloaded by DUKE UNIV on June 28, 2012 | http://pubs.acs.org
Publication Date (Web): December 20, 2009 | doi: 10.1021/bk-2009-1029.ch008

Downloaded by DUKE UNIV on June 28, 2012 | http://pubs.acs.org
Publication Date (Web): December 20, 2009 | doi: 10.1021/bk-2009-1029.ch008

Doubts have been raised about the theoretical possibility of super-compression-induced fusion of deuterated organic liquids like acetone *(6)*. This issue has been resolved within a comprehensive theoretical framework *(4)* by studying the conditions of our bubble fusion experiments, wherein all known phenomena associated with supercompression were modeled (i.e., dissociation, ionization, bubble cluster pressure amplification, shock physics, neutron-tritium production, etc.). Significantly, the equations of state used were developed from actual experimental data.

Typical predicted results of the compression process for conditions during our bubble fusion experiments are shown in Fig. 4 during the final stages of implosion followed by shock reflection. Stages 21 to 23 represent the implosion phases (shown by arrows pointing to the left), whereas stages 24 and 25 represent shock rebound phases from the center of the bubble (depicted by arrows pointing to the right). The top left sub-figure of Fig. 4 shows the variation of acetone vapor density versus distance (*r*) from the center of the bubble. The position r* (~ 28 nm) is the distance from the center where the reflected shock and incoming liquid wall interface collide to produce the most intense degree of compression leading to the density of the vapor core to rise to ~ 10^4 kg/m3 (which is more than 10 times the density of liquid acetone). The top right sub-figure of Fig. 4 depicts the pressure within the bubble with distance from the center where we note that, during Stage 24, the shocked state pressure at r* reaches values in the range of ~ 10^{11} bar. The bottom left sub-figure of Fig. 4 depicts the variation of shock velocity (w) with distance from the center of the bubble. Values as high as ~ 1,000 km/s are reached as the shock approaches distances of about 10 nm from the center before being reflected outward. Finally, the bottom right sub-figure of Fig. 4 depicts variation of temperature with distance for the various stages. Although the highest temperature of ~ 2×10^9 K is attained at the center of the bubble, the values of temperature during shock compression at regions to 100 nm from the center are in the range of 10^7 K to ~ 10^8 K. It is apparent that thermonuclear fusion conditions may occur using the apparatus and method followed in our experiments. These simulations also predicted that inorganic fluids such as heavy water would not be a good choice for attaining thermonuclear fusion in imploding bubbles, a fact that has been confirmed experimentally *(5)*. Therefore, the scientific feasibility of bubble fusion has been established and endorsed by referees and peers in the field *(4)*.

Downloaded by DUKE UNIV on June 28, 2012 | http://pubs.acs.org
Publication Date (Web): December 20, 2009 | doi: 10.1021/bk-2009-1029.ch008

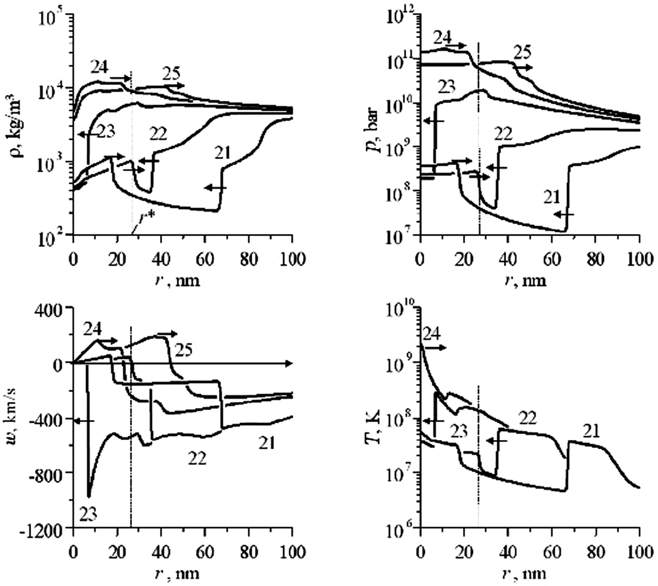

Fig. 4. The final high Mach number stage of vapor bubble implosion. The vapor parameters are shown near the bubble's center between two interacting shock waves (i.e., the sub-picosecond, high Mach number, stage). The vertical dashed line indicates the radial position of the maximum neutron production point, r^*. The numbers denote times: $t_{21} = t^* - 0.11$ ps, $t_{22} = t^* - 0.06$ ps, $t_{23} = t^* - 0.02$ ps, $t_{24} = t^* - 0.01$ ps, and, $t_{25} = t^*$ (4).

Nevertheless, a lingering concern about the use of an external neutron source strongly suggested the need to demonstrate that thermonuclear fusion could also be attained during acoustic cavitation without the use of an external source of neutrons. This remaining technical issue was conclusively resolved in January 2006 when we presented results of our investigations using independent detector systems and the self-nucleation of bubble clusters in various deuterated liquids, including water. Self-nucleation was achieved using randomly generated, mainly ~4 MeV alpha particles from the radioactive decay of dissolved uranyl nitrate. Four independent detection systems shown in Fig. 1 confirmed the production of ≤ 2.45 MeV D-D fusion neutrons and associated gamma rays from neutron capture. Figure 5 displays sample results of D-D neutron emission during self-nucleation with a 17 to 30 SD statistical significance.

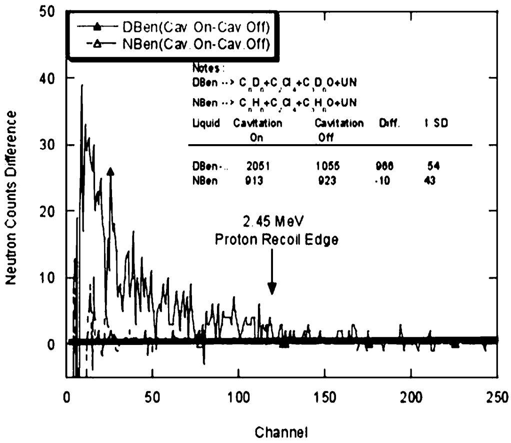

Fig. 5. Neutron pulse height spectrum during self-nucleated bubble fusion experiments (5).

Successful Confirmations and Replications of Bubble Fusion

Several successful replications of bubble fusion experiments have been reported and attested to by four groups of researchers unaffiliated with the original discovery team *(1, 2)* since 2005 for both neutron-seeded and self-seeded experiments. This is in addition to two successful public demonstrations in front of visitors from industry, academia and government *(21)*.

The first successful published replication was by a group led by Yiban Xu et al. of Purdue University and was published in the archival literature in June 2005 *(7a)*. This study used a test section and guidance on operational aspects initially supplied by ORNL, but Xu et al. independently conducted the experiments in their own facility and with an isotope source of external neutrons, versus the use of a PNG as in the ORNL studies *(1, 2)*. Moreover, they performed and reported their own data analyses. Neutron emissions of $\leq$ 2.45 MeV with about 11 SD statistical significance and tritium emissions with ~5 SD statistical significance were also reported for neutron-seeded cavitation in chilled C_3D_6O but not for the control experiments with C_3H_6O. Significantly, this study *(7a, 7b)* showed when to, and when not to, expect bubble fusion. In particular, transition from sphericity during the implosion of bubble clusters implies that bubble fusion will not occur. Later, this group discussed thermal-hydraulic aspects *(7b)*.

Reports of successful production of $\leq$ 2.45 MeV neutrons with chilled C_3D_6O, with neutron-nucleated experiments with 4 to 8 SD statistical significance, were also publicly acknowledged by researchers of Impulse Devices Inc. (IDI) during the February 2006 ICC Workshop in Austin, Texas *(8)*. IDI reported difficulties with reproducibility of these data because of equipment breakage and other issues, but importantly, the researchers obtained null results for all control conditions.

Downloaded by DUKE UNIV on June 28, 2012 | http://pubs.acs.org
Publication Date (Web): December 20, 2009 | doi: 10.1021/bk-2009-1029.ch008

Downloaded by DUKE UNIV on June 28, 2012 | http://pubs.acs.org
Publication Date (Web): December 20, 2009 | doi: 10.1021/bk-2009-1029.ch008

During 2006, an unaffiliated group of researchers reported *(9, 10, 11)* successful bubble fusion attainment in self-nucleated experiments. A group comprising Professor Edward Forringer and two students from LeTourneau University, Texas, USA, conducted experiments using our test cell apparatus during May 2006 with a grant from the Welch Foundation to assess the published bubble fusion results. Their successful results, which confirmed the key elements of our reported bubble fusion discovery, were done with two independent detection systems of their choice – one using a liquid scintillation (LS) detector, the other a set of several passive neutron track detectors. Their work was documented and peer-reviewed by experts from the American Nuclear Society (ANS) and the 2006 international conference – 17th Topical Meeting on the Technology of Fusion Energy – and was presented at these technical meetings in November 2006, along with publication in the archives of the ANS and the Proceedings of the International Conference on Fusion Energy *(9, 10, 11)*.

Similarly, another unaffiliated nuclear physicist, Professor William Bugg, formerly of the University of Tennessee, Knoxville, Tennessee, USA (now research professor at Stanford University, Stanford, California, USA) also reported (*12)* successful verification of neutron emission from his bubble fusion experiments conducted during June 2006.

These two distinctly separate studies constitute additional verification supporting our published results on bubble fusion *(5)* and dismiss the speculations based on misguided reasoning *(13, 14)*.

In addition to the above-mentioned successful verification and successful replication studies of bubble nuclear fusion, two separate successful public demonstrations of self-nucleated bubble fusion experiments were also given to visitors from industry, academia and government at Purdue University on two separate days in March 2006. The successful outcomes have been attested to in internal testimonial documents to Purdue University *(21)*.

Theoretical Monte Carlo Simulations for Confirmation of Reported Bubble Fusion Experimental Neutron Spectra

The experimental results on bubble fusion from our group *(1, 2, 3, 4, 5)*, as well as the verifications and confirmation studies noted above, were performed under radically different experimental conditions. These data were reported as they evolved and, as such, constituted a blind data set of results for comparing against theoretical predictions to assess their validity and to support our claims of bubble fusion.

Unfortunately, during 2006, a misinformed Monte Carlo-based theoretical simulation of our experiment system *(5)* was improperly performed by University of California at Los Angeles (UCLA) researchers *(13)*. The UCLA simulations were improper because they did not properly account for the experimental enclosure. In particular, the intervening thermal-shielding ice packs and the plastic sheet of the experimental enclosure between the test cell and LS detector were omitted. As a consequence, the down scattering of 2.45 MeV neutrons was grossly miscalculated as reported *(13)*.

To remedy the situation, we first undertook an experimental study directly rebutting the conclusions of Refs. 13 and 14, which, after successful peer review, has been published in the archival literature *(15)*. In addition, we undertook and have completed an extensive theoretical study (with two independent methodologies for cross-checking of results) for simulating the neutron spectra not just for one report but for all of the successful bubble nuclear fusion experimental studies since 2002. The methodology and results have gone through time-tested peer reviews and were recently published in the archival literature *(16)*. Both self-nucleated and external-neutron-nucleated acoustic (bubble fusion) cavitation experiments have been modeled and analyzed for the neutron spectral characteristics at the detector locations for all separate, successful bubble fusion studies.

Our predictive approach was first calibrated and validated against the measured neutron spectrum emitted from a spontaneous fission source (^{252}Cf), from a Pu-Be source and from an accelerator-based monoenergetic 14.1 MeV neutron source. Three-dimensional Monte Carlo neutron transport calculations of 2.45 MeV neutrons from imploding bubbles within deuterated acetone and deuterated benzene-acetone-tetrachloroethylene mixtures were conducted next, using the well-known MCNP5 transport code *(17)* for the published experimental studies of Taleyarkhan et al. *(2, 5)* and for the successful confirmation studies of Xu et al. *(7),* Forringer et al., and Bugg *(9, 10, 11, 12).*

The NE-213 liquid scintillation (LS) detector response was calculated using the U.S. Department of Energy's Monte Carlo-based SCINFUL code *(18)*, which has been extensively benchmarked and validated. These calculated results were also cross-checked using a separate independent approach involving weighting and convoluting MCNP5 predictions with published, experimentally measured NE-213 detector neutron response curves for mononenergetic neutrons at various energies by Lee and Lee *(19)*. These response curves were obtained for a LS detector of the same size (5cm x 5cm) and type as the detector used in the various published bubble fusion experimental studies. The results of the modeling-cum-experimentation were found to be consistent with published experimentally observed neutron spectra for 2.45 MeV neutron emissions during acoustic cavitation bubble fusion experimental conditions, with and without ice-pack (thermal) shielding *(16)*.

Calculated neutron spectra with the inclusion of ice-pack shielding are consistent with the published experimental spectra of Taleyarkhan et al. *(5),* and Xu et al. *(7)*, where intervening ice-pack thermal shielding was present in those experimental enclosures. This is shown in Fig. 6 for the alpha-recoil-based, self-nucleated experiments of Taleyarkhan et al. and in Fig. 7 for the external isotope-source neutron-seeded experiments of Xu et al. Both independent Monte Carlo approaches well predict each of the experimentally derived neutron spectra for these two radically different types of experimental campaigns, where intervening ice-pack shielding was present. Furthermore, the MCNP-NE213 approach of Ref. 16 (based on the Lee-Lee data *(19)* taken with realistic LS detectors) provides predictions that also indicate counts above the 2.45 MeV PRE channel; this compares well against the experimental data of Taleyarkhan et al. *(5)* and Xu et al. *(7)*.

Downloaded by DUKE UNIV on June 28, 2012 | http://pubs.acs.org
Publication Date (Web): December 20, 2009 | doi: 10.1021/bk-2009-1029.ch008

Downloaded by DUKE UNIV on June 28, 2012 | http://pubs.acs.org
Publication Date (Web): December 20, 2009 | doi: 10.1021/bk-2009-1029.ch008

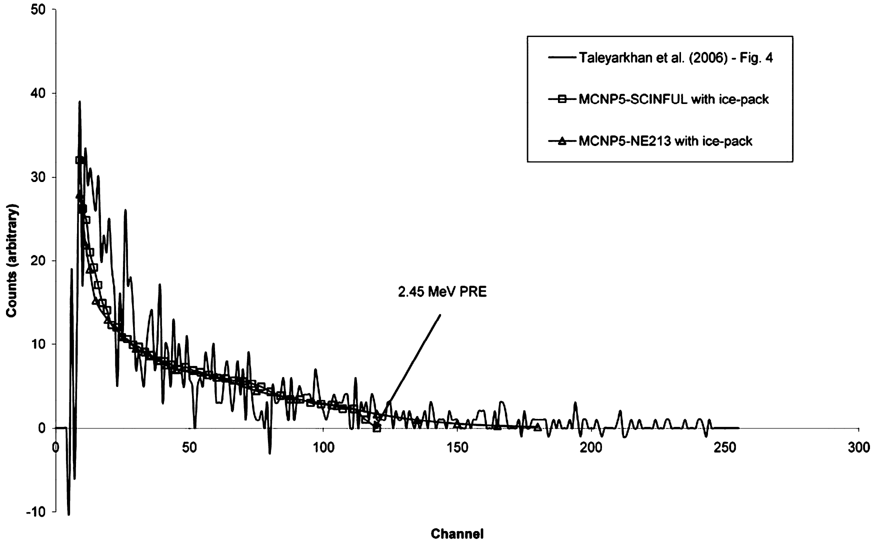

Fig. 6. Predictions (16) of MCNP5-SCINFUL and MCNP5-NE213 (Lee/Lee) Methods vs Measured Neutron Response Spectrum of Taleyarkhan et al. (5); With Ice-Pack Shielding.

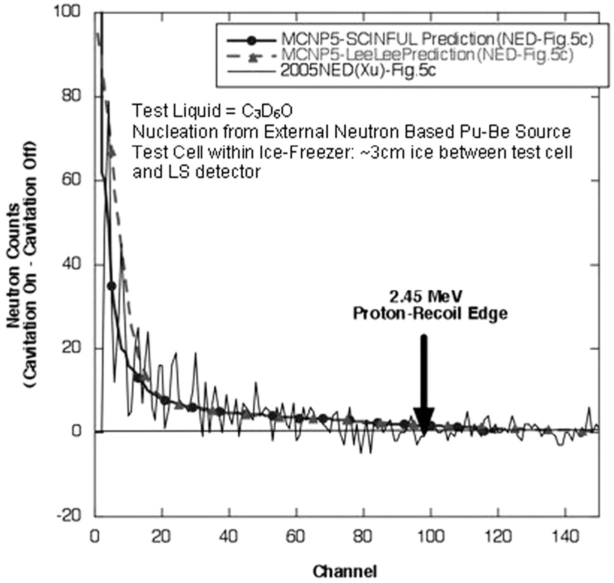

Fig. 7 Predictions (16) of MCNP5-SCINFUL and MCNP5-NE213 (Lee/Lee) Models vs Measured Neutron Response Spectrum (Cavitation On – Cavitation Off) of Xu et al. [(7) – Fig.5c] with Ice-Pack Shielding for External Neutron-Nucleated Fusion Experiments With Deuterated Acetone.

Downloaded by DUKE UNIV on June 28, 2012 | http://pubs.acs.org
Publication Date (Web): December 20, 2009 | doi: 10.1021/bk-2009-1029.ch008

The calculated neutron spectra without the inclusion of ice-pack thermal shielding are also consistent with the published spectra of Forringer et al. *(9, 10)* and Taleyarkhan et al. *(2)*, where intervening ice-pack shielding was not used for the specifically engineered experimental enclosures for these independent experiment campaigns. This is shown in Fig. 8 for the alpha-recoil-based self-nucleated experiments of Forringer et al. and in Fig. 9 versus the external accelerator-based monoenergetic 14.1 MeV neutron-seeded experiments of Taleyarkhan et al. *(2)* Once again, both independent Monte Carlo approaches well-predict each of the experimentally derived neutron spectra for these two different types of experiments, where intervening ice-pack shielding was not present. In Fig. 8, we also include the results obtained by Brian Naranjo *(13)* using the GEANT code *(20)* for the self-nucleation bubble fusion experiment without presence of the intervening ice-pack thermal shielding between the test cell and the LS detector. We see from Fig. 8 that the MCNP-SCINFUL and MCNP-NE213 approaches as well as the GEANT-code-based approach of Naranjo et al. reasonably well predict the measured experimental neutron spectrum of Forringer et al. and are consistent with each other in most respects. However, because of computer code limitations (associated with issues related to inability to model aspects of real-life, non-ideal practical detectors for their resolution capability for neutrons around the PRE channel), both MCNP-SCINFUL and GEANT code simulations predict absence of counts above the 2.45 MeV PRE channel, but the MCNP-NE213 approach predicts counts to occur above the PRE channel and is consistent with the measured data as also seen in the Forringer et al. data. This is as it should be, because the MCNP-NE213 approach is based on realistic LS detector spectra.

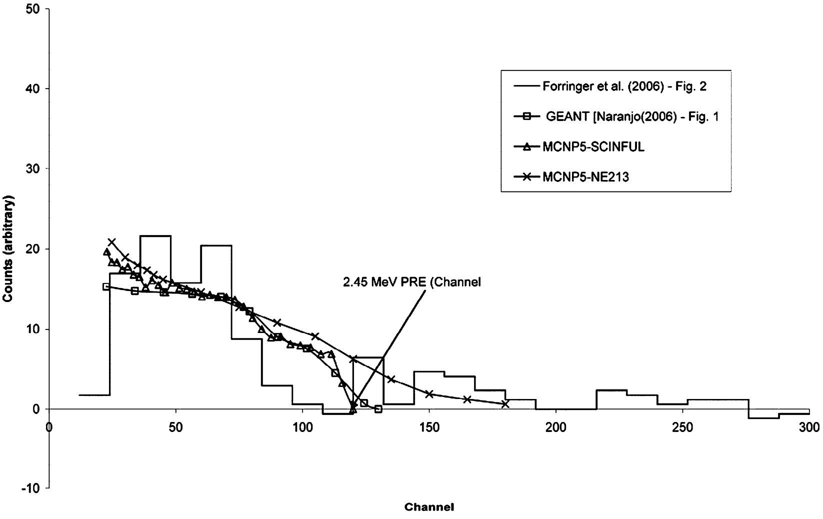

Fig. 8. Predictions (16) of MCNP5-SCINFUL and MCNP5-NE213 (Lee/Lee) Methods vs Measured Neutron Response Spectrum of Forringer et al. (9) for No Ice-Pack Shielding and scaled GEANT code Predictions from Naranjo (13).

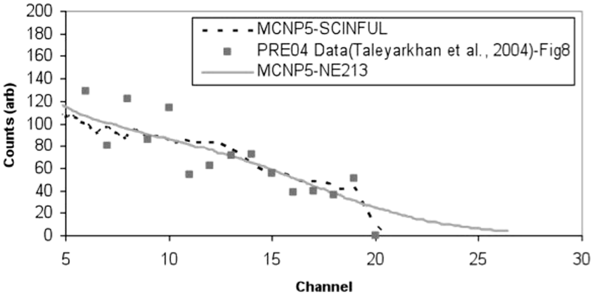

Fig.9. MCNP5-SCINFUL & MCNP5-NE213 Model Predictions (16) vs Excerpted Experimental Data (2) of Taleyarkhan et al. (i.e., difference of counts from Cavitation On minus Cavitation Off from Fig. 8c) with 14.1 MeV PNG Externally Nucleated Bubble Fusion Experiments. Note: Counts above the 2.45 MeV PRE channel #21 are difficult to distinguish because of the large 14.1 MeV neutron background counts of about ~70-80 counts per channel.

Bubble Fusion Neutron Counts Above the 2.45 MeV Proton-Recoil Edge

We have found that the experimentally measured counts of neutron spectra may give rise to counts above the so-called 2.45 MeV PRE. An in-depth study of the various effects reveal that this results from the following:

(i) imperfect resolution of practical versus theoretically ideal detector systems;

(ii) imperfect pulse-shape discrimination detector settings, which leads to gamma photon counts leakage into the neutron counts window;

(iii) neutron pulse pileup, a characteristic feature during bubble fusion induced neutron emissions. Other effects such as fission with uranium in self-nucleated bubble fusion experiments and from possible D-T reactions or ^{13}C-n interactions were found to be negligible. Details are provided elsewhere *(16)*. Because of its importance, however, a brief discussion is provided for the effect of neutron pulse pileup in relation to the physics and phenomenology governing bubble thermo-nuclear fusion.

Downloaded by DUKE UNIV on June 28, 2012 | http://pubs.acs.org
Publication Date (Web): December 20, 2009 | doi: 10.1021/bk-2009-1029.ch008

Pulse-Pileup Effects

The bubble nuclear fusion process involves a novel characteristic feature. That is, during bubble nuclear fusion, the neutron emission is not continuous or random but implosion-based; therefore, the neutron emission is time-structured. Our theoretical paper by Robert Nigmatulin et al., published in the journal *Physics of Fluids (4)*, implies that neutron pileup effects in the LS detectors of the type used in the reported studies of Taleyarkhan et al. *(2),* Xu et al. *(7)* and Forringer et al. *(9, 10, 11)* may indeed play an important role in the data trends recorded from bubble fusion experiments.

The theory of supercompression *(4)* reveals that the bubble implosion process leading to D-D fusion in a single bubble, which is part of a rapidly imploding cluster of bubbles, occurs within the time span of ~ 0.1 ps and that it will emit about 12 neutrons per implosion. We have estimated based on actual bubble cluster images (2) that a typical bubble cluster would comprise ~1,000 bubbles, of which 40 to 50 bubbles within the interior of the cluster may experience supercompression leading to D-D thermonuclear fusion conditions. There is uncertainty involved in estimating the time scale over which the 40-50 bubbles implode, but conservatively, we believe and estimate that these will implode over a time span of ~ 100 ps, emitting 200 to 400 neutrons. From this, we estimate the instantaneous rate of neutron emission to be up to ~ 4×10^{12} n/s; this is a very high rate, which makes it necessary to consider the influence on the detector response, which typically has a much slower response (shaping) time of only ~ 100 ns. That is, if, for example, two 2.45 MeV neutrons arrive at the detector within the response time of 100 ns, the two neutrons could be counted as only one neutron of higher energy than 2.45 MeV, thus giving rise to counts above the 2.45 MeV PRE channel.

The assessment of possible neutron pileup effects on our LS detector was conducted both with an accelerator-based pulsed D-T fusion neutron source at various intensities and through theoretical analyses.

Figure 10 shows the measured LS NE-213 detector's pulse-height spectra of 14.1 MeV neutrons for various target voltages of the accelerator source. The higher the target voltage, the greater is the intensity of neutron production within a given generation time, because of which the instantaneous rate rises with increased target voltage. For the experimental conditions of distance between neutron source and detector, the maximum instantaneous rate is expected to be around 10^{10} to 10^{11} n/s (much smaller than the estimated 10^{12} n/s for the published data from bubble fusion experiments). Even so, one notes the excess counts above the 14.1 MeV PRE for the same type and size of LS NE-213 detectors used for the published bubble fusion studies reported in this paper. Indeed, Fig. 10 demonstrates a steady increase in excess of counts above the PRE channel with increased rate of neutron emission.

A theoretical estimation of pulse-pileup effects was performed, providing estimates that are consistent with data from self-nucleation and external neutron-nucleated bubble fusion experiment observations. Details are to be found in the 2008 *Nuclear Engineering and Design* paper of Taleyarkhan et al. *(16).*

Downloaded by DUKE UNIV on June 28, 2012 | http://pubs.acs.org
Publication Date (Web): December 20, 2009 | doi: 10.1021/bk-2009-1029.ch008

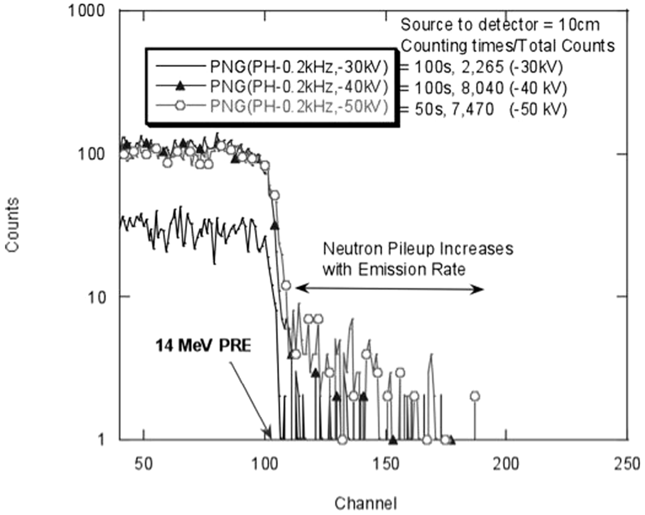

Fig. 10. Pulse height spectra at various PNG target voltages (16). (Note: -50kV data were taken over 50s not 100s.)

Clarifications and Comments on Reported Difficulties With Bubble Fusion Replication Experiments

As with any major technological development, the discovery of acoustic inertial confinement (bubble) thermo-nuclear fusion has created significant debate involving both technical and non-technical issues. An excellent compilation of the various attributes covering the human, technological, political and media-related issues has been developed *(21)*. This is the result of the efforts of editor Steven Krivit and his staff at *New Energy Times, Inc*. The Web-based database represents a valuable reference base for program managers, policymakers, scientists, scholars, historians and journalists.

In this chapter, we provide clarifications on only technical aspects related to two reports *(22,23)* in a credible peer-reviewed journal that discuss the inevitable difficulties associated with bubble fusion experimentation. The *New Energy Times* database *(21)* includes discussion of the underlying dynamics associated with these two scoping attempts, purported bubble fusion experimentation, that have been published in the scientific literature, one by Dan Shapira and Michael Saltmarsh *(22)* and the other by a team of authors from the UCLA-University of Illinois Urbana-Champaign (UIUC) research team *(23)*.

A correction of fact is presented first, in relation to the report of Ref. 22. The report of Ref. 22 as published gives the impression that this was an in-depth study independently conducted by Shapira and Saltmarsh. This is incorrect. The reported data of Ref. 22 were obtained by Shapira (a guest visitor not involved with test cell operations) using a different detector in the laboratory of Taleyarkhan et al. over a two-hour period of data acquisition on a single

Downloaded by DUKE UNIV on June 28, 2012 | http://pubs.acs.org
Publication Date (Web): December 20, 2009 | doi: 10.1021/bk-2009-1029.ch008

afternoon during scoping external neutron-seeded cavitation experiments with chilled deuterated acetone by the Taleyarkhan et al. group in their laboratory.

It is accepted and revealed by the authors of Ref. 22 and clarified elsewhere *(21, 24, 25)* that the result of data acquisition was indeed *positive*, in that, with a larger LS detector than that used by Taleyarkhan et al. *(1, 2)*, statistically significant (up to 10 SD) excess nuclear (neutron-gamma) emissions were indeed measured by Shapira and Saltmarsh *(22)*. These excess nuclear emissions were also time-correlated with SL emission *(25)*.

Shapira and Saltmarsh report their conclusion that the rate of excess neutron-gamma emission signal was smaller than the tritium emission rate reported by Taleyarkhan et al. *(1)*. However, Shapira and Saltmarsh did *not* themselves conduct experiments for, nor did they monitor for, tritium production during the experiment campaign when they obtained their neutron data.

We have cautioned repeatedly *(1, 2, 3, 4, 5)* that the bubble fusion output can vary significantly from experiment to experiment by orders of magnitude depending on several factors, such as drive amplitude, sphericity of bubbles, non-condensible gas content, and temperature of the deuterated liquid. Therefore, the positive outcome they experienced using their different LS detector for the excess rate of neutron-gamma emissions with external neutron-seeded cavitation experiments with chilled deuterated acetone simply cannot be directly related to the tritium production rate measured during experiment campaigns on other days and times by Taleyarkhan et al. *(1, 2)* or by Xu et al. *(7a, 7b)*.

The second reported study claiming lack of success is also discussed in Refs. 21 and 23. A brief clarification is presented in this chapter for completeness. The results of attempts by the UCLA-UIUC team *(23)* were unsuccessful basically because of the group's inability to conduct a mirror experiment as required – that is, to obtain the required test cell performance and operation as required and advised *(1, 2, 4)*. Ref. 23 itself reveals that the group intentionally and deliberately injected non-condensable gas, something we have admonished against. Instead, we have strongly recommended *(1, 2, 3, 4, 5)* that bubble fusion practitioners deliberately make efforts to completely de-gas the deuterated liquid to avoid dissipation of shock energy during implosion. Another principal deviation concerns the deliberate (as admitted in Ref. 23) misplacement of the top reflector in the resonant acoustic test cell. Ref. 23 admits that, because of inexplicable reasons related to test cell performance, the experiment team was forced to disallow positioning of the top reflector at the liquid-air interface. Avoiding the requisite positioning gives rise to spray formation at the liquid interface and interfacial instabilities, which can considerably lower reflected acoustic energy reaching bubbles during the critical implosion phase. Bubble cluster performance in Ref. 23 was that tending toward non-spherical clusters, and the rate and timing of cluster dynamics were also in conflict with advisement. The study of Ref. 23 failed to follow the required protocol for design and operation. Therefore, the reported difficulties in attaining bubble fusion conditions were to be expected, and this group confirmed when not to expect bubble fusion.

Downloaded by DUKE UNIV on June 28, 2012 | http://pubs.acs.org
Publication Date (Web): December 20, 2009 | doi: 10.1021/bk-2009-1029.ch008

Concluding Remarks

This chapter provides an update on the status of bubble fusion and independent replication/confirmation by several groups. Self-sustaining bubble fusion has been successfully demonstrated by our group with and without external neutron sources. Results have been demonstrated conclusively with compelling statistical significance ranging from 10 SD to more than 50 SD. A strong theoretical foundation has been developed that illuminates and supports our experimental observations of D-D fusion.

However, we have also found that obtaining null results is not unusual because the complex thermal hydraulics of bubble cluster implosions is not well-understood and because each test cell so far has been handcrafted using glassware fabricated by various glass blowers. Small dimensional differences of thickness and curvature for the multiple components of the test cell can and do tend to amplify acoustic wave transport characteristics, because of which similar-looking test cells can manifest radically different performance characteristics under the intense conditions of bubble fusion experiments. Especially important appears to be the impact on rate of bubble cluster nucleation, cluster sphericity, and transport through ultimate dissolution within miliseconds. Deviations from sphericity during implosion appear to be the leading reason for null results, a problem which is well-established as a key limiting factor even for laser-based inertial confinement fusion devices such as the well-known National Ignition Facility at Lawrence Livermore National Laboratory, Livermore, California, USA.

In summary, since 2004, there have been at least four successful reports along with two public demonstrations on replication and confirmation of our bubble fusion results by unaffiliated groups, and all significant technical issues that have been brought up in the scientific literature have been addressed conclusively.

Extensive three-dimensional calculations using well-established Monte Carlo code systems, backed with experimentation, confirm for the record that the confusion and controversies noted in past reports *(13, 14)* have resulted from a neglect of important details in the analysis of our bubble fusion experiments. Newer, more detailed results *(15, 16)* demonstrate that intervening shielding, gamma photon leakage and neutron pulse-pileup, from picosecond-duration neutron emissions during bubble implosion, can play important roles and, in fact, yield the unique signatures of the resulting neutron spectra during such experiments.

It is still too early to fully understand the implications of bubble fusion technology and how and when this approach to inertial confinement thermonuclear fusion might attain break-even conditions. Significant scientific and engineering challenges that remain in terms of the on-demand reproducibility of conditions required for supercompression and its scalability, the all-important issue of control, regulation and implementation are discussed in the archival journal *Multiphase Science and Technology (26)*.

Downloaded by DUKE UNIV on June 28, 2012 | http://pubs.acs.org
Publication Date (Web): December 20, 2009 | doi: 10.1021/bk-2009-1029.ch008

Acknowledgments

The research reported on here has been supported by the Russian Academy of Sciences, the Defense Advanced Projects Research Agency, the state of Indiana (Purdue University), the New York State Energy Research and Development Agency, and Rensselaer Polytechnic Institute. Their support is gratefully acknowledged.

References

1. Taleyarkhan, R. P.; West, C.; Cho, J. S.; Lahey, R. T.; Nigmatulin, R. I.; Block, R. C. Evidence for Nuclear Emissions During Acoustic Cavitation. *Science* **2002**, *295*, 1868.
2. Taleyarkhan, R. P.; Cho, J. S.; West, C.; Lahey, R. T.; Nigmatulin, R. I.; Block, R. C. Additional Evidence for Nuclear Emissions During Acoustic Cavitation. *Phys. Rev. E.* **2004**, *69*, 036109.
3. Lahey, R. T., Jr.; Taleyarkhan, R. P.; Nigmitalun, R. I.; Akhatov, I. S. Sonoluminescence and the Search for Sonofusion. In *Advances in Heat Transfer;* Hartnett, J. P., Ed.; Academic Press: **2006**; Vol. 39, pp 1-168.
4. Nigmatulin, R. I.; Akhatov, I.; Bolotnova, R. K.; Topolnikov, A. S.; Vakhitova, N.K.; Lahey, R. T.; Taleyarkhan, R. P. The Theory of Supercompression of Vapor Bubbles and Nano-Scale Thermonuclear Fusion. *Physics of Fluids* **2005**, *17*, 107106-1.
5. Taleyarkhan, R. P.; West, C.; Lahey, R. T.; Nigmatulin, R. I.; Block, R. C.; Xu, Y. Nuclear Emissions During Self-Nucleated Acoustic Cavitation. *Phys. Rev. Lett.* **2006,** *96*, 034301-1.
6. Didenko, Y. T.; Suslick, K. The energy efficiency of formation of photons, radicals and ions during single-bubble cavitation. *Nature* **2002,** *418*, 294.
7. a) Xu, Y.; Butt, A. Confirmatory Experiments for Nuclear Emissions During Acoustic Cavitation. *Nuclear Engineering and Design* **2005,** *235*, 1317.

   b) Xu, Y.; Butt, A.; Revankar, S. Bubble Dynamics and Tritium Emission During Bubble Fusion Experiments. *Paper 548-Proceedings of the Eleventh International Conference on Nuclear Reactor Thermal Hydraulics.* Avignon, France. October 2-6, 2005.
8. Innovative Confinement Concepts Workshop (Skunkworks Session), Austin, Texas, February, 2006. Impulse Devices Inc. staff R. Tessien declared their findings of successful replication of Taleyarkhan et al. *(1, 2)* results for neutron emission from deuterated acetone but not from control experiments with normal acetone on verbal basis to audience as part of the invited lecture by R. P. Taleyarkhan.
9. Forringer, E. R.; Robbins, D.; Martin, J. Confirmation of Neutron Production During Self-Nucleated Acoustic Cavitation. In *Transactions*

Downloaded by DUKE UNIV on June 28, 2012 | http://pubs.acs.org
Publication Date (Web): December 20, 2009 | doi: 10.1021/bk-2009-1029.ch008

of the American Nuclear Society Winter 2006 Meeting, Albuquerque, NM, November 12-16, 2006; Yoelin, C.A.; Rule, J. B.; Eds.; American Nuclear Society: La Grange Park, IL, 2006; Vol. 95, pp 736-737.

10. Forringer, E. R.; Robbins, D.; Martin, J. Confirmation of Neutron Production During Self-Nucleated Acoustic Cavitation of Deuterated Benzine and Acetone Mixture. *Proceedings of the 17th Topical Meeting on the Technology of Fusion Energy*, Albuquerque, NM, November 12-16, 2006.
11. Bubble Fusion Confirmed by LeTourneau University Research. Le Tourneau University press release, Nov. 17, 2006.
12. Bugg, W. Report on Activities on June Visit. Report to Purdue University, June 9, 2006 (transmitted from W. Bugg to R. P. Taleyarkhan, Purdue University).
13. Naranjo, B. Comment on "Nuclear Emissions During Self-Nucleated Acoustic Cavitation." *Phys. Rev. Lett.* **2006,** *97*, 149403.
14. Reich, E. Fusion Verdict: Misconduct. *Nature*, July 28, 2008, 454379a.
15. Taleyarkhan, R. et al. Reply. *Phys. Rev. Lett.* **2006,** *97*, 149404.
16. Taleyarkhan, R. et al. Modeling, Analysis, and Prediction of Neutron Emission Spectra From Acoustic Cavitation Bubble Fusion Experiments. *Nuclear Engineering and Design*, **2008,** *238*, 2779-2791.
17. Monte Carlo Team, MCNP – A General Monte Carlo N-Particle Transport Code, Ver. 5, Vol. 1: Overview and Theory, LANL Report LA-UR-03-1987. Los Alamos National Laboratory, Los Alamos, N.M., USA., 2003.
18. Dickens, J. K. SCINFUL: A Monte Carlo Based Program to Determine a Scintillator Full Energy Reponse to Neutron Detection for EN Between 0.1 and 80 MeV; User's Manual and FORTRAN Program Listing, ORNL-6462. United States Department of Energy Radiation Safety Information Computational Center (RSICC) Report, PSR-267. Oak Ridge, TN, USA, 1988.
19. Lee, J. H.; Lee, C. S. Nuclear Instrum. Methods Phys. Res. A. **1998,** 402.
20. Agnostinelli, S. et al. Geant4 – A Simulation Toolkit. *Nuclear Instrum. Methods Phys. Res. A.* **2003,** *506*, 250-303.
21. New Energy Times, Inc. bubble fusion Web-portal site. http://newenergytimes.com/v2/bubblegate/BubblegatePortal.shtml.
22. Shapira, D.; Saltmarsh, M. Nuclear Fusion in Collapsing Bubbles: Is It There? An Attempt to Repeat the Observation of Nuclear Emissions From Sonoluminescence. *Phys. Rev. Lett.* **2002,** *89*, 104302.
23. Camara, C. G.; Hopkins, S.; Suslick, K.; Putterman, S. Upper Bound for Neutron Emission From Sonoluminescing Bubbles in Deuterated Acetone. *Phys. Rev. Lett.* **2007,** *98*, 064301.
24. Nigmatulin, R. I.; Taleyarkhan, R. P.; Lahey, R. T. Evidence for nuclear emissions during acoustic cavitation revisited. *Proceedings of the Institution of Mechanical Engineers, 2004, J. Power and Energy* **2005,** *218(5)*, Part A: Special Issue Paper; pp 345-364.

Downloaded by DUKE UNIV on June 28, 2012 | http://pubs.acs.org
Publication Date (Web): December 20, 2009 | doi: 10.1021/bk-2009-1029.ch008

25. Taleyarkhan, R. P.; Block, R. C.; West, C. D.; Lahey, R. T. Comments on the Shapira and Saltmarsh Report. *Science* **2002,** *295*, Ref. 32; also on www.bubblegate.com.
26. Taleyarkhan, R. P.; Lahey, Jr., R. T.; Nigmatulin, R. I. Bubble Nuclear Fusion Technology – Status and Challenges. In *Multiphase Science & Technology: A Quarterly;* Matar, O.; Delhaye, J.-M., Eds.; Begell House: Redding, CT, 2005; Vol. 17, No. 3; pp 191-224.

Downloaded by DUKE UNIV on June 28, 2012 | http://pubs.acs.org
Publication Date (Web): December 20, 2009 | doi: 10.1021/bk-2009-1029.ch008

Chapter 9

Sonofusion, Deuterons to Helium Experiments

Roger S. Stringham

First Gate Energies, PO Box 1230, Kilauea, HI 96754

Downloaded by PENNSYLVANIA STATE UNIV on June 28, 2012 | http://pubs.acs.org
Publication Date (Web): December 20, 2009 | doi: 10.1021/bk-2009-1029.ch009

Experimentally, heat and ^{4}He are generally the byproducts of sonofusion. Sonofusion uses the leverage of argon-saturated cavitation-induced D_2O bubbles and their collapse to transient high-energy density jets to implant deuteron clusters into a target lattice matrix. The coherent electromagnetic environment within these transient clusters produces deuteron fusion events. Mass spectra and calorimetric measurements of the fusion products are described. What has been increasingly evident in sonofusion is the parallel that exists between sonofusion and high-density experiments of inertial confined fusion *(1)*, Bose-Einstein condensates, astrophysical phenomena, and muon fusion. All of these help to explain our ecological fusion results.

Introduction

The sonofusion process produces heat, ^{4}He, and other fusion products. These products originate in very high transient densities produced by the collapse of transient cavitation bubbles and in DD muon fusion *(2)*. Muon fusion has about 100 times the density and 20 percent of the separation of deuterons in sonofusion clusters. At 100 ^{o}K, the muon fusion ion DDμ easily fuses the deuterons, but the two-atom system uses a different channel to produce ash products because it cannot distribute the heat of fusion to its surroundings as in the Bose-Einstein condensate sonofusion cluster, a superfluid. The low mass of two deuterons of muon fusion does not compare to that of the million deuterons in the coherent cluster of sonofusion. The cluster is similar to a nano-star with less than a picosecond lifetime. It differs in that it consists of only plus-charged deuterons. The escape pressures, although large, are overwhelmed by the

In Low-Energy Nuclear Reactions and New Energy Technologies Sourcebook Volume 2; Marwan, J., et al.;
ACS Symposium Series; American Chemical Society: Washington, DC, 2010.

compression pressures derived from the electromagnetic acceleration of the implanted free electrons to the deuteron cluster's plus charge.

The transient high-density environment follows a natural picosecond process initiated by transient cavitation bubbles in water. The density range of coherent matter extends from 10^{14} particles/cc found in ultra-cold crossover systems to 10^{30} particles/cc found in the cooling small white dwarf star and muon fusion's DDμ. There is a critical-temperature, Tc, limit on the temperature of these systems. An obtainable upper density of around 10^{27} particles/cc is possible when the sonofusion cluster environment exists for a picosecond. The temperatures in the cluster environment are relatively cool because of deuteron plasma evaporation from the cluster's surface that cools the cluster *(3)*.

This cooling allows for De Broglie matter wave overlap to incorporate the Bose-Einstein condensate properties into the sonofusion cluster. The cluster deuteron bosons are in their ground state, with the closest energy state an Mev higher. The naked deuteron described by the Nucleus Shell model has no electrons in its nucleus or cluster. Ordinary matter, where nuclei and electrons with their 0.1 ev energy states above the ground state, will inhibit the formation of Bose Einstein Condensates. The phase change Tc is increased for these deuteron clusters because of the Mev separation between energy states of the model deuteron. The transient existence of this bubble-produced cluster in the target foil is similar to DDμ and has the DD spacing of less than the De Broglie wavelength in deuteron clusters.

The multi-bubble cavitation system produces millions of ejecta sites as shown in scanning electron microscope photos of exposed target foils. In the 1.6 MHz sonofusion systems, the period of this cycle is less than a micro-second. After implantation, the fusion contact time of a picosecond is enough for a DD fusion event, which will destroy the cluster and end all fusion in that cluster. The initiated fusion heat pulse results in ejecta sites for low-frequency cavitation systems. Ejecta sites decrease in size but increase in number as the acoustic frequency is increased. From the transient cavitation bubble, heat, ^{4}He, and ejecta sites are the experimental results on which sonofusion rests.

As the sonofusion bubble collapses, a dense plasma jet is injected into the cavitating D_2O, and the jet accelerates as it implants into the target foil, where fusion occurs in squeezed and cooled clusters. The energy produced by the fusion reaction terminates the cluster with a spherical heat pulse that expands to the target lattice surface, where it ejects metal from the target foil as a vapor. The volcano-like eruption from the target foil leaves an ejecta site frozen in the target foil that is ideally suited for analysis by scanning electron microscopy. Details can be found in the author's earlier papers and in reference *(4)*.

Short History of Sonofusion

The author's first experiments in sonofusion started early in 1989, following the announcement by Martin Fleischmann and Stanley Pons. Although not initially known as sonofusion, cavitating D_2O with palladium target foil experiments began within a week of the Fleischmann and Pons announcement. The initial experiments were at 20 KHz in large and cumbersome 20 kilogram devices that over 19 years have evolved to 1.6 MHz 20 gm devices with about the same excess-heat output. Over this period, the device size was reduced and

Downloaded by PENNSYLVANIA STATE UNIV on June 28, 2012 | http://pubs.acs.org
Publication Date (Web): December 20, 2009 | doi: 10.1021/bk-2009-1029.ch009

piezo frequency increased for the evolving sonofusion systems. In the last 10 years, it was slowly realized that the high transient density of inertial confined fusion, new astrophysical information and ultra-low-temperature bosons/fermions can be extended and linked to sonofusion. The sonofusion systems are 1,000 times faster and billions of times smaller in volume and number of particles than hot-fusion inertially confined systems. The number of micro-bubbles produced per second (about 10^{14}) is additive and typically produces 40 watts of excess heat in the 1.6 MHz systems discussed in this paper.

The Cavitation Bubble

A quick view of cavitation and some of the basic information on the well-documented cavitation process that produces very high transient energy densities follows. Cavitation is known to be destructive to ship propellers and pump impellers and the industrial movement of liquids. This cavitation process has been researched in great detail *(5)*. To produce a transient cavitation bubble environment, we use a piezo resonating crystal and, in recent years, a 1.6 MHz piezo device producing a variable-size bubble population in D_2O. A selected initial bubble radius (Ri) grows isothermally, increasing its mass and radius to a maximum (Ro), where it collapses adiabatically to a final radius (Rf) producing sonoluminescence and a high-density jet.

Downloaded by PENNSYLVANIA STATE UNIV on June 28, 2012 | http://pubs.acs.org
Publication Date (Web): December 20, 2009 | doi: 10.1021/bk-2009-1029.ch009

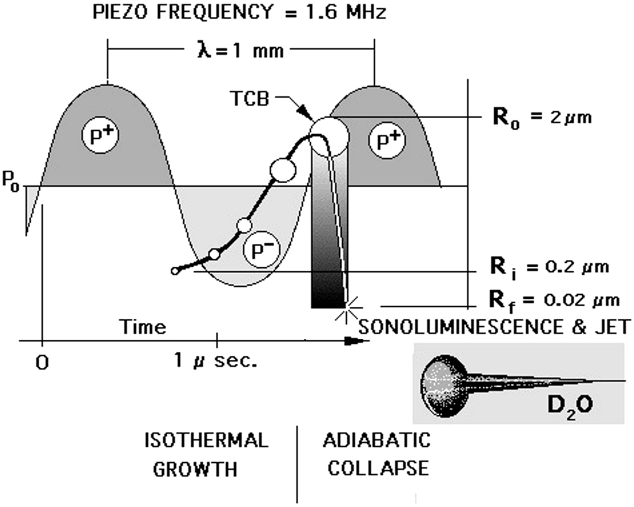

Figure 1. 1.6 MHz cavitation bubble sequence.

Figure 1 shows the piezo-driven ultrasound system that produces a sinusoidal wave in circulating D_2O. This wave consists of a negative and positive pressure wave oscillating around the average external pressure at a frequency of 1.6 MHz. The pressure pulse is proportional to the voltage amplitude and piezo displacement. One sinusoidal wavelength defines the time for a generation of bubbles that cycles through a birth, collapse, and jet formation cycle as the D_2O prepares for its next low-pressure cycle and generation of transient cavitation bubbles. At 1.6 MHz, this is a fast sequence taking about 100 nanoseconds for the adiabatic collapse.

An oscillator-driven 1.6 MHz piezo resonance system produces millions of bubbles with an initial radius of around 0.2 microns. As the bubble expands in the low-pressure isothermal growth, it picks up D_2O vapor mass from the bubble's interface. Progressing, the acoustic pressure passes into the positive pressure zone of the acoustic wave, where the partially evacuated bubble reaches its maximum radius of about 2 microns. At this point, the partially evacuated bubble starts its sub-microsecond collapse. In the collapse, the bubble surface accelerates toward its center at Mach 4 velocity *(6)*. The bubble's somewhat leaky adiabatic collapse has a final radius of about 0.02 microns. At this point, two events occur: A burst of photons is emitted as sonoluminescence, and the plasma contents of the bubble are transferred to a jet, where electromagnetic compression further squeezes the jet's contents.

There is a tremendous increase in the bubble's energy density during its collapse, while the external pressure controls the initial energy density over the circulating D_2O. A crude one-acoustic-cycle example of a transient cavitation bubble's adiabatic collapse shows a one-hundred-fold decrease in the bubble's radius. An increase in the bubble's content mass leads to about a one-million-fold increase in the bubble's energy density. The energy is enough to dissociate some of the D_2O in the bubble contents.

When the transient cavitation bubble reaches its final radius, a narrow pulse of sonoluminescence photons is emitted, and a collapsed bubble forms a jet. The jet has a sheath of electrons carried over from the bubble's interface. The jet is a high-density deuteron plasma confined by electromagnetic pressure *(7)*. This is the first step in producing heat and ^{4}He in a sonofusion system. See figure 2.

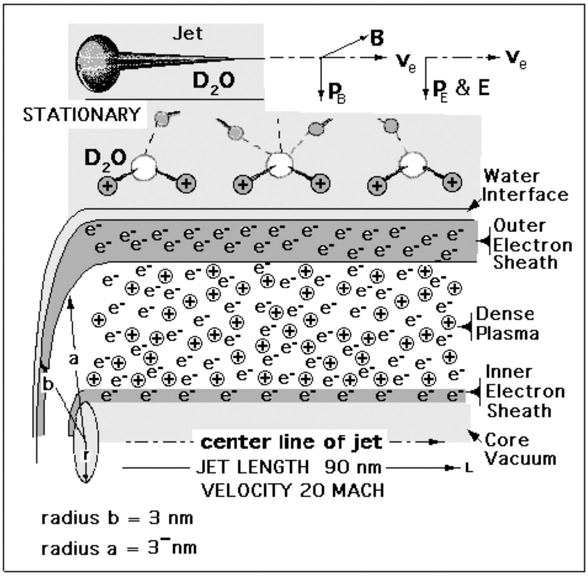

Figure 2. The complex plasma configuration of the transient compressed jet.

Downloaded by PENNSYLVANIA STATE UNIV on June 28, 2012 | http://pubs.acs.org
Publication Date (Web): December 20, 2009 | doi: 10.1021/bk-2009-1029.ch009

The tremendous energy-density gain of a collapsed cavitation bubble via its sub-microsecond implosion process produces two effects. These are sonoluminescence photons and a deuteron accelerator in the form of a jet that follows from the transient cavitation bubble implosion. The cavitation technology is well-understood except for the sonoluminescence generation, where the emitted photon's wavelength is longer than its origin, which is the transient cavitation bubble's final diameter *(8)*. A benefit of using D_2O is that its dissociated fragments return to D_2O and produce a small steady-state concentration of D_2 and DOOD, which is ideal for a commercial operation. Other more complex cavitating deuterium-containing liquids will form oligomers contaminating the circulating liquid.

Downloaded by PENNSYLVANIA STATE UNIV on June 28, 2012 | http://pubs.acs.org
Publication Date (Web): December 20, 2009 | doi: 10.1021/bk-2009-1029.ch009

Related Technology

One of the remarkable aspects of sonofusion development is that the application of much of the technology originates in hot fusion research and applies to the containment of the D^+ plasma in the sonofusion jet and deuteron clusters. The hot fusion community has in-depth studies of sausage and kink pinches in the plasma that appear several milliseconds after the plasma initiation in Tokomak-like plasma systems. These same studies of z-pinches can be applied to the much-denser sonofusion plasma systems. The electromagnetic forces that terminate these hot fusion plasmas are the very forces that compress the much smaller transient cavitation bubble, jet, and cluster in sonofusion. The attempts of the various hot fusion systems to control the plasma with electromagnetic forces to extend the plasma's useful life have failed. Continuous circulation of hot fusion plasma was to have been the answer for the world's growing energy problem. These results have been a major disappointment for the hot fusion community. However, the z-pinch developing technology parallels the sonofusion technology where pressure generation confines the transient cavitation bubble jet's contents into its long and pointed geometry for picosecond confinement times.

Extrapolation of hot fusion z-pinch, imploding wire, frozen deuterium fiber, and inertial confinement fusion backlighting technology *(9, 10)* to sonofusion has been very helpful in explaining the characteristics of the sonofusion process *(11)*. The pressures that hold, compress, and accelerate the jet plasma for its implantation into the target foil are analogous to the squeezing of high-density z-pinch pressures. The scaling down of high-density z pinch methods to the jet size will place these systems into the sonofusion range. A comparison of high-density z-pinch methods and other fusion systems to sonofusion has been made. High-density plasma jets are natural constructions along the lines of a plasma capacitor with sheath electrons at the exterior and interior of the jet plasma and are transient multi-layered systems. See figure 2. In astrophysics, the multi layers refer to compartmentalized plasma systems often associated with Alfven waves *(12)* [the Alfven waves and jets recently described from measurements made by the Hinode solar telescope]; however, the sonofusion jet is surrounded by the dielectric D_2O *(13)*, with the jet volume limited to the nano size range (90 nm long and 3 nm in radius for the 1.6 MHz jet). The jet with a velocity *(6)* in the Mach 20 range (30 k/sec) has electromagnetic fields that contribute to the z-pinch shaping of the sonofusion jet. Backlighting experiments in 2008 show the transient production of electromagnetic fields of 10^9 V/m and 60 Tesla in their inertial fusion implosions *(10)*. These experiments produced compressed densities of 0.3 Kgm/cc, more dense than the sun. Assuming liquid deuterium has a density of 0.19 gm/cc at one atmosphere, the density of the deuteron cluster for sonofusion is around 4+ kilogram/cc. These inertially confined backlighting crushed capsules are much larger in volume and in the number of particles encapsulated than in the sonofusion clusters, but there is a strong similarity between them, although sonofusion environments are ten times more dense. The contents of the sonofusion jet, containing about 10^7 deuterons, are compressed by electromagnetic forces more effectively than in the high-current discharge into the frozen deuteron fiber *(9)*. Hot fusion inertial confinement experiments also show some parallels to the much smaller one-million-deuteron cluster systems produced by sonofusion methods.

Downloaded by PENNSYLVANIA STATE UNIV on June 28, 2012 | http://pubs.acs.org
Publication Date (Web): December 20, 2009 | doi: 10.1021/bk-2009-1029.ch009

No Gamma Radiation

The transient cluster density is the origin of DD fusion events; the clusters have an approximate density of 10^{27} deuterons/cc with the clusters being more or less equal in density and number of deuterons. For example, a cluster temperature at 2,000 ^{o}K with four times the De Broglie overlap would lead to a coherent Bose Einstein condensate cluster environment for the sonofusion of DD → heat and ^{4}He. Gammas are not produced because the boson cluster's De Broglie wave overlap will distribute the DD fusion energy throughout the cluster as heat before the gamma-producing reaction can take place. [S. Chubb, T. Chubb, P. Hagelstein, Y. Kim and others who have presented theories on why gammas are not present, most recently at ICCF 12, Nov.-Dec. 2, 2005, Yokahama, Japan.] This heat is the result of the excess power, Qx, that is measured by calorimetry. A plasma cluster environment is commonplace in the astrophysical star community *(14)*.

Experimental Evidence 20 and 40 KHz

The left side of figure 3 shows cavitation-exposed 100μm-thick Pd target foil, and the right side shows the ejecta site count and size for the surface area in the graph. It shows the ejecta size distribution vs. the vent site diameter in nm. The diameter of ejecta sites is proportional to the volume of ejecta and is in turn a function of the ejecta energy. Through this simple relationship, the energy of the ejecta event is calculated from the various ejecta volumes. The instant the cavitation process is stopped, the foil is frozen and is an ideal candidate for a scanning electron microscope analysis of the foil surface. In the interior of the larger vent sites, scanning electron microscopy reveals spheres of recondensed target foil that were loosely coalesced or fused in and on the target foil vent site surface. The spheres are typically 1 micron or less in diameter. The path from the jet plasma formation to the ejecta site is reasonable but is not the only path to

DD fusion. A number of sonofusion reactors have been used to gather data, each with some improved operating characteristics *(15)*. [The reactors used from 1989 to 2000 were in the frequency range of 20 to 46 KHz and were quite cumbersome compared to the 1.6 MHz devices. These reactors – MI, MII, MIII, and MIIII – are reviewed in (*16*).]

Scanning electron microscopic analysis of the target foils shows a distribution of many ejecta sites that range from 50 nm to 3,000 nm in diameter at 40 KHz. These sites are very common and are continually being created and destroyed by jet implants into the target foil, much like the changing surface of the moon during meteor bombardment. When cavitation is stopped, a record of the last events remains frozen at that specific time on the target surface. The population diameter versus the calculated site energy of ejecta at the time of formation shows a maximum population of ejecta sites with a diameter of approximately 100 nm. A survey for ejecta sites of 1 square µm of Pd surface shows the population distribution of figure 3.

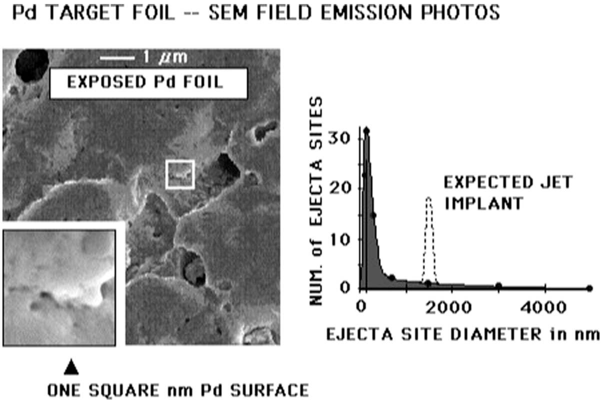

Figure 3 is a FE SEM photo (6400 JOEL instrument) of a 46 KHz cavitation exposed 100m-thick Pd target foil from a run at Stanford Research International, SRI.

Fusion Heat Pulse

It is possible to calculate the energy required to vaporize and accelerate a volume of target lattice from an ejecta site into the cavitating D_2O, and such a calculation over several areas of ejecta sites yields similar results. For example, a count of 51 ejecta sites found in a random 80 µm^2 area of exposed target results in a population size distribution of ejecta sites. The calculation involves the velocity of the shock wave in the palladium target, the energy of palladium atomization, the diameter, and the number of vaporized palladium atoms in the ejecta. As an example, consider a single fusion event ejecta site about 100 nm in diameter; the spherical heat pulse expands from the implanted fusion point in the lattice 50 nm below the surface of the target. The shock wave of the fusion

Downloaded by PENNSYLVANIA STATE UNIV on June 28, 2012 | http://pubs.acs.org
Publication Date (Web): December 20, 2009 | doi: 10.1021/bk-2009-1029.ch009

heat pulse expands from the deuteron cluster through the lattice to the target surface as a spherical heat pulse. The contents of this heat pulse are ejected as a plume into the circulating D_2O with a velocity of 4,000 m/sec and a temperature of about 4,000 °K. The energy in the heat pulse is on the order of 10^{-11} Joules for the 100 nm diameter ejecta site. The important factor in this calculation is the 377 KJ/moles heat of vaporization for the 10^{12} ejected palladium atoms. The energy of about 10 fusion events is about $4x10^{-11}$ Joules that triggers a heat pulse during the one-cycle bubble collapse. The fusion event terminates as an ejecta site. A single fusion event has a diameter of 50 nm and is the most numerous at the high frequency of 1.6 MHz. See figure 3.

Downloaded by PENNSYLVANIA STATE UNIV on June 28, 2012 | http://pubs.acs.org
Publication Date (Web): December 20, 2009 | doi: 10.1021/bk-2009-1029.ch009

Helium Mass Spectral Analysis

Helium was collected by vacuum transport in 50 cc stainless-steel sample volumes for mass spectral measurements from the M II 20 KHz reactor. The data presented here represented by ejecta energy and volume is proportional to its formation energy; it can be related to the minimum volumes corresponding to one sonofusion event of about 20 Mev. These smallest and second-most-common ejecta sites are evidence of a single fusion event for these clusters. The larger sites are multiple events representing perhaps a million events. The ^{4}He that was ejected with the vaporous foil was collected in sample volumes and sent out for analysis [Brian Oliver; DOE MS analysis of ^{4}He &^{3}He for EQuest Sciences, report; 1995; Helium Analysis of Gas Samples. B. M. Oliver, Rockwell International, Canoga Park, CA 91309. What was EQuest? It was a research and development laboratory working with the harvesting of energy from transient cavitation bubble initiated fusion - Sonofusion. EQuest visited LANL at the invitation of Tom Claytor and Dale Tuggle with George Chambers present from the NRL in Washington, DC, facilitated by Russ George. In 1998, I closed EQuest Sciences, transferring all assets to First Gate Energies, with some personnel changes.].

Table 1 shows the results of these fusion product measurements for ^{4}He and T $\rightarrow ^3$He. These collected gases were measured for the amount of helium present. Included in the measurements are 1 A, B, and C. This was the background amount of helium and served as a calibration for this set of measurements. The helium measurements that will be discussed are 3 A, B, and C. Brian Oliver performed the mass spectral analysis at the Department of Energy facility at Rockwell International. Initially, he had no knowledge of the history of the gas sample volumes 1, 2, and 3 sent to him. There were later measurements on sample volume 2 not shown in the data of Table 1. Sample volume 2 was taken from a target foil of titanium, and measurements over time were consistent with tritium decay to helium 3. Table I includes the analysis for ^{3}He products from tritium decay in measurements 2 A, B, and C but would require too lengthy an explanation to be included in this paper. The ^{3}He tritium issue should be covered with a complete divulgence and interpretation of the data.

The preparation for mass spectrum analysis of gas sample 3 was associated with instrument and carbon column vacuum bake-outs and standardized with calibrated helium gas mixtures. This methodology was reflected in Oliver's draft report. The liquid-nitrogen-chilled carbon column removed all potential eluting interference of low mass species. No ^{3}He above background was found, but the ^{4}He was 552 ppm, 100 times more than found in normal air. The absence of the helium-associated gamma points to the 23.6 Mev fusion energy as the source of the calorimetric-measured Qx. This conversion of fusion energy to a heat pulse is covered in the text *(16, 17)*.

Table 1

Sample Cyl.	Measured ^{3}He (10^{14} atoms)	Measured ^{4}He (10^{14} atoms)	^{4}He in Cyl. (10^{14} atoms)	^{4}He in ppm (10^{14} atoms)
1 A	<0.0002	0.2506	4.632	.417
B	nm	0.2436	4.760	.484
C	nm	0.2237	4.621	.470
			Mean +/-1σ	
2 A	0.0042	0.7696	31.31	2.548
B	0.0042	0.75221	31.37	2.552
C	0.0039	0.7357	31.46	2.560
			Mean +/-1σ	
3 A	<0.0002	188.2	7483	553.5
B	<0.0002	182.6	7447	550.9
C	nm	178.3	7460	551.8
			Mean +/-1σ	

Experimental (1.6 MHz devices)

Calorimetry for the 1.6 MHz 20 gram devices follows and is further described in figure 4. The basis used for the calorimetry was watts-in equals watts-out. This is the case in the calibration mode, Qi = Qo. When running in cavitation mode, power out is typically greater than power in, resulting in excess power, Qx. The acoustic input power Qa should be equal to Qo, but if the Qo measurement is greater than Qa, then that difference is excess heat, Qx, from the DD fusion reaction. The calorimetric measurement of Qo – Qa = Qx, where Qx is the result of two D boson ions fusing in the sonofusion cluster. $Qx = mc^2$ watts and is coupled to ^{4}He production as represented by $D^+ + D^+ \rightarrow {}^4He^{++} + 23.6$ Mev. This is the sonofusion model *(18)*.

The flow-through type of calorimetry used for low-mass sonofusion devices takes advantage of the large mass of D_2O flow compared to the mass of the device and the violent acoustic mixing in the 1 cc reaction volume of the D_2O flow. The residence time of D_2O in the device was about a second. A calibration mode performed with a Joule heater within the device's D_2O flow volume matched the run mode. The graphs of these two modes allow for calorimetry of +/- 2 watts.

Downloaded by PENNSYLVANIA STATE UNIV on June 28, 2012 | http://pubs.acs.org
Publication Date (Web): December 20, 2009 | doi: 10.1021/bk-2009-1029.ch009

Downloaded by PENNSYLVANIA STATE UNIV on June 28, 2012 | http://pubs.acs.org
Publication Date (Web): December 20, 2009 | doi: 10.1021/bk-2009-1029.ch009

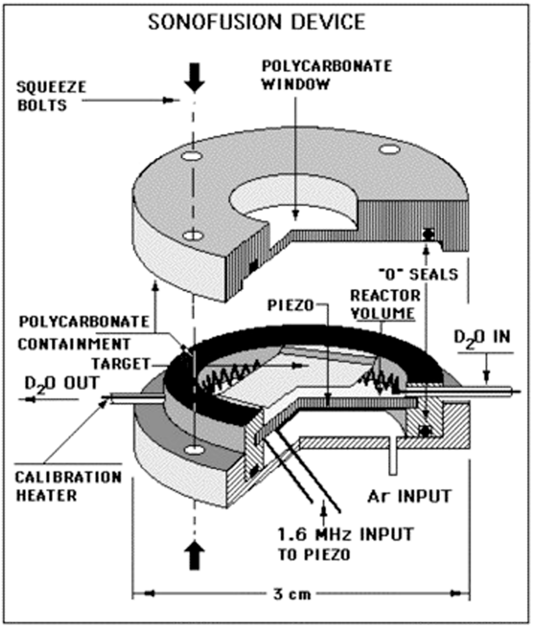

Figure 4 is a schematic of a 1.6 MHz SF device with polycarbonate containment and window and its geometric configuration.

In running mode, the determination of excess heat was accomplished using the D_2O flow-through calorimetric measurements of the 1.6 MHz piezo-driven low-mass 20 gm device. The reaction volume of this device was 1 cc. See figure 5. The inlet and outlet temperatures of the D_2O flowing through the device were measured to produce a differential temperature called DT; the flow rate was measured in cc/sec and multiplied by DT to give calories/sec. This result was multiplied by 4.184 Joules/calorie to give the total heat out in watts (Qo). At this point, output power contains both the 1.6 MHz acoustic input to the device Qa and excess heat Qx. So Qo = Qa + Qx. The efficiency of Qi was measured at 0.33 (2). Some of Qi powers a transformer and the 1.6 MHz oscillator. The efficiency of Qi to produce Qa = .33 Qi. To show the dynamics of Qx production, one can plot in real time the Qx production, Qo - Qa versus Qi.

The squeeze bolts provide a seal for the Ar that makes for a watertight device. The polycarbonate window piece, with the “O” ring gasket, seals the reaction volume. The window allows for the count of sonoluminescence photons via a photomultiplier, PMT. With the squeeze in place, the target foil is held tightly and acts as a shield for the window, blocking most of the cavitation’s activity from damaging the window. The high-resistance wire calibration heater is placed peripheral to activity of the 1.6 MHz acoustic fields generated in the circulating water.

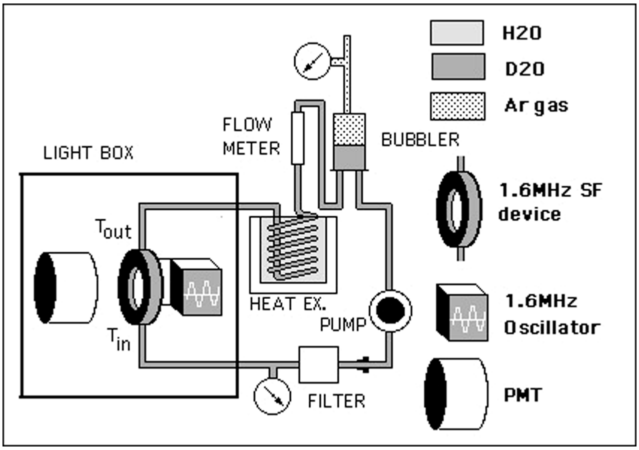

Figure 5. The experimental sonofusion system was set up to measure calorimetry via the temperature difference between the input and output.

The residence time for D_2O in the 1 cc reactor volume is less than 1 second at a flow rate of 1 cc/sec. The external pressure for these runs was 1 atmosphere of argon. The sonofusion device uses a joule heater replacing Qa and Qx in the calibration mode. One must be careful to guard against radio-frequency interference during thermocouple measurements. Measurements show that some heat is lost via convection from the device's surface, and it is possible for very small superheated steam bubbles to escape the DT measurement. These errors reduce the measured values of Qx from their real value and are deemed conservative errors.

Figures 4 and 5 describe the 1.6 MHz experimental system that produced the data in figure 6 and the graph of the calorimetric-measured excess power, Qx. New systems with DC inputs to power the oscillator and a better DC calibration heater are being tested for a portable exhibition device. It will consist of two modes in one device, where the calibration and running modes can be toggled back and forth. By comparing data from the two modes, observers will see a clear distinction. Excess power will be observed only in the running mode.

Downloaded by PENNSYLVANIA STATE UNIV on June 28, 2012 | http://pubs.acs.org
Publication Date (Web): December 20, 2009 | doi: 10.1021/bk-2009-1029.ch009

DATA

Watts Qx	Watts Qi	k Counts SL
12.5	29.0	2.7
18.3	29.4	4.2
16.4	29.4	4.4
28.6	43.4	7.5
34.3	50.4	10.5
38.2	50.4	10.5
7.5	17.0	1.1
4.0	9.4	7.0
3.1	4.2	1.0
0.6	2.0	0.0

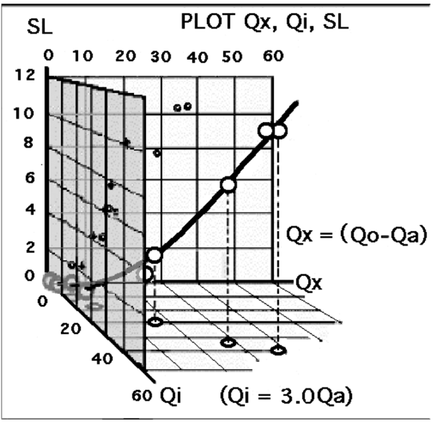

Figure 6 lists the data on the left and shows its plot on the right. Calorimetric experiments using a low-mass (20 gm) 1.6 MHz SF device produced this data.

Discussion

An examination of data from many experiments led to the described model for sonofusion that is supported by recent progress of inertial confinement fusion, astrophysics, ultra-cold Bose-Einstein condensates and Bardeen, Cooper, and Schrieffer (BSC) systems. One should differentiate between two types of fusion events: sustained events and one-time events. Sustained fusion found in the environments of stars and hot fusion reactors of magnetically contained plasma are continuous sources of fusion power. The one-time fusion event is self-destructive and is finished in one cycle. Systems such as sonofusion, fusion bombs, and inertial confinement fusion are one-time fusion events. Sonofusion is a self-destructive system consisting of a transient cavitation bubble, jet, and cluster. The total sonofusion process ranges from 0.1 to 25 microseconds. The 1.6 MHz sonofusion system in the bubble phase gains 10^9 particles producing sonofusion and target-implanting jets containing about 10^7 particles in a volume of $5x10^{-19}$cc. The jet-implanted cluster of a million deuterons produces a one-time high-density fusion event.

Analysis by Brian Oliver at the Department of Energy, as seen in Table 1 sample 3 A, B, and C, shows measurements of ^{4}He in product gases at a level of 552 ppm that translates to $1.2x10^{18}$ atoms of ^{4}He during a 19-hour period *(17)*. Billions of the sonofusion bubbles per second initiate systems producing on the order of 10^{13} micro-fusion events per second. This ^{4}He production occurs without any measured long-range radiation. It should be pointed out that, in muon fusion at densities ~ 10^{30} D/cc, deuterons fuse at temperatures below 100 ^{o}K. This is a density-driven system with no dependence on temperature. If the same deuteron density occurred in a white or black dwarf star, one would expect deuterons to fuse readily. Sonofusion, under the correct conditions, may approach the density of a small white dwarf star and muon fusion *(1, 2)*. Other data sources that support this model are the many scanning electron microscope

Downloaded by PENNSYLVANIA STATE UNIV on June 28, 2012 | http://pubs.acs.org
Publication Date (Web): December 20, 2009 | doi: 10.1021/bk-2009-1029.ch009

photos of ejecta sites and calorimetric measurements of heat, and recent backlighting inertial confinement fusion experiments describe measuring very high electric and magnetic fields *(10)*.

Summary

This paper views the high density of sonofusion systems as the important parameter in the transient cluster. Increasing the cluster density, maintaining low temperatures, using higher-frequency piezo systems, and decreasing the size of the sonofusion device are good guidelines for future progress in the alternate-energy sonofusion search. An attempt has been made to look for a path that incorporates most of the experimental technology called micro-fusion, bubble fusion, and sonofusion into a reasonable model of what today is called sonofusion. Transient cavitation bubbles create plasma jets that implant target foils, producing fusion events in transient clusters that terminate with a fusion heat pulse (Qx). The technology of sonofusion, inertial confined fusion, muon fusion, electromagnetic fusion, frozen deuterium fiber z-pinch implosions, imploding wire and the low-temperature studies of Bose Einstein condensates, Bardeen-Cooper-Schrieffer systems and their boson fermion crossover relationships are all related technologies that are helpful to the understanding of sonofusion.

Electromagnetic forces squeeze clusters of deuterons, +1 bosons.

The deuteron Mev energy states separations providing for high Tc values.

The compression of the cluster to Bose Einstein C. produces coherence.

Plasma cooling of cluster contents produce sub de Broglie wavelengths.

The ejecta site volume correlates to the number of 24 Mev events in a cluster.

Size of the heat pulse correlates to the frequency of the resonate piezo.

Helium and Qx are environmentally friendly, and the products sonofusion.

Downloaded by PENNSYLVANIA STATE UNIV on June 28, 2012 | http://pubs.acs.org
Publication Date (Web): December 20, 2009 | doi: 10.1021/bk-2009-1029.ch009

Acknowledgement

I would like to thank Julie Wallace and others who helped edit and make this readable, and Dick America, Jim Reiker, and Brian Marcus for their support.

References

1. Liberman, M. A.; De Groot, J. S.; Toor, A.; Spielman, R. B. *Physics of High-Density Z-Pinch Plasmas*; Springer-Verlag: NY, 1998; p 37.
2. Alvarez, L. W. et al. Catalysis Nuclear Reactions by μ Mesons. *Phys. Rev.* **1993**, *105*, 1127.
3. Hickling, R. Transient, High-Pressure Solidification Associated With Cavitation in Water. *Phys. Rev. Lett.* **1994**, *73(21)*, 5853.
4. Stringham, R. The Cavitation Micro Accelerator. In *Proceedings of the Eighth International Conference on Cold Fusion,* Lerici (La Spezia), Italy, May 21-26, 2000; Scaramuzzi, F., Ed.; Italian Physical Society: Bologna, Italy, 2000; 299.
5. Brenner, M. P.; Hilgenfeldt, S; Lohse, D. Single Bubble Sonoluminescence. In *Rev. of Modern Phys.* **2002,** *74(2)*, 425-484.
6. Weninger, K. R.; Evans, P. G.; Putterman, S. J. Time correlated single photon Mie scattering from a sonoluminescing bubble. *Phys. Rev. E.* **2000**, *61(2)*, 3.

7a. Tomita, Y.; Shima, A. High-speed photographic observations of laser induced cavitation bubbles in water. *Acoustica* **1990,** *71*, 161.

7b. Felix, M. P.; Ellis, A. T. Laser-induced liquid breakdown: A step by step account. *Appl. Phys. Lett.* **1971,** *19*, 484.

7c. Lautterborn, W.; Bolle, J. Experimental investigations of cavitation - bubble collapse in the neighborhood of a solid boundary. *Fluid Mech.* **1975**, *723*, 91.

8. Ruuth, S. J.; Putterman, S.; Merriman, B. Molicular dynamics simulation of the response of a gas to a spherical piston. *Phys. Rev. E.* **2002,** *66*, 036310-1 to 14.
9. Liberman, M. A.; De Groot, J. S.; Toor, A.; Spielman, R. B. *Physics of High-Density Z-Pinch Plasmas*; Springer-Verlag: NY, **1998**; pp 19, 238-241.
10. Petrasso, R. D. et al. Proton Radiography of Inertial Fusion Implosions. *Science*, Feb. 29, 2008, *319*, 1223-1225.

11a. Stringham, R. Predictable and Reproducible Heat. In *Proceedings of the Eighth International Conference on Cold Fusion*, Lerici (La Spezia), Italy, May 21-26, 2000; Scaramuzzi, F., Ed.; Italian Physical Society: Bologna, Italy, 2000; 299.

11b. Stringham, R. Cavitation and Fusion. In *Condensed Matter Nuclear Science: Proceedings of the 10th International Conference on Cold Fusion*, Cambridge, MA, Aug. 24-29, 2003; Hagelstein, P. L.; Chubb, S. R., Eds.; World Scientific Publishing Co.: Singapore, 2006.

12. Cirtain, J. W.; Golub, L.; Lundquist, L.; van Ballegooijen, A.; Savcheva, A.; Shimojo, M.; DeLuca, E.; Tsuneta, S.; Sakao, T.; Reeves, K.; Weber, M.; Kano, R.; Narukage, N.; Shibasaki, K. Evidence for Alfven Waves in Solar X-ray Jets. *Science*, Dec. 7, **2007**, 138, p 1571.
13. Eberlein, C. Theory of quantum radiation observed as sonoluminescence. *Phys. Rev. A.* **1996**, *53(4)*, 2772.

Downloaded by PENNSYLVANIA STATE UNIV on June 28, 2012 | http://pubs.acs.org
Publication Date (Web): December 20, 2009 | doi: 10.1021/bk-2009-1029.ch009

14. Isayev, A. A. Two-Body Correlation Functions in Nuclear Matter With Neutron-Proton Condensate. *J. Exp. Theor. Phys. Lett.* **2005**, *82(9)*, 551556.
15. Stringham, R. Anomalous Heat Production by Cavitation. In *Proceedings of the 1998 IEEE Ultrasonics Symposium,* Sendai, Japan; Oct. 5-8, 1998; Vol. 2, 1107.
16. Stringham, R. Bubble-Driven Fusion. In *Condensed Matter Nuclear Science: Proceedings of the 14th International Conference on Cold Fusion,* Washington, DC; Aug. 10-15, 2009; Nagel, D.; Melich, M. E., Eds.; (in press)
17. Stringham, R. Low Mass 1.6 MHz Sonofusion Reactor. In *Condensed Matter Nuclear Science: Proceedings of the 11th International Conference on Cold Fusion*, Marseilles, France; Oct. 31-Nov. 5, 2004**;** Biberian, J. P., Ed.; World Scientific Publishing Co.: Singapore, 2006.

Downloaded by PENNSYLVANIA STATE UNIV on June 28, 2012 | http://pubs.acs.org
Publication Date (Web): December 20, 2009 | doi: 10.1021/bk-2009-1029.ch009

Downloaded by CORNELL UNIV on June 28, 2012 | http://pubs.acs.org
Publication Date (Web): December 20, 2009 | doi: 10.1021/bk-2009-1029.ch010

Chapter 10

Overcoming the Coulomb Barrier and Related Effects Through Resonant Electrodynamics and Quantum Mechanics in the Fleischmann-Pons Excess Heat Effect

Scott R. Chubb

Infinite Energy Magazine and Research Systems, Inc, **903 S. Frederick St., #6, Arlington, VA 22204, EMAIL: chubbscott@mac.com, chubbscott@aol.com**

Science requires measurements. Interpreting measurements involves recognizing patterns. How this happens is intimately related to the instruments that are used and how the measurements are performed. Abstractly, this can be viewed in a somewhat radical way: Nature is telling us something, but how we interpret it involves how we understand what Nature is telling us. An important point is that, for communication to take place, involving real-life experiences, electromagnetism is required. In higher-energy environments, how this takes place can be inferred in an approximate manner, in which changes in electromagnetism, as a function of time, can be treated as being independent of time. In solids, when many particles are allowed to interact, this assumption is not required, and this can lead to important consequences. This alternative perspective can explain how the Fleischmann-Pons effect can take place.

Introduction

Absence of a recognized mechanism to overcome the Coulomb barrier is widely viewed as the a priori reason that the Fleischmann-Pons excess heat effect cannot be the result of a nuclear process. However, considerable

In Low-Energy Nuclear Reactions and New Energy Technologies Sourcebook Volume 2; Marwan, J., et al.; ACS Symposium Series; American Chemical Society: Washington, DC, 2010.

confusion about whether this particular barrier is relevant exists because what happens in the Fleischmann-Pons excess heat effect is so radically different from what takes place in thermonuclear fusion. I argue that this barrier is quite artificial and that the Fleischmann-Pons excess heat effect can be explained by understanding subtleties involving how reactions can occur through quantum mechanics (QM). In particular, I am suggesting that general ideas involving resonance can explain, through electrodynamics, many of the observations associated with the Fleischmann-Pons excess heat effect. Thus, I argue that the real barrier for understanding how cold fusion reactions can take place in a room temperature environment is not overcoming the Coulomb barrier but is understanding subtleties related to how reactions can occur, based on the known laws of QM. Specifically, QM does not require that the picture used in thermonuclear fusion apply. A more logical picture includes electromagnetism in a time-dependent fashion and the idea that many particles can be involved.

Then, seemingly impossible aspects of the conventional picture become not so impossible but, in fact, quite reasonable. A key source of confusion is that, as opposed to a situation in which potentially reacting deuterons (d’s) are required to have such high velocity that they can be treated as if changes in their electromagnetic interaction (EMI) are important only very near the location of the reaction, where the conventional tunneling picture applies (involving a static Coulomb potential) in a situation involving many charged particles, the effects of EMI can result in time-dependent changes that can become important far from the reaction. In fact, in what appears to be the most relevant, thermonuclear fusion reactions (in which helium-4, in the form of alpha particles is released), evidence exists that the conventional Coulomb barrier must be modified significantly *(1, 2, 3)* in order to incorporate time-dependent features of the EMI that are necessary to impose the requirement that, far from the reaction, the incident d’s must have positive Bose Exchange symmetry and have net, vanishing spin. In this paper, I discuss a particular mechanism involving resonant electromagnetic dynamics.

The associated picture is consistent with the conditions that are present in the experiments, the known laws of physics, and the underlying ideas suggested by Giuliano Preparata. Predictions based on this alternative picture imply that particular size crystals involving Palladium (Pd) and particular, externally applied electromagnetic fields can be used to trigger excess heat in the Fleischmann-Pons excess heat effect.

In the next section, I provide an overview of some of the commonly believed ideas about the Coulomb barrier that have resulted in considerable confusion about the Fleischmann-Pons excess heat effect. In addition, I explain how conventional QM deals with forms of interaction in general terms and how these can result in a counter-intuitive picture in which collisions can be very different from those in the conventional Coulomb barrier situation because they do not have to take place at a point. Instead, collisions can take place over a finite distance through an effect that is referred to as resonance or near-resonance, in which in a particular region of space momentum is effectively conserved in a nonlocal fashion. In conventional solid-state physics, the associated effects are quite well-known, but a rigorous treatment of their origin

Downloaded by CORNELL UNIV on June 28, 2012 | http://pubs.acs.org
Publication Date (Web): December 20, 2009 | doi: 10.1021/bk-2009-1029.ch010

has not been adequately presented. In dealing with the cold fusion problem, I have suggested such a treatment *(4, 5)*.

In the following section, I discuss two pictures that involve nearly resonant forms of collisions in an approximately ordered solid. The first of these is based on an approximate model that was introduced to overcome perceived deficiencies involving how the Coulomb barrier frequently has been viewed in the fusion process. But this model uses a language (time-dependent perturbation theory involving bound, ion band states) that is very different from the conventional scattering/tunneling language that is associated with the more conventional picture associated with the Coulomb barrier. In the second picture, a generalization of the first picture is presented, using a language that is consistent with more general aspects of QM, based on nearly resonant collisions that can take place involving the lowest energy excitations of an ordered solid, which can include the possibility that all of the particles in the solid can be allowed to move all at once rigidly. Here, for illustrative purposes, a semi-classical limit is used to demonstrate how the associated nearly resonant collisions can lead to nuclear-scale forms of overlap.

More quantitative arguments that are based on the more general theory are presented elsewhere *(1, 2, 3, 4, 5)*. Here, a generalization of conventional energy band theory was developed, in order to deal with the underlying quantum-electrodynamics (QED), that I presented earlier *(1, 2)*. From these more general arguments, both the earlier picture and its generalization (in the second model) can be shown to involve forms of nearly resonant collisions. In the second model, external electromagnetic fields can induce adiabatic changes in the associated scattering.

In the initial picture, the energy of the interaction is assumed to result from a uniform shift in the zero of energy. In the second model, these forms of motion occur as a result of a uniform shift in the zero of momentum, and the reaction involves a different final state in which changes at the boundary of the ordered region of the solid occur through a transition in which the momentum from the change in mass (from the d+d→^{4}He reaction) is transferred to the center of mass of the lattice as a whole. In this situation, the change in the final state involves coupling through nearly resonant collisions in which momentum is either transferred to potentially interacting helium-4 nuclei (in larger crystals) or directly to the lattice (in smaller nm-scale crystals).

The earlier quantitative arguments *(1, 2, 3, 4, 5)* focused on a limit involving the lowest-lying excitations, in finite crystals. In the final section, I use some of these ideas as a starting point for suggesting a number of experiments, involving applying electromagnetic fields in a time-dependent fashion. The underlying physics that I suggest involves the potential effects associated with the nearly resonant forms of collisions, which are discussed in the next three sections of the paper. An important point is that, through these kinds of collisions, as opposed to the violent effects that are conventionally associated with thermo-nuclear fusion, an entirely different form of reaction can be possible in which very small changes effectively take place. Within this alternative context, as opposed to creating many energetic forms of excitation within the interior of the solid, a new picture can be appropriate, involving a situation in which the solid as a whole or in part is allowed to move in a

Downloaded by CORNELL UNIV on June 28, 2012 | http://pubs.acs.org
Publication Date (Web): December 20, 2009 | doi: 10.1021/bk-2009-1029.ch010

coherent manner without altering the energies and relative positions of the particles that are located inside it. Then, the underlying mechanism does not significantly excite the solid, and near ground-state configurations associated with potential overlap within the interior of the solid are not significantly affected. As a consequence, an entirely different and novel kind of situation potentially can take place, in which the ground state of a solid is not significantly altered as a result of the reaction.

The time-dependent effects that form the basis of my suggestions about potential experiments are based on the assumption that this kind of picture is valid. Here, the requirement that, for the d+d→^{4}He reaction to take place, it is necessary that the net magnetic spin between potentially interacting deuterons (d's) vanishes. Potentially, this fact can be used to establish a preferential path. In particular, by using potential resonant forms of interaction, involving externally applied fields that interact with the d's, possible forms of interacton can be created that can be directed in a way that potentially can minimize energy within the interior regions of the solid, by requiring that the ^{4}He that is created leaves the solid in a manner that involves a minimal amount of disruption of the underlying periodic order. A potentially realistic procedure for initiating this kind of effect involves applying a well-known protocol, nuclear magnetic resonance (NMR), in which the spins of potentially reacting d's are pumped resonantly through an applied time-dependent electromagnetic field that is tuned in a particular manner to the natural precession frequency associated with the motion of the spins of the deuterons, which occurs when a DC magnetic field is simultaneously applied externally.

Downloaded by CORNELL UNIV on June 28, 2012 | http://pubs.acs.org
Publication Date (Web): December 20, 2009 | doi: 10.1021/bk-2009-1029.ch010

The Barrier Is Not the Coulomb Barrier -- It Is Quantum Mechanics

The idea that Nature is telling us something by sending us signals and requires us to receive them involves a process of interpreting what Nature is telling us. To understand what Nature is telling us requires us to think about the signal and what it represents. In thermonuclear fusion, this process is relatively simple because an obvious model exists: Thermonuclear fusion occurs on the Sun, and it involves hot plasmas, where high-velocity hydrogen nuclei (protons, or proton-neutron pairs — d's) can collide in a process that we also seem to think we understand. But our understanding of this is approximate. It is based on a theory that was created well before details about later information involving experiments that could be explained by a more refined understanding of QM were known. For this reason, it is appropriate to re-examine some of the more common assumptions about the Coulomb barrier and their relevance in our understanding of the Fleischmann-Pons excess heat effect. With this in mind, I asked three people who have been paying close attention to issues related to the Fleischmann-Pons excess heat effect about the importance of overcoming the Coulomb barrier. Their opinions and my opinion are expressed in the following statements:

1. Robert Park, a senior scientist and former director of public information of the American Physical Society, says that according to

most nuclear physicists, you can't overcome it. [(2008) private communication]

2. David Nagel says nuclear physicists seem to be wrong. But there is no accepted theory that can account for it. [(2008) private communication]
3. Talbot Chubb says nuclear physicists don't understand it but solid-state physicists do. Accepted theory involving nuclear physics is wrong. Ground-state quantum mechanics explains it. [(2008) private communication]
4. Time-dependent quantum mechanics says it can be overcome using conventionally accepted theory, and this will eventually be accepted. My claim is based on material presented here and in Refs. 1, 2, 3, 4, 5.

In fact, no one knows whether these statements are relevant. With the exception of Statement 4 (which reflects my view), what I suggested in each of these opinions is not based on an objective scientific analysis. I believe, however, there is value in including these statements because, in each case, I suggest that the particular opinion has resulted from biases and perceptions about the Coulomb barrier that are not relevant to the Fleischmann-Pons excess heat effect but reflect a more basic source of confusion: interpreting and understanding what Nature is telling us through QM.

In conventional physics and chemistry, the kind of radical effect that Fleischmann and Pons observed was not at all expected, and, even after many years, the statement by Park reflects the predominant opinion of most scientists. Park is very concerned about and interested in the outcome of the debate that has taken place, and I suspect that, as additional facts are revealed, he may change his mind. The statement by Nagel reflects the opinion of an individual who has initiated a useful, scientific dialogue and debate about the subject. He also has recognized that the lack of scientific discourse about the subject has precluded realistic intellectual investment of time, much less real investment, through significant funding.

Talbot Chubb has collaborated with me in developing the initial ideas associated with our ion band state model of the Fleischmann-Pons excess heat effect. His opinion reflects a more open-minded perspective, associated with invoking ideas about quantum mechanics and solid-state physics. With time, I have sharpened the associated arguments that are the basis of his opinion. Some of these ideas are the basis of Statement 4. Each view captures an important perspective. Obvious differences in opinion are implicit in these different statements that reflect biases about a seemingly transparent assumption: Opinions about the Coulomb barrier have relevance in understanding the Fleischmann-Pons excess heat effect (and why because of these opinions — in statements 1 and 2 — it does not seem possible that the Fleischmann-Pons excess heat effect can result from nuclear reactions). An important point, associated with statements 3 and 4, involves the potential role of QM and the idea that, through QM, it is possible to go beyond the limitations of the assumptions associated with statements 1 and 2.

In fact, statements 3 and 4 are based on a model involving QM that makes sense in the context of what is known *(4)* about palladium-deuteride (PdD). But

Downloaded by CORNELL UNIV on June 28, 2012 | http://pubs.acs.org
Publication Date (Web): December 20, 2009 | doi: 10.1021/bk-2009-1029.ch010

the fact that QM might even be involved in a different way in the PdD situation (as opposed to a situation involving the conventional Coulomb barrier tunneling problem) does not seem to have been widely understood or appreciated. In particular, preconceived ideas about the Coulomb barrier, although seemingly quite relevant and obvious (as expressed in statements 1 and 2), are quite inappropriate and quite wrong in situations in which many particles potentially interacting electromagnetically can be involved. In this alternative situation, the relevant dynamical situation can become (and probably is required to be) considerably more complicated. The real situation, even in thermonuclear fusion, does involve QM but in a very limited way, and this fact apparently also has not been widely appreciated.

Two perceived pictures of the Coulomb barrier involve classical physics and semi-classical physics *(1-5)*. In the first of these, each deutron (d) is pictured as a proton-neutron pair that cannot collide with a second d because of the infinite forces that occur classically as a result of Coulomb repulsion. Although this picture seems to explain why fusion cannot occur, this isn't true: It oversimplifies the situation. A more realistic picture occurs when point-particle d's are replaced by waves, which, in *(1-5)*, are schematically shown as pancakes, which are used to mimic the kinds of structures that QM requires; these structures can collide (their wave functions can have overlap). This can take place, despite the fact that the classical expressions for the energy and force become infinite. This picture is more realistic. But the associated mathematics is approximate because it requires the d's to have high velocity.

An important point is that the conventional Coulomb barrier involves an assumed form of collision that is very limited. In particular, although it is convenient to view a potential collision as it occurs classically or semi-classically, in quantum mechanics, a more general definition applies. In particular, in quantum mechanics and in general terms, collisions involve changes in energy. In principle, they can take place through any possible form of process, which can be viewed as occurring over a measurable time scale or over a time scale that cannot be measured directly. In the latter situation, a mathematical representation exists, defined by an effective form of power, $P_{virtual}$:

$$P_{virtual} \equiv \frac{2\pi}{\hbar}\langle Initial|V|Final\rangle\langle Final|V|Initial\rangle,$$

which defines a form of virtual process that can be initiated through a change in potential energy V, that occurs when an initial state $\langle Initial|$ is perturbed by V and a final state $|Final\rangle$ is created (which is defined by the exact Hamiltonian). When the exact Hamiltonian applies, $P_{vvirtual}$ defines a possible form of collision that can lead to a scattering event. In this last equation, each virtual process can be viewed as involving a transition in the forward direction in time through a matrix element of the form, $\langle Initial|V|Final\rangle$ multiplied by a matrix element $\langle Final|V|Initial\rangle$, associated with how the process can proceed backward in time. Two important points are that both processes are initiated through a change in the potential energy V and that, when energy and

Downloaded by CORNELL UNIV on June 28, 2012 | http://pubs.acs.org
Publication Date (Web): December 20, 2009 | doi: 10.1021/bk-2009-1029.ch010

particle number are conserved globally, forward virtual changes very often are balanced by backward changes and no net change in power is allowed to take place. A net change in power can occur when energy is conserved. During ICCF1, Schwinger explicitly cited this relationship *(6)*, implicitly using a well-known equation (referred to as the Lippmann-Schwinger equation) that has not been widely appreciated in the analysis of cold fusion theory:

$$\text{Rate of reaction}=\frac{2\pi}{\hbar}\left\langle Initial\middle|V\delta(H-E_{Initial})V\middle|Final\right\rangle$$

$$=\frac{2\pi}{\hbar}(\textstyle\sum_f \rangle Initial|V|Final\langle\rangle Final|V|Initial\langle \delta(E_{Initial}-E_{Final}))\text{, (1)}$$

where $E_{Initial}$ and E_{Final}, respectively, are the energies of the initial and final states and the summation includes all final states.

In fact, this alternative way of understanding the collision process provides a generalization of the classical concept. In particular, in Eq. 1, the more appropriate idea implicitly is presented. In the expression, any number of particles over any length and time scale can be involved in each virtual process. Specifically, as defined by Eq. 1, in QM, a rate is formed as a weighted sum of the possible virtual power changes that can be created through virtual processes. The possible power (the virtual power) resulting from any virtual process can be arbitrarily large or small, and each process in principle is reversible. When the sum over final states conserves energy (which is implied through the notation involving the delta function in Eq. 1), the process can take place. Time reversibility is broken because it is never possible to determine the change in potential, the initial state and the final state precisely. The associated relationship (Eq. 1) in principle is exact. It provides a prescription for modeling new and novel effects that is considerably richer than is possible in Gamow theory. In particular, Gamow theory in the fusion process assumes that a single final state is involved with a collision (consisting of three nucleons moving away from a fourth nucleon) at high velocity except in regions in the immediate vicinity of the collision and that the essential dynamical changes in the potential energy (V, in Eq. 1) involve the strong force exclusively. This picture ignores many possible final states and implicitly fails for this reason.

Resonant and Near-Resonant Interactions

A problem involving the possibility that light being transmitted and received in the future in the absence of collisions could alter how it was transmitted and received in the past was suggested by John Wheeler to his (at the time) young graduate student Richard Feynman. This idea required that Feynman think in basic terms about how light might interact with matter at its most fundamental level. Intuitively, one might view this problem in a paradoxical way: What happens in the future could affect the past. In fact, as opposed to viewing this problem in this particular way, an alternative way of looking at it involves an important assumption associated with how quantum

Downloaded by CORNELL UNIV on June 28, 2012 | http://pubs.acs.org
Publication Date (Web): December 20, 2009 | doi: 10.1021/bk-2009-1029.ch010

mechanics works: In the absence of collisions, it is impossible to know anything at a fundamental level and (possibly more significant) how natural forms of harmony (or resonance) might exist in which it is simply impossible to distinguish between the past and future or even in situations in which seemingly natural boundaries are present that can prevent unexpected collisions from taking place. In suggesting this seemingly odd and bizarre idea, Wheeler asked Feynman to address a fascinating question that might be impossible to answer: If a tree falls in a forest and no one is around to hear it, does the tree make a sound? Possibly equally remarkable is the conclusion, based on what is known about the existing theory of electromagnetism, that he suggested: A sound might not be created.

In doing this, Wheeler and Feynman reinvented the kinds of ideas associated with how QM works and the forms of harmony and resonance that I just mentioned, which are not widely appreciated, associated with time-reversal invariance and causality that (I think) have direct bearing on questions related to cold fusion. In particular, Wheeler and Feynman made use of ideas related to what we know and can never know about electrodynamics and the fact that precise solutions of the associated equations are allowed to become non-local both in time and space. By invoking this, they postulated the somewhat spooky idea that, for radiation ever to be transmitted, it is necessary to have well-defined receivers and transmitters. Wheeler suggested that, if this does not take place, no signal is ever transmitted.

Implicitly, in order to account for how the associated signal is transmitted, Feynman invoked a form of the effect that I have referred to as resonance or harmony. When this kind of effect is approximate, a condition that I will refer to as near-resonance can take place, in which collisions can take place, but their magnitude and duration can be vanishingly small. In both situations, as opposed to a conventional effect (involving how light and electrons interact only involves how light is emitted in the future), Feynman and Wheeler thought about a very different effect, involving conditions in which how light is emitted involves a situation in which how it interacts with electrons in the future can affect how it has interacted with electrons in the past. They suggested that how this occurs appears to involve a situation in which what happens in the future in anticipation of what will take place can affect what has taken place in the past. This idea is entirely non-classical in the real universe, and it appears to violate causality. But because, in QM, by construction in the absence of collisions time has no preferential direction, such a violation does not take place.

An important point is that, implicitly, the notion that past and future solutions of Maxwell's equations could be subtracted from each other in a self-consistent manner (which formed the basis of the Wheeler/Feymann theory of electrodynamics that Feynmann later used in his formuation of QED) is related to a more general phenomenon: resonance. In approximate terms, resonance occurs when solutions to a particular form of wave equation, which in isolation are allowed to become singular, are added or subtracted from each other in such a way that, at the neighborhood where their singular behavior is assumed to take place, the singularity is removed.

Downloaded by CORNELL UNIV on June 28, 2012 | http://pubs.acs.org
Publication Date (Web): December 20, 2009 | doi: 10.1021/bk-2009-1029.ch010

Downloaded by CORNELL UNIV on June 28, 2012 | http://pubs.acs.org
Publication Date (Web): December 20, 2009 | doi: 10.1021/bk-2009-1029.ch010

In a more precise definition, resonance can be defined to take place when each virtual matrix element $\langle Initial|\mathbf{V}|Final\rangle$ can be related to the current and density matrix elements $\langle Initial|\vec{j}|Final\rangle$ and $\langle Initial|\rho|Final\rangle$, through a surface region integration representation (when energy is conserved), in which flux contributions at the boundaries of the collision region are only involved. (In general, current and density variations are required to be involved throughout space.) In particular, the rate of change of the overlap between initial and final states and its rate of change with respect to time (in the interaction picture) can be used to define the collision matrix element $\langle Initial|\mathbf{V}|Final\rangle$ that is used to define the virtual power (Eq. 1). {**Note**: $\rangle Initial|\mathbf{V}|Final\langle = i\hbar[\partial(\rangle Initial(t)\,|\,Final(t)\langle)/\partial t]$ when $\rangle Initial(t)|$ and $|Final(t)\langle$ evolve in time, in the interaction picture representation, when they (as well as the density operator $\rho(r) \equiv \sum_{r_i} \delta(r - r_i)$ and total current operator $j(r)$) evolve in time, in the Schroedinger picture representation, $\langle Initial|\mathbf{V}|Final\rangle$ (which is the same when all quantities are expressed in a common representation) can be expressed using a surface integral expression that vanishes in regions where collisions take place.} This alternative definition can be related to the (Schroedinger picture, see Note above) off-diagonal many-particle current (associated with all, neutral or charged particles) and density (associated with the same particles) matrix elements (see Note above) $\langle Initial|\vec{j}|Final\rangle$ and $\langle Initial|\rho|Final\rangle$, through an integral representation that reduces to a simpler (surface region integration) representation, when energy is conserved, involving flux contributions at the boundaries of the collision region from currents located outside ($\langle Initial|\vec{j}|Final\rangle$) and inside ($\langle Initial|\vec{j}_{inside}|Final\rangle$)*(1-5).*

The condition associated with future and past forms of scattering being in harmony with each other occurs when particle number and energy are conserved throughout space. The resonant condition occurs when the contribution $\rangle Initial|\vec{j}_{inside}|Final\langle$ involving a flux contribution from inside the region vanishes. Then, $\rangle Initial|\mathbf{V}|Final\langle$ depends only on contributions $\rangle Initial|\vec{j}|Final\langle$ that occur at the boundaries of the region. Effectively, when this occurs, the collision process can become non-local, and through near-resonant conditions that almost mimic resonance, non-local forms of collisions can occur that can result in gradual increases in momentum.

In particular, as opposed to a situation in which particles collide in the interior of the collision region, in perfectly resonant situations all of the particles that are external to it pass through it, as if the region is transparent. In near-resonant situations, all of the particles pass through it, or some of them may remain near the boundary or be reflected in such a way that momentum is transferred non-locally. In both situations, the changes in potential only occur either at the boundaries of the region or in regions external to it.

How Resonant Electromagnetic-Dynamics Explains the Fleischmann-Pons Effect

Implicitly, in an approximately ordered solid, a form of Galilean relativity exists, associated with the fact that, in the limit in which there are no collisions, it is impossible to tell whether the ordered regions in the solid are in motion or at rest. This can have especially interesting consequences when collisions are weak because their contributions in Eq. 1 can be stifled as a result of periodic order. The associated effect is a specific example of the more general phenomenon discussed in the last section: near-resonance and nearly resonant collisions. This occurs when contributions from many virtual collision matrix elements (many values of $\rangle Initial\left|\mathbf{V}\right|Final\langle$ in Eq. 1) become very small in a particular region of space. In particular, perfect resonance occurs when energy is conserved and the contribution to the flux from the many-particle current matrix elements $\rangle Initial\left|\vec{j}\right|Final\langle$) and inside ($\langle Initial|\vec{j}_{inside}|Final\rangle$ involves a situation in which $\rangle Initial\left|\vec{j}(r)\right|Final\langle = \rangle Initial\left|\mathbf{V}\right|Final\langle$ and $\langle Initial|\vec{j}_{inside}|Final\rangle$=0. Then, because energy is conserved in Eq. 1, in this kind of situation the total contribution from collisions in the interior vanishes (so in this region $\langle Initial|\mathbf{V}|Final\rangle = 0$) and with respect to $\langle Initial|$ and $|Final\rangle$, the total Hamiltonian (H in Eq. 1) can be viewed as being a self-adjoint (Hermitean) operator.

Formally, as a consequence, perfect resonance can be used to justify the approximate boundary conditions associated with the single-particle, energy band theory developed by Bloch, which is the basis of heat and charge transport in solids, with the understanding that the theory can be applied even in situations in which the crystal lattice that is used has finite extent, provided the energies of the various states that are used are all very close to one another in value. As I have pointed out elsewhere *(1-5)*, the associated conditions are guaranteed to apply to the full many-body Hamiltonian when the initial and final states involve many particles, provided the energies of the states involve the ground state and the lowest-lying excitations, which, by construction, are all required to be related to one another through rigid Galilean transformations, in which all of the particles are allowed to move at once rigidly without the separation between any particle and the remaining particles being altered.

When this occurs, it is possible to justify conventional band theory, based on a more rigorous argument. In particular, as opposed to assuming that the basis of the theory involves stationary, bound, eigenstates of an approximate single-particle Hamiltonian, involving an infinitely repeating, periodic lattice, the theory can be viewed as a near-resonance limit, involving the full Hamiltonian, as it applies to a periodically ordered, finite lattice that is allowed to move rigidly within the interior of a solid, and the associated eigenstates are

Downloaded by CORNELL UNIV on June 28, 2012 | http://pubs.acs.org
Publication Date (Web): December 20, 2009 | doi: 10.1021/bk-2009-1029.ch010

wave function resonant states that preserve periodic order. Because, in fact, it is never possible to determine the boundary of a solid *(4, 5)* formally, the associated picture can be viewed as a definition. This alternative perspective justifies formally the implications of the initial ion band state model *(1, 2)*, in which an approximate Fermi golden rule fusion rate calculation and the possibility of overcoming the Coulomb barrier were inferred from approximate eigenstates derived from a two-body d-d wave function that possesses Bloch symmetry (similar to the comparable symmetry that occurs when non-interacting d's occupy ion band states *(7)* in both their dependence on their center-of-mass and relative d-d separation variables). In this model, the Fermi golden rule is used to evaluate the fusion reaction rate using initial and final states that only change in regions (which are located at the interior boundaries of the ordered lattice) where nuclear overlap takes place, based on the assumption that, in both the initial and final states, the same wave function applies in regions where overlap does not take place, but as the separation variable vanishes or its magnitude approaches the magnitude of a Bravais Lattice vector, overlap becomes possible by allowing the change in momentum to become infinite.

When the d-concentration is sufficiently small, this assumed, asymptotic, energy-minimizing solution satisfies a resonant condition, while the Fermi golden rule rate expression occurs through nearly resonant forms of collisions, associated with small (infinitesimal) perturbations in the zero of energy of the electromagnetic potential, defined by Eq. 1, in regions where nuclear overlap can occur, both in interior and external regions of the lattice.

This initial calculation of fusion rate is justified only when the energy per unit cell is on the order of the smallest (optical) phonon energies (~20 meV), which means the lattice must have 23.8 MeV/0.02 eV~10^9 unit cells. However, a considerably smaller lattice size is possible in the presence of very weak externally applied forces. In this case, an alternative model associated with near-resonance can take place, in which the zero of momentum adiabatically changes without exciting the system. This can occur, provided the effective change in virtual power associated with the process is sufficiently small. In particular, as a function of time, when an external field $\vec{E}$ is applied, nearly resonant fluctuations in the center of mass momentum can take place that can increase in magnitude with time.

When the complete many-body expression is included (through Eq. 1, based on a generalization of multiple scattering theory *(1, 2, 3, 4)*), as the available momentum builds up, virtual collisions can couple resonantly between the lowest-lying excitations of the solid when the product of the force ($e\vec{E}$) on each d associated with a collision with the time *t* that is involved (which, in one dimension, for example defines a particular momentum $p(t) = e\vec{E}t$) obeys a matching condition in which, for example, again in one dimension, the associated deBroglie wavelength $\lambda_{deBroglie}$ satisfies the relationship $\lambda_{deBroglie} = \dfrac{h}{p(t)} = \dfrac{N}{n}a$ (*h*=Planck's constant, n = integer ≤ N, 2N=number of lattice sites). In the many-body generalization *(4, 5)*, whenever this condition occurs once, it can occur 2N times. In the simplest limit, N=n,

Downloaded by CORNELL UNIV on June 28, 2012 | http://pubs.acs.org
Publication Date (Web): December 20, 2009 | doi: 10.1021/bk-2009-1029.ch010

$2N\lambda_{deBroglie} = a$, and as p(t) increases in time, $\lambda_{deBroglie}$ can approach nuclear dimension. The apparent simplicity of this picture involves relating the microscopic physics to the semi-classical limit involving how light interacts with matter. Here, the underlying idea that coherent oscillations of charge that Giuliano Preparata suggested could be important in the long-wave limit in the associated interaction is absolutely correct. His observation about this is truly important.

A Potentially Useful Resonant Effect in the Fleischmann-Pons Excess Heat Effect, Involving Magnetism

Previously *(1-5)*, I identified basic relationships associated with the conventional transport theory of charge and heat identified by Bloch that can be generalized to situations involving d's (or protons or other fundamental particles) that can occupy or interact through energy band states in which, as opposed to viewing the associated states as arising in an approximate, semi-classical limit involving an approximate single particle Hamiltonian, an alternative, rigorous many-body picture can be used. Here, the associated states can be defined in terms of the ground state and the lowest-lying excitations *(5)* of a finite solid. Within this context, the picture outlined in the last section and through the more detailed arguments *(1-4)* associated with generalizations of multiple-scattering theory results in potential forms of coupling that can occur through vanishingly small changes in energy from potential collisions within an ordered solid. This provides a basis for understanding how to overcome the Coulomb barrier.

Within this approximation, locally no appreciable change in energy or change in velocity is required to take place (although the momentum p potentially can vary appreciably because although, for situations involving neutral particles, p is defined by the relaitonship p=mv, where m is the mass of the particle and v is its velocity, in QM - and in general, for charged particles - p=mv+e/cA, where e is the charge of the particle, A is the vector potential that results from any motion, and c is the speed of light). An important point is that when many charged particles are allowed to move at once, implicitly forms of light are involved as a result of this last relationship. Then, forms of resonant coupling can take place. In the limit associated with the lowest forms of excitation, these can be modeled based on a relatively simple description associated with semi-classical band state theory transport phenomena *(1, 2)*.

Tangentially, implicit in this discussion, potential triggering mechanisms can be inferred, based on general ideas involving nearly resonant forms of collisions in which the solid as a whole or a fraction of it can move rigidly in a rectilinear manner. Here, the key dynamical quantities all are present as a result of the somewhat counter-intuitive idea that an applied, electric field potentially can induce the Fleischmann-Pons excess heat effect directly, or in a situation in which an existing field associated with electrolysis has been in place and a second DC, electric or magnetic field is introduced, new, counter-intuitive effects associated with high energy particle emission *(8, 9)* can also be induced.

Downloaded by CORNELL UNIV on June 28, 2012 | http://pubs.acs.org
Publication Date (Web): December 20, 2009 | doi: 10.1021/bk-2009-1029.ch010

In the earlier argument, the possibility of the Fleischmann-Pons excess heat effect being initiated was inferred from requirements associated with the lowest-energy configuration and the kind of Galilean relativistic effect mentioned in the last section. This particular limit was identified based on the assumption that, in the Fleischmann-Pons excess heat effect, the existing situation asymptotically involves the lowest-lying excitations of the solid. In fact, however, in the situation associated with the SPAWAR experiments *(7,8)*, I suggested that an idea closely related to the long wave-length plasma oscillatory coupling identified by Giuliano Preparata, involving what Preparata referred to as “trapped photons,” could be used to account for the creation of high-energy particles.

Here, the lowest-energy forms of excitation occur when the solid as a whole moves rigidly, but in the reference frame of the solid, time-dependent coupling to the electromagnetic field can take place, even when the externally applied fields are static. Implicitly, as a consequence, approximately elastic forms of coupling (in the limit of perfect resonance) between the solid and the electromagnetic field are allowed to take place. An interesting generalization of the associated limit involves the possibility that the lowest-lying excitations can couple to externally applied time-dependent external fields.

Within this context, in *(1, 2)*, I suggested that a weak perturbation can take place, in which the solid is allowed to move rigidly in a time-dependent fashion in which, within the solid, no effective forms of collision (as in a resonant situation) are allowed to take place. Then, for example, it is possible to generalize the idea of a rectilinear translation by allowing the solid to rotate and/or rotate and move rectilinearly at the same time. The important point involves the idea that the associated forms of motion can occur either in the reference frame associated with the static fields within the laboratory, in which no relative motion is assumed, or within the reference frame in which the solid is allowed to move and/or externally applied fields are introduced that are time-dependent.

When the potential forms of excitation are sufficiently small, the limits that were identified initially apply. Then, the interaction between particles in the solid with the applied electromagnetic field becomes approximately elastic, and the possible forms of electromagnetic propagation obey the condition:

$$\omega(\vec{k}) = c\,|\vec{k}| = ck \equiv \omega(\vec{k}+\vec{G}) = c\,|\vec{k}+\vec{G}|, \quad (2)$$

where $|\vec{k}| = \dfrac{2\pi}{\lambda}$ is the magnitude of the wave-vector associated with the transmitted signal (λ is the wavelength of the transmission) and $\vec{G}$ is a reciprocal lattice vector, associated with the periodic order of the lattice. Eq. 2, in fact, is a well-known condition associated with resonant (Bragg) scattering that has been used to determine the structure of solids.

In fact, the concept of a reciprocal lattice vector $\vec{G}$ associated with a well-defined lattice involves a semi-classical limit. Within the context of the more general theory *(1-5)*, the idea of a well-defined lattice becomes an idealization. Instead of this semi-classical idea, forms of potentially resonant coupling are allowed to occur when a degree of periodic order associated with

Downloaded by CORNELL UNIV on June 28, 2012 | http://pubs.acs.org
Publication Date (Web): December 20, 2009 | doi: 10.1021/bk-2009-1029.ch010

the initial idealization is allowed to take place for finite periods of time, defined by any of the discrete periodic, Fourier transformations of the potential and energy that might be relevant, in situations in which the solid (or a fraction of it) is allowed to move rigidly.

Then, as opposed to defining $\vec{G}$, based on a well-defined lattice, an idealized limit exists in which the lattice can involve primitive lattice vectors $\vec{R}$ that asymptotically can become arbitrarily large (and the associated primitive values of $|\vec{G}|$ can become arbitrarily small), subject to the constraint that $\vec{R} \bullet \vec{G} \equiv n2\pi$, where n is an integer. Within the context of finite crystals, as a consequence values of $\vec{G}$ in Eq. 2 cannot be defined in a rigorous fashion. Instead, ranges of possible values of $\vec{G}$ possibly can be inferred.

However, ideas identified previously *(1-5)* as associated with the generalized forms of collisions apply, based on the more general idea that nearly resonant forms of coupling can occur that are consistent with Eqs. 1 and 2. Then, in particular, when externally applied electromagnetic fields are introduced in an appropriate (adiabatic limit), Eq. 2 can apply in situations in which internal degrees of freedom associated with d-nuclei, as they might interact with conventional forms of electromagnetism in free space, might also apply, but also through resonant conditions, in which the solid as a whole can move rigidly (in which the frequencies associated with possible photon adsorption and transmission approximately obey Eq. 2), based on the idea that the d-nuclei are allowed to occupy or interact with ion band states.

An important and interesting consequence of this is associated with the possibility of introducing forms of electromagnetic interaction that potentially are directed in a manner that preferentially might be useful for triggering nuclear reactions. In particular, in the thermonuclear d+d→^{4}He reaction, for the reaction to take place, it is necessary that the d's preferentially be prepared in a state that has vanishing total spin and that the d's possess Bose exchange symmetry far from the location of the reaction.

The possibility that externally applied fields can preferentially couple to the d's in an approximately elastic fashion, with possible changes in the magnetic spin that would be important in the d+d→^{4}He reaction, involves a transition in which the initial d+d wave function has vanishing net spin. By creating a preferential path, directed away from a region, involving the solid (where the possible He by-product could remain trapped), it is entirely possible that interaction could be enhanced as a result of this last requirement. Witthin this context, it makes sense to suggest that, by creating vanishing spin, even in a time-dependent fashion, a triggering process might be enhanced.

When this is assumed, Eqs. 1 and 2 have interesting implications in situations involving an externally applied magnetic field in a configuration that mimics conventional NMR or involving a situation in which many possible resonant frequencies (defined by Eq. 2) are allowed. In particular, if a constant, external magnetic field, $\vec{B}$, is directed parallel to a potentially reactive PdD electrode, this field possibly can induce a preferential path in which in directions perpendicular to the surface the spin degrees of freedom associated with d's that can occupy ion band states will precess in such a way that their net spin can

Downloaded by CORNELL UNIV on June 28, 2012 | http://pubs.acs.org
Publication Date (Web): December 20, 2009 | doi: 10.1021/bk-2009-1029.ch010

vanish. The associated coupling is most beneficial in this situation because, when $\vec{B}$ is parallel to the surface, the path associated with vanishing spin occurs in the plane that is perpendicular to $\vec{B}$ (which is normal to the surface). The associated path for potential reactions is consistent with the requirement that the ^{4}He that is created from potential reactions will leave the lattice in a manner that minimizes potentially disruptive changes in periodic order, which are expected to occur when ^{4}He accumulates inside the lattice.

In order to initiate this kind of coupling, in addition to the externally applied $\vec{B}$ field, as in the situation in free space, a radio frequency (RF) or microwave form of electromagnetism can be applied. The resonant condition can occur in this kind of situation when the RF or microwave field has an angular Larmor frequency $\omega = \frac{e|\vec{B}|}{mc}$ (as in NMR) or when $\omega = |\frac{e\vec{B}}{mc} + c\vec{G}|$. Thus, as in the generalization associated with elastic coupling to the lattice (in a situation involving pure resonance) associated with Eq. 2, in a nearly resonant situation many potential values of alternative larmor frequencies are possible. Here, $\vec{G}$ is allowed to take on values associated with the discrete Fourier transform of the potential within the solid. Because the degree of periodic order can be approximate and the (Bravais) lattice vectors can be discretely defined (and potentially can become arbitrarily large), many possible values associated with nuclear magnetic resonance are allowed to take place. As a consequence, the associated coupling can induce resonant forms of interaction involving many different frequencies. The optimal one is associated with the requirement that potential cracks and disruptions of periodic order are minimized.

Downloaded by CORNELL UNIV on June 28, 2012 | http://pubs.acs.org
Publication Date (Web): December 20, 2009 | doi: 10.1021/bk-2009-1029.ch010

Ackowledgements

I would like to acknowledge valuable discussions with Mitchell Swartz, David Nagel, Talbot Chubb, Ileana Rosario, and Dennis Letts. Partial support for this work has been provided through a grant from the New Energy Foundation.

References

1. Chubb, S. R. Roles of Approximate Symmetry and Finite Size in the Quantum Electrodynamics of d+d -> 4He in Condensed Matter Nuclear Science. *Conference on Eighth International Workshop on Anomalies in Hydrogen/Deuterium Loaded Metals*, 13-18 October 2007, Catania, Italy.
2. Chubb, S. R.. Resonant Electromagnetic Interaction in Low Energy Nuclear Reactions. In *Low-Energy Nuclear Reactions Sourcebook;* Marwan, J.;

Krivit, S. B., Eds.; American Chemical Society: Washington, DC, 2008; pp 99-123.

3. Chubb, S. R. Roles of Approximate Symmetry and Finite Size in the Quantum Electrodynamics (QED) of Deuteron (D) – D Fusion in PdD. In *Condensed Matter Nuclear Science, Proceedings of the Thirteenth International Conference on Condensed Matter Nuclear Science*, Sochi, Russia, 25 June-1 July, 2007; Bazhutov, Y., Ed.; Publisher Center MATI: Moscow, 2008, p 596.
4. Chubb, S. R. Nuts and Bolts of the Ion Band State Theory. In *Condensed Matter Nuclear Science: Tenth International Conference on Cold Fusion,* Cambridge, MA, Aug. 24-29, 2003; Hagelstein, P. L.; Chubb, S. R., Eds.; World Scientific Publishing Co.: Singapore, 2006; p 735.
5. Chubb, S. R. Role of Broken Gauge Symmetry in Transport Phenomena Involving Neutral and Charged Particles in Finite Lattices. http://arxiv.org/pdf/cond-mat/0512363
6. Schwinger, J. Nuclear Energy in an Atomic Lattice. In *The First Annual Conference on Cold Fusion,* March 28-31, 1990, Salt Lake City, Utah. National Cold Fusion Institute: University of Utah Research Park, Salt Lake City, Utah, 1990; pp 130-136.
7. Chubb, T. A.; Chubb, S. R. Overcoming the Coulomb Barrier in Cold Fusion. *J. Condensed Matter Nucl. Sci.* **2008**, *2*, 1–9.
8. Szpak, S., Mosier-Boss, P. A.; Gordon, F. Further evidence of nuclear reactions in the Pd/D lattice: emission of charged particles. *Naturwiss. 94(6)*, pp 511-514.
9. Szpak, S.; Mosier-Boss, P. A.; Gordon, F.; Dea, J.; Miles, M.; Khim, J.; Forsley, L. SPAWAR Systems Center-Pacific Pd:D Co-Deposition Research: Overview of Refereed LENR Publications. *Fourteenth International Conference on Cold Fusion,* Aug. 17-21, 2008, Washington, D.C. http://www.lenr-canr.org/acrobat/SzpakSspawarsyst.pdf

Downloaded by CORNELL UNIV on June 28, 2012 | http://pubs.acs.org
Publication Date (Web): December 20, 2009 | doi: 10.1021/bk-2009-1029.ch010

Downloaded by COLUMBIA UNIV on June 28, 2012 | http://pubs.acs.org
Publication Date (Web): December 20, 2009 | doi: 10.1021/bk-2009-1029.ch011

Chapter 11

The Basics of Deuteron-Cluster Dynamics as Shown by a Langevin Equation

Akito Takahashi

Technova Inc., Uchisaiwaicho 1-1-1, Chiyodaku, Tokyo, 100-001 Japan

Pertaining to quantum mechanics, the basics of a new approach using the stochastic differential equation (the Langevin equation) are written for quantifying the dynamic motion of known molecules as D_2^+, D_2 and D_3^+ as well as the D-atom state. The role of Platonic symmetry in these known molecules is discussed for deducing a simple one-dimensional (R_{dd} dependent; here R_{dd} is the distance between the nearest d-d pair) Langevin equation and using quantum-mechanical ensemble averaging to obtain an equation for expectation value. The methodology is applied for more complicated D-clusters such as 4D/TSC and 6D/OSC, which would keep Platonic symmetry by introducing the force fluctuation deviating from ideal Platonic symmetry. Time-dependent TSC and OSC trapping potentials, which take balance to get back to Platonic symmetry from the distorted states, were defined and used for a numerical solution of the Langevin equation.

In Low-Energy Nuclear Reactions and New Energy Technologies Sourcebook Volume 2; Marwan, J., et al.;
ACS Symposium Series; American Chemical Society: Washington, DC, 2010.

Introduction

This paper gives the follow-up basics for our paper published in *Low-Energy Nuclear Reactions Sourcebook, Vol. 1 (2).*

The reports of apparent hard radiation less excess heat with helium-4 ash are of key results in condensed matter nuclear science (CMNS) experiments, especially in dynamic PdDx systems. We have done a long series of studies for modeling D-cluster (or multi-body deuteron) fusion reaction mechanisms in order to reach our latest theory based on Langevin equations *(1, 2)*.

This paper describes the quantum-mechanical basics of the formulation of Langevin equations (stochastic differential equations) for D-cluster dynamics, especially for D-atom, D_2 molecule, D_2^+ ion, D_3^+ ion, 4D/TSC (tetrahedral symmetric condensate) and $6D^{2-}$/OSC (octahedral symmetric condensate). This paper provides an extended explanation of our previous paper *(14)* for the Catania Workshop.

First, one-dimensional Langevin equations for D-clusters with the R_{dd} d-d distance are formulated under Platonic symmetry *(1, 3)* conditions of multi-particle D-cluster systems with deuterons and quantum-mechanical electron centers. The known D (or H) molecular systems can be regarded as three-dimensional symmetric geometry keeping Platonic symmetry *(14)*. Under orthogonally coupled Platonic symmetry for a Platonic deuteron system and a Platonic electron system, a simple one-dimensional Langevin equation for the inter-nuclear d-d distance R_{dd} can be formulated *(14)*, as we will show in this paper with further explanations for the known deuteron molecules and clusters.

The ensemble averaging of a one-dimensional Langevin equation with the weight of quantum-mechanical wave functions for electrons and deuterons can be done by assuming the Born-Oppenheimer treatment for the separability of electron and deuteron wave functions. Usually, the electron wave length is much larger than the deuteron wave length, so the Born-Oppenheimer treatment is appropriate. We can further derive a time-dependent equation for expectation value $<R_{dd}>$, which is nonlinear but can be solved by the Verlet time step method *(2)*. We show in this paper that only 4D(or H)/TSC can condense to be a very small charge-neutral entity with about a 10-20 fm radius among considered cluster states.

At the final stage of 4D/TSC condensation in about $2x10^{-20}$ s, 4D fusion with 2 ^{4}He products takes place with almost 100 percent probability, according to our HMEQPET calculation for barrier factors and a fusion rate formula by Fermi's first golden rule *(2, 3, 4, 5, 6, 7)*.

We show in Chapter 2 the derivation of Langevin equations for known systems such as D-atom, D_2 molecule, D_2^+ ion, and D_3^+ ion. This procedure gives the basics of methodology for formulating Langevin equations of complex D-cluster systems as 4D/TSC and 6D/OSC in Chapter 3. By analogy, we apply the methodology and derive Langevin equations for 4D/TSC and 6D/OSC condensation motions.

Downloaded by COLUMBIA UNIV on June 28, 2012 | http://pubs.acs.org
Publication Date (Web): December 20, 2009 | doi: 10.1021/bk-2009-1029.ch011

Langevin Equations for Known D(H)-Atom and Molecules

The Langevin Equation in General

The Langevin equation is useful to treat dynamic motion of particles under friction (or constraint) and random fluctuation of force-field. This is a kind of stochastic differential equation from a mathematical viewpoint. The generally known form is:

$$m\frac{d^2R}{dt^2} = -F_c - \varsigma\frac{dR}{dt} + f'(t) \qquad (1)$$

Here m is the particle mass, R is particle position, F_c is the Coulombic force, ς is the coefficient for friction (or constraint) and f'(t) is the randomly fluctuated force term (usually white noise, but we need modification for complex systems), for our deuterons plus electrons systems. The Langevin equation takes the balance of force with the fluctuation force source term f'(t), in which we include the quantum-mechanical effect. This equation is complementary to the quantum mechanical Schroedinger equation, which balances the system's total energy (Hamiltonian) with the Heisenberg Uncertainty Principle (HUP) in operator forms.

Downloaded by COLUMBIA UNIV on June 28, 2012 | http://pubs.acs.org
Publication Date (Web): December 20, 2009 | doi: 10.1021/bk-2009-1029.ch011

Langevin Equation for D-Atom

In Fig.1, a simple quantum-mechanical image of D-atom is drawn. In the view of Platonic symmetry, D-atom is the orthogonal coupling of central point (deuteron) and sphere (electron-wave) to form symmetry in three-dimensional space. The Langevin equation is given as the balance of the centripetal force of Coulombic attraction between a plus-charged deuteron and a minus-charged electron and the centrifugal force of electron rotation motion around the center-of-mass point (actually very close to the center position of deuteron wave):

$$m_e\frac{d^2R_{de}}{dt^2} = -\frac{e^2}{[R_{de}]^2} + \frac{m_e v_e^2}{R_{de}} + f(t) \qquad (2)$$

Downloaded by COLUMBIA UNIV on June 28, 2012 | http://pubs.acs.org
Publication Date (Web): December 20, 2009 | doi: 10.1021/bk-2009-1029.ch011

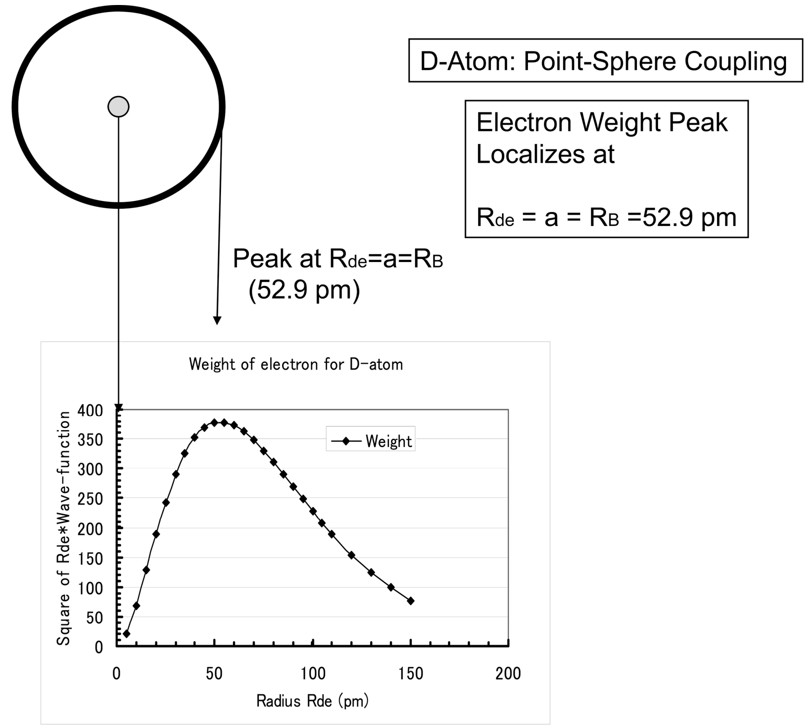

Fig. 1. Quantum-mechanical image of D-atom.

Here, m_e is the electron mass, R_{de} is the d-e distance, e is the unit charge and v_e is the electron velocity.

Basic quantum-mechanical data for D(H)-atom are:

$$\Psi_{100}(r) = \frac{1}{\sqrt{\pi a^3}} e^{-r/a} \qquad \text{; 1-S electron wave function} \qquad (2\text{-}2)$$

$$\left\langle \Psi_{100} \middle| E_{C-D} \middle| \Psi_{100} \right\rangle = \int_0^\infty (-e^2/r)\Psi_{100}{}^2 4\pi r^2 dr = -1.44/r \qquad \text{; Coulomb energy} \qquad (2\text{-}3)$$

Using $r=R_B$=52.9 pm, we get <Coulomb Energy>= -27.2eV.
Using the ground state energy of the system,

$$\left\langle H \right\rangle = \left\langle \Psi_{100} \middle| H \middle| \Psi_{100} \right\rangle = \left\langle \Psi_{100} \middle| -\frac{\hbar^2}{2m}\nabla^2 - \frac{e^2}{r} \middle| \Psi_{100} \right\rangle = E_0 = -13.6eV \qquad (2\text{-}4)$$

we obtain <mean electron kinetic energy>=13.6eV.

The de Broglie wave length $\lambda = h/(mv)$ corresponding to this mean electron kinetic energy is 332 pm, which satisfies the condition that $2\pi R_B = 332pm$, namely the Bohr's condition or the continuity of wave function for one turn around the center of mass point (very close to the deuteron or proton position in this case). For λ> 332 pm, the centrifugal force of orbital electron, $(mv)^2/R_{de}$ is smaller than the centripetal Coulombic attractive force, e^2/R_{de}^2. Forλ< 332 pm, the centrifugal force is greater than the centripetal force.

Therefore, the λ= 332 pm state (corresponding to the mean electron kinetic energy 13.6 eV) is the only steady state, namely the ground state for the d-e or p-e system. No other electron kinetic energy states than 332 pm can satisfy the Heisenberg uncertainty principle (HUP) and the exact balancing of the centrifugal force and the centripetal force. Thus, the electron motion around a deuteron (or proton) with different kinetic energy from 13.6 eV should draw spiral motion to get back to the 332 pm ground state.

We have no friction in this case for formulating a Langevin equation. By taking the ensemble average of Eq. (2) with the weight of squared 1-S wave function $\Psi_{100}{}^2$, we obtain

$$m_e \frac{d^2\langle R_{de}\rangle}{dt^2} = -\left\langle \frac{e^2}{R_{de}^2} \right\rangle + \left\langle \frac{m_e v_e^2}{R_{de}} \right\rangle = 0 \qquad (3)$$

The right side becomes zero, because of the average kinetic energy $\langle E_{KE}\rangle = \frac{1}{2} m_e \langle v_e^2 \rangle = \frac{e^2}{2R_B} = 13.6eV$ and the average Coulomb energy

$\langle E_C \rangle = -\frac{e^2}{R_B} = -27.2eV$ as well-known for a hydrogen (or deuterium) atom.

However, the exact mathematical proof is needed, because we regarded the factor $1/R_{de}$ as separable in the ensemble averaging.

We can integrate Eq. (3) over time to get

$$m_e \frac{d\langle R_{de}\rangle}{dt} = F(T) = \int_0^T f(t)dt = \langle f(t) \rangle = 0 \qquad (4)$$

The time-average (integral) of random fluctuation f(t) is equal to the ensemble average <f(t)> because of the ergodic process. We integrate Eq. (4) to obtain the well-known result:

$$\langle R_{de}\rangle(t) = R_0 = R_B = 52.9pm \qquad (5)$$

Namely, the expectation value $\langle R_{de}\rangle$ of the radial electron orbit is constant to be Bohr radius R_B = 52.9 pm. The dynamic motion of an electron starting at an arbitrary position should converge to this ground state after spiral motion.

Downloaded by COLUMBIA UNIV on June 28, 2012 | http://pubs.acs.org
Publication Date (Web): December 20, 2009 | doi: 10.1021/bk-2009-1029.ch011

Quantum Mechanical Ensemble Average for D-Cluster

Because we can see that the positions of both electrons and deuterons fluctuate quantum-mechanically for D-cluster systems, we need to average with both weights of wave functions for electrons and deuterons. Applying the Born-Oppenheimer (adiabatic) approximation for total wave function, we can do step-wise averaging for electron waves and for deuteron waves. The adiabatic wave function for D_2 molecule is

$$\Psi(R_{dd};r_{A1},r_{A2},r_{B1},r_{B2}) = \Psi_{2D} \cdot X(R_{dd}) \tag{6}$$

The electron wave function of D_2 molecule is given *(4)* by

$$\Psi_{2D} = \frac{1}{\sqrt{(2+2\Delta)}}\left[\Psi_{100}(r_{A1})\Psi_{100}(r_{B2}) + \Psi_{100}(r_{A2})\Psi_{100}(r_{B1})\right]X_s(S1,S2) \tag{7}$$

And the wave function for a d-d pair is approximated by the Gaussian wave function as, rewriting X with Ψ and putting $R_{dd} = R$,

$$\Psi(R,R') = \frac{1}{\sqrt{2\pi\sigma^2}}\exp(-(R'-R)^2/(2\sigma^2)) \tag{8}$$

The quantum-mechanical ensemble average of observable G is given for every step:

$$\langle G\rangle_{ensemble} = \langle\Psi|G|\Psi\rangle \tag{9}$$

Langevin Equation for D_2 Molecule

The electron localization (weight distribution) of a D_2 molecule is roughly understood by the normalization equation of electron wave function as

$$(4\pi)^4\int_0^\infty\int_0^\infty\int_0^\infty\int_0^\infty \Psi_{2D}^2(r_{A1},r_{A2},r_{B1},r_{B2})r_{A1}^2r_{A2}^2r_{B1}^2r_{B2}^2dr_{A1}dr_{A2}dr_{B1}dr_{B2} = 1 \tag{10}$$

$$\int_0^\infty\int_0^\infty\int_0^\infty\int_0^\infty \rho(r_{A1},r_{A2},r_{B1},r_{B2})dr_{A1}dr_{A2}dr_{B1}dr_{B2} = 1 \tag{11}$$

$$\rho(r_{A1},r_{A2},r_{B1},r_{B2}) = \frac{(4\pi)^4}{2+2\Delta}\left\{\begin{array}{l}\left[r_{A1}^2\Psi_{100}^2(r_{A1})r_{B2}^2\Psi_{100}^2(r_{B2})\right]r_{A2}^2r_{B1}^2 \\ +\,2\left[r_{A1}\Psi_{100}(r_{A1})r_{A2}\Psi_{100}(r_{A2})r_{B1}\Psi_{100}(r_{B1})r_{B2}\Psi_{100}(r_{B2})\right]r_{A1}r_{A2}r_{B1}r_{B2} \\ +\left[r_{A2}^2\Psi_{100}^2(r_{A2})r_{B1}^2\Psi_{100}^2(r_{B1})\right]r_{A1}^2r_{B2}^2\end{array}\right\} \tag{12}$$

Downloaded by COLUMBIA UNIV on June 28, 2012 | http://pubs.acs.org
Publication Date (Web): December 20, 2009 | doi: 10.1021/bk-2009-1029.ch011

Because the $\left|r\Psi\right|^2$-type term is the element of the particle density localization function, localized peaks appear at $r_{A1}=r_{A2}=r_{B1}=r_{B2}=a=R_B$ (52.9 pm); namely, the drawn sphere with Bohr radius is a good measure of electron localization.

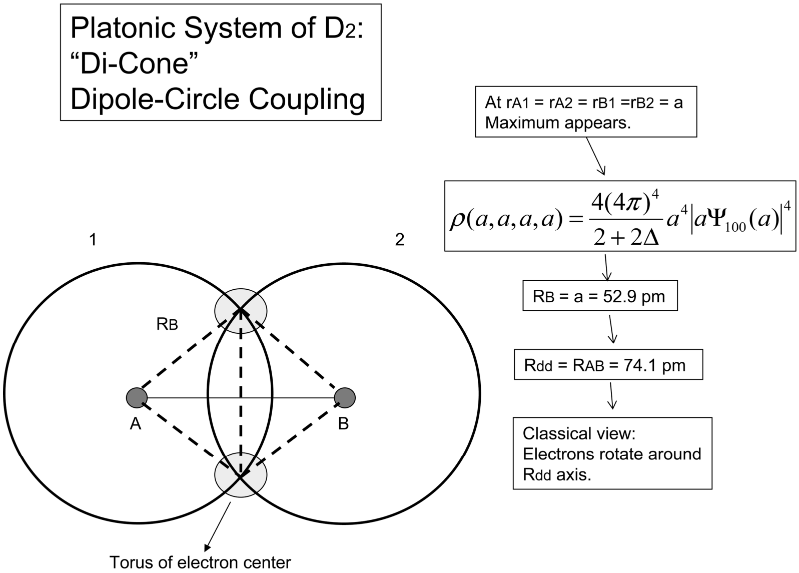
Platonic System of D2:
"Di-Cone"
Dipole-Circle Coupling
At rA1 = rA2 = rB1 =rB2 = a
Maximum appears.
$\rho(a,a,a,a)=\frac{4(4\pi)^4}{2+2\Delta}a^4\left|a\Psi_{100}(a)\right|^4$
RB = a = 52.9 pm
Rdd = RAB = 74.1 pm
Classical view:
Electrons rotate around
Rdd axis.
1
2
RB
A
B
Torus of electron center

Fig. 2. Localization of electron wave and semi-classical image of D_2 molecule.

In the view of Platonic symmetry, a D_2 molecule is an orthogonal coupling of the d-d line (dipole) and the circle (torus of electron center) to form a dicone (see the bottom left figure in Fig. 2). The freedom of the electron's motion is constrained by the existence of a counterpart deuteron and two electrons to form the torus of electron centers, but averaged centrifugal force exists as the rotation of electrons around R_{dd} axis.

Major quantum-mechanical parameters for D_2 molecule are

$$\left\langle\Psi_{2D}\left|H\right|\Psi_{2D}\right\rangle=-35.1eV \quad \text{; total energy of the } D_2 \text{ system} \qquad (12\text{-}2)$$

$$\left\langle E_{C-2D}\right\rangle=4(-\frac{e^2}{a_B})+2(\frac{e^2}{\sqrt{2}a_B})=-70.3eV \quad \text{; Coulomb energy} \qquad (12\text{-}3)$$

$$\left\langle E_{ke-2D}\right\rangle=\left\langle H_{2D}\right\rangle-\left\langle E_{C-2D}\right\rangle=70.3eV-35.1eV=35.2eV$$
$$\text{; mean kinetic energy of two electrons} \qquad (12\text{-}4)$$

We now know that the mean kinetic energy of one electron in the D_2 system is 17.6 eV. The de Broglie wave length of 17.6 eV electron is 230 nm, which satisfies the condition $2\pi R_e=230nm$ with $R_e = R_{ee}/2 = R_B/\sqrt{2}$. This feature provides us with a semi-classical image that two quantum-mechanical electron

Downloaded by COLUMBIA UNIV on June 28, 2012 | http://pubs.acs.org
Publication Date (Web): December 20, 2009 | doi: 10.1021/bk-2009-1029.ch011

centers are rotating around the center-of-mass point of the system and draw a torus (circle).

The Langevin equation for D_2 molecule thus becomes

$$m_d \frac{d^2 R_{dd}}{dt^2} = -(4\sqrt{2} - 2)\frac{e^2}{R_{dd}^2} + \frac{2 m_e v_e^2}{(R_{ee}/2)} - \frac{\partial V_{s2}(R_{dd};1,1)}{\partial R_{dd}} + f(t) \tag{13}$$

Here, the Coulomb force term under Platonic symmetry is derived by a derivative (minus sign) of Coulomb energy,

$$E_C = -4\frac{e^2}{R_{de}} + \frac{e^2}{R_{dd}} + \frac{e^2}{R_{ee}} \tag{14}$$

$$E_C \approx -4\sqrt{2}\frac{e^2}{R_{dd}} + 2\frac{e^2}{R_{dd}} \tag{15}$$

By taking the QM-ensemble average with the weight of the squared electron wave function,

$$m_d \frac{d^2 \langle R_{dd} \rangle}{dt^2} = -\left\langle \frac{5.26}{R_{dd}^2} \right\rangle + 4\left\langle \frac{m_e v_e^2}{R_{ee}} \right\rangle - \frac{\partial V_{s2}(R_{dd};1,1)}{\partial \langle R_{dd} \rangle} + \langle f(t) \rangle \tag{16}$$

The first and second term of Eq. (16)'s right side cancel each other *(4)*, and we obtain

$$m_d \frac{d^2 \langle R_{dd} \rangle}{dt^2} = -\frac{\partial V_{s2}(R_{dd};1,1)}{\partial \langle R_{dd} \rangle} + \langle f(t) \rangle \tag{17}$$

By taking the ensemble average with the Gaussian wave function of the d-d pair, we see that the second term of Eq. (17) <f(t)> becomes zero, because we have no distortion in the d-d dipole line by the QM fluctuation, which causes deviation from the Platonic symmetry. Thus, Eq. (17) becomes the well-known Newtonian mechanical equation, constrained by molecular trapping potential V_{s2} (R_{dd};1,1), which we must, however, calculate by quantum mechanics. Mathematical formulas for trapping (shielded) potentials of D_2 and D_2^+ systems are given in our previous papers *(2, 5)*. Plotted data for two potentials are shown in Fig. 3a.

Downloaded by COLUMBIA UNIV on June 28, 2012 | http://pubs.acs.org
Publication Date (Web): December 20, 2009 | doi: 10.1021/bk-2009-1029.ch011

Downloaded by COLUMBIA UNIV on June 28, 2012 | http://pubs.acs.org
Publication Date (Web): December 20, 2009 | doi: 10.1021/bk-2009-1029.ch011

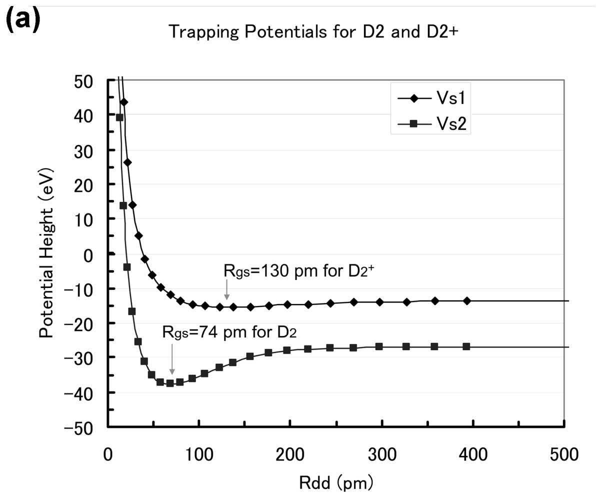

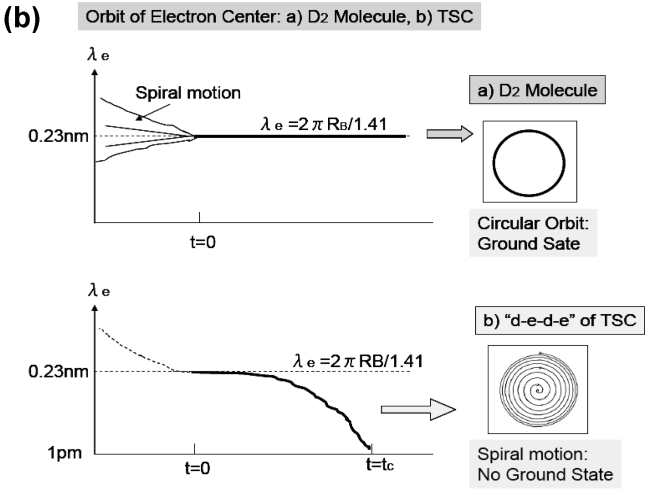
(b)
Orbit of Electron Center: a) D2 Molecule, b) TSC
λe
Spiral motion
0.23nm
λe =2π RB/1.41
t=0
a) D2 Molecule
Circular Orbit:
Ground Sate
λe
0.23nm
λe =2π RB/1.41
1pm
t=0
t=tc
b) "d-e-d-e" of TSC
Spiral motion:
No Ground State

Fig. 3a. Trapping potential of d-d pair for D_2 molecule and D_2^+ ion.
Fig. 3b. Feature of spiral motion for D_2 system: a) stable D_2 molecule, b) a face of TSC under condensation. (12).

As understood by the potential shape for the D_2 molecule given in Fig. 3a, the Langevin equation for expectation value $<R_{dd}>$ always gives convergence to R_{gs} =74 pm after the time-dependent spiral motion starting from arbitrary position R_{dd} (t=0). If $R_{dd} > R_{gs}$, we have acceleration force. If $R_{dd} < R_{gs}$, we have deceleration force. The feature is drawn in Fig. 3b.

Langevin Equation of D_2^+ Ion

The D_2^+ ion molecule is the three-body system of d-e-d. The electron wave function is given by the normalized linear combination of 1-S wave functions from two deuteron positions. The energy eigen-value of the electron as a function of d-d distance R_{dd} is given by the variational method as $V_s(R_{dd};1,1)$, the curve for which is given in Fig. 3a.

The electron center (the averaged position with weighting of the squared wave function) makes a torus around the center-of-mass of the d-e-d system (very close to the mid-point of R_{dd}). In the view of Platonic symmetry, the D_2^+ molecule is the elongated dicone.

As an analogy to the D_2 molecule, the Langevin equation for the D_2^+ ion (stable in a vacuum) is thus given by

$$m_d \frac{d^2 R_{dd}}{dt^2} = -2\frac{e^2}{R_{de}^2} + \frac{e^2}{R_{dd}^2} + \frac{m_e v_e^2}{R_e} - \frac{\partial V_s(R_{dd};1,1)}{\partial R_{dd}} + f(t) \tag{18}$$

By taking the QM-ensemble average with the electron wave function and the Gaussian d-d wave function, we obtain

$$-e^2\left\langle \frac{2}{R_{de}^2} - \frac{1}{R_{dd}^2} \right\rangle + \left\langle \frac{m_e v_e^2}{R_e} \right\rangle = 0 \tag{19}$$

$$m_d \frac{d^2 \langle R_{dd} \rangle}{dt^2} = -\frac{\partial V_s(R_{dd};1,1)}{\partial \langle R_{dd} \rangle} \tag{20}$$

The potential curve is shown in Fig. 3a. In the view of Platonic symmetry, the D_2^+ ion molecule is an elongated dicone with R_{dd}=130 pm (approximate value for the ground state), with a rotating triangle of d-e-d face around the R_{dd} axis. The dynamic motion of the deuteron according to Eq. (20) gives convergence to $R_{dd}=R_{gs}$=138 pm after spiral motion. The eigen-value of the three-system Hamiltonian is calculated by GW2 code$^{2)}$ as -15.1eV. The system's Coulomb energy is -28.7 eV. We obtain the electron mean kinetic energy of 13.6 eV. The radius of torus for the rotation of the quantum-mechanical electron center around the center-of-mass (very close to the mid-point of the d-d dipole) is calculated as 52.9 pm (equal to the Bohr radius). The d-d distance of ground state is 138 pm. These are the conditions to make the system energy of d-e-d a three-body minimum.

In the view of classical mechanics, the straight lineup of the d-e-d system gives the minimum system energy, and it would converge to the mid-point to form a "very dimished size dde system," which might cause strong interaction, namely d-d fusion. However, fulfilling this requirement means that the sizes of the deuterons and electrons must be zero (just points); this is the consequence of Newtonian mechanics, and the charge density and the mass density should diverge to infinity at the points. This is the great contradiction against nature for

Downloaded by COLUMBIA UNIV on June 28, 2012 | http://pubs.acs.org
Publication Date (Web): December 20, 2009 | doi: 10.1021/bk-2009-1029.ch011

classical mechanics. To avoid the divergence, particles should have finite sizes reflecting the HUP.

In the quantum-mechanical view, the weight of the charge density at the center-of-mass point (very close to the middle line of the d-d dipole) is just zero because of the HUP. That is, the much larger de Broglie wave length of the electron than that of the deuterons should make the effective quantum-mechanically averaged charge center exist at the rotating torus around the center-of-mass point. Consequently, the d-e-d system draws a rotating triangle around the d-d dipole line, in the semi-classical view. This is the energy-minimized state of the d-e-d three-body system in quantum mechanics.

In the following, for complex D-cluster systems, Eq. (17) and Eq. (20) with those potentials provide intrinsic components of friction (constraint) by QM electron waves with D-cluster condensation.

Downloaded by COLUMBIA UNIV on June 28, 2012 | http://pubs.acs.org
Publication Date (Web): December 20, 2009 | doi: 10.1021/bk-2009-1029.ch011

Langevin Equations of Expectation Values for Complex D-Clusters

In complex D-cluster systems under Platonic symmetry, averaged rotation motion of particles over the whole system is prohibited by the constraints of many particle arrangements. This form *(3)* of self-organization makes possible simpler treatment to derive a one-dimensional Langevin equation. The term "form" is a meta-physical concept.

The QM-ensemble average in an electron wave function can be subdivided as multiple constraint functions of either the d-e-d or the d-e-d-e potential derivative as

$$\left\langle Constra\,\mathrm{int} \right\rangle_{electron-wave} = -N_f \frac{\partial V_{si}(R_{dd};1,1)}{\partial R_{dd}} \tag{21}$$

Here, N_f is the number of faces of the Platonic polyhedron for a D-cluster and i=1 for the d-e-d (D_2^+ type) face and i=2 for the d-e-d-e (D_2 type) face.

The Langevin equation for a D-cluster under Platonic symmetry with N_e number of d-d edges and N_f number of faces is written as

$$N_e m_d \frac{d^2R}{dt^2} = -\frac{k}{R^2} - N_f \frac{\partial V_s}{\partial R} + f(t) \tag{22}$$

Here, k is constant (11.8 for 4D/TSC, 29.3 for $6D^{--}$/OSC, 6.13 for $3D^+$, and zero for D_2 and D_2^+).

The QM-ensemble average with the d-d wave function (assuming Gaussian form) is given by

$$N_e m_d \left\langle \Psi(R,R') \middle| \frac{d^2R}{dt^2} \middle| \Psi(R,R') \right\rangle = -\left\langle \Psi(R,R') \middle| \frac{k}{R^2} \middle| \Psi(R,R') \right\rangle$$
$$- N_f \left\langle \Psi(R,R') \middle| \frac{\partial V_s}{\partial R} \middle| \Psi(R,R') \right\rangle + \left\langle \Psi(R,R') \middle| f(t) \middle| \Psi(R,R') \right\rangle \quad (23)$$

with a Gaussian wave function for a d-d pair of the D-cluster,

$$\Psi(R,R') = \frac{1}{\sqrt{2\pi\sigma^2}} \exp(-(R'-R)^2/(2\sigma^2)) \quad (24)$$

We derive a Langevin equation for the expectation value $<R_{dd}> = <R>$ as

$$N_e m_d \frac{d^2 <R>}{dt^2} = -\frac{k}{R^2} - N_f \frac{\partial V_s}{\partial R} + <f(t)> \quad (25)$$

For a complex D-cluster, the <f(t)> value does not always equal zero because of the deviation of the D-cluster system from ideal Platonic symmetry, because of the distortion of the system by the quantum-mechanical fluctuation of d-positions. The perturbed force component from this QM distortion is given approximately from the next formula, which is the change of the system Coulomb energy derivative, as

$$-\frac{\partial \Delta E_C}{\partial R} \approx -k\frac{1}{2}\left(\frac{1}{(R+\Delta R)^2} + \frac{1}{(R-\Delta R)^2}\right) + k\frac{1}{R^2}$$
$$\approx -\frac{k}{2R^2}\left(1 - \frac{2\Delta R}{R} - \left(\frac{\Delta R}{R}\right)^2 + 1 + \frac{2\Delta R}{R} - \left(\frac{\Delta R}{R}\right)^2\right) + \frac{k}{R^2} \quad (26)$$
$$= \frac{k}{R^2}\left(\frac{\Delta R}{R}\right)^2$$

By using a Gaussian squared wave function for the d-d pair fluctuation, we write

$$(\Delta R)^2 = (\sigma R)^2 \quad (27)$$

The change of Coulomb force from distortion is given by the following simple formula:

$$\text{<Change of Coulombic Force>} = \frac{k\sigma^2}{(R_{dd})^2} \quad (28)$$

Downloaded by COLUMBIA UNIV on June 28, 2012 | http://pubs.acs.org
Publication Date (Web): December 20, 2009 | doi: 10.1021/bk-2009-1029.ch011

Langevin Equation of D_3^+ Ion Molecule

It is well-known that the tri-atomic hydrogen molecular ion D_3^+ (or H_3^+) is generated in ion source and glow-discharged plasma and is very stable in a vacuum. However, quantum-molecular physics for the system is a difficult problem to solve by many-body Schroedinger equations, and studies are continuing in astrophysics. The D_3^+ molecule is the d-e-d-e-d five-body system.

The analogy of the present methodology for D (or H)-cluster under the orthogonal coupling of Platonic symmetries for electrons and deuterons (or protons) can provide a rather simple way of modeling its dynamics. Applying Eq. (25), we obtain the Langevin equation of a D_3^+ molecule, for the expected value $<R_{dd}>$:

$$3m_d \frac{d^2\langle R_{dd}\rangle}{dt^2} = -\frac{6.13}{\langle R_{dd}\rangle^2} - 6\frac{\partial V_s(R_{dd};1,1)}{\partial \langle R_{dd}\rangle} + \langle f(t)\rangle \tag{29}$$

Here, the force is given with a unit of [keV/pm]. The image of D_3^+ ion is given in Fig. 4.

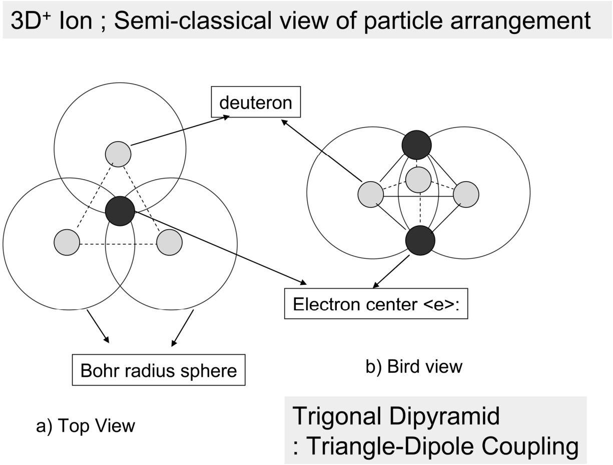

Fig. 4. Tri-atomic hydrogen (deuterium) molecular ion and its Platonic arrangement.

The system Coulomb energy and its derivative can be calculated by a simple geometry exercise for the Platonic symmetry system of a trigonal di-pyramid, which is the orthogonal coupling of the third regular triangle and the <e> - <e> line (dipole). Here, two electron centers (or electron balls) appear in the system, and system-averaged rotation of electrons is prohibited (no averaged centrifugal force). However, partial electron rotation motion remains around a d-d line as a face of the system.

Downloaded by COLUMBIA UNIV on June 28, 2012 | http://pubs.acs.org
Publication Date (Web): December 20, 2009 | doi: 10.1021/bk-2009-1029.ch011

By distorting ideal Platonic symmetry from the QM fluctuations of deuteron positions, we have positive <f(t)> bias. Because we have three d-d edges in the system, three times Eq. (28) becomes the bias (about 30 percent of the main Coulomb acceleration force). Therefore, the total potential of the system becomes, in the expected value equation,

$$V_{3D+main}(R_{dd}) = -\frac{6.13}{R_{dd}} + 6V_s(R_{dd};1,1) + (\text{<f(t)> component}) \qquad (30)$$

The calculated curve of this potential is shown in Fig. 5.

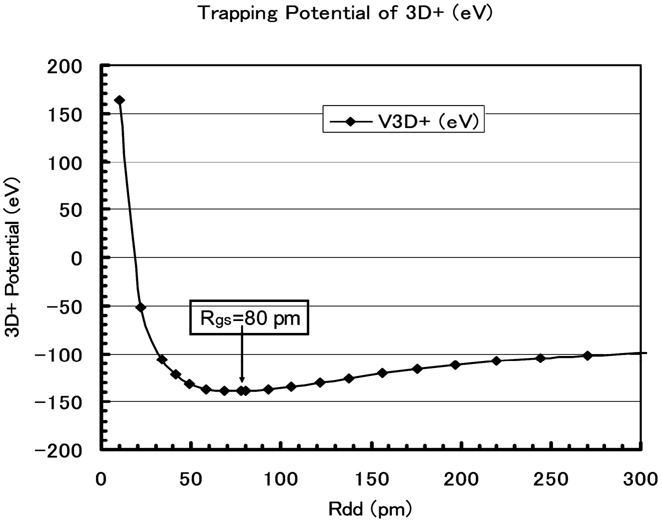

Fig. 5. Trapping potential of D_3^+ ion molecule with Langevin equation for expectation value of d-d distance of 3d regular triangle.

The tri-atomic hydrogen ion is thus stable and has its ground state at R_{gs}= 80 pm. As a reference, Helm et al. (Freiburg University, 2003; google triatomic hydrogen ion and Helm) gave about R_{gs} = 85 pm *(8)*, which agrees very well with our result, taking into account that the appropriate sigma value of the wave function *(2)* is about 30 percent of R_{dd}.

We can conclude that our approach with one-dimensional Langevin equations for D-cluster systems look successful. We are ready to apply it to more-complex systems.

Downloaded by COLUMBIA UNIV on June 28, 2012 | http://pubs.acs.org
Publication Date (Web): December 20, 2009 | doi: 10.1021/bk-2009-1029.ch011

Langevin Equation for 4D/TSC and Numerical Solution

Downloaded by COLUMBIA UNIV on June 28, 2012 | http://pubs.acs.org
Publication Date (Web): December 20, 2009 | doi: 10.1021/bk-2009-1029.ch011

Double Platonic Symmetry

In Fig. 6, we show the feature of an electron cloud for 4D/TSC (t=0), compared with those of a D-atom and a D_2 molecule.

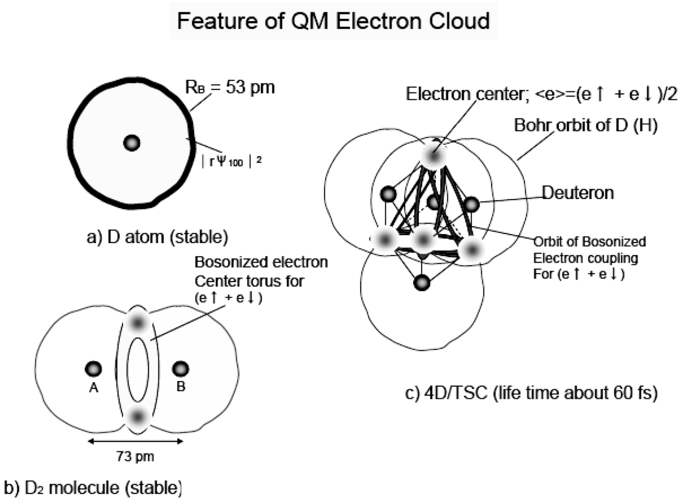
Feature of QM Electron Cloud
RB = 53 pm
| rΨ100 | 2
a) D atom (stable)
Bosonized electron
Center torus for
(e↑ + e↓)
A
B
73 pm
b) D2 molecule (stable)
Electron center; <e>=(e↑ + e↓)/2
Bohr orbit of D (H)
Deuteron
Orbit of Bosonized
Electron coupling
For (e↑ + e↓)
c) 4D/TSC (life time about 60 fs)

Fig. 6. Feature of QM electron clouds for 4D/TSC (t=0), compared with those of D-atom and D_2 molecule.

The form *(3)* of the 4D/TSC (t=0) wave function is given *(1, 3, 4)* as

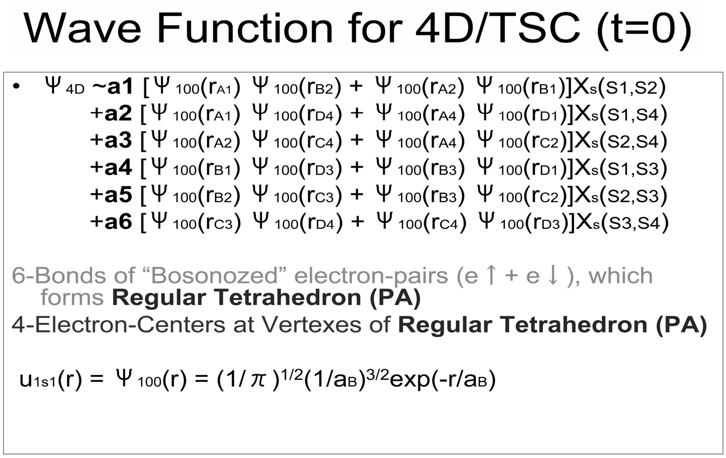

Wave Function for 4D/TSC (t=0)

$$
\begin{aligned}
\bullet\quad \Psi_{4D} \sim \mathbf{a1}\, & [\Psi_{100}(r_{A1})\ \Psi_{100}(r_{B2}) + \Psi_{100}(r_{A2})\ \Psi_{100}(r_{B1})]X_s(S1,S2) \\
+\mathbf{a2}\, & [\Psi_{100}(r_{A1})\ \Psi_{100}(r_{D4}) + \Psi_{100}(r_{A4})\ \Psi_{100}(r_{D1})]X_s(S1,S4) \\
+\mathbf{a3}\, & [\Psi_{100}(r_{A2})\ \Psi_{100}(r_{C4}) + \Psi_{100}(r_{A4})\ \Psi_{100}(r_{C2})]X_s(S2,S4) \\
+\mathbf{a4}\, & [\Psi_{100}(r_{B1})\ \Psi_{100}(r_{D3}) + \Psi_{100}(r_{B3})\ \Psi_{100}(r_{D1})]X_s(S1,S3) \\
+\mathbf{a5}\, & [\Psi_{100}(r_{B2})\ \Psi_{100}(r_{C3}) + \Psi_{100}(r_{B3})\ \Psi_{100}(r_{C2})]X_s(S2,S3) \\
+\mathbf{a6}\, & [\Psi_{100}(r_{C3})\ \Psi_{100}(r_{D4}) + \Psi_{100}(r_{C4})\ \Psi_{100}(r_{D3})]X_s(S3,S4)
\end{aligned}
$$

6-Bonds of "Bosonozed" electron-pairs (e↑ + e↓), which forms **Regular Tetrahedron (PA)**

4-Electron-Centers at Vertexes of **Regular Tetrahedron (PA)**

$$u_{1s1}(r) = \Psi_{100}(r) = (1/\pi)^{1/2}(1/a_B)^{3/2}\exp(-r/a_B)$$

Top equation (31)

This TSC system has the double symmetry of regular tetrahedrons for deuterons and electron centers, namely *double Platonic symmetry*, which is the most ideal system for three-dimensional condensation squeezing into the central focal point (center-of-mass; CMS).

Langevin Equation for 4D/TSC and Solution

The system of Coulomb energy and its derivative are given in our previous work *(1, 2)*. We present here the resulting final Langevin equation for the Monte-Carlo calculation:

$$6m_d \frac{d^2R_{dd}(t)}{dt^2} = -\frac{11.85}{[R_{dd}(t)]^2} - 6\frac{\partial V_{s2}(R_{dd}(t);1,1)}{\partial R_{dd}(t)} + \langle f(t) \rangle + f'(t) \qquad (32)$$

with

$$f'(t) = f(t) - \langle f(t) \rangle \qquad (33)$$

$$f(t) = [-\frac{\partial \Delta E_c(R_{dd})}{\partial R_{dd}}]\mathrm{mod}[X^2(R'_{dd};R_{dd}(t))] \qquad (34)$$

$$\mathrm{X}^2(R'_{dd};R_{dd}(t)) = \frac{1}{\sqrt{2\pi\sigma^2}}\exp[-(R'_{dd}-R_{dd}(t))^2/(2\sigma^2)] \qquad (35)$$

For QM-ensemble averaged equation, we obtained *(2)*

$$6m_d \frac{d^2\langle R_{dd} \rangle}{dt^2} = -\frac{11.85}{\langle R_{dd} \rangle^2} - 6\frac{\partial V_s(\langle R_{dd} \rangle;m,Z)}{\partial \langle R_{dd} \rangle} + 6.6\left\langle \frac{(R'-R_{dd})^2}{R_{dd}{}^4} \right\rangle \qquad (36)$$

The time-dependent TSC trapping potential for this equation was given *(2)* as

$$V_{tsc}(R':R_{dd}(t)) = -\frac{11.85}{R_{dd}(t)} + 6V_s(R_{dd}(t);m,Z) + 2.2\frac{|R'-R_{dd}(t)|^3}{[R_{dd}(t)]^4} \qquad (37)$$

Here, we fixed m=2 and Z=2 for V_s (dde*(2,2) potential) for the numerical calculation.

The third term on the right side of Eq. (36) gives about 15 percent positive bias to the main Coulomb force (first term) and was merged *(2)* in the first term by multiplying factor 0.85 in the numerical calculation by the Verlet method.

In Fig. 7, we show the calculated trapping potential of 4D/TSC, compared with that of $6D^{2-}$/OSC (shown later). 4D(or H)/TSC keeps on average the always-accelerating force in its condensation motion; hence, it can condense

Downloaded by COLUMBIA UNIV on June 28, 2012 | http://pubs.acs.org
Publication Date (Web): December 20, 2009 | doi: 10.1021/bk-2009-1029.ch011

until the TSC-min state (about 10-20 fm radius) comes, as illustrated in Fig. 8. On the other hand, $6D^{2-}$/OSC converges to R_{dd}=40 pm on the way to condensation (we derive the equation later). *Within these five kinds of D-clusters, only 4D/TSC can condense to a very small charge-neutral entity.*

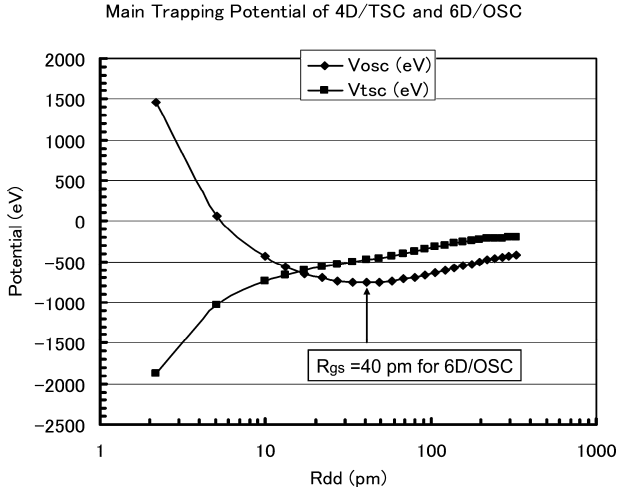

Fig. 7. Central trapping potential (at R=R') of 4D(or H)/TSC, always attractive, compared with $6D^{2-}$/OSC potential, which has converging point (about 40 pm) at its ground state.

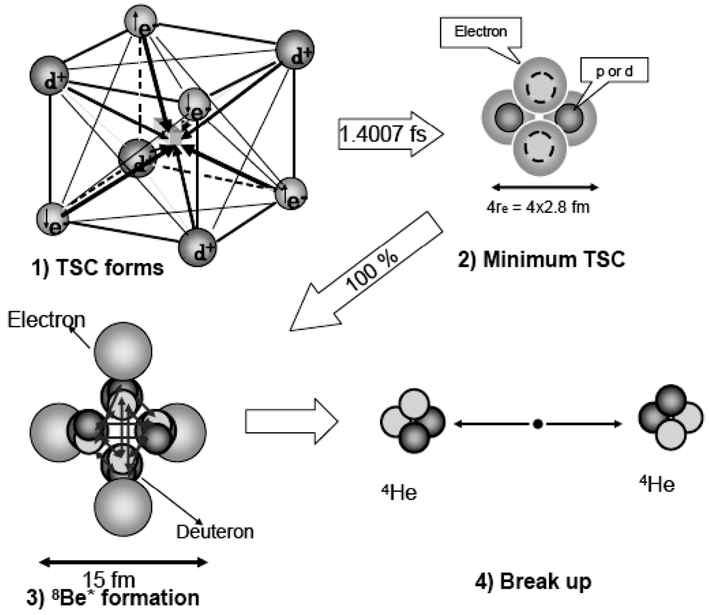
d+
e-
1.4007 fs
Electron
p or d
4re = 4x2.8 fm
1) TSC forms
2) Minimum TSC
100 %
Electron
Deuteron
15 fm
3) 8Be* formation
4He
4He
4) Break up

Fig. 8. Condensation of 4D/TSC and 4D-fusion to two ^{4}He-particles break-up.

Downloaded by COLUMBIA UNIV on June 28, 2012 | http://pubs.acs.org
Publication Date (Web): December 20, 2009 | doi: 10.1021/bk-2009-1029.ch011

The numerical solution of Eq. (36) was obtained by a computer code based on the Verlet time-step method *(2)*. A standard result is shown in Fig. 9.

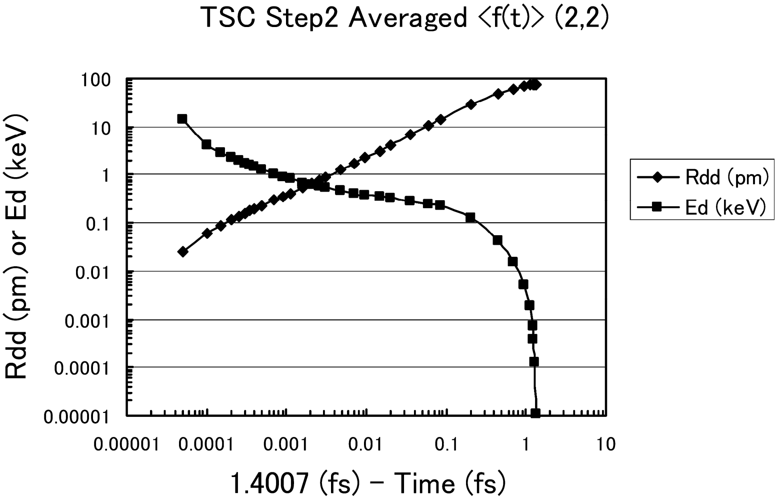

Fig. 9. Numerical results of 4D/TSC condensation motion; time-variation of <R_{dd}> and mean deuteron kinetic energy <E_d>.

The condensation time of 4D/TSC is as fast as 1.4007 fs. As we show in the next section, 4D fusion reaction takes place with almost 100 percent probability in the final stage of condensation within the time interval of about $2x10^{-20}$ s. For other details of the time-dependent behavior of TSC dynamics with different conditions, see our previous paper *(2)*. Because the effective time interval $2x10^{-20}$s, with averaged effective deuteron energy of about 10 keV, surprised us, we can say that the cluster deuteron fusion by the TSC condensation mechanism is not "cold fusion." The relative kinetic energy of about 10 keV for the 4D simultaneous fusion reaction seems comparable to the target d-t plasma temperature 10 keV of the ITER device (hot fusion), by chance.

To make the visible fusion rate in the condensed matter environment room temperature, the deuteron cluster (or a d-d pair) should be confined within a very deep trapping potential (time-dependent, in the case of TSC) to keep elevated the kinetic energy of deuterons because of the requirement of HUP. However, the event happens very quickly as $2x10^{-20}$ s.

To trigger the TSC condensation, we need the initial state interaction in the dynamics of solid-state-physics level to form TSC (t=0) state. For example, the TSC (t=0) state was speculated to form by the optical phonon excitation in the PdD regular lattice *(1)*.

Because the potential depth of PdD Bloch potential trapping deuterons in Pd lattice is about 0.2 eV, we need 0.2 eV at most for the incubation of the TSC(t=0) state.

We got about a 100 percent 4D fusion yield per TSC generation in our previous study *(2)*, and we know that $2x10^{11}$ 4D-fusion/s corresponds to one watt. The necessary input energy is $0.2eVx1.6x10^{-19}x2x10^{11} = 6.4x10^{-9}$ joule, for

Downloaded by COLUMBIA UNIV on June 28, 2012 | http://pubs.acs.org
Publication Date (Web): December 20, 2009 | doi: 10.1021/bk-2009-1029.ch011

generating one joule of energy by the TSC-induced 4D fusions, if we have full D-loaded Pd, namely PdD, on the near surface of the PdDx sample. The nominal gain of this reaction is about 10^8. In other words, if the TSC generation probability is larger than 10^{-8} for the dynamic condition of the PdD lattice, we will have more output energy than input energy.

Because the production of 2×10^{11} TSC/s corresponds to about the portion of 10^{-11} of PdD density (on the order of 10^{22} per cm^3) in cubic centimeters, the transient phenomena causing TSC generation are considered to be in the very dissipative structure, much less than ppm and ppb levels, of PdD lattice dynamics or surface dynamics, which the usual solid-state or surface physics has never treated.

As discussed in our past works *(5, 7, 9, 11, 12)*, 4D/TSC(t=0) state may be formed in the PdD dynamics by the optical phonon excitation (see Fig.10).

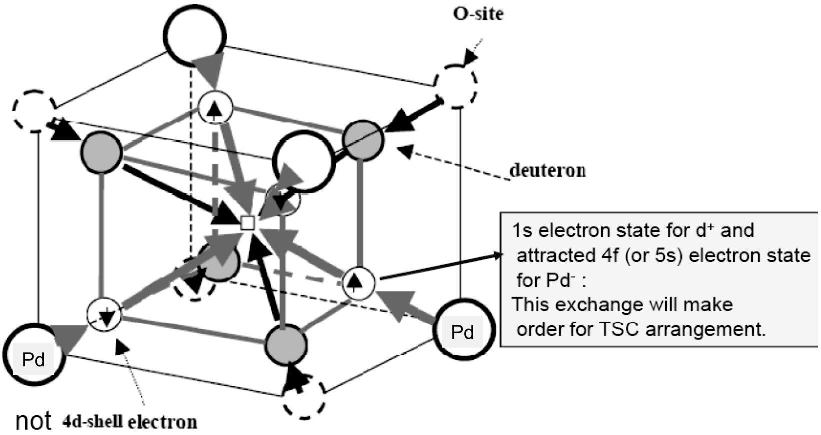

1s electron state for d^+ and attracted 4f (or 5s) electron state for Pd^- : This exchange will make order for TSC arrangement.

Fig. 10. Incubation of 4D/TSC (t=0) in the PdD dynamics under D-phonon excitation. The exchange of 1s electron for the d+ sate and the 5s (or 4f) electron of Pd- state may arrange the TSC configuration.

We made a crude estimation of the 4D cluster formation probability of more than 10^{-6} in our past work *(5, 7, 9)*. We now consider that we need much less probability as 10^{-11} to be studied in the dissipative dynamics.

The PdD (PdDx: x=1) lattice may be formed in the thin near surface zone of Pd lattice which absorbs deuterons in octahedral sites. However, the fully loaded PdD state would block deuteron diffusion into a much deeper zone. Therefore, we need as wide a surface area as possible in the Pd zone. This may be the main reason that we need nano-modificated Pd metal samples to cause the CMNS effect with a visible amount of reaction rates.

Of course, for the practical research and development of a power-generating device, we need additional inputs. However, we have a good principle on which to base a clean radiation-less nuclear energy device if the rapid condensation mechanism of 4D/TSC works well in real devices.

Downloaded by COLUMBIA UNIV on June 28, 2012 | http://pubs.acs.org
Publication Date (Web): December 20, 2009 | doi: 10.1021/bk-2009-1029.ch011

Langevin Equation for $6D^{2-}$/OSC

To fulfill orthogonally coupled Platonic symmetry for a 6D-cluster, eight electron centers should appear on the center lines of eight regular triangle faces of a 6d octahedron; see Fig. 11. Therefore, to keep the geometrical symmetry, the Platonic OSC should be at a 2- negative ion state.

The Langevin equation for $6D^{2-}$/OSC becomes

$$12m_d \frac{d^2 R_{dd}(t)}{dt^2} = -\frac{29.3}{[R_{dd}(t)]^2} - 24\frac{\partial V_s(R_{dd}(t);1,1)}{\partial R_{dd}(t)} + \langle f(t) \rangle + f'(t) \qquad (38)$$

The effective trapping potential of this system was given in Fig. 7, which tells us that $6D^{2-}$/OSC does not make ultimate condensation. However, in the transient condensation process, we may have a small probability that the d-d distance would approach in shorter d-d distances than 40 pm of its ground state, and the 6D fusion rate may be enhanced somehow. We need a numerical study for this.

We need a different study on whether there is a condensing system of a neutral 6D-cluster (face-centered dodecahedron *(11)* by coupling two octahedrons (one of six deuterons and the other of six electron centers)).

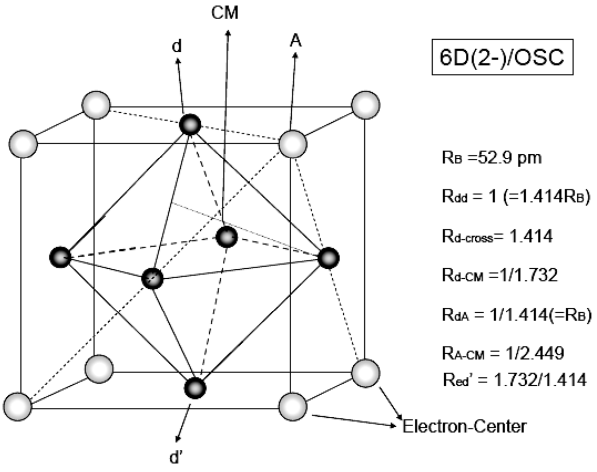

Fig. 11. Geometrical view of $6D^{--}$/OSC structure.

Because we know the proposed 6D/OSC in the condensed matter should be charge-neutral (rapid charge neutralization should happen), we might consider the eight QM electron centers with 6/8 charge weight at each point to keep the charge neutrality of the 6D system and its Platonic symmetry. We need further study to validate whether 6D/OSC (neutral) would make ultimate condensation like 4D/TSC (neutral).

Downloaded by COLUMBIA UNIV on June 28, 2012 | http://pubs.acs.org
Publication Date (Web): December 20, 2009 | doi: 10.1021/bk-2009-1029.ch011

HMEQPET Method for Fusion Rate Quantification

A slice of time-dependent TSC trapping potential at the final stage (TSC-min) of condensation is shown in Fig. 13.

The depth of the trapping potential is -130.4keV. The calculated relative kinetic energy of the d-d pair is 13.68keV. In an approximate view, this potential can be regarded as an adiabatic potential having the d-d pair quasi-ground state with E_{gs}=13.68 keV trapped in 130.4keV deep potential for a very short time-interval of 10^{-20} s. In every time step of the numerical calculation (by the Verlet method *(2)*), we can draw approximate adiabatic potential which changes continuously with the change of time.

The kinetic energy of the particle is given by $E = \frac{1}{2}mv^2$. The de Brpglie wave length is given by $\lambda = \hbar/(mv)$.

The mean electron kinetic energy increases in a d-e-d-e face during the condensation motion, as shown in Fig. 12. The electron wave length with increased kinetic energy (or momentum) can be replaced with heavy mass fermion to keep the same d-e-d-e size. The HMEQPET method is based on this idea.

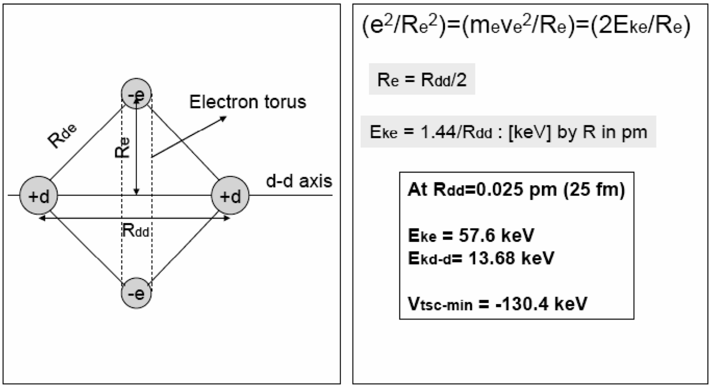

$(e^2/R_e^2)=(m_e v_e^2/R_e)=(2E_{ke}/R_e)$

$R_e = R_{dd}/2$

$E_{ke} = 1.44/R_{dd}$: [keV] by R in pm

At R_{dd}=0.025 pm (25 fm)

E_{ke} = 57.6 keV
$E_{kd\text{-}d}$= 13.68 keV

$V_{tsc\text{-}min}$ = -130.4 keV

Fig. 12. Model of a d-e-d-e face of TSC 6 faces; time-dependent continuous diminishment of size keeping a pseudo-molecular system with higher electron mean kinetic energy is assumed here.

From Fig. 12, the mean kinetic energy of an electron in a d-e-d-e face is 57.6keV at R_{dd}=25fm. Because TSC at t=0 has mean electron kinetic energy of about 18eV (17.6 eV in exact number), the equivalent mass of heavy fermion is estimated to be $\sqrt{57.6x1000/18} = 56.57$ times the electron mass. The depth of dde*(56.57,2) potential is about -4.8keV, comparable to the trapping potential of a muonic d-d molecule (See Table-1 and Table-2).

Downloaded by COLUMBIA UNIV on June 28, 2012 | http://pubs.acs.org
Publication Date (Web): December 20, 2009 | doi: 10.1021/bk-2009-1029.ch011

Table 1: Typical-point-wise HMEQPET potentials to be replaced with time-dependent TSC trapping potential

Molecule	b_0 (pm)	R_{min} (pm)	$V_{s\text{-}min}$ (keV)	$E_{d\text{-}d}$ (keV)	R_{gs} (pm)	E_{gs} (keV)
D_2	22	70	-0.0378	0.00268	76.69	-0.03514
dde*(2,2)	4.5	19.3	-0.1804	0.01013	21.82	-0.1702
dde*(5,2)	1.9	7.6	-0.4509	0.02080	8.72	-0.4301
dde*(10,2)	0.90	3.8	-0.9019	0.0418	4.36	-0.8601
dde*(20,2)	0.45	1.9	-1.8039	0.0837	2.18	-1.720
dde*(50,2)	0.18	0.76	-4.5097	0.2094	0.873	-4.300
dde*(100,2)	0.09	0.38	-9.0194	0.4196	0.436	-8.600
dde*(200,2)	0.045	0.19	-18.039	0.8430	0.218	-17.196
dde*(500,2)	0.018	0.076	-45.097	2.135	0.0873	-42.968
dde*(1000,2)	0.009	0.038	-90.194	4.336	0.0436	-85.858
dde*(2000,2)	0.0045	0.019	-180.39	8.984	0.0218	-171.41

Because the depth of the 4D/TSC trapping potential at R_{dd}=25fm was -130.4keV, we must assume much heavier fermion to quantitatively approximate the TSC trapping potential by EQPET dde*(m,Z) potential *(2)*.

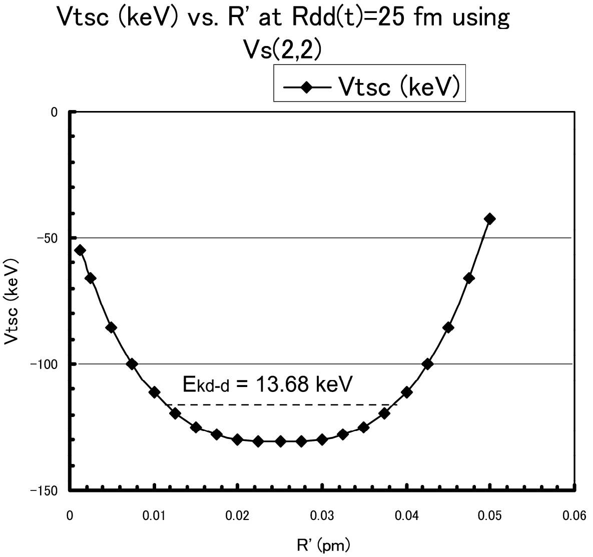

Fig. 13. TSC trapping potential at the final stage (TSC-min) of condensation motion by Langevin equation.

We used Gaussian wave function for the d-d pair in Langevin equations. As discussed *(2)*, we cannot use Gaussian wave function for the estimation of Coulomb barrier penetration probability (barrier factor), because the tail

Downloaded by COLUMBIA UNIV on June 28, 2012 | http://pubs.acs.org
Publication Date (Web): December 20, 2009 | doi: 10.1021/bk-2009-1029.ch011

distribution of Gaussian function is not accurate enough. Instead, we can use the trapping potentials of a dde*(m,2) EQPET molecule and Gamow integrals. The assumed quasi-particle state is a heavy Cooper pair e*(m,2) of two heavy electrons in a d-e-d-e system.

If a one-to-one relationship exists between m and $<R_{dd}>(t)$, we can replace all the time-dependent TSC trapping potentials with $V_s(R_{dd}(t);m,2)$ potentials of HMEQPET continuously by adopting the real number of m.

The typical parameters of calculated $V_s(R_{dd}(t);m,2)$ potentials are shown in Table 1. From this table, we eventually found the following empirical laws:

$$b_0(m,2) = 0.206 R_{gs}(m,2) \qquad (39)$$

$$m = 9000 / b_0(m,2) \qquad (40)$$

Here, the b_0 and R_{gs} values are given in an fm unit.

The muonic dd-molecule has R_{gs}=805 fm, and the state of m=54m_e of HMEQPET potential corresponds to it. The final stage of TSC potential corresponds to m=2000m_e.

Calculated barrier factors by the HMEQPET method were given in Table-2.

Table 2: Calculated time-dependent barrier factors under TSC condensation

Elapsed Time (fs)	R_{dd} : d-d distance (pm)	P_{2d} : 2D barrier factor	P_{4d} : 4D barrier factor
0	74.1 (D2 molecule size)	1.00E-85	1.00E-170
1.259	21.8 (dde*(2,2): Cooper pair)	1.30E-46	1.69E-92
1.342	10.3	2.16E-32	4.67E-64
1.3805	4.12	9.38E-21	8.79E-41
1.3920	2.06	6.89E-15	4.75E-29
1.3970	1.03	9.69E-11	9.40E-21
1.39805	0.805 (muon-dd molecule size)	1.00E-9	1.00E-18
1.39960	0.412	9.40E-7	2.16E-13
1.40027	0.206	3.35E-5	1.12E-9
1.40047	0.103	1.43E-3	2.05E-6
1.40062	0.0412	1.05E-2	1.12E-4
1.40070	0.0206 (TSC-min size)	4.44E-2	1.98E-3

Downloaded by COLUMBIA UNIV on June 28, 2012 | http://pubs.acs.org
Publication Date (Web): December 20, 2009 | doi: 10.1021/bk-2009-1029.ch011

In Low-Energy Nuclear Reactions and New Energy Technologies Sourcebook Volume 2; Marwan, J., et al.;
ACS Symposium Series; American Chemical Society: Washington, DC, 2010.

Conclusions

1) The quantum-mechanical Langevin equation (stochastic differential equation) is complementary to the Schroedinger equation of standard quantum mechanics.
2) Platonic symmetry appears in a D-atom, D_2, D_2^+, D_3^+ molecule, and 4D/TSC, and we could introduce the dynamics approach based on Langevin equations.
3) Platonic symmetry appears in the initial state interactions in the CMNS of 4D/TSC for both the Coulombic interaction and the strong interaction.
4) Dynamic Platonic symmetry is key for the super-screening of Coulomb repulsion and 4D simultaneous cluster fusion.
5) We have obtained good solutions of molecular dynamics with Langevin equations for such Platonic symmetrical systems as D, D_2, D_3^+ and 4D(or H)/TSC.
6) It was shown that about 100 percent 4D-fusion per TSC generation is possible, by the present work, in condensed matter nuclear effects.
7) Only 4D (or H)/TSC can condense ultimately to a very small charge-neutral entity with 10-20 fm radius size, according to the five kinds of D(or H)-clusters studied in this work.
8) Bosonized e(spin=1/2)+e(spin=-1/2) coupling for the d-e-d-e system makes D_2 type faces of 4D(or H)/TSC to help its ultimate condensation.
9) $6D^{2-}$/OSC converges its condensation at about R_{dd}=40 pm, but a closer d-d distance in transient condensation may appear with a small probability.
10) Single quantum-mechanical <e- >-center states for the d-e-d (D_2^+) faces of the D_3^+ ion molecule and the $6D^{2-}$/OSC cluster should enhance constraint (friction) for their condensation motion.
11) The HMEQPET method is a useful tool to approximate the time-dependent TSC trapping potential and to calculate sufficiently accurate time-dependent barrier penetration probabilities for estimating fusion reaction rates.
12) Fusion rate formulas for time-dependent D-cluster condensation were given.
13) We need further efforts to study the solid-state/surface physics conditions to efficiently incubate TSC(t=0) transient clusters in metal-deuterium and metal-hydrogen systems.
14) The final state interaction of ^{8}Be* is complicated, because of unknown spin-parity and isospin states, to study further.

Acknowledgements

The author is grateful to Prof. Akira Kitamura (Kobe University) and Dr. Tetsuo Sawada (Nihon University) for their kind comments and critiques for improving this work. He is also grateful to Technova Inc. for its support of this work.

Downloaded by COLUMBIA UNIV on June 28, 2012 | http://pubs.acs.org
Publication Date (Web): December 20, 2009 | doi: 10.1021/bk-2009-1029.ch011

References

1) Takahashi, A.; Yabuuchi, N. Condensed Matter Nuclear Effects Under Platonic Symmetry. In *Condensed Matter Nuclear Science, Proceedings of 13th International Conference on Condensed Matter Nuclear Science*, Sochi, Russia, 25 June-1 July, 2007; Bazhutov, Y., Ed.; Publisher Center MATI: Moscow, 2008, pp 554-568.
2) Takahashi, A.; Yabuuchi, N. Study on 4D/TSC Condensation Motion by Non-Linear Langevin Equation. In *ACS Symposium Series 998; Low Energy Nuclear Reactions Source Book;* Marwan, J.; Krivit, S., Eds.; American Chemical Society, Oxford University Press: Washington DC, 2008, pp 57-83.
3) Yabuuchi, N., Takahashi, A. Form of Nuclear Fusion in Solid Crystals. In *Condensed Matter Nuclear Science, Proceedings of 13th International Conference on Condensed Matter Nuclear Science*, Sochi Russia, 25 June-1 July, 2007; Bazhutov, Y., Ed.; Publisher Center MATI: Moscow, 2008, pp 793-802.
4) Takahashi, A.; Yabuuchi, N. On Condensation Force of TSC. *J. Condensed Matter Nuclear Science* **2007**, *1*, 97-105.
5) Takahashi, A. Deuteron Cluster Fusion and Ash. *J. Condensed Matter Nuclear Science* **2007**, *1*, 62-85.
6) Hale, G.; Tally, T. Deuteron-Induced Fusion in Various Environments. *Trans. Fusion Technology* **1994**, *26*, 442-450.
7) Takahashi, A.; Yabuuchi, N. Fusion Rates of Bosonized Condensates. *J. Condensed Matter Nuclear Science* **2007**, *1*, 106-128.
8) Petsalakis, I. D. Theoretical Calculations on Electronic Transitions for H-3. *J. Chem. Phys.* **1983**, *87*, 3806.
9) Takahashi, A. TSC-Induced Nuclear Reactions and Cold Transmutations. *J. Condensed Matter Nuclear Science* **2007**, *1*, 86-96.
10) Hamada, T.; Johnston, I. A Potential Model Representation of Two-Nucleon Data Below 315MeV. *Nuclear Physics* **1962**, *34*, 382.
11) Takahashi, A. A Theoretical Summary of Condensed Matter Nuclear Effects. *J. Condensed Matter Nuclear Science* **2007**, *1*, 129-141.
12) Takahashi, A. Dynamic Mechanism of TSC Condensation Motion. In *Condensed Matter Nuclear Science: Proceedings of 14th International Conference on Cold Fusion*, 17-21 August, 2008, Washington DC, (in press).
13) Takahashi, A. Some Consideration of Multi-Body Fusion in Metal Deuterides. *Trans. Fusion Technology* **1994**, *26*, 451-454.
14) Takahashi, A.; Yabuuchi, N. D-Cluster Dynamics and Fusion Rate by Langevin Equation. In *Proceedings of Eighth International Workshop on Anomalies in Hydrogen/Deuterium Loaded Metals*, 13-18 October 2007.

Downloaded by COLUMBIA UNIV on June 28, 2012 | http://pubs.acs.org
Publication Date (Web): December 20, 2009 | doi: 10.1021/bk-2009-1029.ch011

Downloaded by UNIV OF GUELPH LIBRARY on June 28, 2012 | http://pubs.acs.org
Publication Date (Web): December 20, 2009 | doi: 10.1021/bk-2009-1029.ch012

Chapter 12

Quark-Gluon Model for Magic Numbers Related to Low Energy Nuclear Reactions

H. Hora[1,2#], N. Ghahramani[1]*, G. H. Miley[3], M. Ghanaatian[4], M. Hooshmand[4], K. Philberth[5], and F. Osman[1]**

[1]School of Computing and Mathematics, University of Western Sydney, Penrith NSW, Australia
[2]Department of Theoretical Physics, University of New South Wales, Sydney 2052, Australia
[3]Department of Nuclear, Plasma and Radiological Engineering, University of Illinois, Urbana, IL 61801, USA
[4]Department of Physics, Shiraz University, Shiraz, Iran
[5]Thanning, 82544 Egling, Germany
***on Sabbatical Leave from Shiraz University, Iran**
****now Department of Mathematics, Trinity College, Summer Hill 2130, Australia**

A new three-fold symmetry is presented for derivation of the magic numbers of nuclei and is compared with the model based on the Boltzmann distribution from the standard abundance distribution (SAD) of nuclei in the universe in the endothermic branch. This results in a 3^n relation leading to the motivation to explore the quark state in nuclei. But this is in contrast (duality) to the fact that the confinement of nuclei by a generalized Debye layer can be based only on a nucleon, not on a quark structure. This Debye model result led to a change in the Fermi energy of the nucleons into the relativistic range at higher-than-nuclear density, resulting in a mass independent state at higher-than-nuclear densities for the quark state in neutron stars. This result and the 3^n-relation motivated consideration of the quark state in nuclei. Success is reported by quark-like statistics for nuclei reproducing magic numbers up to 126, identical with the Boltzmann model. But for the next-higher number, the Boltzmann model definitely arrives at 180, while the new quark-like model leads to the number 184.

In Low-Energy Nuclear Reactions and New Energy Technologies Sourcebook Volume 2; Marwan, J., et al.;
ACS Symposium Series; American Chemical Society: Washington, DC, 2010.

The paradox may be solved by accurate measurements of a local Maruhn-Greiner maximum from low energy nuclear reactions (LENR).

Introduction

Perhaps the following experimental indications from low energy nuclear reactions (LENR) – as a generalization and extension of cold fusion to heavy nuclei based on reproducible observations and theoretical consistencies – mix facts of nuclear structure and quark-gluon properties with conclusions on how endothermic heavy nuclei may have been created. More of the following questions are unsolved than solved. Perhaps many connections between such observed hard facts as nuclear magic numbers or as hard astrophysical observations with measurements of LENR may become a further mosaic stone for understanding the nuclear reactions of hydrogen isotopes in certain solid metals such as palladium and others.

The following results are a combination of several separate developments: how to describe the state of quarks in nuclei and to relate them to the magic numbers of protons or neutrons within a nucleus. This is a point of duality because the nuclei show properties of nucleons, which will also be explained by reviewing a model based on the Boltzmann equilibrium, while the new results show properties that are determined by quarks in nuclei as if the nucleons are fully split into their quark constituents. There were indications of how the thermodynamical state of quarks in motion within quantum gluon plasma (QGP) soup are not absolutely free (*1*), which is known from the lattice theory of quantum chromo dynamics (QCD), where the gluons are connected with a force much weaker than the binding force.

These considerations evolved from a model of magic numbers based on observations of the standard abundance distribution (SAD) of the elements in the universe, which will be summarized in Section 2. These results were entirely motivated by the processes explained in Section 5. But any mixing of sections 2 and 5 should be avoided for reasons of clarity. On the other hand, accurate experimental results from Section 5 indicate a paradox between magic numbers derived from the Boltzmann model of Section 2 and the new results derived from the QGP in section 4. Section 3 summarizes results from a generalization of the Debye length, known from plasma physics. It demonstrates properties of the QGP both for nuclei and for the state of higher-than-nuclear density known from neutron stars or from nuclear generation after the big bang, where the assumption of Boltzmann equilibrium was essential. This leads to new results on the derivation of magic numbers from the QGP. It may lead to an explanation of how endothermic nuclei may have been generated.

Downloaded by UNIV OF GUELPH LIBRARY on June 28, 2012 | http://pubs.acs.org
Publication Date (Web): December 20, 2009 | doi: 10.1021/bk-2009-1029.ch012

Boltzmann Distribution From SAD for Magic Numbers

Downloaded by UNIV OF GUELPH LIBRARY on June 28, 2012 | http://pubs.acs.org
Publication Date (Web): December 20, 2009 | doi: 10.1021/bk-2009-1029.ch012

One of the important patterns leading to the development of nuclear shell structure is so-called magic numbers. These numbers were first noticed by Elsässer (*2*) in 1933. What makes these numbers magic are the properties of the nuclei with proton or neutron numbers equal to one of these magic numbers. For protons, the magic numbers are 2, 8, 20, 28, 50, and 82, and for neutrons, these numbers are 2, 8, 20, 28, 50, 82 and 126. Among other properties, the important properties of magic nuclei are their stability, abundance, decay energy and electric quadrupole.

There were attempts to reproduce these numbers by a mathematical scheme similar to the number Z_e of electrons in the shell number n of atoms, where the result was fully confirmed by Schrödinger's quantum mechanics as $Z_e = 2n^2$ (n = 1, 2, 3, …), where the factor 2 results from the Pauli exclusion principle. For the magic numbers of the nuclei, the numerical derivation was much more complicated, which is known from Bagge (*3, 4*). There were two sequences derived with the numbers:

$$M_{an} \in \mathbf{2, 8, 20}, 40, 70, 112 \tag{1}$$

$$M_{bn} \in 2, 6, 14, \mathbf{28, 50, 82, 126} \tag{2}$$

The speculative numerical system (*3, 4*) was based on the two possibilities to begin with a sequence 2, 3, 4 … with the following procedures:

2 3 4 5 6 7 8 … being the difference to:
1 3 6 10 15 21 28 … again as difference:
1 4 10 20 35 56 84 … times two:
2 8 20 40 70 112 … to arrive at sequence (1)

and alternatively to begin the sequence 1, 2, 3, …

1 2 3 4 5 6 7 … being the difference to:
1 2 4 7 11 16 22 … again difference to:
1 3 7 14 25 4 63 … times two:
2 6 14 28 50 82 126 … one arrives at sequence (2)

The magic numbers were those printed in bold in sequences 1 and 2, showing where the jump happens from one to the other sequence. The jump was explained by the nuclear shell model by Maria Goeppert-Mayer (*4*) and by Jenssen (*5*), where a difference between spin and spin-orbit properties of the nucleons was the cause. The magic numbers appeared also in the measured SAD in the universe, Fig. 1 (*6, 7*), given by the nucleon number $A = Z + N_n$ with the number of protons Z and the number of neutrons N_n, where the magic numbers are at the drastic maxima between the much lower abundances between. Fig. 1 shows only the nuclei above A = 60, where nuclear creation has to be endothermic, while the synthesis of nuclei by fusion from smaller nuclei is exothermic for A < 60 (*8*), not resulting in such a general curve as that given in Fig. 1.

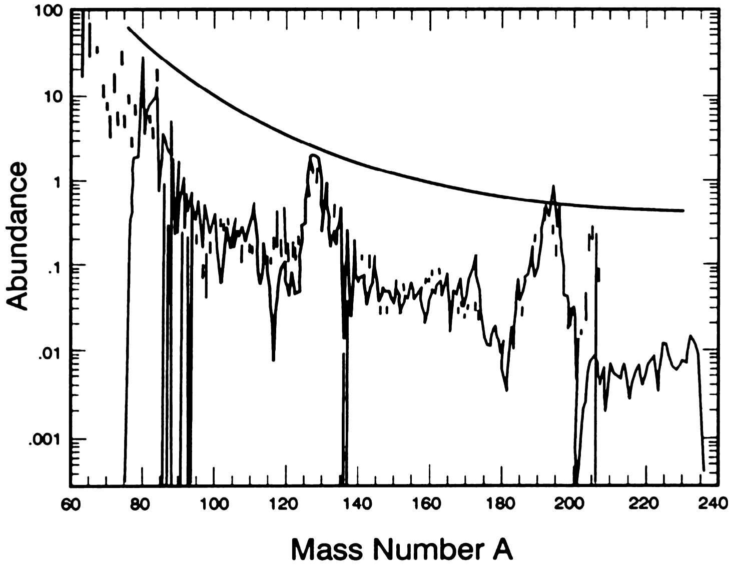

Figure 1. Measured standard abundance distribution of elements (SAD) (3) in the Universe.

The abundance number N, depending on the proton number Z for A > 60, is given by a Boltzmann distribution from the measurements of Fig. 1:

$$N(Z) = N' \exp(-Z/Z') \qquad (3)$$

where the number Z' = 10 fits best (*9*). In view of the following Section 5 with the paradox, we have to extend the former procedure (*9, 10*) to higher magic numbers. We evaluate the ratios

$$R(n) = [N(Z_{n+1})/N(Z_n)] = \exp[(-Z_{n+1} - Z_n)/Z'] \qquad (4)$$

where the Z_n-values are the magic numbers (n = 0, 1, 2, …)

$$Z_0 = 2;\ Z_1 = 8;\ Z_2 = 20 \quad \text{for ratios R up to the magic number 20} \qquad (5)$$
$$Z_2 = 28;\ Z_3 = 50;\ Z_4 = 82;\ Z_5 = 126 \quad \text{for magic numbers above 20} \qquad (6)$$

Downloaded by UNIV OF GUELPH LIBRARY on June 28, 2012 | http://pubs.acs.org
Publication Date (Web): December 20, 2009 | doi: 10.1021/bk-2009-1029.ch012

Table 1. Sequences n - 0, 1, 2, 3, … of magic numbers Z_n and ratios $R(n) = \exp[-(Z_{n+1} - Z_n)/Z']$ with Z'=10 of Eq. (4) based on the SAD measurements of Fig. 1, compared with the 3^n values for Eq. 7. The exception for magic numbers 20 and 28 proves the jump between the Bagge Sequences (1) and (2).

n	Magic number	R(n)	3^n
0	2	1.822	1
1	8	3.321	3
2(as n+1 in (20))	20	-	-
2(as n in (20))	28	9.025	9
3	50	24.53	27
4	82	81.45	81
{4}	{114}	{24.53}	{27}
5	126	221.4	243
{5}	{126&184}	{330.29}	{243}
6	180	735.0	729
{6}	{184}	{1069.6}	{729}
7	246	2440.6	2187

Table 1 shows that the ratios R(n) are very close to

$$R(n) = 3^n \tag{7}$$

where the former concluded new magic numbers were given by

$$Z_6 = 180; \quad Z_7 = 246 \quad \text{and} \quad Z_8 = 324 \tag{8}$$

As seen in Table 1, the otherwise-concluded (*12)* magic numbers 114 instead of 126, 184 instead of 180, and 228 instead of 324 do not fit with Eq. 7. In Fig. 2, the higher values are shown in open circles for demonstrating the numerical fitting and where, in waved brackets in Table 1 and as crosses in Fig. 2, the values for the not-fitting earlier suggested numbers (*12*) are given.

The threefold multiplicity Eq. 7 (*9*) was a reason to suggest that the magic numbers may indicate a quark or some other property not yet known but coming in triplets for the shells in nuclei.

Downloaded by UNIV OF GUELPH LIBRARY on June 28, 2012 | http://pubs.acs.org
Publication Date (Web): December 20, 2009 | doi: 10.1021/bk-2009-1029.ch012

Downloaded by UNIV OF GUELPH LIBRARY on June 28, 2012 | http://pubs.acs.org
Publication Date (Web): December 20, 2009 | doi: 10.1021/bk-2009-1029.ch012

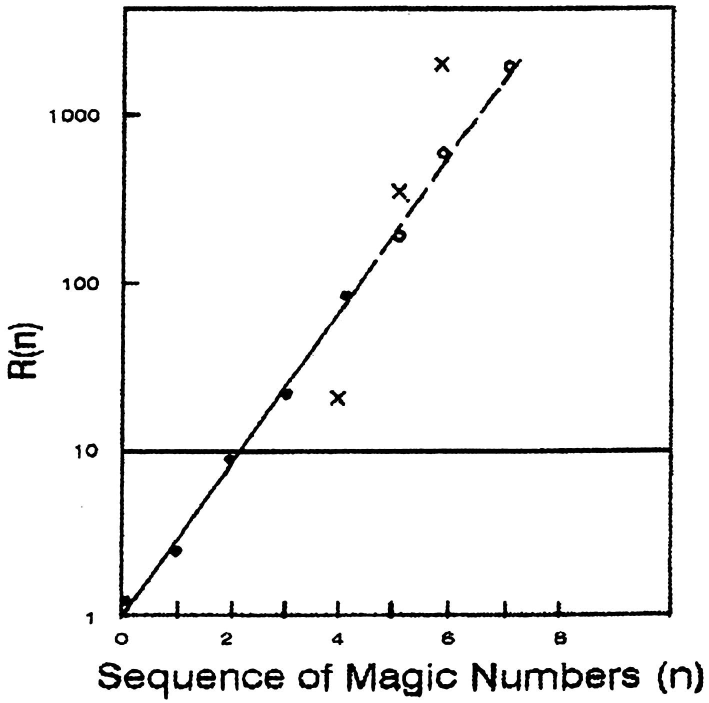

Figure 2. Values R(n), Eq. 7 for the sequence of the magic numbers n with the specifically defined exception between the magic numbers 20 and 28 because of the jump defined and confirmed for the Bagge sequences 1 and 2. The full dots were achieved up to the magic number 126 (9, 11), and the circles were concluded from Eq. 8. The table was extended to check the validity of the magic number 180 from the Boltzmann model in contrast to magic numbers (crosses) concluded before (12) with special attention to number 184 for n = 6.

Generalized Debye Layer Confinement for Nucleons With Fermi Distribution

At the surface of plasmas, electrical double layers are produced with a thickness given by the Debye length:

$$\lambda_D = [kT/(4\pi e^2 n_e)]^{1/2} = 743\ [T\{eV\}/n_e\{cm^{-3}\}]^{1/2}\ cm \tag{9}$$

where T is the temperature, e the charge and n_e the density of the electrons. The electrostatic field energy per surface of the layer results in a surface tension of the plasma resulting in forces that straighten – for example, the plume of the surface of a laser-produced plasma when it is expanding into a vacuum:

$$\sigma_e = 0.27\ T^2/(8\pi e^2 \lambda_d) \tag{10}$$

The surface potential of kT/2 corresponds to the work function for electrons being emitted through the double layer (*13*).

Considering the degenerate electrons in a metal within the ion lattice results in a similar double layer where, instead of the temperature, the Fermi energy of the electrons is causing a Debye length in the range of angstrom and the work function of few eV. Applying this to the surface tension and surface forces results in a quantum theory of surface tension in agreement with the measured values in metals (*14*). The essential mechanism for the acting forces in the surfaces are the gradients of the densities of the particles. The next step of generalization considers the nucleons (protons and neutrons) of nuclei instead of electrons and uses the subrelativistic Fermi energy (15,16):

$$E_F = (3n_{Nu}/\pi)^{2/3}h^2/(8m_{Nu}) \qquad (11)$$

instead of the temperature T in Eq. 9, using nucleons with a mass m_{Nu} and density n_{Nu} instead of electron in Eq. 9. The nucleon Debye length is then

$$\lambda_N = [E_F/(4\pi e^2 n_{Nu})]^{1/2} \propto n_{Nu}^{-1/6} \qquad (12)$$

To confirm this as fact, we take the experimentally known values of nucleon densities, scattering very closely around the nucleon density in a nucleus

$$n_{Nu} = 8.5\text{x}10^{37}\ \text{cm}^{-3} \qquad (13)$$

resulting in Fermi energy for nucleons of 36 MeV, to arrive at a Debye length of

$$\lambda_N = 3.4\text{x}10^{-13}\ \text{cm} \qquad (14)$$

This length corresponds quite well with Hofstadter's measured density decay of about 3 Fm of nucleons at the surface of heavy nuclei down to about calcium (see Fig. 14b of Ref. Hahn et al. (*17*) in rather good agreement with the nucleon Debye length (*12*). One may not consider this fact as a coincidence but as a result of the just-given steps for the generalization of the generalized Debye length for the conditions of the nucleons in a nucleus.

After this basic and very convincing result, we may consider Eq. 10 to understand why the 3Fm-Hofstadter decay is so independent of the compared value of the nucleon Debye length, Eq. 12. The nucleon density in the inner part of the nuclei is nearly the same for all nuclei between vanadium and bismuth, which fact was involved in the average value of Eq. 13. These nuclei show then a rather unchanged decay profile because of the then-unchanged Debye length (see Fig. 14b of Ref. (*17*).

Up to this point, the empirical nucleon density, Eq. 13, was used as an empirical input for demonstration consistency. Now we are looking for a relation without such empirical input and are using an expression of the surface tension in analogy to the plasmas in order to see how this could confine an ensemble of protons and neutrons, see Fig. 3. Obviously, there are strong Coulomb forces trying to drive the protons apart. Another force against confinement of the nucleons is the quantum pressure expressed by Fermi energy

Downloaded by UNIV OF GUELPH LIBRARY on June 28, 2012 | http://pubs.acs.org
Publication Date (Web): December 20, 2009 | doi: 10.1021/bk-2009-1029.ch012

Downloaded by UNIV OF GUELPH LIBRARY on June 28, 2012 | http://pubs.acs.org
Publication Date (Web): December 20, 2009 | doi: 10.1021/bk-2009-1029.ch012

when locating a particle in a volume V that, from the quantum relation with the necessary momentum corresponding to an energy $E_{F,}$ increases with another exponent for smaller and smaller V than that for the Coulomb repulsion. The Fermi and the Coulomb energy are equal at a radius of 285 Fm (*15*), such that, for smaller radii, Fermi energy is the dominating part of the internal energy of the nuclei. Looking into cases of small radii, we can consider the Coulomb forces and other components as small perturbations that are neglected here.

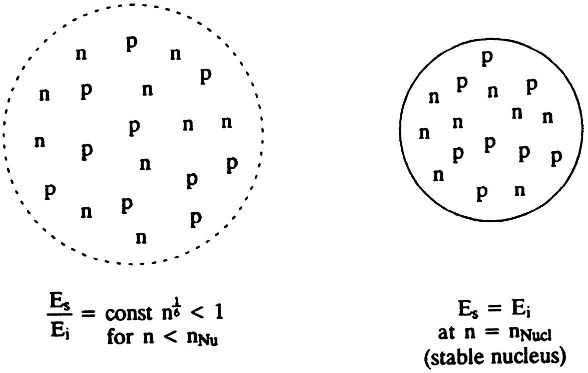
n p n p n p n p n p n n n p n p p p n p n p p n
p n p n p n n n n p p p p p n p n
$\frac{E_s}{E_i}$ = const $n^{\frac{1}{6}}$ < 1
for n < n_{Nu}
$E_s = E_i$
at n = n_{Nucl}
(stable nucleus)

Figure 3. Confining nucleons (protons p and neutrons n) by a surface energy ES against internal energy Ei (dominated by Fermi energy EF) at shrinking radius (15).

The following success will justify the procedure to compare the Fermi energy of the proton and neutron ensemble of Fig. 3 with the surface energy given from a surface tension using a Debye length given by the Fermi energy of the nucleons. Therefore, without specifying the detailed interpretations, we define surface energy in the same way from surface tension as an expression, Eq. 11, by using the Fermi energy of the nucleons. The surface tension for the nuclei is then

$$\sigma_e = 0.27\, E_F^2/(8\pi e^2\lambda_N) \tag{15}$$

The Fermi energy can be expressed generally; see Eq. 17 (*18*).

$$E_F = [3/(\pi)^{2/3}/4]\, [h^2 n_{Nu}^{2/3}/(2m_{Nu})]\, (\lambda_C/2)^{-1}[n_{Nu} + 1/(\lambda_C/2)^3]^{-1/3} \tag{16}$$

where n is the nucleon density. This splits into the branches

$$E_F = \begin{cases} [3/(\pi)^{2/3}/4]\, h^2 n_{Nu}^{2/3}/(2m_{Nu}) & \text{(subrelativistic)} \quad (17a) \\ [3/(\pi)^{2/3}/4]\, hc n_{Nu}^{1/3}/(2\pi) & \text{(relativistic)} \quad (17b) \end{cases}$$

using λ_C the Compton wave length h/(2πmc) with "2π" which option is just ascertained by the following treatment modifying the preceding work (*15*). The surface energy of the nucleus is then

$$E_{surf} = 0.27[3A(4\pi)^{1/2}]^{2/3}\, 3^{1/3}\, E_F^{2/3} /(\pi^{1/2}\, 2^{5/2}\, n_{Nu}^{1/6}\, e) \qquad (18)$$

For comparison between the surface energy and the internal energy, we have

$$E_{surf}/(AE_F) = \begin{cases} 0.27\,(3^{3/2}/2^{10/3})\, hn_{Nu}^{1/6}/(em_{Nu}^{1/2}A^{1/3}) & \text{(subrelativistic)} \quad (19a) \\ 0.27\,[3^{8/3}/(2^{7/3}\,\alpha^{1/2}\, A^{1/3})] & \text{(relativistic)} \quad (19b) \end{cases}$$

using the fine structure constant $\alpha = 2\pi e^2/(hc)$. From Eq. 19a, we see that the nucleus cannot be confined for too low a density. The nucleus is stable only when the density reaches a value of the n_n where the ratio, Eq. 19a, is equal to 1. This is the case at the well-known value of the nuclear density as checked – for example, for bismuth (*15*). The surface Debye layer has a thickness of about 2 to 3 Fm. With these not empirically derived parameters close to Eq. 15 again, the measured Hofstadter decay of the surface charge of heavy nuclei is reproduced.

At relativistic densities just above that of the sub-relativistic case reproducing the well-known density of nuclei, we see that the value, Eq. 19b, no longer depends on the nucleon mass or density. We have no nucleation by the surface energy and a soup of matter. Even the independence of the mass shows that we can either have hadrons (as assumed in neutron stars) or a quark-gluon plasma. Only when this dense matter is expanding at the big bang or from a neutron star, the nucleation is from the Debye layer confinement just at the well-known nucleon density in nuclei.

Considering the value of Eq. 19a to be unity of the nucleation when reaching the nuclear density, the surface energy will produce sub-relativistic nuclear densities with the limit for this nuclear-chemical equilibrium, where higher values for A than 247 are not possible. This may just explain why the nucleation by expansion of a quark-gluon plasma at higher-than-nuclear density from the relativistic branch of the nucleon Fermi energy to the lower nuclear density can produce elements only up to uranium or perhaps curium, at the most, within such equilibrium processes. Higher trans-uranium nuclei by heavy ion collisions as an extremely non-equilibrium process are then really man-made, following the rule of magic numbers, as was shown before. Any such expansion from higher- to lower-than-nuclear density will produce the nuclei up to A = 247 and will provide the endothermic-generated nuclei just by the equilibrium processes.

Downloaded by UNIV OF GUELPH LIBRARY on June 28, 2012 | http://pubs.acs.org
Publication Date (Web): December 20, 2009 | doi: 10.1021/bk-2009-1029.ch012

Quark-Gluon Plasma in Nuclei for Derivation of Magic Numbers

These considerations about the quark state of nuclear matter, again with the results of Section 2, motivated us to find out whether the magic numbers in nuclei may be derived from properties of the quark-gluon plasma. By adopting the $R(n)=3^n$ relation, Eq. 7, the jump between the Bagge sequences appears naturally without any explanation such as spin coupling. In case such an explanation of the quark structure of nuclear shells is adopted, this approach is definitely different from the conventional shell model, and the dual (complementary) nature of the nuclei should be considered. In the framework of $R(n)=3^n$, one may conclude that, in order to form a stable nuclear shell, three quarks from the higher shell must be coupled to one quark from the lower shell.

Abundance Distribution Diagram and Magic Numbers

Close attention to the abundance distribution diagram reveals that different elements with different proton and neutron numbers in nature have been made with unique abundances. On the other hand, in the presented quark-gluon model, a number of quarks (2, 3, 4, …) surround a central u-quark. Let's consider these systems statistically to see whether they have the same probability. In this QGP model, a central u-quark is located at the center of a cube within a regular lattice. Eight quarks are at each corner of the cube covering the central one. In order to form a proton, two of these eight quarks must be d-quark. But how probable is this formation? To answer this question, it is known from lattice QCD theory that, in normal quark-gluon plasma media, only light quarks exist freely, so let's assume that only three flavors exist: u, d and s. Of eight quarks with three flavors, the probability of abundance for each one is 8/3 but the probability of having two of them with the same flavor is

$$3\ \{8!/[2!(8-2)!]\}\ 2^6 / 3^8 = 82.193 \ldots \tag{20}$$

and the probability of getting three of them with the same flavor is

$$3\ \{8!/[3!(8-3)!]\}\ 2^5 / 3^8 = 82.193 \ldots \tag{21}$$

This means that the probability of having a central u-quark with two or three d-quarks is the same. For more than three d-quarks, the probability drops to one-third. In other words, two or three d-quarks easily locate around a central u-quark to form a proton. The magic numbers 8, 20 and 126 correspond then to systems with 3, 4 and 7 d-quarks.

Downloaded by UNIV OF GUELPH LIBRARY on June 28, 2012 | http://pubs.acs.org
Publication Date (Web): December 20, 2009 | doi: 10.1021/bk-2009-1029.ch012

Colored Quark-Gluon Plasma and Magic Numbers

The hot QGP is believed to come into existence right after a big bang and, by relativistic expansion, cool down and change to a proton and a neutron. In the continued process of expansion, different nuclei are formed (nucleation) through the Boltzmann equilibrium process. These formed nuclei are most stable at magic numbers. We intend to investigate how and under what conditions the quarks with colour and flavour form a proton and a neutron and what the origin of magic numbers is in such QGP. We do not intend to describe the quark distribution after the formation of a proton, which is given in terms of structure functions (*1*). If the QGP is considered as thermodynamical media, then it should proceed toward maximum disorder. How such a system approaches equilibrium should be investigated. The thermodynamical state is a stable system with a maximum probability state – that is, the most probable state with a maximum number of complexion.

Now consider a thermodynamical state of quarks in motion. In such QGP soup, the quarks are not absolutely free (*1, 19)*. This is known from lattice QCD theory. In fact, in such QGP soup, the gluons connect to the nearby quarks with a force much weaker than the binding force. In Fig. 4. the QGP media are assumed as an ideal gas model. In such a model, consider a quark to be trying to form a nucleon, capturing two quarks of different flavor. In such competing space between quarks, different nucleon formation cases happen. In Fig. 5, quarks are considered in lattice media, and the central u-quark seeks two d-quarks to form a proton.

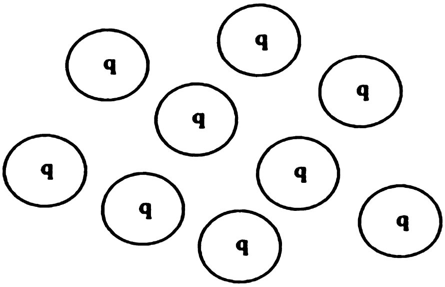

Figure 4. Quark-Gluon plasma media as an ideal gas.

If there are only two d-quarks with no colour neighbouring the central u-quark, then there is no competition, and state ud_1d_2 is formed. But from the standard model, each quark has three colors, and d_1 and d_2 must be of a different color - say green and blue. Therefore, two competing cases exist: a red u with blue d_1 and green d_2 or with green d_1 and blue d_2. So we get number 2 as the first magic number.

Now consider that there are three d-quarks neighbouring the central u-quark. Then there are three cases: ud_1d_2, ud_1d_3 and ud_2d_3. If their colour is also taken into account, then there are six cases in addition to the previous two cases, and we get eight cases to form a proton – that is, the second magic number. Let's consider four neighbouring d-quarks. If only two of them compete, we have two

Downloaded by UNIV OF GUELPH LIBRARY on June 28, 2012 | http://pubs.acs.org
Publication Date (Web): December 20, 2009 | doi: 10.1021/bk-2009-1029.ch012

cases. If three of them participate in this competition, then we have six cases. If all four compete, then we get 12 cases. The total number of cases is therefore

$$2+6+12=20 \tag{22}$$

This is the third magic number.

In both the spin and spin-orbit coupling interpretations to explain magic numbers and numerical explanation of Bagge (*3*), two separate sequences, 1 and 2, were needed with the jump from the first sequence to the second sequence to obtain number 28.

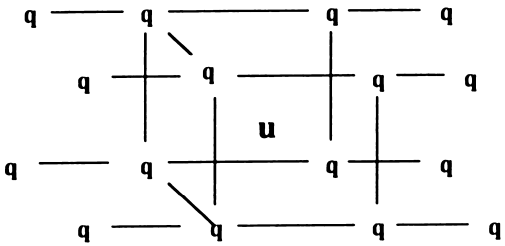

Figure 5. Cubic quark-gluon plasma lattice with central u-quark.

If we consider five quarks neighbouring the central one, the competition between these five quarks in addition to previous ones gives us 40 cases, which is exactly the fourth number from the first sequence. For six and seven neighbouring quarks, 70 and 112 cases are obtained, and the same historical problem exists. To resolve this problem in our model, the QGP condition is used, and imposed quarks are introduced. From lattice QCD theory, it is clear that quarks are not free, that some weak attractive forces (*1*) exist between quarks in QGP soup. That is why it is called a soup.

Now suppose there are four d quarks neighbouring the central u-quark. As shown before, 20 cases are competing to form a proton. If each d-quark is considered to be close to its own neighbours, as seen in Fig. 6, and if, for example, d is absorbed by it, then the closest quark to d that has the strongest attraction force to d will accompany it and participate. Let's call it d', and this is named as an imposed quark.

This quark comes from the second level. Therefore, with one imposed quark for each initial four d-quarks, we have $ud_1d'_1$,$ud_2d'_2$,$ud_3d'_3$ and $ud_4d'_4$. Considering their colours, there are eight cases in addition to the previous 20 cases, adding to 28 competing states to form a nucleus.

Let's consider five d-quarks surrounding the central u-quark. Then we have 20 new cases in addition to 10 imposed cases, adding to 50 cases:

$$20+20+10=50 \tag{23}$$

which consist of ud_1d_2, ud_1d_3, ud_1d_4, ud_1d_5, ud_2d_3, ud_2d_4, ud_2d_5, ud_3d_4, ud_3d_5, ud_4d_5 and $ud_1d'_1$, $ud_2d'_2$, $ud_3d'_3$, $ud_4d'_4$, and $ud_5d'_5$.

Now let's consider six d-quarks around the central u-quark. Then we have

Downloaded by UNIV OF GUELPH LIBRARY on June 28, 2012 | http://pubs.acs.org
Publication Date (Web): December 20, 2009 | doi: 10.1021/bk-2009-1029.ch012

$$40+30+12=82 \tag{24}$$

For seven d-quarks participating

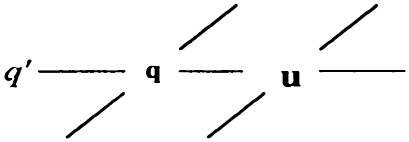

Figure 6. Imposed quark q' in a cubic QGP lattice with central u-quark.

$$70+42+14=126 \tag{25}$$

Eventually, for eight d-quarks, we get 184 cases. This is a new magic number that is obtained in this model. For more than eight quarks, one has to consider the imposed quarks from the third level, and no additional magic number is obtained.

Paradox About High Magic Numbers Determined by LENR Experiments

It is remarkable that the QGP model confirms the same magic numbers up to 126 as the Boltzmann distribution model based on the standard distribution SAD measurements. In both cases, there is no link to the spin and spin-orbit nuclear shell model. After this impressive confirmation of the results and the clarification of the jump of the Bagge sequences for the magic numbers, it is then a paradoxical phenomenon that the next higher magic numbers are different for the models. It was necessary to clarify in all details in Section 2 that the Boltzmann distribution model arrives at 180 with a clear difference from the number 184. See Table 1 and Fig. 3, as checked that the numbers next to 180 deviate from the optimum given at 180. On the other hand, the result of 184 by the QGP model is transparent and convincing.

An experimental result available for several years may lead to a clarification. The experiment is from the field of low energy nuclear reactions (LENR) of very high concentrations of hydrogen isotopes dissolved in palladium. Although most of the reported claims from all kinds of researchers are unacceptable for physicists, the measured generation of all kinds of nuclei up to the heaviest after a many-weeks-long reaction was convincing, using excellent instrumentation in the Frederick Seitz Laboratory at the University of Illinois. The abundance of the nuclei depending on the charge number Z was in full agreement with the cosmic abundance of Fig. 1, which fact alone underlines the value of these results as elaborated in detail (*9, 11, 20*). The details (*11*) after reports at conferences (*20*) [It should be mentioned that Dirac argued against the procedures of renormalization by neglecting an infinite term only because it was inconvenient. The justification for this procedure was that reasonable results were achieved. The convincing physics procedure for the neglect was given by

Downloaded by UNIV OF GUELPH LIBRARY on June 28, 2012 | http://pubs.acs.org
Publication Date (Web): December 20, 2009 | doi: 10.1021/bk-2009-1029.ch012

Peter H. Handel (Univ. Missouri, St. Louis, private communication) based on the theory of quantum noise (see Hora, H.; Handel, P. H. New Experiments and Theoretical Development of the Quantum Modulation of Electrons (Schwarz-Hora effect). *Advances in Electronics and Electron Physics;* Hawkes, P. W., Ed. Academic Press: NY, 1987; **69**, pp 55-113.] arrived at reasonable interpretations, last but not least (*21*) from the observation of a local maximum at the absolute minimum of the distribution of the generated nuclei, Fig. 7. The appearance of the maximum was fully similar (*11, 22*) to the nuclear fission of uranium and neighbour nuclei if the fissioning nuclei are in an excited state, as discovered by Maruhn and Greiner (*22*).]

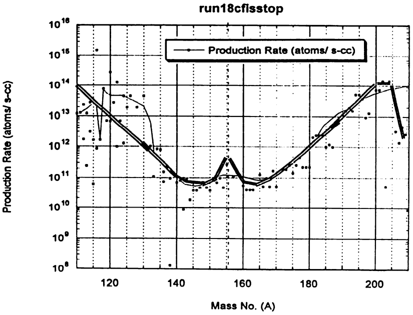

Figure 7. Production rate probability at low energy nuclear reactions (LENR) depending on the nucleon mass A (20,21,23).

Uranium fission resulted in elements at an absolute minimum at A = 119 with a widespread neighbourhood. This was in full analogy and for LENR with an absolute minimum A near 155, Fig. 7. It was remarkable that Maruhn-Greiner (*21*) local maxima appeared in both cases. This confirmed the earlier suggestion (*23*) that the generation of the heavy elements is through compound nuclei that finally are splitting into the nuclei near A = 155. It is assumed that these very heavy compound nuclei would preferably have magic numbers. A preference was assumed to be Z = 126, and the magic number 180 was considered for the neutrons. However, the element 306 with the half of 153 does not exactly fit the accurate experiments reported in Fig. 7. This figure shows precisely that the Maruhn-Greiner maximum clearly is at 155, not at 153. Therefore, the hypothetical compound nucleus would be with A = 310, and when keeping 126 for Z, the number of the neutrons would be 184. This agrees with the result of the QGP in Section 4 – apart from all these just-mentioned hypothetical assumptions – and is then probably an indication that the next higher magic number after 126 is 184, not 180.

A solution of this paradox may be rather interesting because it interlinks questions of the quark and nucleon state in nuclei, the endothermic element generation in the universe, the Debye layer model for nucleon confinement, the quark-gluon soups at higher-than-nuclear densities and several other details, such as the Greiner theory for the island of superheavy nuclei near Z = 126 (*24*).

As indicated in the very first paragraph, all the considerations presented here may be seen as being very hypothetical or speculative, but it may help to

Downloaded by UNIV OF GUELPH LIBRARY on June 28, 2012 | http://pubs.acs.org
Publication Date (Web): December 20, 2009 | doi: 10.1021/bk-2009-1029.ch012

acknowledge the facts of the rather diversified points known from the field of cold fusion and the generalized LENR.

Modified text published with permission of "Physics Essays" Vol. **21, 200-206 (2008). Helpful support by Dr. Emilio Panarella is most gratefully appreciated.*

Downloaded by UNIV OF GUELPH LIBRARY on June 28, 2012 | http://pubs.acs.org
Publication Date (Web): December 20, 2009 | doi: 10.1021/bk-2009-1029.ch012

References

1. Ghahramani, N.; Boroun, G. R. Extraction of the structure function F2(xQ2) at lower-x from the cross-section derivative. *Phys. Letters B.* **2002,** *B528*, 239; Fritzsch, H.; Gell-Mann M.; Leutwyler, H. Advantages of the color octet gluon picture. *Phys. Letters B.* **1973**, *47*, 365.
2. Elsässer, W. Maxima of nuclear binding energy in the abundance distribution. *J. Physique et le Radium* **1934**, *5*, 625.
3. Bagge, E. The shell structure of nuclei. *Naturwissenschaften* **1948**, *35*, 376.
4. Goeppert-Mayer, M. On closed shells in Nuclei II. *Phys. Rev.* **1949,** *75*, 1969.
5. Haxel, O.; Jensen, J. D. H.; Suess, H. E. Model interpretation of distinguished nucleon numbers at nuclear structure. *Zeitschr. f. Physik* **1950**, *128*, 295.
6. Audouze, J.; Vauclair, S. *Introduction to Nuclear Astrophysics: The Formation and the Evolution of Matter in the Universe;* D. Reidel Publishing Co.: Dordrecht, Holland, 1980.
7. Rauscher, T.; Applegate, J. H.; Cowan, J. J.; Thielemann, F. K.; Wiescher, M. Production of heavy elements in inhomogeneous cosmologies. *Astrophys. J.* **1994**, *429*, 499.
8. Kippenhahn, R.; Weigert, A. *Stellar Structure and Evolution.* Springer-Verlag: Heidelberg, Germany, 1990.
9. Hora, H. Magic Numbers and Low Energy Nuclear Transmutations by Protons in Host Metals. *Czechosl. J. Phys.* **1998**, *48*, 321; Hora, H.; Miley G. H.; Kelly, J. C. Low Energy Nuclear Reactions of Hydrogen in Host Metals. In *Current Trends in Inertial Fusion Research Proceedings of the third Symposium;* Panarella, E., Ed.; National Research Council of Canada Research Press: Ottawa, Canada, 2002; p 527.
10. Osman, F.; Ghahramani, N.; Hora, H. Debye sheath mechanism at laser plasma interation and generalization to nucler forces and quark-gluon plasma. *Laser & Part. Beams* **2005**, *23*, 461.
11. Hora, H.; Miley, G. H. Heavy Nuclide Synthesis by Neutrons in Astrophysics and by Screened Protons in Host Metals, *Czechosl. J. Phys.* **2000**, *50*, 433; Hora, H.; Miley, G. H.; Osman, F. Heavy Nuclide Synthesis by Neutrons in Astrophysics and by Screened Protons in Host Metals. *Astrophys. Space Sci.* **2005**, *298*, 247.

12. Sobiczewski, A. Review of recent SHE predictions. *Phys. Scripta* **1974**, *10A*, 47-52.
13. Hora, H. *Plasmas at High Temperature and Density.* Springer-Verlag: Heidelberg, Germany, 1991.
14. Hora, H.; Gu, M.; Eliezer, S.; Lalousis, P.; Pease, R. S.; Szichman, H. On Surface Tension in Plasmas. *IEEE Trans. Plasma Sci.* **1989**, PS-17, 284.
15. Hora, H.; Miley G. H., Eds. *Edward Teller Lectures,* Imperial College Press: London, England, 2004; p 112.
16. Hora, H. *Plasma Model for Surface Tension of Nuclei and the Phase Transition to the Quark Plasma.* Report CERN-PS/DL-Note-91/05; Hora, H. From laser-produced Debye layers in plasmas to a theory of nuclear forces and quark-glyon plasmas. *Laser & Part. Beams* **2006**, *24*, 35.
17. Hahn, B.; Ravendahl, D. G.; Hofstadter, R. High-energy electron scattering and the charge distributions of selected nuclei. *Phys. Rev.* **1956**, *101*, 1131.
18. Eliezer, S.; Ghatak, A. K.; Hora, H.; Teller, E. *Intoduction to Equations of State.* Cambridge Univ. Press: Cambridge, England, 1986.
19. Wilson, K. G. The renormalization group and critical phenomena. *Rev. Mod. Phys*. **1983**, *55*, 583.
20. Miley, G. H.; Patterson, J. A. Transmutation in Thin-Film Nickel Coatings Undergoing Electrolysis. *J. New Energy* **1996,** *1*, 11; Miley, G. H.; Narne, G.; Williams, M. J.; Patterson, J.; Cravens D.; Hora, H. Quantitative Observations of Transmutation Products Occuring in Thin-Film Coated Microspheres During Electrolysis. In *Proceedings of the Sixth International Conference on Cold Fusion: Progress in New Hydrogen Energy*, Hokkaido, Japan, Oct. 13-18, 1996; Okamoto, M., Ed.; New Energy and Industrial Technology Development Organization: Tokyo, 1996; pp 629-644.
21. Hora, H.; Miley, G. H. Maruhn-Greiner maximum from uranium fission for confirmation of low energy nuclear reactions LENR via a compound nucleus with double layer magic numbers. *J. Fusion Energy* **2007,** *26*, 349, 357.
22. Maruhn, J.; Greiner, W. Theory of Fission-Mass Distributions Demonstrated for ^{226}Ra, ^{236}U, ^{258}Fm. *Phys. Rev. Letters* **1974,** *32*, 548.
23. Miley, G. H. Possible Evidence of Anomalous Energy Effects in H/D-Loaded Solids-Low Energy Nuclear Reactions (LENRS). *Journal of New Energy* **1997**, *2(3-4)*, 6-13.
24. Greiner, W. Extension of the periodic system in the sectors of strangeness and antimatter. *Nuovo Cimento A* **1997,** *110A*, 1237.

Downloaded by UNIV OF GUELPH LIBRARY on June 28, 2012 | http://pubs.acs.org
Publication Date (Web): December 20, 2009 | doi: 10.1021/bk-2009-1029.ch012

Downloaded by PENNSYLVANIA STATE UNIV on June 28, 2012 | http://pubs.acs.org
Publication Date (Web): December 20, 2009 | doi: 10.1021/bk-2009-1029.ch013

Chapter 13

Radiochemical Comparisons on Low Energy Nuclear Reactions and Uranium

George H. Miley[1], Heinrich Hora[2], Karl Philberth[3], A. Lipson[1] and P.J. Shrestha[1]

[1]**Department of Nuclear, Plasma and Radiological Engineering, University of Illinois, Urbana, IL 61801, USA**
[2]**Department of Theoretical Physics, University of New South Wales, Sydney 2052, Australia**
[3]**Thanning, 82544 Egling, Germany**

The discovery of nuclear fission by Otto Hahn and Friedrich Strassmann was based on a very rare microanalytical result that provided the first realization that neutrons could fission uranium. However, this was only the beginning of many discoveries about this complex process. An analogy related to the discovery of low energy nuclear reactions (LENRs) is noted here. It is remarkable that the reaction product distribution measured in LENR experiments using thin-film palladium/nickel electrodes heavily loaded with either hydrogen or deuterium has a strong similarity to the element distribution from uranium fission. Thus, the LENR reaction process is hypothesized to pass through a heavy complex nucleus similar to the fission process in uranium. Further, a detailed structure is observed in the LENR distribution corresponding to the Maruhn-Greiner local maximum of the distribution within the large-scale minimum of the fission product distribution curve. This observation leads to the proposed explanation that the fissioning compound nucleus in the LENR case is element $^{306}X_{126}$ with double magic numbers. A major difference, however, is that in uranium fission the compound nucleus arises after single-neutron absorption, whereas in LENR a multi-body process is needed to create the heavy complex nucleus. Indeed, subsequent analysis of the various observations associated with these LENR experiments

In Low-Energy Nuclear Reactions and New Energy Technologies Sourcebook Volume 2; Marwan, J., et al.; ACS Symposium Series; American Chemical Society: Washington, DC, 2010.

suggests that the multi-body reaction involved follows from the formation of Bose-Einstein condensed clusters formed in dislocation void regions in the electrode. Consequences and proposed future studies based on this cluster conjecture are discussed.

Downloaded by PENNSYLVANIA STATE UNIV on June 28, 2012 | http://pubs.acs.org
Publication Date (Web): December 20, 2009 | doi: 10.1021/bk-2009-1029.ch013

Introduction

Large numbers of indications have been reported from laboratories worldwide supporting the claim of nuclear reactions occurring at low temperatures in solids loaded with a very high concentration of hydrogen isotopes (*1*). Most early observations attributed this to D-D cold fusion reactions. However, some years after the original cold fusion announcement, a startling but reproducible result indicated that another type of reaction can occur: transmutation reactions involving the loaded deuterium (or in some cases hydrogen) and the electrode metal atoms themselves (*2,3*). Here, we concentrate on a specific class of that type of reaction where a large array of transmutation products appears, suggesting that a fission-like process is involved *(2, 3)*. Such reactions involving transmutation have been termed low energy nuclear reactions (LENRs). Note, however, that this term includes direct reactions involving transmutations to single isolated products as well as the product array reactions discussed here.

The product array experiments exhibit a number of important characteristics that will be discussed here. For example, the array of products generally has a distribution of heavy nuclei vs. proton number Z which has maxima that correlate with a Boltzmann distribution (*4*). As discussed later in detail, analysis of this distribution allowed a derivation of the magic numbers of the nuclei involved (*5*) that shows a threefold multiplication of the shell structure, consistent with a quark property within the nuclei (*4,5*).

Another distinctive feature found in this product array is the observation of a local maximum in the large-scale minimum of the element distribution (*4,5*) near the nucleon number A = 153. This unique feature is similar to the distribution of the fission products of uranium around A = 119. In uranium, this important detailed structure is attributed to the Maruhn-Greiner process where the intermediate compound (or complex) nucleus in the fission process is excited to energies in the MeV range. Thus, it has been postulated that an excitation of the intermediate compound nucleus may occur in the LENR array experiment where a fission reaction via an excited nucleus with A = 306 appears to be involved *(4, 6*). However, in this case, as stressed later by Akita Takahashi *(7),* the excitation energy of the intermediate compound nucleus in LENR is much less than in uranium fission. The reason is that the multi-body formation of the compound nucleus builds up less internal energy than the neutron absorption reaction in uranium. This leads to a "soft" fission in LENR, explaining the very low level of emission of energetic radiations such as gamma rays (vs. low energy beta and x-rays) during the process.

We recall next that the uniqueness of the chemical analysis of extremely low quantities of barium (*8*) was the observation that led to the discovery of fission. The first view was that the uranium fission process simply generated nuclei of medium atomic weight. With time, it was eventually realized that the detailed process is much more complicated, often including radioisotopes that decay with beta emission. This is the basis for proposing that the LENR process is similarly a process in combination with beta decays or, as initially explained, a deuterium cluster reaction process (*4*) with a reaction branch yielding ^{3}He. We discuss these various reaction processes in more detail next.

The Hahn-Strassmann Discovery of Nuclear Fission

It is remarkable that the discovery of nuclear fission was based only on the chemical detection of small quantities of alkaline earth elements, especially barium. The uranium sample before neutron bombardment had a concentration of barium far below the minimum detection limit. However, a clearly detectable barium concentration was observed after the neutron bombardment. It is understandable that, only weeks before the Hahn-Strassmann publication (*8*), the radiation physicist Lise Meitner (*9*) could not believe the data showing traces of barium. She requested a repeat of all experiments before drawing a conclusion that nuclear fission must have occurred.

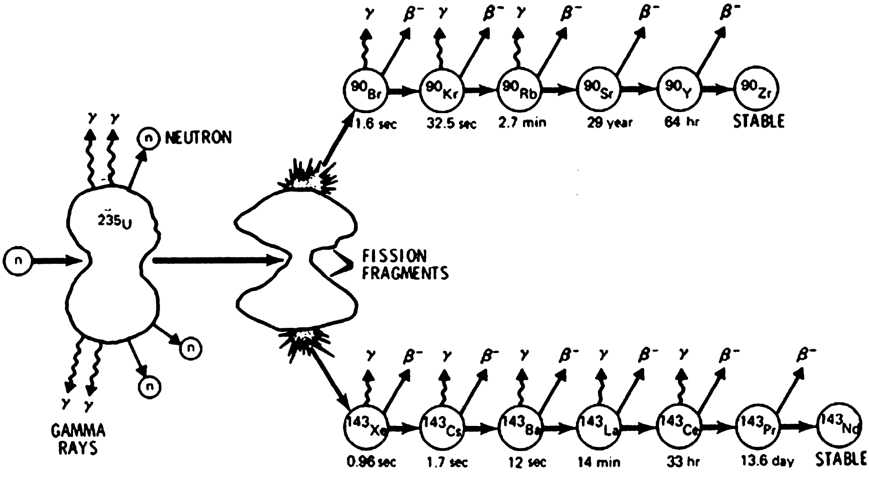

Figure 1. Reaction of a neutron with ^{235}U leading to a branch with 11 beta decays until stable nuclei are produced (8).

The very complicated details about what was happening in the uranium fission process were only explained later, leading to recognition that the neutron reaction with ^{235}U leads to neutron multiplication and the possibility of achieving a critical mass fission assembly. One of the numerous explanations offered for these reactions is shown in Fig. 1, where eleven additional beta decays (*10*) are required to arrive at the reaction:

Downloaded by PENNSYLVANIA STATE UNIV on June 28, 2012 | http://pubs.acs.org
Publication Date (Web): December 20, 2009 | doi: 10.1021/bk-2009-1029.ch013

$$^{235}U_{92} + n \;=\; ^{90}Zr_{45} + ^{143}Nd_{60} + 3n + 199\text{MeV} + 11\beta^- \qquad (1)$$

In this reaction branch, the only alkaline earth elements products are radioactive, ^{143}Ba (12s) and ^{90}Sr (29y), which can be sufficient for detection immediately after completion of the experiment. In other branches, longer lifetime barium appears, but it too undergoes radioactive beta decay. If Hahn and Strassmann (*8*) had waited to check their samples much later after the experiment, the barium would have dropped below detection limits, and they would not have discovered fission. At that time, this could not have been understood without knowing the very complicated reaction branches, such as those given in Fig. 1. Thus, all kinds of suspicions might have arisen about the initial experiments with the barium detection.

With so many possible problems with the measurements, it was not surprising that Emilio Segre stated later that the way fission was discovered is really a miracle. The only method of detection was based on the tedious measurement of barium, not any other elements. But still, this turned out to be sufficient to conclude that the uranium nuclei were split into two fragments, i.e. reaction products. This history appears relevant now in the sense that early workers doing LENR array transmutation studies were also faced with experiments fraught with possible errors and giving a maze of complicated reaction product data. Now, very distinctive features, some coming from analogy with uranium fission, have been recognized, and the mystery of this reaction mechanism is being unraveled.

Downloaded by PENNSYLVANIA STATE UNIV on June 28, 2012 | http://pubs.acs.org
Publication Date (Web): December 20, 2009 | doi: 10.1021/bk-2009-1029.ch013

Uranium Fission and the LENR Transmutation Array

The distribution of the nuclei after fission of uranium or plutonium shows a minimum at the half-nucleon mass A of the initial nuclei, i.e. at a nuclear mass of 119, see Fig. 2 (*11*). This distribution with the absolute minimum, however, refers to fissioning nuclei having very low excitation energy. If the fissioning nuclei are excited to a higher energy in the MeV range, a local maximum appears within the absolute minimum of the fission products. An analysis based on a liquid drop model of the nucleus reproduces this local maximum with the physics added by Joachim Maruhn and Walter Greiner (*12*). Their calculations are based on collective mass parameters from the BSC formulation, where the key parameter λ is the scale length in the Schrödinger equation for the splitting of heavy nuclei. This follows the models of nuclear molecules (*13*) but uses an adjustment fit according to the theory of fragmentation dynamics in nucleus-nucleus collisions (*12*).

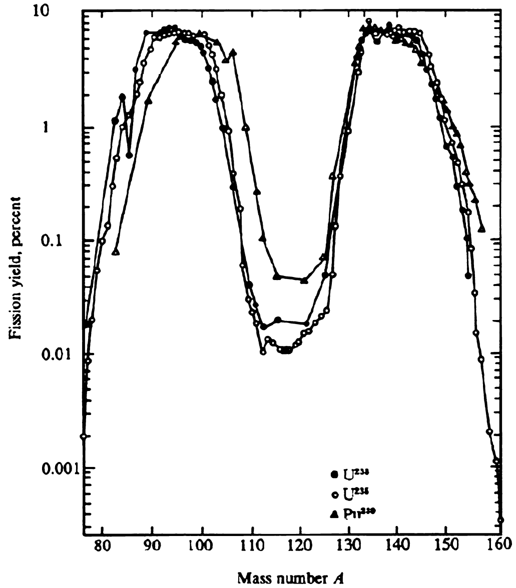

Figure 2. Fission mass distribution curves as measured for ^{233}U, ^{235}U and ^{239}Pu, from (11).

Fig. 3 shows the resulting fission mass distribution for ^{236}U for the elongation $\lambda = 1.8$ at different excitation temperatures of the splitting nucleus. As seen, the initial absolute minimum near A = 119 contains a distinctive local maximum if the nucleus is excited to 1 - 7 MeV before fission.

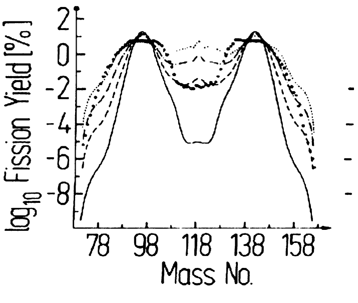

Figure 3. Fission mass distribution curves for ^{236}U calculated if the nucleus at the time of fission is excited to a temperature 0, 0.5, 1.0, and 7.0 MeV (upward sequence of plots) for the length parameter $\lambda = 1.8$ in the Schrödinger equation (12).

As discussed later, this feature has also been observed in the LENR distribution and thus provides an additional very important point of agreement between LENR and uranium fission.

Downloaded by PENNSYLVANIA STATE UNIV on June 28, 2012 | http://pubs.acs.org
Publication Date (Web): December 20, 2009 | doi: 10.1021/bk-2009-1029.ch013

Downloaded by PENNSYLVANIA STATE UNIV on June 28, 2012 | http://pubs.acs.org
Publication Date (Web): December 20, 2009 | doi: 10.1021/bk-2009-1029.ch013

The LENR product distribution shows other important features that suggest the basic nuclear physics involved. Figure 4 shows the generation of nuclei after several weeks' reaction period (*2*) in multi-layer, thin-film palladium highly loaded with hydrogen.

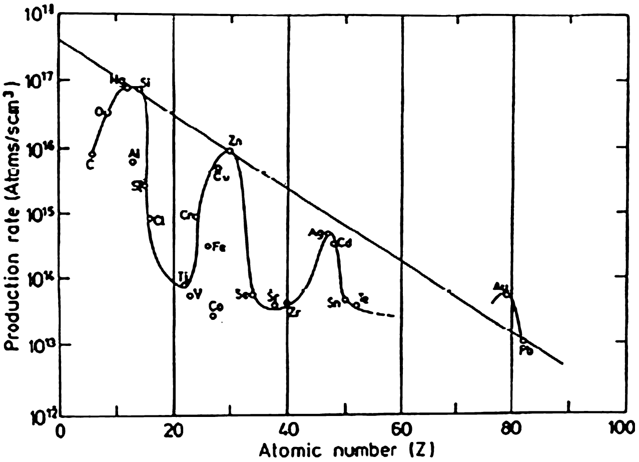

Figure 4. Measured production rates for reaction products from thin film LENR experiments vs. proton number (2,3). The solid line represents a Boltzmann distribution, Eq. (2).

The line drawn in the figure follows a Boltzmann distribution of the measured maxima (*14*). This gives the relation:

$$N(Z) = N' \exp(-Z/Z') \qquad (2)$$

where Z' is found to be 10. Other numbers for Z' (e.g. 9 or 11) do not fit. This is especially important in that it provides a unique evaluation of magic numbers. This same distribution, cf. Eq. 2, can be seen in the standard abundance distribution (SAD) of the elements in the Universe (*13*) for elements above iron, as seen from Fig. 10 of Ref. 15.

Returning to the Maruhn-Greiner effect, we now focus on detailed measurements of the minimum in Fig. 4 for Z between about 50 and 80 shown in Fig. 5 (*16*).

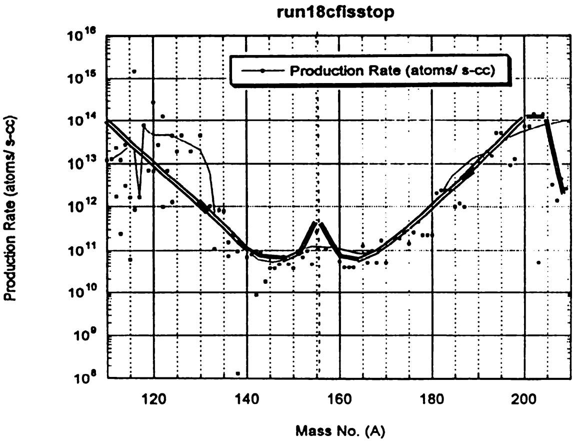

Figure 5. Detailed nuclear mass spectrum of the LENR reaction products generation probability at the highest-Z minimum of Fig. 4.

It is most significant that the minimum near A = 155 is amazingly similar to the uranium fission of Fig. 2. The distribution clearly shows an additional local maximum which appears to represent a Maruhn-Greiner local maximum (cf. Fig. 3). This strongly suggests that this LENR data results from a fission process from an excited short-lived compound nucleus corresponding to A = 306. Although this state is excited, the soft-fission aspect noted earlier suggests the excitation energy is much less than that of the uranium in Fig. 2.

Magic Numbers From LENR Data

From evaluation of Eq. 2 based on the LENR measurements and from the SAD measurements in the Universe, the following **bold** magic numbers can be identified (*14*):

$$M_{an} \in \mathbf{2, 8, 20}, 40, 70, 112, \tag{3}$$

$$M_{bn} \in 2, 6, 14, \mathbf{28, 50, 82, 126}, \tag{4}$$

Erich Bagge (*17, 18*) originally derived the sequences 3 and 4 from numerical speculations needed to achieve agreement with various nuclear measurements. But he could not explain the jump from one sequence to the other. We outline here the numerological procedure of Bagge (*17, 18*) as used before (*14*) to interpret magic numbers in terms of the maxima that occurs within the broad minimum of the distribution of the LENR products.

Downloaded by PENNSYLVANIA STATE UNIV on June 28, 2012 | http://pubs.acs.org
Publication Date (Web): December 20, 2009 | doi: 10.1021/bk-2009-1029.ch013

First, we consider the number sequences:
2 3 4 5 6 7 8…………being the difference to:
1 3 6 10 15 21 28…………again after the difference:
1 4 10 20 35 56 84…………times two arrives at the final series:

2 8 20 40 70 112. (3’)

Next, using the same procedure, we obtain the following sequence:
1 2 3 4 5 6 7…..
1 2 4 7 11 16 22….
1 3 7 14 25 41 63…..

2 6 14 28 50 82 126. (4’)

The resulting sequences (3’) and (4’) here correspond directly to the prior (3) and (4). Thus, this procedure, based on the observed LENR Boltzmann distribution, Eq. 2, can be used to directly explain the jump in the sequence that so concerned Bragge. Previously, to explain this jump, J. Hans Jensen and Maria Goeppert-Mayer had to involve the change from spin to spin-orbit properties within the nuclei (see ref. 18).

A further consequence of the LENR-SAD evaluation (*14*) leads to the ratios R (n) (n = 1, 2, 3…) of the Boltzmann probabilities, Eq. 2, namely

$$R\,(n) = 3^{n}. \qquad (5)$$

This suggests a threefold property of stable configurations at magic numbers in nuclei, consistent with a quark property. Based on sequence (4), the previously uncertain magic number 126 was included along with new magic numbers 180, 246 and 324. However, this result was viewed as quite uncertain. Thus, the intermediate, very short-lived compound nucleus ^{306}X identified in the LENR transmutation experiments becomes extremely significant for having the magic numbers of 126 protons and 180 neutrons, fitting well this proposed sequence. This is analogous to the double magic numbers 82 and 126 in the very stable nucleus ^{208}Pb.

This identification of the sequence of (4) and the conjecture of the magic number 126 illustrate how LENR research has unexpectedly led to important new basic nuclear physics data. As more LENR data is obtained, further insights into nuclear structure should emerge.

LENR Transmutation Experiment Issues

Not all workers in cold fusion accepted the observation of the "miracle" of the broad array of transmutation products when it was first presented in ICCF meetings and published in Refs. 2 and 3. They had anticipated a conventional cold fusion $D + D \rightarrow {}^{4}He$ reaction of the Pons-Fleishmann type. However, almost from the beginning, cold fusion critics had disputed the possibility of this

Downloaded by PENNSYLVANIA STATE UNIV on June 28, 2012 | http://pubs.acs.org
Publication Date (Web): December 20, 2009 | doi: 10.1021/bk-2009-1029.ch013

Downloaded by PENNSYLVANIA STATE UNIV on June 28, 2012 | http://pubs.acs.org
Publication Date (Web): December 20, 2009 | doi: 10.1021/bk-2009-1029.ch013

reaction because of the need for anomalous tunneling through the Coulomb barrier, plus its deviation from the traditional D-D reaction channels and the need for a massive collective mechanism to quickly transfer the energy of the excited reaction products to the lattice. Possible answers to these issues were just beginning to emerge when this new claim came forth implying that reactions involving the very high Z metal atoms in the lattice and D (or, in some cases, H) could occur under appropriate conditions. The immediate reaction by many in and out of the cold fusion field was simply to pass this claim off as experimental error. The easy accusation was that impurities in the cell were being confused with the reaction products. Impurities are, of course, an obvious potential pitfall in such experiments where, like the early barium detection studies of uranium fission, reaction product levels approach impurity limits. However, the experimentalists doing this work were well-aware of that issue and had taken extreme precautions to minimize impurity levels. The electrolytic cell and support system (pump, piping, etc.) was designed with high-purity plastics and glass to eliminate corrosion products from metal parts. Two exceptions were the metallic electrodes, which used high-purity metals, and the electrolytic salts. Still, despite such precautions, there will always be some level of various impurity elements in the apparatus components and electrolytic solution. Thus, great attention was devoted to precision measurements of key impurities in these materials in order to clearly define background limits. Ultimately, all components were analyzed using neutron activation analysis (NAA) for nine key elements (having the highest concentration and offering reasonably high neutron cross sections) identified in the reaction products. NAA provides a volumetric identification of elements as opposed to other probe analysis which interrogates local volumes. This provided a very accurate measure of background impurities of the elements that were of paramount interest as potential reaction products. And, as it turned out, many elements observed were well above the maximum background limits. This precision background purity measurement allowed a definitive identification of these transmutation products. To study other elements not amenable to NAA, a novel method, “combined NAA/SIMS,” was developed for a quantitative measure of the full reaction product array. This technique has been documented in detail in a publication in the *Journal of Radioanalytical and Nuclear Chemistry* – see Ref. 19. In this procedure, the nine key elements that were amenable to NAA were analyzed, using a NIST calibration to obtain absolute weights. NAA provides a positive identification of elements, avoiding the possible molecular species error that can plague SIMS (also avoiding the difficulty of obtaining overall mass yields with SIMS because of the localized characteristic of the probe beam involved). On the other hand, SIMS can identify many more elements than NAA because a usable neutron reaction cross section is not needed. Thus, the SIMS measurements were used to fill in missing elements. Consequently, that data (which included SIMS identification of the nine NAA elements) was normalized to the key NAA element measurements. This procedure then allowed assignments of approximate mass yields to the non-NAA elements observed with SIMS. The SIMS element data then had much more uncertainty associated with it than the NAA measured elements, but it still provided a reasonably accurate estimate of the full spectrum of reaction products. An independent check of these results was done at the Illinois State

Water Survey Laboratory with Inductively Coupled-Plasma Mass Spectrometry (IC-PMS) for one sample, and reasonable agreement was found.

Additional data that supports the identification of transmutation elements vs. natural-element impurities was the measurement of isotope ratios of key product elements. These ratios showed deviations from natural isotope ratios in key cases. The most accurate isotope ratio measurements used NAA on Cu and on Ag, where a definitive deviation from the natural element ratios was found. Other ratios relied on SIMS measurement.

Other supporting evidence includes subsequent measurements for electrodes using metals other than Pd, e.g. Ni and Ti (*20*). These showed a pattern similar to the Pd case but, as anticipated, some systematic differences occurred because of mass differences. In addition, product density profiles were measured using SIMS across the thickness of the thin-film electrodes. As anticipated for products created internally (vs. external impurities), peaks were found near the multi-layer interfaces. In several cases, electrodes removed from the cell after operation were placed on photographic film, and the long time exposure (several days) showed a distinct pattern over the electrode area, attributed to beta emission or possibly soft x-rays (2).

Another important issue that was investigated is whether the energy balance for the reaction giving these products is consistent with excess heat observed in these experiments (*21)*. The mass yield of the reaction product array was used to calculate the mass defect between the products and the reacting Pd and D (or H). This then was used to calculate energy release rates which compared favorably with the excess heat observed in these experiments (*22*). Although the uncertainty limits in these calculations were large, the rough agreement with excess-heat measurements provides added confidence in the experimental observations.

Finally, it was emphasized in the original paper disclosing this data that others (T. Mizuno, and John Bockris, sees Refs. 2, 3) had previously measured product arrays with somewhat similar product array patterns. However, their analysis had not provided absolute mass yield data like the new results, nor did they have much of the added supporting data noted above.

As time has gone on, many other amazing transmutation experiments have been done with LENRs, but most have focused on specific transmutations giving isolated products rather than a broad array. A review of all results up to a few years ago is presented in Ref. 23.

In view of this overwhelming data, many former skeptics (but not all) now accept transmutations in LENR. But, of course, the accuracy and details of given reactions can always be debated. The point is that this battle to gain respectability for transmutations has been in many ways analogous to the early days, when the fission of uranium was first reported. In retrospect, it can be realized how difficult it was for chemists like Otto Hahn et al. (*8*) to convince physicists such as Lise Meitner that fission could occur. In the case of uranium fission, however, the massive inflow of money and scientists during the Manhattan Project moved the uranium fission field ahead much more rapidly than has happened in the underfunded, undermanned field of transmutations in LENR. Also, the early bitter controversy after the original much-publicized announcement of cold fusion resulted in many unethical behaviors by scientists

Downloaded by PENNSYLVANIA STATE UNIV on June 28, 2012 | http://pubs.acs.org
Publication Date (Web): December 20, 2009 | doi: 10.1021/bk-2009-1029.ch013

Downloaded by PENNSYLVANIA STATE UNIV on June 28, 2012 | http://pubs.acs.org
Publication Date (Web): December 20, 2009 | doi: 10.1021/bk-2009-1029.ch013

(both proponents and critics) that hurt progress in the field in general, e.g. see Ref. 24 and related papers in that journal.

It is interesting to note that even hot-fusion research encountered a similar unexpected anomaly. It was initially thought that, to overcome the Coulomb repulsion, it was necessary for nuclear reactions to use energies much higher than MeV per nucleon. But it was discovered by James Cockroft and Ernest Walton (*25)* that 150 keV protons could disintegrate boron nuclei and, finally, that deuteron interaction energies of less than 10 keV led to the fusion reactions (*26)*. These nuclear reactions of nearly 1,000 times lower energies than expected were indeed an extreme anomaly, and perhaps because of this, not much attention was given to these results discovered in routine studies at the then Mecca of nuclear research, the Cavendish Laboratory. At the time, there was no physics theory to understand this anomaly, and this added to the temptation to ignore the data. Gradually, various fits with numerous parameters were employed to describe the measured cross sections, see e.g. (*27*). Later, tunneling theory was applied, and as late as 2000, a theory using Schrödinger potentials with imaginary parts led to improved basic understanding (*28*).

As an aside, it is interesting that there appears to be another tie between fission and LENR history. It has been pointed out by M. Shaheen, et al. (*29*) that data from samples take at the famous Oklo natural fission reactor in Africa indicate that some simultaneous LENR reactions may have occurred. If this hypothesis can be confirmed, the frequently asked questions about where cold fusion occurs in nature would be answered.

Bose-Einstein Deuteron Clusters

Thus far, we have stressed the amazing resemblance between measurements of the LENR product distribution on the proton number Z (or the nucleon number A) and the corresponding product distribution from the fission of uranium. An additional consistent pattern in the LENR data is that it follows the Boltzmann distribution with $Z_o = 10$ as noted earlier in Eq. 2, leading to the derivation of the magic numbers and the quark-like 3^{rd} law for the probability ratios for magic numbers.

We now turn to consider the obvious question of how the multi-body reactions needed to form the compound fissioning nucleus can occur in a low-temperature solid. Based on the early measurements of Prelas et al. (*30*), it was concluded earlier (*31*) that the deuterons absorbed in the palladium have a Coulomb screening factor of 14 compared with a factor of 5 for screening in high-temperature plasmas. Also, by comparing with the very anomalous long-distance reactions for hot fusion and with the short distances for muionic fusion, it can be concluded that the reactions in palladium occur at distances of 2 to 3 pm with a reaction time in the range of Ms (megaseconds). Similar distances and times are also known from the K-shell electron-capture radioactivity. Thus, the estimates appear not necessarily unreasonable.

As transmutation array data accumulated and associated features of the experiments (localized volumes with large concentrations, spotty exposure patterns seen on x-ray film exposures, etc.) were found, workers began to associate the reactions with localized regions where condensed matter states (termed "clusters") of D (or H) were postulated to have formed *(32-34)*. In his book, Ed Storms (*35*) calls such sites "nuclear-reactive," but at that time, he did not have sufficient data to identify their structure or how to purposely create them.

The cluster conjecture eventually led to a series of SQUID-type electromagnetic measurements at the University of Illinois that indicated such clusters formed a type II superconducting state *(36)*. The hypothesis then is that this superconducting cluster state represents the nuclear-reactive site such as envisioned by Storms (*35*). However, the volume associated with these clusters is only a small fraction of the total electrode volume, so recent work has focused on developing ways to nano-manufacture electrode structures that lead to a larger volume density of cluster regions in the electrodes *(33, 34)*. If the cluster volumetric density can be increased, a significant increase in the overall reaction rate in the electrode should be possible. Thus, this insight into the existence of cluster states provides a road map for developing a high-performance LENR cell *(34)*.

The mechanism for forming the cluster and its subsequent reaction is under study. The deuterons can be viewed as moving as electric neutral particles like a Maxwellian plasma within the palladium. If their interaction distance is less than 2 pm, this solid-state plasma is reactive. It is calculated (*4*) that the 2 pm distance between the electrically neutral deuterons arrives at gravitational attraction or Casimir attraction in the range of an energy density of 0.1 eV/cm^3. This attractive force is competitive against thermal motion. If clusters of about 150 neutral deuterons are produced, their diameter is in the range of 10 pm. Because the DeBroglie wave length of each deuteron at room temperature is in the >10 pm range, the cluster can assume a Bose-Einstein quantum state with non-distinguishable deuterons. (Recently, Yeong Kim (*37)* also proposed the formation of Bose-Einstein states in LENR electrons). This state is thought to correspond to the superconductivity regions measured by SQUID, as previously noted. During a time of less than 1 Ms, such a cluster can move within 2 pm distance to a palladium nucleus. Then, for example, the following illustrative reaction may occur:

$$^{108}\mathrm{Pd}_{46} + 156\,\mathrm{D} = {}^{306}\mathrm{X}_{126} + 38\,{}^{3}\mathrm{He}_{2} + \mathrm{E} \qquad (6)$$

expressing the mass per nucleon m_X by proton masses in X to arrive at

$$m_X = 1.004946 \text{ minus the relative part of E.} \qquad (7)$$

This mass is not necessary excessive, as seen by comparing the very low value m_{Fe}=0.9988376 with the value of m_U = 1.0001868 when splitting into ^{121}Sb with m_{Sb} = 0.99824. A comparable value can be seen from the splitting of the compound nucleus X of Eq. 6 into ^{153}Eu. This gives m_{Eu} 0.9988375. Based on the energy per nucleon in $^{306}X_{126}$ of 5.73 MeV minus the contribution going into the reaction energy E. Based on these analogies, the energies involved in the LENR process appear to be reasonable in magnitude for such a compound nuclear reaction process (*6*). If the lifetime of the double magic number

Downloaded by PENNSYLVANIA STATE UNIV on June 28, 2012 | http://pubs.acs.org
Publication Date (Web): December 20, 2009 | doi: 10.1021/bk-2009-1029.ch013

intermediary compound nucleus $^{306}X_{126}$ is in the range of seconds, it should be detectable from very energetic K-shell x-ray emission. Indeed, that could explain the x-ray film exposure observed following long-run, thin-film electrode experiments noted earlier. There are also other possibilities, including reactions that are similar to Eq. 6 but which involve multi Pd nuclei. Indeed, some of the earlier experiments that used light water (i.e. H clusters) were postulated to involve a variety of multi-body reactions between H and Pd (*2, 3, 38, 39*).

Another observation from the experiments (*2*) should be noted in view of the speculations about a compact nucleus X generation. The postulate of fissioning through an excited state that produces the local maximum at the broad minimum of Fig. 5 via Eq. 6 suggests that ^{3}He should be detected in these experiments. Prior studies did not attempt its detection. Thus, future work might focus on that issue. Another future direction is to further investigate whether the fission into the elements around A = 153 proceeds by a similar process.

Because the clusters have an enormous specific weight from their very high density, other measurements to directly confirm them might be pursued. One possibility is to check whether the reaction is favored by surface plasmas, because the clusters would be drawn down by gravitation.

Some added comments should be included here about the previously derived (*5, 14*) magic number 180 from the 3^n-law, Eq. 5. The theory of confining the nucleons in a nucleus by a Debye layer mechanism and the identification of a quark structure for preferred shells because of the 3^n-law was evaluated in detail for the first time by Nader Ghahramany et al. (*40, 41*). Using this data, they observed the details of the predicted quark-gluon statistics with a very convincing result. However, they arrived at a magic number 184 instead of 180. However, Fig. 5 indicates that the local maximum for the LENR-generated elements is not at 153 (which would indicate a compound nucleus $^{306}X_{126}$); instead, the peak appears to be clearly at 155. This indicates very convincingly that the compound nucleus $^{310}Y_{126}$ (not X) is involved, indicating the magic number for the neutrons of 184 in the Y-nucleus. Thus, because of the very accurate measurement of Fig. 5, there is strong proof of the Debye layer model for nuclei (*31, 36,40*). This LENR data mutually confirms the compound nuclear assumption of Eq. 6, as well as the result of very weak forces between quarks. It is also consistent with the 2 pm deuterium cluster hypothesis.

Finally, we note that the Coulomb screening effect (*19, 20, 22-24, 31,42*) for the deuterons in solid-state plasma in highly loaded metals has been gaining more attention as its importance is recognized. Indeed, recent measurements have confirmed anomalous screening in a variety of substrate metals. An illustration is the estimated effective screening potential of 470 eV (*15, 31*) of D in a highly loaded hydride which roughly agrees with recent direct measurements of > 320 eV (*42*).

Downloaded by PENNSYLVANIA STATE UNIV on June 28, 2012 | http://pubs.acs.org
Publication Date (Web): December 20, 2009 | doi: 10.1021/bk-2009-1029.ch013

Conclusion

The distribution minima for LENR and for uranium fission at A = 153 and 119, respectively, plus the local Maruhn-Greiner maxima in both have been shown to exhibit strong similarities. Based on this strong similarity, we have suggested that the reaction product array from LENR occurs by fission of a heavy compound nucleus. The question remains, however, whether the LENR process proceeds by reactions similar to that of Eq. 1 for uranium with inclusion of sequent beta decays or whether LENR proceeds without the beta processes as given by Eq. 6. The reason may be that the LENR processes are many orders of magnitudes slower than uranium type fission processes so that there is sufficient time to generate lower energy stable isotopes.

It was noted that photographic film exposures tend to support the beta decay route, but much more work is needed to be definitive. In any case, it is remarkable that the LENR soft-fusion process results in nearly stable nuclei with only a low level of energetic emission of nuclear particles or of low-energy radiation.

Still, it has to be taken into account that some measurements, e.g. Mark Prelas et al. (*30*), show a very low intensity of gamma lines of very high energies. This may indicate that the LENR generation of an array of heavy nuclei from the very high density screened deuterons in palladium is much more complicated than expressed by Eq. 6. The point is emphasized by the identification by various researchers of other selective LENR reactions that lead to individual transmutation products (unlike the array discussed here). These results clearly show that a variety of nuclear reactions can occur that do not involve fission. Along those lines, it should be stressed that nonfission (individual) product patterns were noted to occur in the prior thin-film experiments along with the fission-like pattern (see discussion in the early studies cited here (*2, 3*)).

The ability to fully control the type of transmutation reaction (fission-type array vs. single-product production) has not been achieved, although this is possible to some extent through the selection of the electrode construction and electrolyte solution (or gas) using results reported in the literature as a guide.

A most important concept proposed here is the possible role of a Bose-Einstein condensed matter cluster that has strong implications for control of reactions. As described, this provides a road map for improving the overall reaction rates in LENR cells. If achieved, that would significantly enhance our ability to study LENR reactions and at the same time potentially lead to practical units for either energy production or transmutation applications.

Downloaded by PENNSYLVANIA STATE UNIV on June 28, 2012 | http://pubs.acs.org
Publication Date (Web): December 20, 2009 | doi: 10.1021/bk-2009-1029.ch013

References

1. Paneth, F.; Peters, K. The transmutation of hydrogen into helium. *Berichte der Deutschen Chemischen Gesellschaft* **1926**, *59*, 2039; The transmutation of hydrogen into helium. *Nature* **1926**, *118*, 526; Paneth, F., The

transmutation of hydrogen into helium. *Nature* **1927**, *119*, 728; Fleischmann, M.; Pons, S. Electrochemically induced nuclear fusion of deuterium. *J. Electroanalyt. Chem.* **1989**, *261*, 301.

2. Miley, G. H.; Patterson, J. A. Transmutations in Thin-Film Nickel Coatings Undergoing Electrolysis. *J. New Energy* **1996,** *1*, 11; Miley, G. H.; Narne, G.; Williams, M. J.; Patterson, J.; Cravens D.; Hora, H. Quantitative Observations of Transmutation Products Occuring in Thin-Film Coated Microspheres During Electrolysis. In *Proceedings of the Sixth International Conference on Cold Fusion: Progress in New Hydrogen Energy*, Hokkaido, Japan, Oct. 13-18, 1996; Okamoto, M., Ed.; New Energy and Industrial Technology Development Organization: Tokyo, 1996; 629-644.
3. Miley, G. H.; Patterson, J.A. Nuclear Transmutations in Thin-Film Nickel Coatings Undergoing Electrolysis. In *Proceedings of the Second Conference on Low Energy Nuclear Reactions*, *Journal of New Energy, 1(3)*, College Station, Texas, Sept. 13-14, 1996.
4. Hora, H.; Miley, G. H. Maruhn-Greiner maximum from uranium fission for confirmation of low energy nuclear reactions LENR via a compound nucleus with double layer magic numbers. *J. Fusion Energy* **2007**, *26*, 349, 357.
5. Hora, H.; Miley, G. H. New magic numbers from low energy nuclear transmutations predict element 306X126 for compound reactions. *Czechoslovak J. Phys*. **1998**, *48*, 1111.
6. Miley, G. H. Low-energy nuclear reactions. *Transact. Am. Nucl. Soc*. **1997**, *76*, 155; Hora, H.; Patterson, J. A.The d and p reactions in low-energy nuclear fusion, transmutation, and fission. *Transact. A. Nuc. Soc.* **1997,** *76*, 145-146.
7. Takahashi, A.; Ohta, M.; Mizuno, T. Production of Stable Isotopes by Selective Channel Photofission of Pd. *J. Applied Physics* **2001**, *40*, 7031-7046.
8. Hahn, O.; Strassmann, F.; Generation of active barium isotopes from uranium and thorium by neutron irradiation. *Naturwissenschaften* **1939**, *27*, 11.
9. Crawford, E.; Lewin-Sime, R.; Walker, M. A Nobel Tale of Postwar Injustice. *Physics Today* **1997**, *50(9)*, 26.
10. Kneif, R. A. Nuclear reactor theory. *Encyclopedia of Physical Science and Technology;* Academic Press: San Diego, CA, 1987: Vol. 9, p 393.
11. Feltus, M. A. Nuclear fission. *Encyclopedia of Physical Science and Technology;* Academic Press: San Diego, CA, 2002; Vol. 5, p 900.
12. Maruhn, J.; Greiner, W. Theory of Fission-Mass Distributions Demonstrated for ^{226}Ra, ^{236}U, ^{258}Fm Theory of Fission-Mass Distributions Demonstrated for ^{226}Ra, ^{236}U, ^{258}Fm *Phys. Rev. Letters* **1974**, *32*, 548; Maruhn, L. A.; Greiner, W.; Scheid, W. *Theory of fragmentation in fission, fusion and heavy ion scattering*, in *heavy ion collision;* North Holland Publishing Co.: Amsterdam, Holland, 1980; pp 387-465.
13. Greiner, W.; *Nuclear Molecules*; Park, J. W.; Scheid, W., Eds.; World Scientific: Singapore, 1995.
14. Hora, H. Magic Numbers and Low Energy Nuclear Transmutations by Protons in Host Metals. *Czechoslovak J. Phys*. **1998**, *48*, 32.

Downloaded by PENNSYLVANIA STATE UNIV on June 28, 2012 | http://pubs.acs.org
Publication Date (Web): December 20, 2009 | doi: 10.1021/bk-2009-1029.ch013

15. Rauscher, T.; Applegate, J. H.; Cowan, J. J.; Thielemann, F.-K.; Wiescher, M. Production of heavy elements in inhomogeneous cosmologies. *Astrophys. J.* **1994**, *429*, 499.
16. Hora, H.; Miley, G. H.; Kelly, J. C. *Current Trends in International Fusion Research – Proceedings of the Third Symposium*: NRC Research Press, National Research Council of Canada: Ottawa, Canada, 2002; p. 527; Hora, H.; Miley, G. H.; Osman, F. *Astrophysics and Space Sciences*, **2005**, *298*, 247; Hora, H.; Miley, G. H. *Czechosl. J. Phys.* **2000**, *50*, 433.
17. Bagge, E. Der Schalenbau der Atomkerne (the shell structure of the nuclei). *Naturwissenschaften* **1948**, *35*, 376.
18. Haxel, O.; Jensen, J.; Suess, H. E. Modellmäßige Deutung der ausgezeichneten Nukleonenzahlen im Kernbau (model interpretation of distinguished nuclon numbers in structure of nuclei). *Zeitschr. f. Physik* **1950**, *128*, 295.
19. Miley, G. H.; Narne, G.; Woo, T. Use of Combined NAA and SIMS Analyses for Impurity Level Isotopte Decection. *J. Radioanalytical and Nuclear Chemistry*, **2005**, *263*, 691-696.
20. Miley, G. H. Evidence for anomalous energy effects — low energy nucler reactions (LENRs). In *Proceedings of Asti Workshop on Anomalies in Hydrogen/Deuterium Loaded Metals*, Asti, Italy, November 27-30, 1997; Societa Italiana di Fisica: Bologna, Italy, 1999.
21. Castano, C. H.; Lipson, A. G.; Kim, S. O.; Miley, G. H. Calorimetric Measurements during Pd-Ni thin film–cathodes Electrolysis in Li_2SO_4/H_2O Solution. In *Condensed Matter Nuclear Science: Proceedings of the Ninth International Conference on Cold Fusion*, Beijing, China, May 19-24 2002; Li, X. Z., Ed.; Tsinghua Univ. Press: Beijing, 2002; p .
22. Miley, G. H. On the Reaction Product and Heat Correlation for LENRs. In *Proceedings of the Eighth International Conference on Cold Fusion,* Lerici (La Spezia), Italy, May 21-26, 2000; Scaramuzzi, F., Ed.; Italian Physical Society: Bologna, Italy, 2000; p 419-424.
23. Miley, G. H.; Shrestha, P. J. Review of Transmutation Reactions in Highly Loaded Lattice. In *Condensed Matter Nuclear Science: Proceedings of the Tenth International Conference on Cold Fusion*, Cambridge, MA, Aug 24-29, 2003; Hagelstein, P. A.; Chubb, S. R., Eds.: World Scientific Publishing Co.: Singapore, 2006; p 86.
24. Miley, G. H. Some personal reflections on scientific ethics and cold fusion. *J. Accountability in Research: Policies and Quality Assurance* **2000**, *8*, 1.
25. Cockroft, J. D.; Walton, E. T. S. Experiments with high velocity positive ions. II. Disintegration of elements by high velocity protons. *Proc. Roy. Soc. London A,* **1932,** *137***,** 229.
26. Oliphant, M. L. E.; Harteck, P.; Rutherford, L. Transmutation effects observed with heavy hydrogen. *Proc. Roy, Soc. London A,* **1934**, *144*, 692.
27. Clark, R. L.; Hora, H.; Ray, P. S.; Titterton, E. W. Transmutation effects observed with heavy hydrogen. *Phys. Rev. C* **1978**, *18*, 1127.
28. Li, X. Z.; Tian, J.; Mei, M. I.; Li, C. X. Sub-barrier fusion and selective resonant tunneling *Phys. Rev. C* **2000**, *61*, 024610; Li, X. Z.; Liu, B.; Chen, S.; Wei, Q. M.; Hora, H. Fusion Cross Sections in Inertial Fusion Energy. *Laser and Paticle Beams* **2004**, *22*, 469.

Downloaded by PENNSYLVANIA STATE UNIV on June 28, 2012 | http://pubs.acs.org
Publication Date (Web): December 20, 2009 | doi: 10.1021/bk-2009-1029.ch013

29. Shaheen, M., Ragheb, M., Miley, G. H., Hora, H., Kelly, J. Anomalous Deuteron to Hydrogen Ratio in Oklo Samples and the Possibility of Deuteron Disintegration, In *Proceedings of the Second Annual Conference on Cold Fusion,* Como, Italy, 1991; Bressani, T.; Del Giudice, E.; Preparata, G., Eds.; Societa Italiana di Fisica: Bologna, Italy, 1991; p 221.
30. Prelas, M. A.; Boody, F.; Gallaher, W.; Leal-Quiros, E.; Mencin, D.; Taylor, S. Cold fusion using Maxwellian plasmas and sub-atmospheric deuterium gas loading. *J. Fusion Energy* **1990***, 9*, 309.
31. Hora, H.; Kelly, K. C.; Patel, J. U.; Prelas, M. A.; Miley, G. H.; Tompkins, J. W. Screening in cold fusion derived from D-D reactions. *Phys. Letters A*, **1993**, *175*, 138.
32. Miley, G. H.; Lipson, A.; Hora, H.; Shrestha, P. J. Cluster Reactions in LENRs. Presented at *Eighth International Workshop on Anomalies in H/D Loaded Metals*, Catania, Sicily, October 12-18, 2007
33. Miley, G. H.; Shrestha, P. J. *Transmutation Reaction and Associated Low-Energy Nuclear Reactions Effects in Solids;* Low Energy Nuclear Reactions Sourcebook, American Chemical Society, Oxford University Press, 2008.
34. Miley, G. H.; Hora, H. Energetics of Condensed Matter Cluster Reactions in Nano-Structured Palladium. In *Proceedings of 237th American Chemical Society National Meeting*, Salt Lake City, UT, March 22-26, 2009.
35. Storms, E. *The Science of Low Energy Nuclear Reactions.* World Scientific Publishing: Singapore, 2007.
36. Lipson, A.; Castano, C.; Miley, G. H.; Mitin, A.; Lyakhov, B. Emergence of a High Temperature Superconductivity in Hydrogen Cycled Pd Compounds as an Evidence of a Superstoihiometric H/D Sites. In *Condensed Matter Nuclear Science: Proceedings of the Eleventh International Conference on Cold Fusion,* Marseilles, France, Oct. 31-Nov. 5, 2004; Biberian, J., Ed.; World Scientific Publishing Co.: 2006; pp 128-146.
37. Kim, Y. E. Theory of Low-Energy Deuterium Fusion in Micro/Nano-Scale Metal Grains and Particles. *Presented at the Fourteenth International Conference on Cold Fusion,* August 17-21, 2008, Washington D.C.
38. Miley, G. H. Evidence for anomalous energy effects — low energy nucler reactions (LENRs). In *Proceedings of Asti Workshop on Anomalies in Hydrogen/Deuterium Loaded Metals*, Asti, Italy, November 27-30, 1997; Societa Italiana di Fisica: Bologna, Italy, 1999.
39. Miley, G. H.; Selvaggi, G.; Tate, A.; Okuniewski, O.; Williams, M.; Chicea, D.; Hora, H.; Kelly, J. Advances in Thin-Film Electrode Experiments. In *Proceedings of Eighth International Workshop on Anomalies in H/D Loaded Metals*, Catania, Sicily, October 12-18, 2007.
40. Hora, H. Plasma Model for Surface Tension of Nuclei and the Phase Transition to the Quark Plasma. *F report* CERN-PS/DL-Note-91/05; *Edward Teller Lectures*, Hora, H.; Miley, G. H., Eds.; Imperial College Press, London, 2005, p 96; Osman, F.; Ghahramany, N.; Hora, H. Screening in cold fusion derived from D-D reactions. *Laser and Particle Beams*, **2005**, *23*, 461; Hora, H. From laser produced Debye layers in plasma to a theory of nuclear forces and quark-gluon plasmas, *Laser and Particle Beams* **2006**, *24*, 35.

Downloaded by PENNSYLVANIA STATE UNIV on June 28, 2012 | http://pubs.acs.org
Publication Date (Web): December 20, 2009 | doi: 10.1021/bk-2009-1029.ch013

41. Ghahramani, N.; Hora, H.; Miley, G. H.; Philberth, K.; Osman, F. Nuclear magic numbers based on a quark-like model is compared with the Boltzmann distribution model from nuclear abundance in the universe and low energy nuclear reactions. *Physics Essays* **2008,** *21*, 201. Hora, H; Ghahramani, N.; Miley, G.H.; Ghanaatian, M.; Hooshmand, M.; Philberth, K.; Osman, F.; Quark-gluon model for magic numbers related to low energy nuclear reactions. *Low Energy Nuclear Reactions and New Energy Technologies Sourcebook Vol.2*, S. Krivit & J. Marwan eds. American Chemical Society, Oxford University Press, Washington, D.C., ISBN 978-0-8412-2454-4
42. Huke, K.; Cerski, P. et al. Enhancement of deuteron-fusion reactions in metals and experimental implications. *Phys. Rev. C* **2008**, *78*, 015803; Czerski, K.; Huke, A.; Biller, A. Screening of deuterons in metals for fusion *Europhysics Letters*, **2001**, 54, 449.

Downloaded by PENNSYLVANIA STATE UNIV on June 28, 2012 | http://pubs.acs.org
Publication Date (Web): December 20, 2009 | doi: 10.1021/bk-2009-1029.ch013

Downloaded by STANFORD UNIV GREEN LIBR on June 28, 2012 | http://pubs.acs.org
Publication Date (Web): December 20, 2009 | doi: 10.1021/bk-2009-1029.ch014

Chapter 14

A Primer for Electro-Weak Induced Low Energy Nuclear Reactions

Y.N. Srivastava [1], A. Widom [2], L. Larsen [3]

[1] Dipartimento di Fisica & INFN, Universita'degli Studi di Perugia, 06123 Perugia, Italy
[2] Physics Department, Northeastern University, Boston MA 02115, U.S.A
[3] Lattice Energy LLC, 175 North Harbor Drive, Chicago IL 60601, U.S.A.

In a series of papers, cited in the main body of the paper below, detailed calculations have been presented which show that electromagnetic and weak interactions can induce low energy nuclear reactions to occur with observable rates for a variety of processes. A common element in all these applications is that the electromagnetic energy stored in many relatively slow-moving electrons can, under appropriate circumstances, be collectively transferred into fewer, much faster electrons with energies sufficient for the latter to combine with protons (or deuterons, if present) to produce neutrons through weak interactions. The produced neutrons can then initiate low energy nuclear reactions through further nuclear transmutations. The aim of this paper is to extend and enlarge on various examples analyzed previously, present simplified order-of-magnitude estimates for each and illuminate a common unifying theme among them.

PACS numbers: 12.15.Ji, 23.20.Nx, 23.40.Bw, 24.10.Jv, 25.30.-c

Introduction

In a set of papers *(1, 2, 3, 4, 5, 6)*, diverse physical processes have been considered and detailed computations on them performed to reveal conditions under which, in each case, the result is a low energy nuclear reaction (LENR) induced by electro-weak interactions. Even though weak interactions are an

In Low-Energy Nuclear Reactions and New Energy Technologies Sourcebook Volume 2; Marwan, J., et al.;
ACS Symposium Series; American Chemical Society: Washington, DC, 2010.

integral part of the standard model of fundamental interactions, which unifies the electromagnetic force with the weak and the strong (nuclear) force, nonetheless low energy applications of weak interactions in condensed matter devices are novel and hence unfamiliar. Practically all existing condensed matter devices are essentially of electromagnetic origin. There are sound reasons for the latter circumstance. Charged particles in condensed matter (electrons or ions) normally possess low kinetic energies (typically a few *eV* or less), yet they can trigger substantial electromagnetic processes which one can usefully harness. In sharp contrast, for an electron to undergo a weak interaction, say, with a proton in an ion and produce a neutron requires *MeV* range of energies (because the neutron is heavier than the proton by about 1.3 *MeV* and hence there is an energy threshold which must be overcome). It follows then that, for neutron production (and subsequent nuclear transmutations) through weak interactions, special conditions in condensed matter systems must be found that accelerate an electron to *MeV* range of energies. Successful avenues to accomplish precisely this purpose have been described in the six papers cited above. The present paper is devoted to delineating the unifying features and to an overall synthesis of these rather different collective processes.

In *(1)*, metallic hydride surfaces on which plasma oscillations exist were analyzed. It was shown that the collective surface plasmon polariton oscillations on the surface can contribute some of their electric energy to an electron so that the following reaction becomes kinematically allowed

$$W_{electric} + e^- + p \rightarrow n + \nu_e. \tag{1}$$

The relevant scale of the electric field $\mathcal{E}$ and the plasma frequency needed to accelerate electrons to trigger neutron production is found to be

$$\frac{c\mathcal{E}}{\Omega} = \left(\frac{mc^2}{e}\right) \approx 0.5 \times 10^6 \; Volts, \tag{2}$$

where c is the speed of light, m is the mass and ($-e$) the charge of the electron.

The particular condensed matter environment leads in this case to ultra-cold (that is, ultra-low-momentum) neutrons. These neutrons born ultra-cold have extraordinarily large nuclear absorption cross sections and thus a high probability of producing nuclear transmutations and an extremely low probability of neutrons escaping beyond micron-scale and smaller surface regions in which they are formed. There is also a high suppression in the production of high-energy gamma rays *(2)*. For such metallic chemical cells, comprehensive calculations of the rates of LENRs *(4)* were made that confirmed a robust production of large fluxes of ultra-low-momentum neutrons.

In *(5)*, a magnetic analog of the above (the so-called exploding wire problem) was analyzed. We found that a strong electric current carrying wire (A wire is our generic name for any object that carries a current I a distance Λ that is large on the scale of the thickness d of a flowing charged particle beam.) can, under suitable conditions, channel the collective magnetic energy sufficiently once again to excite a certain fraction of electrons to undergo the weak interaction process

Downloaded by STANFORD UNIV GREEN LIBR on June 28, 2012 | http://pubs.acs.org
Publication Date (Web): December 20, 2009 | doi: 10.1021/bk-2009-1029.ch014

$$W_{magnetic} + e^- + p \rightarrow n + \nu_e. \tag{3}$$

The scale of current required here was shown to be of the order of the Alfvén current I_o

$$I_o = \left(\frac{mc^2}{e}\right)\left(\frac{4\pi}{R_{vac}}\right) \approx 17\ KiloAmperes \tag{4}$$

Observation of copious neutrons in exploding wire experiments is by now legion *(7, 8, 9, 10, 11, 12)*. Experimentally, neutron production also has been confirmed for lightning *(13)*, the big exploding wire in the sky, when typical currents are about 30 *KiloAmperes* and higher.

Quite recently *(6)*, another application of the magnetic mode inducing LENR has been made to unravel the mystery surrounding observed particle production and nuclear transmutations in the solar corona and in solar flares *(14, 15, 16, 17, 18, 19, 20, 21, 22)*. Spectacular pictures of flux tubes are now available *(23)* showing giant magnetic flux tubes exiting one sunspot and entering another. We show theoretically *(6)* how these can lead to steady LENR. In fierce solar flares, we find that, as a flux tube disintegrates, it generates electric fields strong enough to accelerate electrons and protons toward each other with a center of mass energy of 300 *GeV*, equivalent to the highest-energy electron-proton colliding beam (HERA) built on Earth. For a strong solar flare that occurred July 14, 2000, we computed the flux of muons that reach Earth. Our theoretical flux agrees quite nicely with the experimental data by the L3+C Collaboration at LEP through their observation of high-energy muons produced in coincidence with this huge flare *(22)*.

In this paper, we will try to provide a unified picture of electro-weak (EW) induced LENRs, bringing out the essential physics and omitting many technical details, all of which can be found in our earlier papers. Order-of-magnitude estimates of relevant parameters for different physical processes using the electric and/or the magnetic modes will be presented to stress the feasibility of LENRs. The paper is organized as follows. In Sec. 2, general considerations revealing the basic idea behind EW induction of LENR are given. In Sec. 3, the case of metallic hydride cells where electric charge fluctuations play a major role is discussed, along with estimates of expected rates of nuclear transmutations. Estimates of the mean free path for the ultra-low-momentum neutrons and MeV range gamma rays are shown to be so short as to confine them to the material, i.e. they get absorbed on the surface. In Sec. 4, we consider strong electric currents flowing through thin wires to show how the collective magnetic mode energy generates a huge chemical potential in the MeV range sufficient to induce LENRs. In Sec. 5, applying the mechanism presented in Sec. 4, we show how a giant transformer - or a betatron - is generated for the solar corona leading to LENRs and, for solar flares, the production of extremely high-energy particles exposing the rich structure of the standard model. Sec. 6 closes the paper with a summary of our results, along with concluding remarks and outlook.

Downloaded by STANFORD UNIV GREEN LIBR on June 28, 2012 | http://pubs.acs.org
Publication Date (Web): December 20, 2009 | doi: 10.1021/bk-2009-1029.ch014

Genesis of Electro-Weak Induced LENR

A free neutron can and does decay through weak interaction into a proton, an electron and an $\bar{\upsilon}_e$

$$n \rightarrow p + e^- + \bar{\nu}_e, \qquad (5)$$

because the Q-value for this reaction, Q = $(M_n - M_p - \mathrm{m})c^2 \approx 0.78$ *MeV* is positive. On the other hand, the production of a neutron through the inverse reaction $e^- + p \rightarrow n + \upsilon_e$ for electrons and protons of very low kinetic energy (generally to be found in condensed matter systems) is kinematically forbidden unless the energy of the incident (ep) system can be augmented by this Q value.
Hence, to induce LENR through weak interaction such as

$$W + e^- + p \rightarrow n + \nu_e, \qquad (6)$$

to be kinematically allowed, we require an energy W ≥ 0.78 *MeV* to be fed in to the (e–p) system originally with negligible kinetic energy. Thus, our first task is to find a mechanism within a condensed matter system that can supply *MeV* scale energies to accelerate an electron to overcome the threshold barrier. Because electrons are accelerated by an electric field through the equation $\dot{p} = (-e)$ **E**, let us assume that on a metal surface a sinusoidal electric field exists:
$\mathbf{E} = \mathbf{E_0}\cos(\Omega\tau)$ of frequency Ω . The average change in the momentum ($\triangle p$) is then easily obtained through $(\triangle p)^2 = (e^2\bar{E}^2/\Omega^2)$. The average (squared) total energy $\bar{K}^2$ for an electron of rest mass *m* with an original small momentum **p** is given by

$$\bar{K}^2 = (mc^2)^2 + (c\mathbf{p})^2 + \frac{e^2c^2\bar{E}^2}{\Omega^2} = (c\mathbf{p})^2 + (mc^2)^2\left[1 + \frac{\bar{E}^2}{\mathcal{E}^2}\right], \qquad (7)$$

where the relevant scale of the required electric field for neutron production is set by $\varepsilon = (\mathrm{mc}/\hbar)(\hbar\Omega/e)$ [Under the same electric field, the protons will gain an equal and opposite momentum to that of the electrons; hence, their CM would stay at rest (if we neglect their very small initial momenta).]. For metallic hydride surfaces on which plasma oscillations exist, typical values for the surface plasmon polariton frequencies are in the range $(\hbar\Omega/e) \approx (5-6) \times 10^{-2}$ *Volts*, thereby requiring $\varepsilon \approx 2 \times 10^{11}$ *Volts/meter*. To put it in perspective, let us recall that typical atomic electric fields are of this order of magnitude. In particular, the electric field when located a Bohr radius ($a \approx 0.5$ *Angstrom*) away from an isolated proton is given by $\varepsilon(a) = (e/a^2) \approx 5 \times 10^{11}$ *Volts/meter*. Coherent proton oscillations on a metallic hydride monolayer will be shown in the next section to produce electric fields and plasma frequencies of the order of magnitudes needed for neutron production. There, we shall show that neutrons are born with very small momentum (ultra-cold) because their production is collective through a large number of protons coherently oscillating over a macroscopic region of the monolayer surface. Because the nuclear absorption

Downloaded by STANFORD UNIV GREEN LIBR on June 28, 2012 | http://pubs.acs.org
Publication Date (Web): December 20, 2009 | doi: 10.1021/bk-2009-1029.ch014

cross section of ultra-low-momentum neutrons is extremely large, it has two desirous effects: (i) the nuclear transmutation probability is large, which makes the rates substantial and (ii) the mean free path for a neutron to escape outside the metal surface is reduced to atomic distances. Hence, no free thermal-energy-or-higher neutrons are produced by this process in condensed matter systems. In addition, a photon shield is created by mass-renormalized electrons, which inhibits *MeV* range gamma rays from escaping the surface region. We shall review it in the next section.

Let us now turn to the magnetic mode of exciting electron capture by proton in a strong current-carrying wire in the steady state. For a wire of length Λ carrying a steady current *I* with N flowing electrons, the collective kinetic energy from the motion of all the electrons is most simply described through the inductive energy formula

$$W = (1/2c^2)LI^2, \tag{8}$$

where $L = \eta\,\Lambda$ is the inductance and η (of order unity) is the inductance per unit length. If an electron is removed (by any means, such as when an electron is destroyed in a weak interaction), the change in the current is

$$\delta I = -e\left(\frac{v}{\Lambda}\right), \tag{9}$$

where v is the mean velocity of the electrons in the current. The chemical potential is then given by

$$\mu = -\frac{\partial W}{\partial N} = -\left(\frac{L}{c^2}\right)I[I(N) - I(N-1)] = \frac{e\eta I v}{c^2}. \tag{10}$$

We may write it in a more useful (system of unit independent) form using the Alfvén current $I_o \approx 17$ *KiloAmperes*, which has been defined in Eq. (4).

$$\mu = (mc^2)\eta\left(\frac{I}{I_o}\right)\left(\frac{v}{c}\right). \tag{11}$$

Thus, we see that even with a moderate $(v/c) \approx 0.1$, if currents are much larger than the Alfvén value, the chemical potential can be of the order of *MeV's* or higher. This is an example of how the collective magnetic kinetic energy can be distributed to accelerate a smaller number of particles with sufficient energy to produce neutrons. Further discussions about the exploding wires are postponed until Sec. 4.

Let us now consider the solar corona for which the magnetic flux geometry is different from that of a wire. In a wire, the magnetic field loops surround the flowing current. In the corona, there are oppositely directed currents of electrons and protons that loop around the walls of magnetic flux tubes. In a steady-state magnetic flux tube that enters the solar corona from one sun spot and returns to another sun spot without exploding, a substantial amount of energy is stored in

Downloaded by STANFORD UNIV GREEN LIBR on June 28, 2012 | http://pubs.acs.org
Publication Date (Web): December 20, 2009 | doi: 10.1021/bk-2009-1029.ch014

the tube's magnetic fields. For a small change δI, in the current going around the vortex circumference, the change in the magnetic energy δεmag is given by

$$\delta\mathcal{E}_{mag} = (\frac{1}{c})\delta\Phi I. \tag{12}$$

If the length L denotes the vortex circumference, then - as described previously - for the destruction of an electron in the weak interaction, the change in the current corresponds to

$$\delta I = -e(\frac{v}{L}), \tag{13}$$

where v denotes the relative tangential velocity between the electron and the proton. Setting $\Phi = B\triangle S$ and $\delta\mathcal{E}_{mag} = -W_{mag}$, we obtain

$$W_{mag} = (eB)(\frac{\Delta S}{L})(\frac{v}{c}). \tag{14}$$

For a cylindrical flux tube,

$$(\frac{\Delta S}{L}) = \frac{\pi R^2}{2\pi R} = \frac{R}{2}. \tag{15}$$

For numerical estimates for the sun, it is useful to rewrite the above as

$$W_{mag} \approx (15\, GeV)(\frac{B}{Kilogauss})(\frac{R}{Kilometers})(\frac{v}{c}). \tag{16}$$

For an estimate, consider some typical values[24][Estimated values used in Eqs. 17 and 21 are typical and well-accepted; see various papers about magnetic fields and solar processes found in *(24).*]

$$\begin{aligned} R &\approx 10^2 Kilometers \\ B &\approx 1 Kilogauss \\ \frac{v}{c} &\approx 10^{-2} \\ W_{mag} &\approx 15\, GeV. \end{aligned} \tag{17}$$

Thus, even when the flux tube does not explode, appreciable neutron production is to be expected. It should be noted that neutrons produced through weak interactions in the higher-energy regime dominated by collective magnetic effects do not necessarily have ultra-low momentum. Unlike condensed matter systems such as metallic hydride chemical cells, neutrons produced collectively in magnetic flux tubes can be quite energetic.

On the other hand, for a spectacular solar flare that lasts for a time $\triangle t$, the loss of magnetic flux tube would yield a mean Faraday law acceleration voltage $\bar{V}$ around the walls given by

Downloaded by STANFORD UNIV GREEN LIBR on June 28, 2012 | http://pubs.acs.org
Publication Date (Web): December 20, 2009 | doi: 10.1021/bk-2009-1029.ch014

$$\bar{V} = \frac{\Delta\Phi}{c\Delta t}. \qquad (18)$$

Inserting as before $\Phi = B\triangle S$, where B denotes the mean magnetic field before the explosion and $\triangle S$ the inner cross-sectional area of the flux tube, we have for the mean acceleration energy

$$e\bar{V} = (eB)\frac{\Delta S}{\Lambda}, where\ \Lambda\ =\ c\Delta t \qquad (19)$$

For a cylindrical geometry, we may again rewrite it in a useful form:

$$e\bar{V} \approx\ (30\ GeV)(\frac{B}{Kilogauss})(\frac{\pi R^2}{\Lambda - Kilometers}). \qquad (20)$$

For a coronal mass ejecting coil exploding in a time $\triangle t \approx 10^2$ seconds, we may estimate

$$\begin{aligned} R\ &\approx\ 10^4 Kilometers \\ B\ &\approx\ 1 Kilogauss \\ \Lambda\ &\approx\ 3 \times\ 10^7\ Kilometers \\ e\bar{V}\ &\approx\ 300\ GeV. \end{aligned} \qquad (21)$$

Downloaded by STANFORD UNIV GREEN LIBR on June 28, 2012 | http://pubs.acs.org
Publication Date (Web): December 20, 2009 | doi: 10.1021/bk-2009-1029.ch014

Physically, it corresponds to a colliding beam of electrons and protons with a center of mass energy of 300 *GeV*. More on these matters will appear in Sec. 5.

Having discussed the mechanisms and making ourselves familiar with the magnitudes of the parameters involved in both the collective electric and magnetic modes of exciting neutron production, we shall devote the next three sections to a more detailed description of how it is realized in the three different physical cases: metallic hydride cells, exploding wires and the solar corona.

Metallic Hydride Cells

Although our discussion would hold for any metallic hydride, we will concentrate here on palladium hydrides, which are particularly suited for our purpose, because on such a loaded hydride, there will be a full proton layer in many-body, micron-scale patches of protons that are scattered randomly across the hydride surface. In such surface patches of protons, there will then exist coherent proton oscillations. At the very same time, electrons composing a thin film covering the entire hydride surface also undergo a collective oscillation known as the surface plasmon polariton (SPP) mode. Let us determine the size of this plasma frequency Ω and estimate the mean electric field $\bar{E} = \sqrt{\bar{E^2}}$ that can be generated on a fully loaded metallic hydride surface.

Suppose a proton of mass M_P is embedded in a sphere with a mean electronic charge density $\rho_e = (-e)n$. If the proton suffers a small displacement $\mathbf{u}$, then an electric field will be created

$$e\mathbf{E} = -\left(\frac{4\pi e^2 n}{3}\mathbf{u}\right) = -M_p\Omega^2\mathbf{u}, \tag{22}$$

to satisfy Gauss' law div**E** = $4\pi\rho_e$. This electric field will try to push back the proton to the center of the sphere. The equation of motion of the proton $M_p\ddot{u} = e\,\mathrm{E} = -\Omega^2 M_p \mathrm{u}$ yields the oscillation. This equation also furnishes the relationship between the mean electric field and the mean proton displacement

$$e^2\bar{\mathbf{E}}^2 = \left(\frac{4\pi e^2 n}{3}\right)^2 \bar{\mathbf{u}}^2. \tag{23}$$

We may estimate the strength of the mean electric field by taking the mean electron number density at the position of the proton:

$$n \approx |\psi(0)|^2 = \frac{1}{\pi a^3}. \tag{24}$$

Defining the atomic electric field at a distance *a* away as

$$\mathcal{E}_a = \frac{e}{a^2} \approx 5.1 \times 10^{11} Volts/meter, \tag{25}$$

we obtain

$$\bar{\mathbf{E}}^2 = \mathcal{E}_a^2\left(\frac{16}{9}\right)\left(\frac{\bar{\mathbf{u}}^2}{a^2}\right) \tag{26}$$

Neutron scattering experiments on palladium hydride clearly indicate a sharply defined oscillation peak for ($\hbar\Omega/\mathrm{e}$) ≈60 *millivolts*, as quoted in Sec. 2. Such a collective proton motion at an infra-red frequency will resonate with electronic surface plasmon polariton electron oscillations, leading to the local breakdown of the Born-Oppenheimer approximation (Let us recall that, in the Born-Oppenheimer (B-O) approximation, the nuclear coordinates are assumed fixed; only the electron coordinates are assumed dynamical. But on the thin surface of a mono layer, where collective surface oscillation modes for both the electrons and the protons exist, the B-O approximation becomes untenable. In the bulk of the metal, the situation is very different because of the screening of charges. The acceleration of electrons and the resultant neutron production being discussed here are all happening in monolayer surface patches, not within the bulk.). They will also lead to large collective proton oscillation amplitudes. This explains the large mean proton displacement $\bar{u}$ ≈2.2 *Angstroms* estimated from the neutron scattering experiments and a mean electric field estimated through Eq. (26)

$$\bar{E} \approx 28.8 \times 10^{11} Volts/meter \tag{27}$$

which is more than 10 times larger than $\mathcal{E}$, thus proving that the plasma oscillations on metallic hydride surfaces do provide internal local electric fields more than sufficient to accelerate the surface plasmon polariton electrons in overcoming the threshold barrier.

Our description about the acceleration of an electron from charge oscillations on the surface can be recast in a manifestly Lorentz and gauge

Downloaded by STANFORD UNIV GREEN LIBR on June 28, 2012 | http://pubs.acs.org
Publication Date (Web): December 20, 2009 | doi: 10.1021/bk-2009-1029.ch014

covariant form to imply that the free electron mass m has been dressed up or renormalized to a higher value $\bar{m} = \beta m$ for the SPP electrons (vedi Eq. (7)). Once $\beta \geq \beta_0 \approx 2.53$, neutron production through weak interaction is kinematically allowed.

For these heavy SPP electrons $\bar{e}^-$ with more than sufficient mass to enable the weak interaction $\bar{e}^- + p \to n + \upsilon_e$ to proceed, we turn to a rough order of magnitude estimate of this reaction rate. For this purpose, we may employ (i) the usual Fermi point-like left-handed interaction with coupling constant G_F (In the Standard Model of particle physics, this process is described through the charged W-boson exchange, whose mass is $M_W \approx 80$ GeV/c^2, corresponding to a rest energy so large on the scale of energies being discussed here that the Fermi point-like limit of the weak interaction is an excellent approximation, with the identification $G_F/(\hbar c)^3 = (\pi\alpha/\sqrt{2})/(M_W c^2 \sin\theta_W)^2 \approx 1.1 \times 10^{-5}$ GeV^{-2}. Here enters also the weak angle through $\sin^2\theta_W \approx 0.23$.), (ii) a heavy electron mass $\bar{m} = \beta m$ and, (iii) the small neutron-proton mass difference $\triangle = (M_n - M_p) \approx 1.3$ *MeV/c.*^{2} To make an order of magnitude estimate of the rate of this reaction, we observe that this rate, which (in lowest order of perturbation theory) is proportional to G_F^2, must on dimensional grounds scale with the fifth power of the electron mass. Hence, a rough dimensional analysis estimate would give

$$\Gamma(\tilde{e}^- p \to n\nu_e) \approx \left(\frac{G_F m^2 c}{\hbar^3}\right)^2 \left(\frac{mc^2}{\hbar}\right) \left(\frac{\tilde{m} - \Delta}{\Delta}\right)^2 \tag{28}$$

Numerically, this would imply a rate

$$\Gamma(\tilde{e}^- p \to n\nu_e) \approx 7 \times 10^{-3} \left(\frac{\tilde{m} - \Delta}{\Delta}\right)^2 \textit{Hertz}, \tag{29}$$

which in turn implies

$$\Gamma(\tilde{e}^- p \to n\nu_e) \approx 1.2 \times 10^{-3}\ (\beta - \beta_o)^2\ \textit{Hertz}. \tag{30}$$

If we assume a surface density of $10^{16}/cm^2$ (heavy SPP electron-proton) pairs, we arrive at the following estimate for the rate of weak interaction neutron production in condensed matter on a loaded metallic hydride surface

$$\tilde{w}(\tilde{e}^- p \to n\nu_e) \approx (1.2 \times 10^{13}\ /cm^2/second)\ (\beta - \beta_o)^2, \tag{31}$$

which is substantial indeed.

The neutrons so produced will be of ultra-low momentum because their production is through the collectively oscillating protons and SPP electrons acting in tandem within patches randomly located on the surface.

In condensed matter LENRs, the many-body system of collective interaction is a surface patch of N_p collectively oscillating protons that are electromagnetically coupled to many nearby collectively oscillating SPP

Downloaded by STANFORD UNIV GREEN LIBR on June 28, 2012 | http://pubs.acs.org
Publication Date (Web): December 20, 2009 | doi: 10.1021/bk-2009-1029.ch014

electrons N_e through local breakdown of the Born-Oppenheimer approximation. After SPP electron mass renormalization and neutron production through the weak interaction take place, the final state of such localized systems contains (N_p − 1) protons, (N_e − 1) SPP electrons and, according to our theory, one freshly produced neutron. Such a system's final state might be naively pictured as containing an isolated free neutron at roughly thermal energies with a DeBroglie wavelength λ of ~2 Angstroms, which would be typical for thermalized free neutrons in condensed matter. Here, that is not the case: In a *many-body collective system's* final state, a particular proton, say number k, has been converted to a neutron. The resulting many-body state *together with all the unconverted protons* may be denoted by the neutron localized $|k\rangle$. However, a neutron produced by a many-body collective system is *not* created in a simple state $|k\rangle$. The wave function of such neutrons within a many-body cluster of N_p identical protons is in reality a *superposition of many N_p localized states*; it is best described by a *delocalized* band state $|\psi\rangle \approx \frac{1}{\sqrt{N_p}}\sum_{k=1}^{N}|k\rangle$.

Thus, the DeBroglie wavelength λ of neutrons produced by a condensed matter collective system must be comparable to the spatial dimensions of the many-proton surface patches in which they were produced. The wavelength of such neutrons may be estimated to be about $\lambda \approx 10^{-3}$ cm[1]; ultra-low momentum of collectively created neutrons follows directly from the DeBroglie relation $p = \frac{h}{\lambda} = \frac{2\pi\hbar}{\lambda} = \frac{\hbar}{\lambdabar}$.

The result for surface patches of collectively oscillating deuterons is identical, except that two ultra-low-momentum neutrons are simultaneously produced instead of one. In either case, the larger the *dimensions* of a patch, the larger the wavelengths of neutrons produced collectively in such patches.

Such long wavelength neutrons will get absorbed with an extremely high probability by the nuclei on the surface because the neutron absorption cross section would be very large. This can be seen by computing the total neutron cross section through the optical theorem, which relates it to the forward elastic (*n* –*Nucleus*) amplitude

$$\sigma_T(n + Nucleus \rightarrow anything) = \left(\frac{4\pi}{k}\right)\Im m f(k, 0). \tag{32}$$

Let $f(k, \mathbf{0}) = a + ib$, with $b \approx 1$ *fermi* (The value for b of ~ 1 fermi is reasonable because it is the scale of strong interaction physics.). Then, we obtain

$$\sigma_T(n + Nucleus \rightarrow anything) = 2\lambda b \approx 2\times 10^8\ barns, \tag{33}$$

a very large value. This not only shows a hefty rate for the production of nuclear transmutations through a rapid absorption of neutrons, but it also shows that the mean free path of a neutron Λ is of the order of a few atomic distances. In fact, given the density of neutron absorbers $n_{\mathrm{abs}} \approx 10^{22}/cm^3$, we may estimate

$$\Lambda^{-1} = n_{abs}\sigma_T;\ \Lambda \approx 50\ Angstroms \tag{34}$$

Downloaded by STANFORD UNIV GREEN LIBR on June 28, 2012 | http://pubs.acs.org
Publication Date (Web): December 20, 2009 | doi: 10.1021/bk-2009-1029.ch014

Hence, in condensed matter systems, practically all such ultra-low-momentum neutrons will get absorbed locally on or very near the surface on which they are produced, with essentially a zero probability of finding substantial fluxes of free unabsorbed neutrons at thermal energies or higher.

The observed electromagnetic radiation from the heavy SPP electrons will be confined essentially to low-energy photons reaching up to soft X-rays with practically no *MeV* range photons being radiated because the mean free path of any produced gamma rays in the few *MeV* range would be very short, about a few *Angstroms*.

To recapitulate: Interactions between surface charges comprising collectively oscillating protons and SPP electrons, in conjunction with a breakdown of the Born-Oppenheimer approximation, provide enough collective energy for the production of heavy mass SPP electrons, which in turn lead to the production of ultra-low-momentum neutrons through the weak interaction. Such neutrons are readily absorbed locally; their production dynamics effectively create their own unique neutron and built-in gamma ray shields. The most easily observed end products would be the results of nuclear transmutations triggered by the absorption of neutrons by nearby nuclei and subsequent decay processes. A plethora of nuclear reactions and products are thereby possible in such systems. One such complete nuclear chain cycle with a high Q-value is as follows. Let us assume that the surface is coated with lithium. Successive absorption of neutrons by lithium will produce

$$\begin{aligned} {}^{6}_{3}Li + n &\rightarrow {}^{7}_{3}Li \\ {}^{7}_{3}Li + n &\rightarrow {}^{8}_{3}Li \\ {}^{8}_{3}Li &\rightarrow {}^{8}_{4}Be + e^{-} + \bar{\nu}_{e} \\ {}^{8}_{4}Be &\rightarrow {}^{4}_{2}He + {}^{4}_{2}He. \end{aligned} \tag{35}$$

The heat produced through the above reaction is quite high:
$Q[{}^{6}_{3}Li + 2n \rightarrow 2\,{}^{4}_{2}He + e^{-} + \bar{\upsilon}_{e}] \approx 26.9$ *MeV*.

On the other hand, ${}^{4}_{2}He$ can successively absorb ultra-low-momentum neutrons and, through the formation of intermediate halo nuclei, reproduce lithium

$$\begin{aligned} {}^{4}_{2}He + n &\rightarrow {}^{5}_{2}He \\ {}^{5}_{2}He + n &\rightarrow {}^{6}_{2}He \\ {}^{6}_{2}He &\rightarrow {}^{6}_{3}Li + e^{-} + \bar{\nu}_{e}. \end{aligned} \tag{36}$$

The heat from the reaction in Eq. (36) is $Q[{}^{4}_{2}He + 2n \rightarrow {}^{6}_{3}Li + e^{-} + \bar{\upsilon}_{e}] \approx 2.95$ *MeV*. The complete nuclear cycle as described in Eqs. (35) and (36) taken together would release substantial total heat through nuclear transmutations. Other lithium-initiated processes would produce both ${}^{4}He$ and ${}^{3}He$.

Downloaded by STANFORD UNIV GREEN LIBR on June 28, 2012 | http://pubs.acs.org
Publication Date (Web): December 20, 2009 | doi: 10.1021/bk-2009-1029.ch014

Exploding Wires

In Sec. 2, we have outlined our explanation of nuclear transmutations and fast energetic neutrons, which have been observed to emerge when large electrical current pulses passing through wire filaments are induced to explode. If a strong current pulse, large on the scale of I_0, defined in Eq. (4), passes through a thin wire filament, then the magnetic field that loops around the current exerts a very large Maxwell pressure on surface area elements, compressing, twisting and pushing into the wire. When the magnetic Maxwell pressure grows beyond the tensile strength of the wire material at the hot filament temperature, the wire first expands, then begins to melt and finally disintegrates. Slow-motion pictures now verify that, indeed, the wire expands, melts and disintegrates. All of this is readily understood. If the heating rate is sufficiently fast, then the hot wire may emit thermal radiation at a very high noise temperature. The thermal radiation from exploding Tungsten filaments exhibits X-ray frequencies indicating very high electron kinetic energies within the filament. Because of the electron kinetic pressure, the wire diameter starts to increase, yielding a filament dense gas phase but still with some liquid droplets. The final explosive product consists of a hot plasma colloid containing some small dust particles of the original wire material. These products cool off into a gas and some smoke, which is usual for explosions.

As discussed in Sec. 2, we want to understand how LENRs can be initiated in an exploding wire current pulse with a strong current (with its peak value substantially higher than I_0) produced by a capacitor discharge with an initial voltage of only 30 *kV (25, 26)*. We also want to understand, by contrast, why, when Ernest Rutherford had fired a much-higher-energy 100 *KeV* but dilute beam of electrons into a Tungsten target, he did not observe any nuclear reactions *(27)*.

A typical electron in the current with a mean kinetic energy 15 *KeV* would have an average speed (v/c) ≈0.25. On the other hand, even for such low mean speed, the chemical potential given in Eq. (11) for (I/I_0) ≈200 becomes large

$$\mu \approx (mc^2)(200)(0.25) = 25\ MeV, \tag{37}$$

comfortably sufficient for an electron to induce a weak interaction LENR. Overall energy conservation would, of course, require that only a certain fraction about (15 *KeV*/25 *MeV*) = 6 x 10^{-4} of the total number of electrons in the current would be kinematically allowed to undergo weak interactions.

Let us now briefly discuss why Rutherford, with his much higher energy - but comparatively dilute - beam of electrons, did not observe any nuclear reactions. The reason is rather simple. In the vacuum, there is a mutual Coulomb repulsion between the electrons in the beam, which compensates the mutual Amperian current attraction. In the exploding wire filament, on the other hand, the repulsive Coulomb part is screened by the background positive charge but leaves intact the Amperian current attraction, thereby allowing the possibility of nuclear reactions.

Downloaded by STANFORD UNIV GREEN LIBR on June 28, 2012 | http://pubs.acs.org
Publication Date (Web): December 20, 2009 | doi: 10.1021/bk-2009-1029.ch014

Solar Corona and Flares

As stated in Sec. 2, oppositely directed Amperian currents of electrons and protons loop around the walls of a magnetic flux tube that exits one sun spot into the solar corona to enter back into another sun spot. The magnetic flux tube is held up by magnetic buoyancy. We consider here the dynamics of how very energetic particles are produced in the solar corona and how they induce nuclear reactions well beyond the solar photosphere. Our explanation, centered around Faraday's law, produces the notion of a solar accelerator very similar to a betatron *(28, 29)*. A betatron is a step-up transformer whose secondary coil is a toroidal ring of particles circulating around a time-varying Faraday flux tube.

We may view the solar flux tube as acting like a step-up transformer that passes some circulating particle kinetic energy from the solar photosphere outward to other circulating particles located in the solar corona. The circulating currents within the photosphere are to be considered as a net current I_P around a primary coil, and the circulating currents high up in the corona as a net current I_S. If K_P and K_S represent the kinetic energies, respectively, in the primary and the secondary coils, the step-up transformer power equation reads

$$|\dot{K}_{\mathcal{P}}| = |V_{\mathcal{P}} I_{\mathcal{P}}| = |V_{\mathcal{S}} I_{\mathcal{S}}| = |\dot{K}_{\mathcal{S}}|, \tag{38}$$

where V_P and V_S represent the voltages across the primary and the secondary coils, respectively. The total kinetic energy transfer reads

$$\Delta K_{\mathcal{P}} = \int (dt) |V_{\mathcal{P}} I_{\mathcal{P}}| = \int (dt) |V_{\mathcal{S}} I_{\mathcal{S}}| = \Delta K_{\mathcal{S}}. \tag{39}$$

In essence, what the step-up transformer mechanism does is to transfer the kinetic energy distributed among a very large number of charged particles in the photosphere - through magnetic flux tubes - into a distant, much smaller number of charged particles located in the solar corona, so that a small accelerating voltage in the primary coil produces a large accelerating voltage in the secondary coil. The transfer of kinetic energy is *collective* from a larger group of particles into a smaller group of particles, resulting in the kinetic energy per charged particle of the dilute gas in the corona becoming higher than the kinetic energy per particle of the much denser fluid in the photosphere.

We may convert the above into a temperature-kinetic energy relationship by saying that the temperature of the dilute corona will be much higher than the temperature of the more dense fluid photosphere. If and when the kinetic energy of the circulating currents in a part of the floating flux tube becomes sufficiently high, the flux tube would become unstable and explode into a solar flare, which may be accompanied by a coronal mass ejection. Magnetic field energy converts rapidly into charged particle kinetic energy. These high-energy products from the explosion initiate nuclear as well as elementary particle interactions, some of which have been detected in laboratories on Earth.

Recent NASA and ESA pictures show that the surface of the sun is covered by a carpet-like interwoven mesh of magnetic flux tubes of smaller, variable dimensions. Some of these smaller structures possess enough magnetic energy

Downloaded by STANFORD UNIV GREEN LIBR on June 28, 2012 | http://pubs.acs.org
Publication Date (Web): December 20, 2009 | doi: 10.1021/bk-2009-1029.ch014

to lead to LENRs through a continual conversion of their magnetic field energy into particle kinetic energy. Occurrence of such nuclear processes in a roughly steady state would account for the solar corona's remaining much hotter than the photosphere. Needless to say, our picture belies the long-held notion that all nuclear reactions are contained within the core of the sun. On the contrary, it provides strong theoretical support for experimental anomalies *(30, 31)* such as short-lived radioactive isotopes *(32, 33, 34)* that have been observed in the spectra of stars having unusually high average magnetic fields (The term "magnetic stars" includes Ap and Bp stars, as well as so-called "magnetars.").

For the transformer mechanism to be fully operational in the corona, the coronal electrical conductivity must not be too large. Useful experimental bounds on an upper limit to this conductivity may be obtained through its effect on measurements of gravitational bending of light near the sun as it traverses the solar corona. Successful measurements of the gravitational bending of electromagnetic waves with frequencies in the visible and all the way down to the high end of the radio spectrum are legion. These experiments provide direct proof that any coronal conductivity disturbance on the expected gravitational bending of electromagnetic waves for frequencies down to 12.5 *GigaHertz* must be negligible. Error estimates from even lower frequency radio wave probes used for gravitational bending *(35, 36)* put the coronal conductivity in the *Megahertz* range. For comparison, we note that the typical conductivity of a good metal would be more than ten orders of magnitude higher (Salty ocean water has a conductivity of about 1.5×10^{11} Hertz.). The corona is close to being an insulator and very far from being as conductive as a metal, and there is no impedimenta toward sustaining electrical fields within it *(37, 38, 39)*. Thus, our proposed transformer mechanism and its subsequent predictions for the corona remain intact.

The spectacular solar flare that occurred on July 14, 2000, and the measurement of the excess muon flux associated with this flare by the CERN L3+C group *(22)* offered a unique opportunity to infer that protons of energies in excess of 40 *GeV* were produced in the solar corona. Likewise, the BAKSAN underground muon measurements *(40)* provided evidence for protons of energies in excess of 500 *GeV* in the solar flare of September 29, 1989. The very existence of primary protons in this high energy range provides strong evidence for the numbers provided in Eq. (21). Hence, for large solar flares in the corona, electrons and protons must have been accelerated well beyond anything contemplated by the standard solar model. This, in turn, provides the most compelling evidence for the presence of large-scale electric fields and the transformer or betatron mechanism because we do not know of any other process that could accelerate charged particles to beyond even a few *GeV*, let alone hundreds of *GeVs*.

Summary and Concluding Remarks

We summarize by saying that three seemingly diverse physical phenomena –metallic hydride cells, exploding wires and the solar corona – do have a unifying theme. Under appropriate conditions which we have now well-

Downloaded by STANFORD UNIV GREEN LIBR on June 28, 2012 | http://pubs.acs.org
Publication Date (Web): December 20, 2009 | doi: 10.1021/bk-2009-1029.ch014

Downloaded by STANFORD UNIV GREEN LIBR on June 28, 2012 | http://pubs.acs.org
Publication Date (Web): December 20, 2009 | doi: 10.1021/bk-2009-1029.ch014

delineated, in all these processes electromagnetic energy gets collectively harnessed to provide enough kinetic energy to a certain fraction of the electrons to combine with protons (or any other ions present) and produce neutrons through weak interactions. The produced neutrons then combine with other nuclei to induce low energy nuclear reactions and transmutations. Lest it escape notice, let us remind the reader that all three interactions of the standard model (electromagnetic, weak and nuclear) are essential for an understanding of these phenomena. Collective effects but no new physics for the acceleration of electrons beyond the standard model need to be invoked. However, we have seen that certain paradigm shifts are necessary. On the surface of a metallic hydride cell with surface plasmon polariton modes, protons collectively oscillate along with the electrons. Hence, the Born-Oppenheimer approximation (which assumes that the proton is rigidly fixed) breaks down and should not be employed. Similarly, in the solar corona, the electronic density and the electrical conductivity are sufficiently low. Hence, there is not much charge screening of the electric fields involved. Strong electric fields generated by time-dependent magnetic fields through Faraday's laws are sustained in the corona, and the betatron (or transformer) mechanism remains functional. Were it not so, electrons and protons could not have been accelerated to hundreds of *GeV's*, and there would have been no production of high-energy muons, certainly not copious enough to have reached Earth in sufficient numbers to have been observed by the L3+C collaboration at LEP *(22)* or by the BAKSAN underground laboratory *(40)*. We are unaware of any other alternative scheme for obtaining this result. The betatron mechanism also naturally explains a variety of observed experimental results, such as unexpected nuclear transmutations in active stellar atmospheres (*41)* and high-energy cosmic rays from the exterior of the sun or any other astronomical object endowed with strong enough magnetic activity, such as active galactic nuclei.

The analysis presented in this paper leads us to conclude that realistic possibilities exist for designing condensed matter LENR devices capable of producing green energy – that is, production of excess heat at low cost without lethal nuclear waste, dangerous gamma rays or unwanted fluxes of energetic free neutrons. The necessary tools and the essential theoretical know-how to design and manufacture such devices appear to be well within the reach of available technology. Vigorous efforts must be made to develop such devices whose functionality requires all three interactions of the standard model acting in concert.

Acknowledgements

Over the past few years, various phases of this work have been presented by us in seminars and lectures at the universities of Milan, Perugia, Rome I and III; Olivetti Research Center in Milan; INFN Italian National Laboratory at Frascati; Inter University Accelerator Center in New Delhi, India; and various U.S. government departments and agencies in Washington, D.C. We take this opportunity to thank our colleagues for inviting us to their institutions and for many interesting and useful remarks.

References

1. Widom, A.; Larsen, L. Ultra low momentum neutron catalyzed nuclear reactions on metallic hydride surfaces. *Eur. Phy. J.* **2006,** *C46*, 107.
2. Widom, A.; Larsen, L. Absorption of nuclear gamma radiation by heavy electrons on metallic hydride surfaces; arXiv:cond-mat/0509269.
3. Widom, A.; Larsen, L. Nuclear abundances in metallic hydride electrodes of electrolytic chemical cells; arXiv: cond-mat/0602472.
4. Widom, A.; Larsen, L. Theoretical standard model rates of proton to neutron conversions near metallic hydride surfaces; arXiv: nucl-th/0608059v2.
5. Widom, A.; Srivastava, Y. N.; Larsen, L. Energetic electrons and nuclear transmutations in exploding wires; arXiv: nuclth/0709.1222v1.
6. Widom, A.; Srivastava, Y. N.; Larsen, L. High-energy particles in the solar corona; arXiv: nuclth/0804.2647v1.
7. Stephanakis, S. et al. Neutron production in exploding-wire discharges. *Phys. Rev. Lett.* **1972**, *29*, 568.
8. Young, F. et al. Neutron and energetic ion production in exploded polyethylene fibers. *J. Appl. Phys.* **1977**, *48*, 3642.
9. Bakshaev, Y. et al. Study of the plasma in a preformed Z-pinch constriction. *Plasma Phys. Rep.* **2001**, *27*, 1039; Bakshaev, Y. et al. Measurements of neutron emission from a Z-pinch constriction, *Plasma Phys. Rep.* **2006***, 32*, 501.
10. Sarkisov, G. et al. Effect of deposited energy on the structure of an exploding tungsten wire core in a vacuum. *Phys. Plasmas* **2005**, *12*, 052702.
11. Velikovich A. et al. Z-pinch plasma neutron sources. *Phys. Plasmas* **2007**, *14*, 022701.
12. Coverdale C. et al. Neutron production and implosion characteristics of a deuterium gas-puff Z pinch. *Phys. Plasmas* **2007**, *14*, 022706.
13. Shah, G.; Razdan, H.; Bhat, C.; Ali, Q. Neutron generation in lightning bolts. *Nature*, **1985**, *313*, 773.
14. Forbush, S. Three unusual cosmic-ray increases possibly due to charged particles from the sun. *Phys. Rev.* **1946**, *70*, 771.
15. Dorman, L.; Venkatesan, D. Solar cosmic rays. *Space Science Reviews* **1993**, *64*, 183.
16. Reames, D.; Ng, C. Heavy-element abundances in solar energetic particle events. *Astrophys. J.* **2004**, *610*, 510.
17. Belov, A.; Eroshenko E.; Mavromichalaki, H.; Plainaki, C.; Yanke, V. Ground-level enhancement of the solar cosmic rays on January 20, 2005. *Proceedings of the 29th International Cosmic Ray Conference. August 3-10, 2005, Pune, India*. Acharya, B. S.; Gupta, S.; Jagadeesan, P.; Jain, A.; Karthikeyan, S.; Morris, S.; Tonwar, S., Eds.; Mumbai: Tata Institute of Fundamental Research, 2005; Vol. 1, p 189.
18. Vashenyuk, E.; Balabin, Y.; Gvozdevsky, B.; Karpov, S.; Yanke, V.; Eroshenko, E.; Belov, A.; Gushchina, R. Relativistic solar cosmic rays in January 20, 2005 event on the ground based observations. *Proceedings of the 29th International Cosmic Ray Conference. August 3-10, 2005, Pune,*

Downloaded by STANFORD UNIV GREEN LIBR on June 28, 2012 | http://pubs.acs.org
Publication Date (Web): December 20, 2009 | doi: 10.1021/bk-2009-1029.ch014

India. Acharya, B. S.; Gupta, S.; Jagadeesan, P.; Jain, A.; Karthikeyan, S.; Morris, S.; Tonwar, S., Eds.; Mumbai: Tata Institute of Fundamental Research, 2005; Vol. 1, p 209.

19. Bostanjyan, N.; Chilingarian, A.; Eganov, V.; Karapetyan, G. On the production of highest energy solar protons at 20 January 2005. *Advances in Space Research* **2007**, *39*, 1454.
20. Shea, M.; Smart, D. Solar proton and GLE event frequency: 1955-2000. In *Proceedings of the 27th International Cosmic Ray Conference,* Aug. 7-15, 2001, Hamburg, Germany; Kampert, K.-H.; Heinzelmann, G., Eds.; Copernicus Gessellschaft, 2001; p 3401.
21. Cliver, E. The unusual relativistic solar proton events of 1979 August 21 and 1981 May 10. *J. Astrophys.* **2006**, *639*, 1206.
22. L3 Collaboration, The solar flare of the 14th of July 2000 (L3+C detector results). *Astronomy and Astrophysics* **2006**, *456*, 351. We thank Dr. E. Fiandrini for pointing out this reference.
23. Priest, E.; Foley, C.; Heyvaerts, J.; Arber, T.; Culhane, J.; Acton, L. The nature of the heating mechanism for the diffuse solar corona. *Nature* **1998**, *393*, 545.
24. Wilson, A., Ed. *Ninth European Meeting on Solar Physics*, 12-18 September 1999, Florence, Italy; European Space Agency: Noordwijk, Netherlands, 1999. ESA SP-448, 1999. ISBN: 92-0902-792-5. Bibliographic Code: 1999ESASP.448.1345E.
25. Wendt, G.; Irion, C. Experimental attempts to decompose tungsten at high temperatures. *Amer. Chem. Soc.* **1922**, *44*, 1887-1894.
26. Wendt, G. The decomposition of tungsten. *Science* **1922**, *55*, 567.
27. Rutherford, E. Disintegration of elements. *Nature* **1922**, *109*, 418.
28. Kerst, D. The acceleration of electrons by magnetic induction. *Phys. Rev.* **1941**, *60*, 47.
29. Kerst, D.; Serber, R. Electron orbits in the induction accelerator. *Phys. Rev.* **1941**, *60*, 53.
30. Fowler, W.; Burbidge, E.; Burbidge, G.; Hoyle, F. The synthesis and destruction of elements in peculiar stars of types a and b. *The Astrophysical Journal* **1965**, *142*, 423.
31. Wurz, P. et al. Elemental composition of the January 6, 1997, CME. *Geophysical Research Letters* **1998**, *25*, 2557.
32. Cowley, C.; Bidelman, W.; Hubrig, S.; Mathys, G.; Bord, D. On the possible presence of promethium in the spectra of HD 101065 (Przybylski's star) and HD 965. *Astronomy and Astrophysics* **2004**, *419*, 1087.
33. Goriely, S. Nucleosynthesis by accelerated particles to account for the surface composition of HD 101065. *Astronomy and Astrophysics* bf **2007**, *466*, 619.
34. Lodders, K. The solar argon abundance; arXiv:0710.4523 (October 2007).
35. Weinberg, S. *Gravitation and Cosmology: Principles and Applications of the General Theory of Relativity*, Chapter 8. John Wiley and Sons: New York, 1972.
36. Muhleman, D.; Ekers, R.; Fomalont, E. Radio interferometric test of the general relativistic light bending near the sun. *Phys. Rev. Lett.* **1970**, *24*, 1377.

Downloaded by STANFORD UNIV GREEN LIBR on June 28, 2012 | http://pubs.acs.org
Publication Date (Web): December 20, 2009 | doi: 10.1021/bk-2009-1029.ch014

37. Foukal, P.; Miller, P. Electric fields in coronal magnetic loops. *Solar Physics* **1983**, *83*, 83.
38. Feldman, U. Electric currents as the main cause of coronal and flare activity in the sun and in many late-type stars. *Physica Scripta*, **2002**, *65*, 185-192.
39. Stasiewicz, K.; Ekeberg, J. Electric potentials and energy fluxes available for particle acceleration in the solar corona. *The Astrophysical Journal* **2008**, *680*, L153-L156.
40. Karpov, S. et al. Muon bursts at the Baksan underground scintillation telescope during energetic solar phenomena. *Il Nuovo Cimento* **1998**, *21C*, 551.
41. Tatischeff, V.; Thibaud, J.; Ribas, I. Nucleosynthesis in stellar flares; arXiv:astro-ph/0801.1777v1.

Downloaded by STANFORD UNIV GREEN LIBR on June 28, 2012 | http://pubs.acs.org
Publication Date (Web): December 20, 2009 | doi: 10.1021/bk-2009-1029.ch014

Author Index

Biberian, J.-P., 9–34
Block, R. C., 139–157

Cherdantsev, Y., 95–117
Chernov, I., 95–117
Cho, J. S., 139–157
Chubb, S. R., 177–192
Cravens, D., 81–93

Dash, J., 61–80

Forsley, L. P. G., 119–135

Ghahramani, N., 219–234
Ghanaatian, M., 219–234
Gordon, F. E., 119–135

Hagelstein, P. L., 81–93
Hooshmand, M., 219–234
Hora, H., 219–234, 235–252

Krivit, S. B., 3–5

Lahey, R. T., 139–157
Larsen, L., 253–270
Letts, D., 81–93
Lipson, A., 95–117, 235–252
Lyakhov, B., 95–117

Melich, M., 95–117
Miley, G. H., 219–234, 235–252
Mosier-Boss, P. A., 119–135

Nigmatulin, R. I., 139–157

Osman, F., 219–234

Philberth, K., 219–234, 235–252

Roussetski, A., 95–117

Saunin, E., 95–117
Shrestha, P. J., 235–252
Silver, D. S., 61–80
Srinivasan, M., 35–57
Srivastava, Y. N., 253–270
Stringham, R. S., 159–173

Takahashi, A., 193–217
Taleyarkhan, R. P., 139–157
Tsivadze, A., 95–117

Wang, Q., 61–80
West, C. D., 139–157
Widom, A., 253–270

Xu, Y., 139–157

Downloaded by 89.163.35.42 on June 28, 2012 | http://pubs.acs.org
Publication Date (Web): December 20, 2009 | doi: 10.1021/bk-2009-1029.ix001

Subject Index

A

Abundance distribution
  magic numbers, 228
  See also Magic numbers
Acoustic inertial confinement bubble nuclear fusion. *See* Bubble nuclear fusion
Aged-TiD-targets study, tritium detection, 47
Ag isotopes, transmutation of Pd to, 76, 77
Alfvén current, electro-weak induced low energy nuclear reactions, 255, 257

B

Barium, transmutation to samarium, 14, 15*f*
Beat frequencies, optical phonon modes and, 86–87
Bhabha Atomic Research Centre (BARC)
  activity after Fleischmann–Pons (F&P) announcement, 36
  autoradiograph of deuterated Ti chip showing tritium hot spots, 46*f*
  autoradiograph of Ti plasma focus electrode, 47*f*
  Desalination Division, 37–38
  deuterium gas/plasma-loaded Ti samples, 45–47
  electrolysis experiments with neutron and tritium generation, 44*t*, 45*t*
  electrolytic cells, 37–41
  five module Pd-Ni electrolyzer, 37, 38*f*
  Gd capture gamma ray counts, 39*f*
  government LENR research, 3–4
  Isotope and Health Physics divisions, 42
  neutron emission from TiD disc, 41*f*
  neutron measurements, 37–41
  neutron output of quiescent Milton Roy Cell, 40*f*
  Neutron Physics Division, 37, 38
  nuclear research and development center, 36
  steady neutron production by New Milton Roy Cell, 40, 41*f*
Biberian, Jean-Paul, LENR research with deuterium gas, 3
Boltzmann distribution
  magic number sequence, 242
  standard abundance distribution (SAD) for magic numbers, 221–223
  See also Magic numbers
Bose–Einstein deuteron clusters, 245–247
Bridgman, Percy, "cold nuclear explosions," 3
Bubble nuclear fusion
  clarifications, 152–153
  compression process, 143
  confirmations, 144–145
  counts above 2.45 MeV proton-recoil edge, 150–151
  D-D neutron emission, 144, 145*f*
  difficulties with replication, 152–153
  experimental, 140, 141*f*
  external accelerator-based monoenergetic 14.1 MeV neutron-seeded experiments, 149, 150*f*
  external neutron source, 144
  implosive collapse of bubbles, 140

Downloaded by 89.163.35.42 on June 28, 2012 | http://pubs.acs.org
Publication Date (Web): December 20, 2009 | doi: 10.1021/bk-2009-1029.ix002

  - internal energy of bubble, 140
  - Mach number stage of vapor bubble implosion, 143, 144*f*
  - NE-213 liquid scintillation (LS) detector response, 147
  - neutron counts, 141, 142*f*
  - neutron pulse height spectrum during self-nucleated, 144, 145*f*
  - neutron spectra with ice-pack shielding, 147, 148*f*
  - neutron spectra with ice-pack thermal shielding, 149
  - phenomenon, 4
  - predictions vs. measured neutron response spectrum with ice-pack shielding, 147, 148*f*, 149*f*
  - pulse-pileup effects, 151, 152*f*
  - replications, 144–145
  - scientific feasibility, 143
  - super-compression-induced fusion, 143
  - theoretical Monte Carlo simulations, 146–149, 154
  - tritium production, 141, 142*f*

Burst method, measurements using dead-time method, 52

C

Calcium oxide (CaO), layers with palladium, 13

Calorimetry
  - experimental sonofusion system, 169*f*
  - instrumentation and, 83–84
  - long-term stability, 84
  - sonofusion experiment, 167–169

Cavitation bubbles
  - energy-density gain of collapsed, 163
  - piezo-driven ultrasound system, 161–162
  - plasma configuration of transient compressed jet, 162*f*

Charged particles
  - deuterated palladium and titanium, 19
  - e-beam generating, 98–99
  - electron beam irradiation of Pd/PdO/Pd:Dx, 101–103
  - emission in Pd/PdO:Dx and TiDx, 112–115
  - emission rate in Pd/PdO:Dx, 108–109
  - *See also* Deuterium excitation in metal deuterides

Clusters, Bose–Einstein deuteron, 245–247

Co-deposition of palladium/deuterium (Pd/D). *See* Radioisotope thermoelectric generator (RTG)

"Cold fusion"
  - announcement by Pons and Fleischmann, 9
  - Pons–Fleischmann type, 242
  - researchers as heretics, 4
  - term, 3

Collective harnessing, electromagnetic energy, 266–267

Collective oscillation
  - interaction of, protons and surface plasmon polariton (SPP) electrons, 263
  - SPP mode, 259

Colored quark-gluon plasma
  - magic numbers, 229–231
  - *See also* Quark-gluon plasma

Compression process, bubble nuclear fusion, 143, 144*f*

Coulomb barrier
  - classical and semi-classical physics, 182
  - collision, 182
  - re-examining common assumptions, 178, 180–181

CR-39 detectors
  - bubble fusion experiments, 140
  - calibration curve for alphas, tritons and protons, 125*f*
  - control experiments, 122–123

Downloaded by 89.163.35.42 on June 28, 2012 | http://pubs.acs.org
Publication Date (Web): December 20, 2009 | doi: 10.1021/bk-2009-1029.ix002

- interaction with neutrons, 131, 132*f*
- Pd/D co-deposition experiments, 131, 132*f*
- sequential etching, 123
- size distribution of tracks for, exposed to ^{241}Am alpha source, 125*f*
- spacer experiments, 121–122, 124–126
- track modeling, 126–127, 128*f*
- *See also* Deuterium excitation in metal deuterides; Radioisotope thermoelectric generator (RTG)

D

Dead-time method
- artificial, 49
- burst neutron measurements, 52
- neutron detection efficiency, 52–53
- superior technique, 53

Deuterium
- autoradiograph of deuterated Ti chip showing tritium hot spots, 46*f*
- D_2 gas/plasma-loaded Ti samples, 45–47
- Langevin equation for, 195–197
- quantum mechanical image, 196*f*
- role of phonons in solid-state fusion, 82

Deuterium clusters
- Langevin equations for complex, 203–204
- quantum mechanical ensemble average for, 198

Deuterium D^{2+} ion, Langevin equation, 202–203

Deuterium excitation in metal deuterides
- alpha particle emission, 112
- background in vacuum chamber, 99*f*
- charged particle emission in vacuum, 112
- charged particle emission rate in Pd/PdO:Dx, 108–109
- CR-39 detectors, 96, 97–99
- D-desorption rate from Pd/PdO:Dx samples, 98*f*
- DD-reaction, 112–113
- desorbed deuterium, 98
- differential spectra of detectors during e-beam irradiation of Pd/PdO:Dx samples, 104*f*, 105*f*
- differential spectrum of 11 μm Al:Pd/PdO:Dx, 101*f*, 103
- differential spectrum of 11 μm Al:TiDx, 109*f*, 111
- differential spectrum of 25 μm Cu:Pd/PdO:Dx, 102*f*, 103
- differential spectrum of 26 μm Cu:TiDx, 110*f*
- differential spectrum of 33 μm Al:Pd/PdO:Dx, 102*f*, 103
- e-beam excitation of TiDx samples, 111
- e-beam irradiated face of TiDx, 111
- e-beam spot bombardment of sample, 97
- electron beam irradiation of Pd/PdO/Pd:Dx, 101, 103
- enhancement factor, 112, 113
- experimental, 96–99
- extrapolation of DD-reaction yield, 114
- foreground and background spectra of 33 μm Al:TiDx, 110*f*
- generated charged particles, 98–99
- nuclear particle detection for CR-39 with Al and Cu filters, 111
- open detector for Pd/PdO:Dx heterostructure, 100*f*
- Pd/PdO:Dx heterostructure under e-beam irradiation, 115–116

Downloaded by 89.163.35.42 on June 28, 2012 | http://pubs.acs.org
Publication Date (Web): December 20, 2009 | doi: 10.1021/bk-2009-1029.ix002

  Pd/PdO:Dx results, 100–109
  Pd/PdO:Dx target, 116
  sample-detector holder, 97*f*
  sequential etching of detectors 1 and 2, 103–104, 107–108
  shift in peak track diameter following sequential etching, 104, 105*f,* 106*f*
  stimulation of Pd and Ti deuteride targets, 115
  thick target yield expression, 112–113
  TiDx foils under e-beam irradiation, 116
  TiDx results, 109–111
  TiDx target, 114–115
  track diameter vs. removed depth for alpha tracks during etching of detectors, 107*f*
  track diameter vs. removed depth for proton tracks during etching of detectors, 106*f*
Deuterium molecular ion D_3^+ ion, Langevin equation, 205–206
Deuterium molecule (D_2)
  Langevin equation, 198–201
  localization of electron wave, 199*f*
  semi-classical image of, 199*f*
  spiral motion for, 201*f*
  trapping potential of d–d pair for, 201*f*
Deuterium-palladium system
  charged particles, 19
  excess heat, 16–17
  low energy nuclear reaction (LENR), 15, 16*f*
  neutrons, 18–19
  new metals, 20
  Pd-CaO multi-layer on palladium, 13
  tritium and mass–3, 19
  See also Palladium deuteride
Deuterium-titanium system
  charged particles, 19
  frequency spectrum measurements with TiD_2 targets, 51
  neutrons, 18, 19
  tritium, 19
Deuteron-cluster dynamics
  double platonic symmetry, 207–208
  HMEQPET method for fusion rate quantification, 213–215
  Langevin equation for 4D/TSC and numerical solution, 207–212
  Langevin equation for D(H)-atom and molecules, 195–206
  See also Langevin equations
Deuteron clusters, Bose–Einstein, 245–247
Double platonic symmetry, 4D/TSC, 207–208
Dual laser stimulation
  beating experiments, 89
  cell in temperature-controlled enclosure, 84*f*
  temperature dependence of excess power, 88–89
  See also Palladium deuteride

E

E-beam irradiation. *See* Deuterium excitation in metal deuterides
Ejecta sites, multi-bubble cavitation, 160
Electric field, Fleischmann–Pons excess heat effect, 188
Electrolysis
  circuit diagram, 68*f*
  diagram of experiment, 63*f*
  heavywater, of Pd foil, 64, 65*f*
  lightwater, of Pd foil, 64, 65*f*
  titanium cathodes, 62
  See also Palladium with hydrogen isotopes
Electrolyte samples
  neutron and tritium generation, 44*t,* 45*t*
  tritium levels in, 42–44

Downloaded by 89.163.35.42 on June 28, 2012 | http://pubs.acs.org
Publication Date (Web): December 20, 2009 | doi: 10.1021/bk-2009-1029.ix002

Electromagnetic dynamics, Fleischmann–Pons effect, 186–188
Electromagnetic energy, collective harnessing, 266–267
Electromagnetic interaction (EMI), time-dependent changes, 178
Electro-weak (EW) induced low energy nuclear reactions (LENR)
  acceleration of electron from charge oscillations on surface, 260–261
  Alfvén current, 255, 257
  change in current, 258
  change in magnetic energy, 258
  collective harnessing electromagnetic energy, 266–267
  collective oscillation surface plasmon polariton (SPP) mode, 259
  condensed matter collective system, 261–263
  exploding wire problem, 254–255, 264
  genesis, 256–259
  highest-energy electron-proton colliding beam (HERA), 255
  interactions between collectively oscillating protons and SPP electrons, 263
  magnetic mode of exciting electron capture, 254–255, 257
  metallic hydride cells, 254, 259–263
  neutron scattering on palladium hydride, 260
  numerical estimates for sun, 258
  solar corona, 257–258, 265–266
  solar flares, 258–259, 265–266
  ultra-cold neutrons, 254
Elements in universe, standard abundance distribution (SAD), 220, 222*f*
Energy, internal, of bubble, 140
Excess heat. *See* Fleischmann–Pons excess heat effect; Heat, excess
Excess power, temperature and production, 88–89
Excitation of deuterium. *See* Deuterium excitation in metal deuterides
Exothermic reaction, optical phonon triggering, in palladium deuteride, 86
Exploding wires, electro-weak induced low energy nuclear reactions, 254–255, 264

F

Fermi distribution, Debye layer confinement for nucleons with, 224–227
Fleischmann, Martin
  "cold fusion" discovery, 3
  deuterated palladium, 81–82
Fleischmann–Pons excess heat effect
  Coulomb barrier, 177–180
  magnetism, 188–191
  quantum mechanics, 180–183
  resonant and near-resonant interactions, 183–186
  resonant effect involving magnetism, 188–191
  resonant electromagnetic-dynamics, 186–188
Frequency spectrum
  Milton Roy electrolytic cell, 50–51
  TiD_2 targets, 51
Fusion, heat pulse, 165–166
Fusion rate, HMEQPET method for, quantification, 213–215

G

Gamma radiation, transient cluster density, 164
Gamow theory, fusion process, 183

Downloaded by 89.163.35.42 on June 28, 2012 | http://pubs.acs.org
Publication Date (Web): December 20, 2009 | doi: 10.1021/bk-2009-1029.ix002

Gas phase. *See* Low energy nuclear reactions (LENR) in gas phase

H

Hagelstein, Peter, phonons and solid-state fusion of deuterium, 82–83
Hahn–Strassmann, discovery of nuclear fission, 237–238
Hawkins, Marvin, deuterated palladium, 81–82
Heat, sonofusion process product, 159
Heat, excess
  deuterium through palladium foils, 16–17, 18*f*
  helium production and, 17, 18*f*
  Holy Grail of researchers, 9–10
  Ni hydrogen experiments, 47–48
  Pd cathode with titanium addition to electrolyte, 69, 70*f*
  Ti additions to experimental cell electrolyte, 69
  See also Fleischmann–Pons excess heat effect
Heat pulse, fusion, 165–166
Heavy water electrolysis
  palladium foil, 64, 65*f*
  See also Palladium with hydrogen isotopes
Helium
  Arata and Zhang system, 11*f*
  double-structure cathode, 11*f*
  excess heat and, detection, 10, 12
  mass flow calorimeter, 11*f*
  mass spectral analysis, 166–167
  production and excess heat, 17, 18*f*
  See also Sonofusion
Helium-4
  fusion product measurement, 166, 167*t*
  production, 17, 18*f*
  sonofusion process product, 159
Heretics, "cold fusion" researchers, 4
HMEQPET method, fusion rate quantification, 213–215
Hot fusion research
  sonofusion development, 163–164
  See also Sonofusion
Hydrogen isotopes. *See* Palladium with hydrogen isotopes

I

India. *See* Bhabha Atomic Research Centre (BARC)
Induction heater, Ti heated in deuterium gas, 46
Isoperibolic calorimetry
  instrumentation and, 83–84
  long-term stability, 84
Isotopes. *See* Palladium with hydrogen isotopes

L

Langevin equations
  4D/TSC and numerical solution, 207–212
  4D/TSC and solution, 208–211
  $6D^{2-}$/OSC, 212
  central trapping potential of 4D(H)/TSC vs. $6D^{2-}$/OSC potential, 209*f*
  condensation of 4D/TSC and 4D-fusion to 4He-particles break-up, 209*f*
  D(H)-atom and molecules, 195–206
  D_2 molecule, 198–201
  D_2^+ ion, 202–203
  D_3^+ ion molecule, 205–206
  D-atom, 195–197
  double platonic symmetry, 207–208
  expectation values for complex D-clusters, 203–204

Downloaded by 89.163.35.42 on June 28, 2012 | http://pubs.acs.org
Publication Date (Web): December 20, 2009 | doi: 10.1021/bk-2009-1029.ix002

Downloaded by 89.163.35.42 on June 28, 2012 | http://pubs.acs.org
Publication Date (Web): December 20, 2009 | doi: 10.1021/bk-2009-1029.ix002

- general, 195
- incubation of 4D/TSC in PdD dynamics, 211*f*
- numerical results of 4D/TSC condensation motion, 210*f*
- one-dimensional, 194
- quantum-mechanical, 216
- TSC trapping potential at final stage, 214*f*
- *See also* Deuteron-cluster dynamics

Larmor frequency, external magnetic field, 191

Linear energy transfer (LET)
- energy as function of water film thickness, 125
- particle energetics, 126

Liquid scintillation counting, tritium levels, 42

Liquid scintillation detector, bubble fusion, 147

Low energy nuclear reactions (LENR)
- Bose–Einstein deuteron clusters, 245–247
- electro-weak (EW) interactions, 253–254
- experimental papers, 4
- government research, 3–4
- magic numbers from, 241–242
- palladium-deuterium system, 15, 16*f*
- paradox about high magic numbers by, 231–233
- research field, 3
- "soft" fission, 236
- transmutations, 236
- uranium fission and, transmutation array, 238–241
- *See also* Bhabha Atomic Research Centre (BARC); Electro-weak (EW) induced low energy nuclear reactions (LENR)

Low energy nuclear reactions (LENR) in gas phase
- Arata and Zhang, 10, 12
- Arata and Zhang double-structure cathode and mass flow calorimeter, 11*f*
- Arata and Zhang system for comparing cell operation, 11*f*
- charged particles, 19
- excess heat, 16–17, 18*f*
- experimental proofs, 16–20
- experimental results, 10–15
- Fralick et al. at NASA in 1989, 10
- helium, 17, 18*f*
- Iwamura and co-workers, 13–14
- neutrons, 18–19
- Piantelli and co-workers, 15, 16*f*
- transmutations, 20
- tritium and mass–3, 19

M

Magic numbers
- abundance distribution diagram and, 228
- Boltzmann distribution from standard abundance distribution (SAD) for, 221–223
- colored quark-gluon plasma and, 229–231
- low energy nuclear reaction (LENR) data, 241–242
- model based on SAD of elements of university, 220, 222*f*
- paradox about, by LENR, 231–233
- production rate probability at LENR, 232*f*
- sequence of, 223, 224*f*
- sequences of, and ratios based on SAD measurements, 223*t*

Magnetars, 266

Magnetic field, external, 190–191

Magnetic stars, 266

Magnetism, resonant effect in Fleischmann–Pons excess heat, 188–191

Downloaded by 89.163.35.42 on June 28, 2012 | http://pubs.acs.org
Publication Date (Web): December 20, 2009 | doi: 10.1021/bk-2009-1029.ix002

- Mass-3, tritium or helium-3, 19
- Mechanisms
  - cluster formation, 246
  - understanding for nuclear-scale energy, 4–5
- Metal deuterides. *See* Deuterium excitation in metal deuterides
- Metal hydrides. *See* Deuterium excitation in metal deuterides
- Metallic hydride cells
  - collective oscillation surface plasmon polariton (SPP) mode, 259
  - condensed matter collective system, 261–263
  - electro-weak induced low energy nuclear reactions, 254
  - interactions between collectively oscillating protons and SPP electrons, 263
  - neutron scattering on palladium hydride, 260
- Miles, Melvin, D-D fusion and He-4, 82
- Milton Roy cell
  - concomitant generation of neutrons and tritium, 43*f*
  - frequency distribution measurement runs, 50–51
  - neutron counts variation during, 37
  - neutron output of quiescent, 40*f*
  - quiescent, study, 50
  - steady neutron production by New, 40, 41*f*
- Modeling. *See* Monte Carlo simulations; Quark-gluon plasma
- Mode resonances, optical phonon, 85–87
- Molybdenum
  - formation in deuterium atmosphere of palladium, 20
  - strontium and deuterium, 14
- Monte Carlo simulations
  - bubble fusion experimental neutron spectra, 146–147, 149, 154
  - external accelerator-based neutron-seeded experiments, 149, 150*f*
  - predictions vs. measured neutron response, 148*f*, 149*f*
- Multi-bubble cavitation, ejecta sites, 160
- Multibubble sonoluminescence effect, bubble nuclear fusion, 4

N

- Neutron activation analysis (NAA)
  - combining secondary ion mass spectroscopy (SIMS), 243–244
  - identification of elements, 243
- Neutron generation, electrolysis experiments with tritium and, 44*t*, 45*t*
- Neutron multiplicity
  - artificial dead-time method, 49
  - burst neutron measurements using dead-time method, 52
  - dead-time method results, 52–53
  - frequency spectrum measurements, 50–51
  - frequency spectrum measurements with TiD_2 targets, 51
  - principle of statistical analysis of neutron output, 49
  - statistical analysis measurements, 53
  - theoretical considerations, 49–50
- Neutrons
  - bubble fusion, counts above 2.45 MeV proton-recoil edge, 150–151
  - burst, using dead-time method, 52
  - concerns about external source of, 144
  - concomitant generation of, and tritium run 2 of Milton Roy cell, 43*f*

Downloaded by 89.163.35.42 on June 28, 2012 | http://pubs.acs.org
Publication Date (Web): December 20, 2009 | doi: 10.1021/bk-2009-1029.ix002

- counts in bubble fusion experiments, 141, 142*f*
- count variation during run 1 of Milton Roy cell, 37*f*
- deuterium-palladium foil, 18–19
- deuterium-titanium system, 18–19
- electrolytic cells and, measurement, 37–41
- emission from TiD disc, 41*f*
- mechanism for neutron bursts, 55
- output of quiescent Milton Roy cell, 40*f*
- production with bubble fusion, 145–146
- pulse-pileup effects, 151, 152*f*
- reaction with ^{235}U leading to branch with beta decays, 237*f*
- steady neutron production by New Milton Roy cell, 40, 41*f*

Nickel hydrogen experiments
- excess heat, 47–48
- tritium measurements, 48
- tritium production, 55

Nuclear emissions
- bubble fusion, 153
- *See also* Bubble nuclear fusion

Nuclear energy release, lattice phonon field, 82

Nuclear fission
- Hahn–Strassmann discovery, 237–238
- mass distribution curves for ^{233}U, ^{235}U and ^{239}Pu, 239*f*
- mass distribution curves for ^{236}U, 239*f*
- nuclear mass spectrum of LENR products generation probability, 241*f*
- rates for products from thin film LENR vs. proton number, 240*f*

Nuclear fusion. *See* Bubble nuclear fusion

Nuclear-scale energy, mechanism development, 4–5

Nucleons
- confining, by surface energy, 226*f*
- Debye layer confinement for, with Fermi distribution, 224–227
- Debye length, 224, 225
- Fermi energy, 225

Nucleus Shell model, deuteron, 160

O

Optical phonon
- beat frequencies, 86*f*, 87*f*
- low-momentum acoustical modes, 89–90
- mode resonances, 85–87
- zero-momentum, 89

Optical phonons. *See* Palladium deuteride

P

Palladium deuteride (Pd/D)
- band diagram for, 83*f*
- beating experiments using dual-laser configuration, 89
- cell configuration, 85*f*
- excess power, 90
- exothermic cathode response, 86
- experimental, 85
- experimental data from three cells, 93*t*
- experimental support for theory, 82–83
- instrumentation and calorimetry, 83–84
- isoperibolic calorimeter and long-term stability, 84*f*
- low-momentum acoustical modes, 89–90
- optical nonlinearity, 89
- optical phonon mode resonances, 85–87
- source of energetic particles, 120

- temperature-controlled enclosure with dual lasers, 84*f*
- temperature dependence of excess power, 88–89
- theoretical ideas, 82
- triggering beat frequencies, 87*f*
- zero-momentum optical phonon band edges, 89
- *See also* Deuterium excitation in metal deuterides; Radioisotope thermoelectric generator (RTG)

Palladium foil
- cavitation-exposed Pd target, 164–165
- new metals on, in deuterium atmosphere, 20
- *See also* Deuterium-palladium system

Palladium with hydrogen isotopes
- Auger electron spectroscopy (AES) analyses, 73*t, 74t*
- circuit diagram for electrolysis, 68*f*
- counts per second for convex side of electrolyzed palladium (Pd) foil, 75*f*
- counts per second for Pd foil control, 75*f*
- D_2O-H_2SO_4 electrolyte and Pt anode, 67
- depth profile of mass 107 to 109 signals for Pd after electrolysis, 76*f*
- depth profiles for Pd isotopes after H_2O and D_2O electrolysis, 65*f*
- diagram of electrolysis experiment, 63*f*
- excess heat after Ti content increase, 69*f*
- excess heat for consecutive runs, 70
- excess thermal power, 62
- excess thermal power with and without mass correction, 70*f*
- experimental methods, 63–64, 67–68
- heavy-water and light-water cells, 63*f*
- Pd cathode with Ti added to electrolyte, 70
- Pd foil by secondary ion mass spectroscopy (SIMS), 64, 65*f*
- Pd transmutation to stable Ag isotopes, 76, 77
- scanning electron microscopy (SEM) photo of concave side of Pd cathode, 73*f*
- SEM photo of convex side of Pd cathode after electrolysis, 74*f*
- side facing anode and back side of Pd electrode, 70, 71*f*
- signal from 110 Pd vs. 104 Pd, 66
- SIMS depth profile from different area of same Pd cathode, 66*f*
- SIMS depth profiles for Pd 104 and Pd 110, 66, 67*f*
- SIMS profiles from different regions of Pd foil, 65, 65–66
- Ti addition to electrolyte and thermal power, 69
- transmutation of Pd to Ag isotopes, 76
- X-ray spectra of concave and convex sides of Pd electrode, 70, 71 *f*
- *See also* Electrolysis with palladium cathodes; Palladium with hydrogen isotopes

Phonons
- role in solid-state fusion of deuterium, 82
- *See also* Palladium deuteride

Plasma focus device
- autoradiograph of Ti, electrode, 47*f*
- high-voltage discharge in method, 46–47

Pons, Stanley
- "cold fusion" discovery, 3

Downloaded by 89.163.35.42 on June 28, 2012 | http://pubs.acs.org
Publication Date (Web): December 20, 2009 | doi: 10.1021/bk-2009-1029.ix002

Downloaded by 89.163.35.42 on June 28, 2012 | http://pubs.acs.org
Publication Date (Web): December 20, 2009 | doi: 10.1021/bk-2009-1029.ix002

  deuterated palladium, 81–82
Pons–Fleischmann reaction, conventional cold fusion, 242
Praseodymium formation, deuterium atmosphere of palladium, 20
Pulse-pileup, neutrons in bubble fusion, 151, 152*f*

Q

Quantum-electrodynamics (QED), energy band theory, 179
Quantum mechanics
Quantum mechanics (QM)
  electron cloud for 4D/TSC, 207*f*
  ensemble average for D-cluster, 198
  Fleischmann–Pons excess heat effects, 178
  image of D-atom, 196*f*
  wave function for 4D/TSC, 207
Quark-gluon plasma
  abundance distribution diagram and magic numbers, 228
  colored, and magic numbers, 229–231
  cubic, lattice with central u-quark, 230*f*
  imposed quark q' with central u-quark, 231*f*
  media as ideal gas, 229*f*
  See also Magic numbers

R

Radiation absorption, metal hydrides, 96
Radiation emissions
  Pd/D co-deposition, 129, 130*f*
  radioisotope thermoelectric generator (RTG), 128–131
  temporal measurements of X-rays and γ-rays, 130–131
  X-rays and γ-rays in Pd/D system, 129, 130*f*
Radioactive sources, radioisotope thermoelectric generator (RTG), 120, 121*t*
Radioisotope thermoelectric generator (RTG)
  computer modeling of track, 128*f*
  computer program TRACK_TEST, 127, 128*f*
  control experiments, 122–123
  CR-39 calibration for alphas, tritons, and protons, 125*f*
  CR-39 detectors, 121, 122*f*
  CR-39 detectors interacting with neutrons, 131, 132*f*
  description, 119
  diameters of ^{241}Am- and Pd/D-generated pits vs. etch time, 123*f*
  experimental, 121–122
  external field experiments, 124
  fogging of photographic film after Pd/D co-deposition, 129, 130*f*
  geometry of track development, 128*f*
  half-life of fuel, 120
  linear energy transfer (LET) curves, 125
  Pd/D system, 120
  properties of sources used in, 121*t*
  radiation emissions, 128–131
  scanning electron microscopy (SEM) of Pd deposit, 125*f*
  schematic of, 120*f*
  schematic of electrochemical cell for spacer experiment, 122*f*
  Seebeck effect, 119
  size distribution of tracks for CR-39 exposed to ^{241}Am alpha source, 125*f*
  size distributions of energetic particles during Pd/D co-deposition, 126
  software of automated scanning system, 126

  - spacer experiments, 124–126
  - temporal measurements of X-rays and γ-rays, 130–131
  - track modeling, 126–127, 128*f*
  - X-rays and γ-ray emissions in Pd/D system, 129, 130*f*

- Reciprocal lattice vector, concept, 189–190
- Replications, bubble fusion, 145–146
- Resonance
  - definition, 185
  - Fleischmann–Pons effect, 186
  - and near-resonant interactions, 183–186

S

- Samarium, transmutation of barium to, 14, 15*f*
- Scientific feasibility, bubble nuclear fusion, 143
- Secondary ion mass spectroscopy (SIMS)
  - combined with neutron activation analysis (NAA), 243–244
  - depth profile from different area of same Pd cathode, 66
  - depth profiles for Pd 104 and Pd 110, 66, 67*f*
  - depth profiles of Pd isotopes with electrolysis, 64, 65*f*
  - mass composition, 14
  - *See also* Palladium with hydrogen isotopes
- Self-nucleation, bubble fusion, 144, 145*f*
- Sequential etching
  - CR-39 detectors, 123
  - detectors, 103–104, 107–108
  - shift in main peak track diameter, 104, 105*f*, 106*f*
  - track diameter vs. removed depth dependences for alpha tracks, 107*f*
  - track diameter vs. removed depth dependences for proton tracks, 106*f*
  - *See also* Deuterium excitation in metal deuterides
- Silver (Ag), transmutation of Pd to stable isotopes of, 76, 77
- Simulations. *See* Monte Carlo simulations
- Software, energy of particles, 126
- Solar corona, electro-weak induced low energy nuclear reactions, 255, 257–258, 265–266
- Solar flares, electro-weak induced low energy nuclear reactions, 255, 258–259, 265–266
- Sonofusion
  - calorimetric experiments, 169, 170*f*
  - cavitation bubble, 161–163
  - cavitation-exposed Pd target foil, 164–165
  - confinement of D^+ plasma, 163
  - experimental, 167–169
  - experimental evidence, 164–165
  - experimental system, 169*f*
  - fusion heat pulse, 165–166
  - fusion products, 159–160
  - He-4 production, 170
  - helium mass spectral analysis, 166–167
  - high density of systems, 171
  - history, 160–161
  - hot fusion research, 163–164
  - lacking gamma radiation, 164
  - plasma configuration of transient compressed jet, 162*f*
  - related technologies, 163–164, 171
  - scanning electron microscopy (SEM) photo of cavitation, 165*f*
  - schematic of 1.6 MHz, device, 168*f*
  - sustained vs. one-time events, 170
- SQUID-type electromagnetic measurements, clusters, 246

Downloaded by 89.163.35.42 on June 28, 2012 | http://pubs.acs.org
Publication Date (Web): December 20, 2009 | doi: 10.1021/bk-2009-1029.ix002

Downloaded by 89.163.35.42 on June 28, 2012 | http://pubs.acs.org
Publication Date (Web): December 20, 2009 | doi: 10.1021/bk-2009-1029.ix002

Srinivasar, Mahadeva, government LENR research, 3–4
Standard abundance distribution (SAD)
  Boltzmann distribution from, for magic numbers, 221–223
  elements in universe, 222*f*
  model for magic numbers, 220
  See also Magic numbers
Strassman and Hahn, nuclear fission, 237–238
Strontium, molybdenum production, 14
Sun
  "magnetars," 266
  "magnetic stars," 266
  solar corona, 255, 257–258, 265–266
  solar flares, 255, 258–259, 265–266
Super-compression-induced fusion, bubble nuclear fusion, 143
Surface plasmon polariton (SPP) mode
  collective oscillation, 259
  interaction of oscillating protons and SPP electrons, 263

T

Temperature, excess-power production, 88–89
Thermal power
  electrolysis with titanium, 62
  See also Heat, excess
Titanium
  addition to electrolyte solution, 68, 69*f*
  autoradiograph of deuterated Ti chip showing tritium hot spots, 46*f*
  autoradiograph of Ti plasma focus electrode, 47*f*
  deuterium gas/plasma-loaded Ti samples, 45–47
  electrolysis with, cathodes, 62
  tritium immobile in, 54
  See also Deuterium-titanium system; Palladium with hydrogen isotopes
Titanium deuterides (TiDx)
  differential spectrum of 11 μm Al:TiDx, 109*f,* 111
  differential spectrum of 26 μm Cu:TiDx, 110*f*
  e-beam irradiated face of, 111
  electron beam in vacuum, 109–111
  experimental, 98
  foreground and background spectra of 33 μm Al:TiDx, 110*f*
  nuclear particle detection, 111
  stimulation of, targets, 115
  target under e-beam bombardment, 116
  TiDx target, 114–115
  See also Deuterium excitation in metal deuterides
Track modeling
  chemical etching, 126–127
  computer program TRACK_TEST, 127, 128*f*
Transmutations
  deuterium through palladium foil, 20
  LENR (low-energy nuclear reactions), 236
  LENR, experiment issues, 242–245
  "miracle" of broad array of products, 242
  Pd to stable Ag isotopes, 76, 77
  uranium fission and LENR, array, 238–241
Trapped photons, 189
Triatomic hydrogen (deuterium) molecular ion
  Langevin equation, 205–206
  Platonic arrangement, 205*f*
  semi-classical view of particle arrangement, 205*f*
Triggering mechanisms, Fleischmann–Pons excess heat effect, 188

Downloaded by 89.163.35.42 on June 28, 2012 | http://pubs.acs.org
Publication Date (Web): December 20, 2009 | doi: 10.1021/bk-2009-1029.ix002

Tritium
  aged-TiD-targets study, 47
  autoradiograph of deuterated Ti chip showing tritium hot spots, 46*f*
  concomitant generation of neutrons and, of Milton Roy cell, 43*f*
  emission rate in bubble fusion, 153
  immobile in titanium, 54
  increase of, in electrolyte following neutron burst, 43*f*
  measurement in electrolyte samples, 42–44
  Ni hydrogen experiments, 47–48
  palladium and titanium with deuterium, 19
  production in bubble fusion experiments, 141, 142*f*
Tritium generation, electrolysis experiments with neutron and, 44*t, 45t*
TSC condensation, time-dependent barrier factors, 215*t*
TSC trapping potential, replacing typical-point-wise HMEQPET potentials with time-dependent, 214*t*

U

Universe, standard abundance distribution (SAD) of elements, 220, 222*f*
Uranium-235
  fission and low-energy nuclear reaction transmutation, 238–241
  neutron reaction, 237–238

W

Water electrolysis
  palladium foil, 64, 65*f*
  See also Palladium with hydrogen isotopes